Stability of Superconducting Strands for Accelerator Magnets

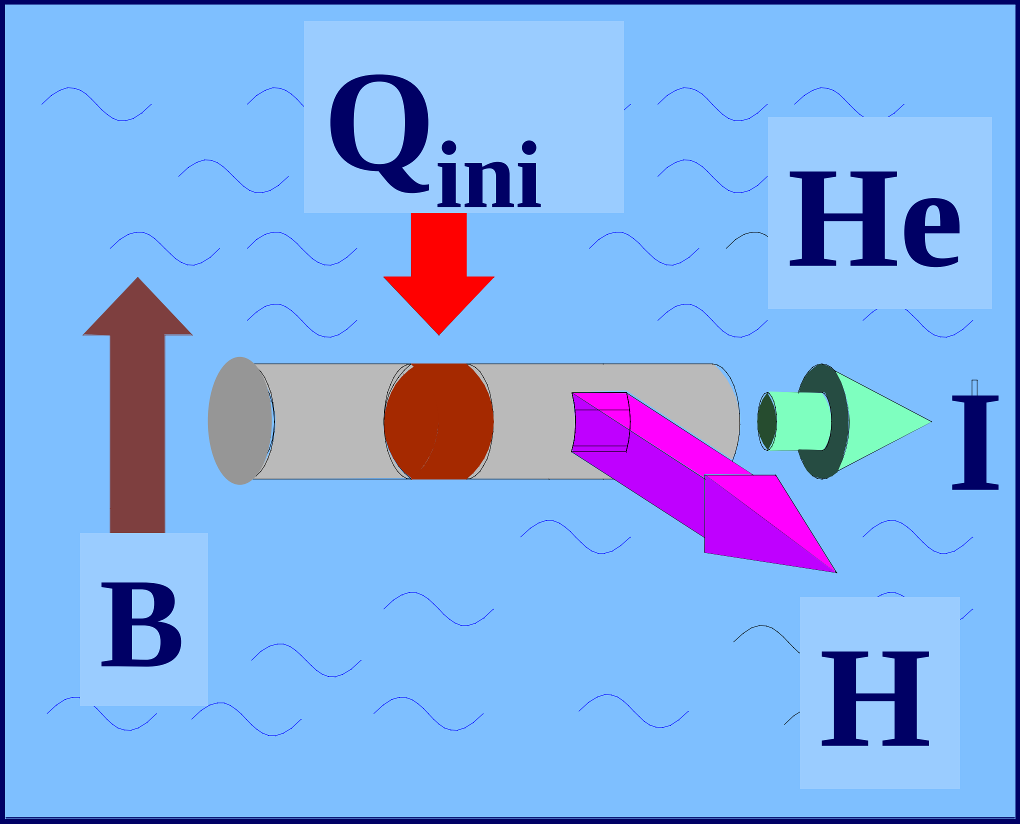

Pierre Bauer

TU

Technische Universität Wien

Dissertation

STABILITY of SUPERCONDUCTING STRANDS for ACCELERATOR MAGNETS

---

ausgeführt zum Zwecke der Erlangung des akademischen Grades eines
Doktors der technischen Wissenschaften unter der Leitung von

Prof. H.K. KIRCHMAYR
INSTITUT für EXPERIMENTALPHYSIK

durchgeführt im

EUROPEAN CENTER FOR PARTICLE PHYSICS CERN
LHC-Division, MMS-Gruppe unter der Leitung von

DANIEL LEROY

eingereicht an der technischen Universität Wien

Technisch-Naturwissenschaftliche Fakultät

von

PIERRE BAUER
Matrikelnummer: 87 03 098
Mondweg 5, 1140 Wien

Wien, am …………………

ACKNOWLEDGMENT

Many thanks to:

Daniel Leroy, Hans Kirchmayr, Martin Wilson, Jean Donnier, Rob Wolf, Arjan Verweij, David Richter, Jean Michel Depond, Jean-Phillipe Marzolf, Luc Oberli, Sander Jongeleen, Seog Whan Kim, Charles Henri Denarie, John Stott, Pierre Jacquot, Jean Louis Servais, Rodolphe Guigue, Angelo Bonasia, Serge Roguet, Dave Adam, Zinour Charifoulline, Sandrine LeNaour, Giancarlo Spigo, Carlo Wyss, Arnaud Devred, Chantal Meuris, Bertrand Baudouy, Arup Ghosh, Elwyn Baynham, Balazs Szeless, Hannes Fikis, Remo Maccaferri, Wim Vollenberg, Sergio Calatroni, Ruediger Schmidt, Marc Teng, Marie-Pierre Fossioz, Claudine Bosteels, Claire-Lise Julien, Celine Krattinger, Sylvie Lachavanne, Jacques Genest, Olivier Monges, Jean-Luc Caron, Jean-Claude Vialis, Andries den Ouden, Vess Kovachev, Alain Lasserre, Edwige Bournonville, Marco Grippeling, Monique Burla, Andrzej Siemko, Robert Herzog, Paolo Fessia, the UCO support, Karl Heinz Schindl, Christian Fabjan, Cecille Granier, Charles Niqueletto and the people who founded and manage(d) the Cern Austrian Doctoral Student Program

for their valuable help and support!

KURZFASSUNG

Die supraleitenden Haupt- (Dipol- und Quadrupol-) Magnete für den Large Hadron Collider (LHC) am Cern bei Genf (derzeit in der Konstruktionsphase) benützen Kabel auf Basis von Kupfer/Niob-Titan Drähten. Diese Drähte haben typischerweise einen Durchmesser von ~1mm, ein Kupfer zu Supraleiter Verhältnis von 1.6 und weisen einen kritischen (=maximalen) Transportstrom von ~750A bei 1.9K/9T auf. Ungefähr 30 dieser Drähte werden zu einem Kabel mit trapezoidalem Querschnitt verflochten. Diese Kabel haben einen kritischen Strom von typischerweise 15kA bei 1.9K/9T. Die Hauptdipolmagnete für den LHC bestehen aus 2 Lagen eines solchen “Rutherford”-Kabels wobei die Kabel so angeordnet sind, dasz sie eine mit $\cos\theta$ modulierte Stromdichte rund um die zentrale Oeffnung erzeugen. Die LHC Beschleunigermagnete sind konzipiert für ein Magnetfeld von ungefähr 9T, werden mit superfluidem Helium auf 1.9K abgekühlt und bei ungefähr 70% ihres kritischen Stroms betrieben. Unter normalen Arbeitsbedingungen sind vor allem die Supraleiter extremen Lorentzkräften ausgesetzt, die Drücke von bis zu 300t/m verursachen. Die Verwendung von Niob-Titan Supraleiter in solchen Umständen führt zu stabilitätsrelevanten Phänomenen wie “training” und dem unvorhersehbaren, irreversiblen und abrupten Zusammenbrechen der Supraleitung bei scheinbar unterkritischen Bedingungen (premature quench). Da es, insbesondere bei der groszen Anzahl von ~1200 Hauptmagneten für den LHC, nicht denkbar ist, dasz jeder einzelne Magnet trainiert wird oder gar bereits arbeitende Magnete hohe Ausfallsraten aufweisen, musz das mechanische design dieser Magnete zur Vermeidung von thermischen und mechanischen Instabilitäten besonders beitragen. Als komplementärer Zugang zu diesem Problem wurde ein Projekt gestartet, welches zum Ziel hat das Verständnis der intrinsischen Stabilität des supraleitenden Kabels selbst zu verbessern. Die hier präsentierte Arbeit versteht sich als Teil dieses Projekts und behandelt die Stabilitaet des kleinsten Elements, des Einzel-Drahtes. Dabei sollte dieses “Unterprojekt” nicht nur die Elementarzelle des komplexeren Kabel-projekts sein, sondern auch ein neues, zusaetzliches Kriterium in der Charakterisierung des Drahtes (strands) bereitstellen.

Als grundlegende Annahme wurde beschlossen, die Stabilität der LHC Leiter bezüglich örtlich und zeitlich beschränkter Störungen zu untersuchen. Das ist angesichts der “quench-Auslöser” (Mikro-Verrückungen eines Drahtes im Kabel, lokale Reibung zwischen Kabel,..) in LHC Magnetprototypen, die oft rasch und lokal bechränkt sind, gerechtfertigt. Die Stabilität eines technischen Supraleiters gegenüber raschen (~µs) und lokalen (~0.5mm) thermischen Störungen kann durch die Meszgrösze Minimale Quench Energie (MQE) quantifiziert werden. Die Minimale Quench Energie MQE ist genau die während kurzer Zeit und in einem Punkt eingebrachte Wärmemenge, die notwendig ist um einen Supraleiter in Arbeitsbedingungen (Magnetfeld, Transportstrom, Temperatur) zu “quenchen”. Erst seit kurzem ist es dank spezieller Heizer auf Basis einer Suspension von Graphit in Epoxy möglich, punktuelle leistungsstarke Heizer für Tieftemperaturaufgaben herzustellen. Wir konnten schlieszlich einen Heizer konstruieren der auf folgendem Prinzip beruht: Ein kleiner (2mm lang, 0.5mm ∅) zylindrischer Körper wird an einem Ende mit einer 40µm dünnen Heizpasteschicht versehen und mittels eines klammerartigen Bauteils gegen den Draht gedrückt. Ein Heizstrompuls (~1A) durchquert die Graphitschicht und führt zu deren Erwärmung, die Wärme erreicht

den Draht in kürzester Zeit. Im Durchschnitt sind 90% des Umfangs des Drahts innerhalb des Apparats gekühlt und man kann davon ausgehen, dasz die Probe mit dem gesamten Kühlbad in Kontakt ist. Als Option ist es möglich den Draht mit einem Schrumpfschlauch vom Kühlmittel zu isolieren. Die im Heizer abgegebene Wärme kann einfach über die zeitliche Integration der elektrischen Heizleistung berechnet werden. Die MQE wird ermittelt indem solange die Pulsenergie variiert wird bis der gerade quenchende und der gerade nicht quenchende Fall gefunden sind.

MQE Messungen wurden an einer Reihe von Drahtprototypen für den LHC vorgenommen mit dem Ziel den Effekt von den folgenden Parametern: Beschichtung, Matrix zu Supraleiter Verhältnis, RRR, "strand-Architektur" und Kühlung im flüssigen Helium, auf die Stabilität zu bestimmen. Spezielle Serien von Proben, die sich nur bezüglich einzelner dieser Parameter unterscheiden, wurden aus der groszen Menge an vorhandenen LHC-Draht-Prototypen zusammengestellt.

Ein Modell, basierend auf den Lösungen der entsprechenden Wärmeleitungsgleichung, wurde entwickelt. Die Schwächen und Stärken des Modells wurden am Vergleich mit dem Experiment erarbeitet. Das Modell wurde verwendet, einerseits zur Erarbeitung des Detail-Verständnisses der Vorgänge rund um einen MQE-Fall und andererseits um die MQE in experimentell nicht erfaszbaren Parameterbereichen zu erforschen.

Das Projekt wurde in Kollaboration mit Gruppen am Appelton Rutherford Labor und dem Brookhaven National Laboratory durchgeführt. Erstere verwendeten eine induktive Wirbelstromheiztechnik und zweitere ebenfalls einen Grahpitheizer, wobei jedoch der Versuch unternommen wurde die Heliumumgebung eines Drahtes in einem echten Kabel-Umfeld zu reproduzieren, d.h. es wurden die Heliummenge in Kontakt mit der Probe und deren gekühlte Oberfläche stark reduziert.

Im wesentlichen hat diese Arbeit gezeigt, dasz aus Stabilitätsgründen:

- RRR gröszer als 100 sein soll (RRR steht für die Qualität des Kupfers in der Matrix),
- Kupfer zu Supraleiterverhaltnis so klein wie möglich sein soll,
- die Beschichtung eher SnAg sein soll als SnNi, CuSn oder ohne,
- die Details der strand Architektur für LHC strands keinen Einflusz haben,
- interne CuNi-Barrieren nicht ratsam sind und
- dasz insbesondere im superfluiden Helium der bei weitem gröszte Beitrag zur Stabilität durch die Kühlparameter (Helium-Volumen, Wärmetransferkoeffizienten der Drahtoberfläche) gegeben ist, die jedoch für die Drähte im realen Kabel-Magnet-Verbund wahrscheinlich nicht die Schwellenwerte erreichen, die notwendig sind um von dem Kühlpotential von superfluidem Helium ernsthaft zu profitieren.

Ferner hat es diese Arbeit erlaubt Gröszenordnungen für die quench Energie, die quench Ausbreitungsgeschwindigkeit und andere mit dem MQE Prozess verbundene Gröszen mit relativ hoher Genauigkeit (dank einer guten Statistik) zu etablieren und das "Standardmodell" der Supraleiterstabilität erstmals teils zu verifizieren, teils zu verbessern.

Nicht stichhaltig waren die Versuche Phänomene wie das premature quenching (quench bei I<Ic) bei kritischen-Strom-Messungen auf eine reduzierte MQE zurückzuführen, wobei jedoch wie schon zuvor weitere experimentelle Hinweise darauf gefunden wurden.

Wir glauben, dasz diese Arbeit Unklarheiten bezüglich der Supraeiterstabilität in LHC Magneten beseitigt hat und, dasz in der Zukunft auch das ITER Projekt, sollte es tatsächlich zur NbTi Variante greifen, davon profitieren wird können.

ABSTRACT

The main superconducting magnets (bending dipoles and focusing quadrupoles) for the Large Hadron Collider (LHC), presently under construction at CERN at the outskirts of Geneva (Switzerland), use superconducting cables made from copper-matrix / niobium-titanium-superconductor strands. The strands for the LHC magnets have typically a diameter of 1mm, a copper to superconductor ratio of 1.6 and a critical current of 750A at 1.9K/9T conditions. Roughly 30 of these strands are twisted together to a Rutherford-type cable with trapezoidal cross-section. The cables have critical currents of roughly 15kA at 1.9K/9T. The main dipole magnets of the LHC are wound from 2 layers of such cables distributed in such a way around the bore (beam-pipe) that the produce a cosine shaped current-distribution. The operation conditions for the conductors in the magnets are roughly an ambient temperature of 1.9K (superfluid helium), a magnetic field of 9T, a transport current of 70% of the critical current and a Lorentz-force level which can achieve some 300 tons per meter. Operating NbTi-based superconductors in such demanding conditions inevitably challenges as well their stability with respect to mechanical and thermal perturbations occurring during ramping and operation. As part of a wider program to improve the understanding of the stability of Rutherford-type superconducting cables in accelerator magnets some efforts have been directed to the investigation of the stability of the sub-unit of the cables: the single strands. The work presented here establishes the effect of all the relevant parameters on the stability of superconducting strands for the LHC main magnets and therefore not only introduces a novel element in the characterization of superconducting strands but also intents to facilitate the understanding of the stability in more complex entities like cables or magnets.

The stability of superconductors with respect to external perturbations of short duration (~µs) and small extent (~0.5mm) is characterized by their Minimum Quench Energy (MQE), i.e. the minimum heat pulse needed to trigger a quench in an operating superconductor in the limit of δ-like perturbations. Point-like and short time heaters have only recently been developed using graphite paste heaters. Several attempts to develop a graphite paste heater technique, which at the same time interacts the least possible with the sample and operates with a low heat loss fraction, finally led to a so called tip-heater design. The tip heater consists of a tip with a thin (~40µm) resistive graphite paste deposit on top. The tip is pressed against the sample by means of a clamp. The heat is generated by a small (~1A) heater current pulse crossing the resistive deposit and then rapidly diffuses through the sample due to the small heater volume <<0.001mm^3. A thermo-retracting sleeve can be used to produce adiabatic conditions. The energy dissipated is calculated from integrating voltage and current over/in the heater over the pulse duration. MQE's are established by repeatedly testing with different pulse energies until the just quenching and the just not quenching case are found. This experimental technique was applied on a series of prototype strands for the LHC magnets with the aim of establishing the effect of various strand parameters, like coating, Cu/Sc ratio, RRR, billet design and cooling on their Minimum Quench Energy. Special strand series have been prepared, which varied with respect to only one of the above mentioned parameters at the time. A theoretical model based on the numerical solution of a one-dimensional heat balance equation was validated comparing it to the measurements.

Thus, having gained confidence in the model, it was used to predict the effect of all the parameters mentioned above in their full range of variation, which in many cases was not totally accessible to measurements.

To improve the reliability of the experimental work other institutions, Brookhaven National Laboratory and Rutherford Appelton Laboratory, were invited to collaborate in this project, using their own measurement technique. The former used a similar graphite paste heater technique with the only difference that instead of operating in the whole spectrum of cooling conditions as in the case of the Cern tip-heater they intended to simulate the restricted cooling environment (reduced amount of cooling liquid in contact with the strand, reduced cooled perimeter fraction) the strand finds in a real cable being part of a magnet. The latter used an inductive heater and specialized in long heater cases (when the heater is much longer than the characteristic length of the MQE process and therefore the case looks like an infinitely long heater case) which are very useful in the investigation of the effect of cooling parameters on quench energy.

Concluding, this work showed that for stability reasons:

- RRR (the quality-factor of the matrix) should be above 100,
- the copper to superconductor ratio as small as possible,
- the coating should rather be SnAg than CuSn, SnNi or bare,
- the billet design in LHC-type strands has no substantial influence,
- internal CuNi- or other thermal barriers should be avoided and
- that the strongest contribution to superconductor stability, especially in superfluid helium, stems from the cooling. Unfortunately strands in a real magnet-cable environment can hardly take advantage of the superfluid stability enhancement because the corresponding cooling parameters do not reach the threshold values.

Furthermore besides giving indications of the MQE and the QE (in long heater measurements) this work established the order of many stability related parameters in LHC strands, like quench propagation velocity, quench decision time and quench decision length with high accuracy. The experimental work allowed to verify the standard-model of superconductor stability and allowed to propose some minor modifications to improve it.

Less successful was the attempt to relate the premature quenching of some samples in Ic-measurements to a lower MQE. Although not totally convincing, nevertheless some further hint towards such a correlation emerged.

We believe that this work has clarified the subject of superconductor stability in the case of the LHC project. On one hand it has maybe shattered some hope that superfluid cooling could be a major stabilizing factor in LHC type magnets. On the other hand it erased myths claiming a big influence of billet design on strand stability performance.

Perhaps in the future, the ITER project, in case it uses the NbTi option, could profit as well from the here presented results.

This PhD-work was conducted at CERN, in the magnet group (MMS) of the LHC division, under the supervision of Daniel Leroy and Luc Oberli. Originally the stability project was launched by Daniel Leroy and Martin Wilson in 1995.

Curriculum Vitae

Pierre Bauer *PHYSICIST IN APPLIED SUPERCONDUCTIVITY*

Personal address

Le Radeau
Rue des Battoirs
01710 Thoiry FRANCE
☎: ++33-4-(04)50 20 80 19

Professional address

C.E.R.N LHC/MMS
1211 GENEVA 23
SWITZERLAND
☎ : ++41-22- 767 95 88
Fax : ++41-22- 767 8110
pbauer@mt.msm.cern.ch

GENERAL

-

Nationality: Austrian & French
Date of birth: July 19, 1969 in Vienna (Austria)
Single, no children

EDUCATION

1996-Present

C.E.R.N. (European Laboratory for Particle Physics)
PhD: "*Minimum Quench Energies of Superconducting Strands for Accelerator Magnets*"
Thesis advisors: Prof. H. Kirchmayr (UT Vienna), D. Leroy (C.E.R.N.), M.N. Wilson (Oxford)

1991-96

UT Vienna - Physics
Degree: MSc in experimental physics, passed with honor
Subject Master thesis: "*Eddy Currents in Technical Superconductors*"
Specialization in solid state physics.

1988-89

University of Vienna - Philosophy

EXPERIENCE

1996-Present

PhD work on Stability of Superconductors; Study of Minimum Quench Energy of strands for the Large Hadron Collider (LHC) magnets:

Development of the experimental technique for Minimum Quench Energy Measurements on strands (involving micro-mechanics, cryogenics, finite element simulations, electrical network analysis). Measurement of the Minimum Quench Energies of 30 prototype strands for the superconducting

LHC-magnets and development of a numerical model for the theoretical analysis of the experiments. Coordination and analysis of MQE experiments conducted at Brookhaven Nat. Lab. (A. Ghosh, W.B. Sampson) and Rutherford-Appelton Lab. (D.E. Baynham) in the frame of a collaboration with CERN.

1995-1996

Master Thesis at the UT Vienna
Design of an inductive magnetization measurement facility for strands operating at 0-50Hz ac-fields (0.5T at 45Hz) in a DC bias field (3T) in collaboration with the AS Bratislava (M. Majoros, M. Pollak)
Theoretical and experimental investigation of the frequency-dependence of the eddy-current loss in technical superconductors (ITER and LHC prototype strands).

PUBLICATIONS

"*Eddy Current Loss in Multifilamentary Superconductors*",
Master thesis, UT Vienna, Jan. 96

"*High Frequency (0-60Hz) Inductive Hysteresis Measurement Facility*",
with H. Kirchmayr and H. Fikis
Superlattices and Microstructures, Vol.21, Suppl. A, p.239-244, 1997

"*Magnetization Measurements on Technical Superconductors at High Frequencies*", with H. Kirchmayr, H. Fikis
IEEE Trans. on appl. Superconductivity, Vol.7, No.2, p.274, June 1997

"*Measurement of AC-field Losses (50Hz) on Ag-sheated* $(Bi,Pb)_2Sr_2Ca_2Cu_3O_{10}$ *Tapes*", with A. Kastler, H. Kirchmayr, H. Fikis;
Proceedings of EUCAS, July 1997

"*Tip Heater for Minimum Quench Energy Measurements on Superconducting LHC Strands*",
Int. Note CERN LHC/MMS 98-01, 1998

Contributions to

"*Quench Detection and Protection of the MQT Magnet Family*",
Int. Note CERN LHC/ICP, M. Teng, 1998

Publications for ASC 98:

“*Minimum Quench Energies of LHC Strands*”,
with L. Oberli, R. Wolf and M.N. Wilson

“*Tip Heater for Minimum Quench Energy Measurements on Superconducting Strands*”,
with J. Donnier and L. Oberli

“*Minimum Quench Energy Measurements on Single Strands for LHC Main Magnets*”,
with A. Ghosh, W. Sampson and L. Oberli

“*Transient Stability of LHC Strands*”,
with E. Baynham, D. Cragg, R. Coombs and R. Wolf

This introductory chapter will first give a brief overview over the Large Hadron Collider Project and the superconducting main magnets for the accelerator. Going from the overall magnet-design to the superconducting cables and strands will serve the purpose of introducing the different physics and technology items related to conductor design. Since this thesis deals with the stability of these conductors the conductor and magnet design will be presented from the stability point of view. This approach will naturally lead to a description of the scope of the thesis. The chapter concludes with the nomenclature.

1. SUPERCONDUCTING STRANDS FOR LHC MAIN MAGNETS

1.1 Large Hadron Collider

The Large Hadron Collider (LHC) [Yellow 95] is a superconducting accelerator for protons and heavy ions in the multi-TeV energy range to be installed at CERN in the existing Large-Electron-Positron-Collider (LEP) tunnel (Figure 1.1-1) with a circumference of 27km. Particle physicists expect new phenomena to appear at the TeV energy range [Fabjan 96]. Contrary to the existing LEP in which are measured precisely well established phenomena the LHC will be a "discovery-machine" aiming to test the standard model of particle physics. The LHC project covers two tasks: the accelerator ring with the superconducting magnets and cavities to accelerate the particles and the four detectors ATLAS, CMS, ALICE and LHC-B, which will record the events created by the collision of the accelerated particles (Figure 1.1-2). The following intents to introduce the subject of this work going from the global view of the accelerator to the superconducting strand of the main magnets, which will be dealt with in the following chapters. The photographs have been supplied by the LHC photothèque.

Figure 1.1-1: Aerial view of the outskirts of Geneva with airport, CERN and dotted the accelerator (LEP) with a circumference of 27km.

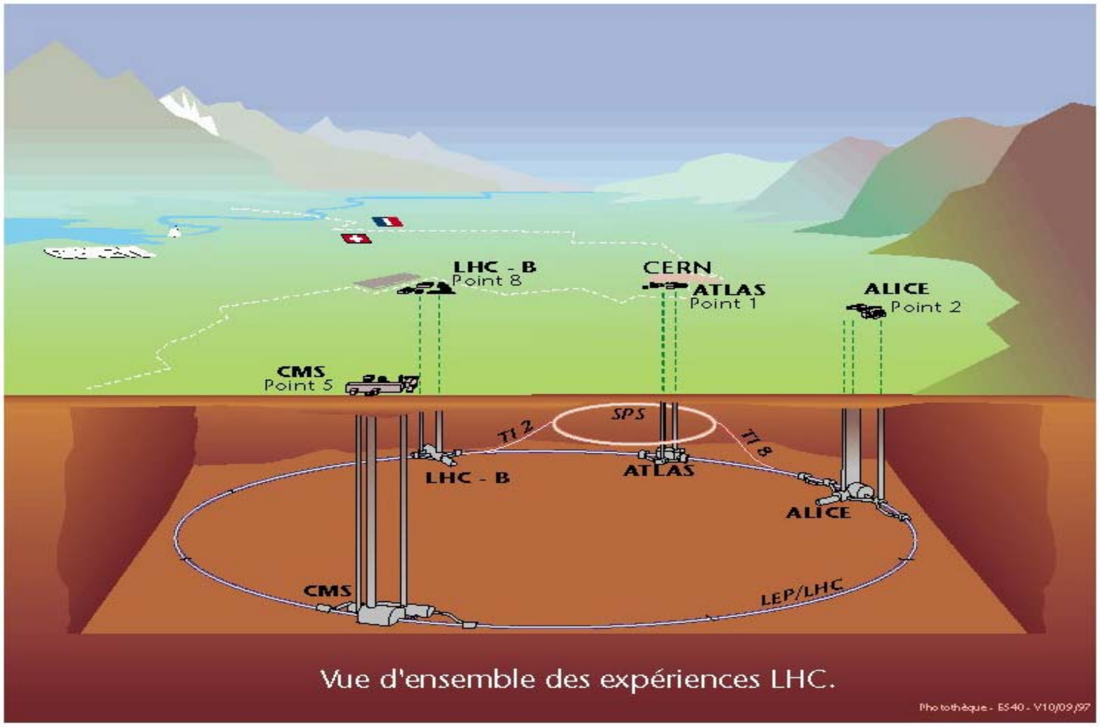

Figure 1.1-2: The LHC accelerator ring: the 4 foreseen detectors are ATLAS, CMS, ALICE and LHC-B. The figure shows as well a former generation accelerator (SPS) which will be part of the chain of pre-accelerators for LHC.

Table 1.1-1 lists the main parameters of LHC-performance.

Energy at collision	7TeV
Energy at injection	450GeV
Dipole field at 7 TeV	8.3274T
Coil inner diameter (300K)	56mm
Distance between aperture axes (1.9 K)	194mm
Luminosity	10^{34}cm^{-2}s^{-1}
Current	0.54A
Bunch spacing	7.48m
Number of particles per bunch	$1.05\text{x}10^{11}$
Normalized r.m.s. transverse emittance	3.75µm
Beta value at IP1 and IP5	0.5m
Total crossing angle	300µrad
Luminosity lifetime	10h
Energy loss per turn	6.7keV
Stored energy per beam	334MJ
Total radiated power per beam	3.6kW

Table 1.1-1: LHC machine parameters;

The LHC is a synchrotron in which a beam of particles is accelerated (by superconducting cavities) and held in a circular orbit by thousands of electromagnets. The magnets make

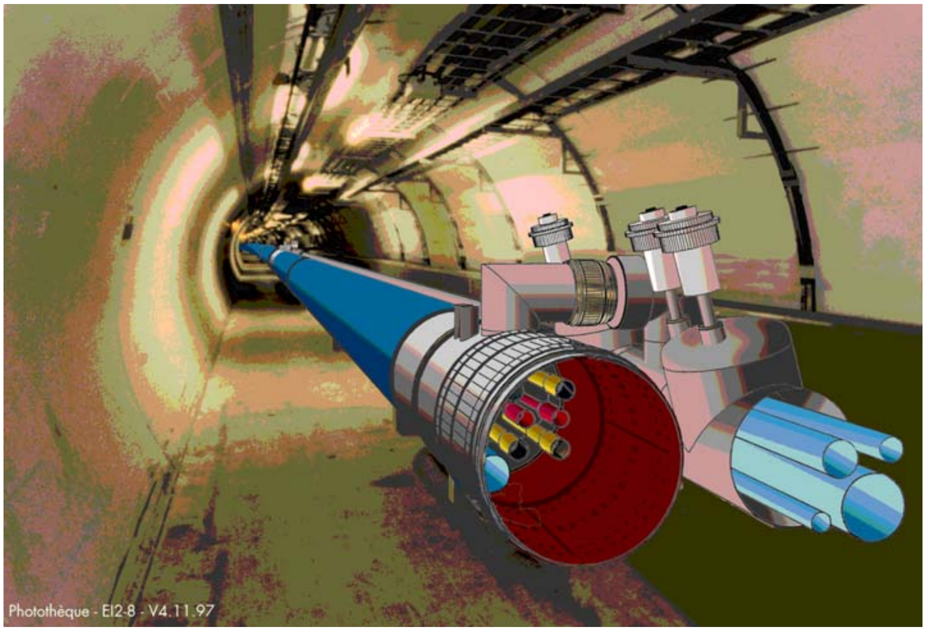

Figure 1.1-3: Artist’s view of superconducting dipole magnets in the accelerator tunnel.

Figure 1.1-4: The first 15m superconducting dipole magnet in its cryostat.

use of NbTi superconductor. To bend proton-beams of some TeV per particle along the curvature of the tunnel, high magnetic fields of approximately 9 T are necessary. The required current density in the electromagnets could be obtained only by operating the magnets at 1.9K in superfluid helium [Perin 91]. Figure 1.1-3 shows an artist’s view of an arc of magnets of the future accelerator in the LEP tunnel. A photograph of the first long prototype dipole magnet is given in Figure 1.1-4. The dipole (bending-) together with the main quadrupole (focusing-)-magnets form the essential elements of the beam guidance. The overall length of the dipole magnet is 15m. 1232 main dipole magnets will be installed in the ring. The main feature of the LHC magnet design is the “two-in-one” concept where both magnetic channels (beam pipes for oppositely directed beams) are incorporated into a single iron yoke and cryostat. The beam tubes (∅ 56mm) can be seen in Figure 1.1-4 together with the helium supplies and electrical connections but the magnet is within the cryostat. Therefore a sketch of the cross-section of the main dipole magnet is shown in Figure 1.1-5.

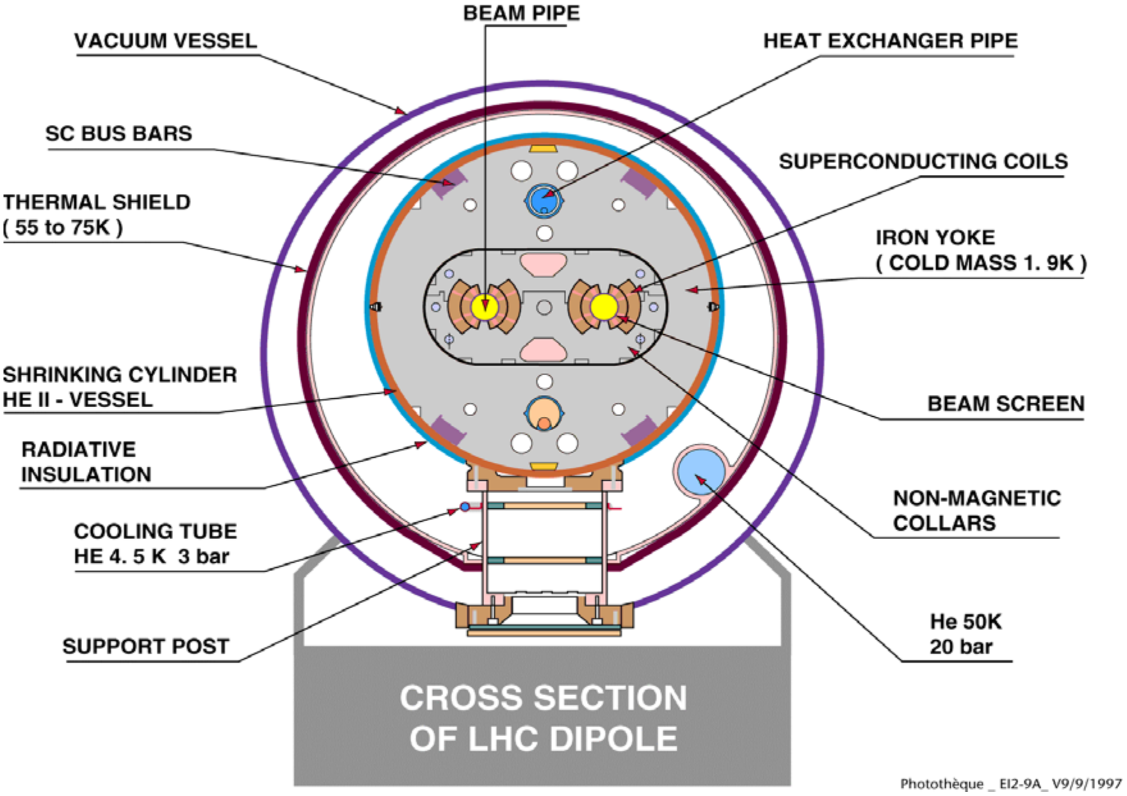

Figure 1.1-5: Cross-section of LHC dipole; The part enclosed by the shrinking cylinder contains the superfluid helium and is called cold mass.

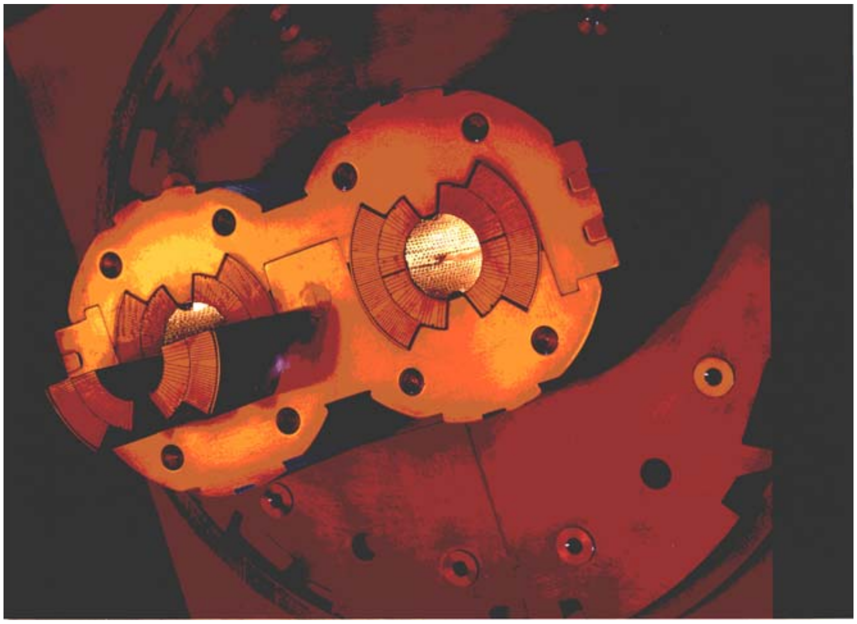

Figure 1.1-6: The collared dipole coils;

A photograph of an assembled prototype dipole magnet (Figure 1.1-6) shows clearly the coils, the collars and in the background the iron yoke. The iron yoke closes the magnetic circuit, and contributes to the mechanical strength of the structure as well as to 20% of the magnetic field density in the bore. The magnet has to be assembled under huge compression [Perini 94] to keep the coils mechanically supported against the Lorentz forces acting during operation and to compensate the differences in thermal contraction of the different materials at cool-down.

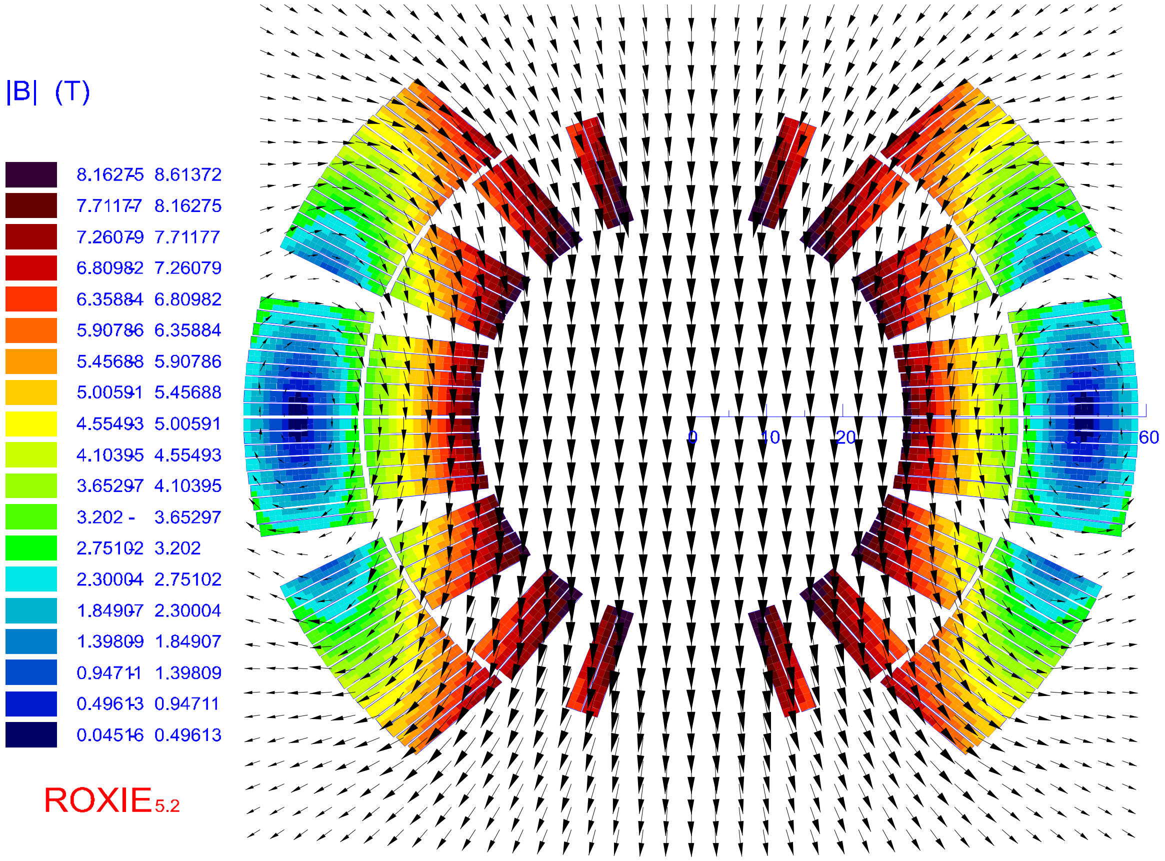

Figure 1.1-7: 2D-field-map of 6-block dipole magnet calculated with ROXIE (S. Russenschuck, personal communication). In this type of plot the field inhomogeneities , which are in the mT-range are invisible. The color code reveals the field strength at the conductor location, the arrows indicate the field direction. In real magnets the spaces between turns are filled with copper wedges.

The extreme complexity of the process stems from two major stipulations:

- accelerator magnets require very precise magnetic fields. Therefore the final position of the conductor has to be controlled to a 5µm precision. Figure 1.1-7 shows a 2D-model calculation of the magnetic field in the cross section of a typical LHC dipole. The magnetic field errors (higher multipole components) are too small to be detectable in such a plot. However the biggest number of the magnets in the ring are corrector magnets annihilating the unavoidable (static and dynamic) field errors of the main magnets.
- the superconducting cables are very sensitive to thermal and electrical disturbances; Very small conductor movements (of some µm) could trigger quenches through frictional heat release. Since the forces on the coils during operation are of the order of 340 tons per meter the structure which gives the relatively soft coils mechanical support has to be well designed and assembled.

The design of the magnet ends requires special attention because there the forces are directed along the longitudinal axis of the magnet (differently from the straight sections where the stress is azimuthal) because the cables bend. Figure 1.1-8 gives an idea of how the cables bend over the beam pipe at the magnet ends.

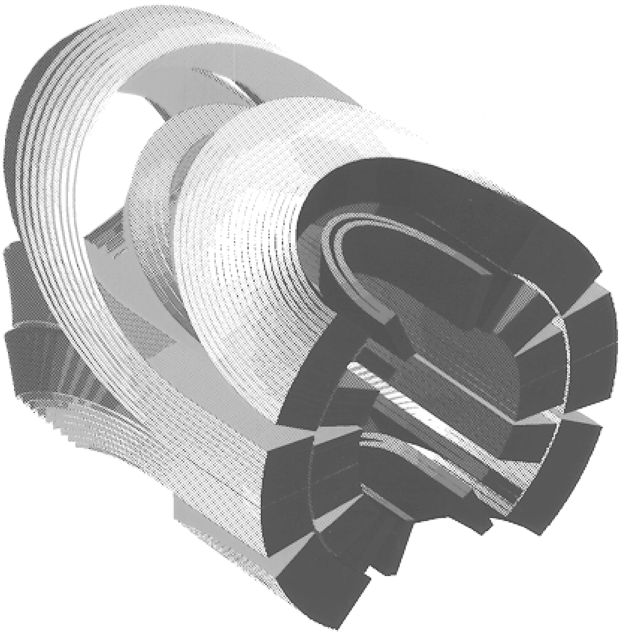

Figure 1.1-8: 3D-plot of the end of a dipole coil; The open spaces are filled with "end-spacers".

Since all the magnets in one octant (154 dipole magnets) of the ring will be connected in series, a quench could destroy a magnet. Therefore a combined system of quench heaters and cold diodes ([Hagedorn 94], [Rodriguez 94]) extracts the energy from a quenching magnet while the whole octant is slowly de-excited (to avoid that the quench spreads to neighboring magnets). However, magnet-quenches should be exceptional and it is the aim of the magnet development to produce magnets with the required field quality which do not train below nominal field. Training, namely the fact that the magnets usually improve their performance from quench to quench during testing of the magnet.

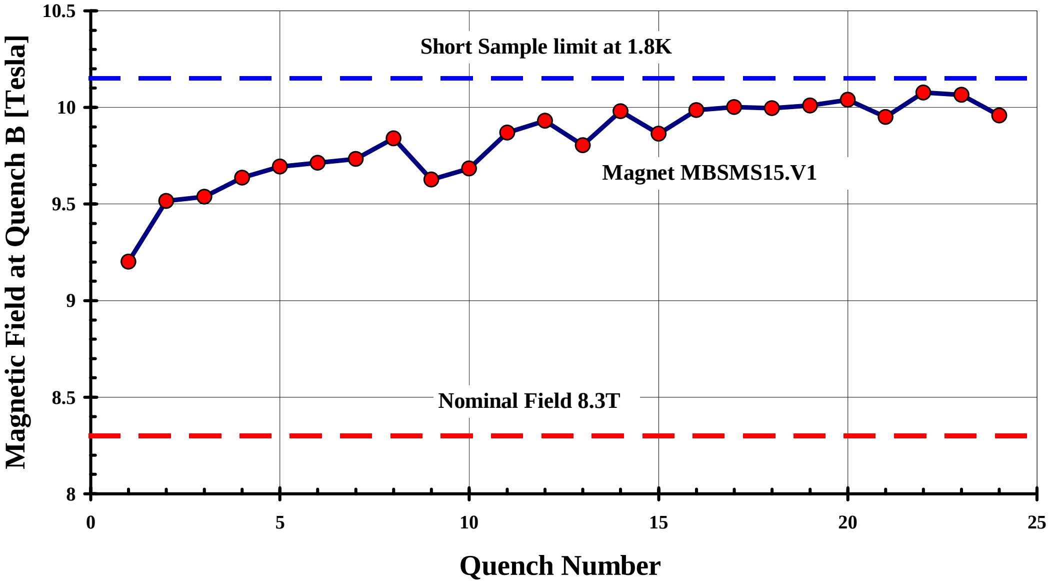

Figure 1.1-9: Training curve of LHC prototype dipole MBSMS.15V1 at 1.8K.

Such a training curve (Figure 1.1-9) ideally converges to the "short sample limit", the maximum magnetic field defined by the critical current of the superconducting cable in the part of the magnet exposed to the peak-field. Superconducting accelerator magnets should reach nominal field without quenches and short sample limit with only a few quenches.

1.2 Superconducting Cables for the LHC Main Magnets

For the superconducting main dipole magnets for the LHC 2370km (~474 tons) of cable 1 (dipole inner layer) and 4600km (~736 tons) of cable 2 (dipole outer layer and quadrupole) will be required. The 1232 arc dipole and the 520 quadrupole magnets of the LHC use NbTi$_{47\%}$ superconducting cables for their coils and operate in superfluid helium at 1.9K temperature at a field varying between 0.58T and 8.4T for the dipoles and at a field gradient up to 223 T/m for the quadrupoles. The dipole coils consists of two layers of Rutherford type cable. Inner / outer layer use a Rutherford type cable made of 28/36 NbTi composite coated strands, 1.065mm / 0.825mm in diameter. The cable and strand

		inner layer	**outer layer**
strand			
	Diameter [mm]	1.065±0.0025	0.825±0.0025
	Copper to Superconductor volume ratio	(1.6-1.7)±0.03	(1.9-2.0)±0.03
	Filament size [µm]	7±0.1	6±0.1
	Filament spacing [µm]	>1	>1
	Number of filaments	(8700-8900)±20	(6300-6550)±20
	RRR	>70	>70
	Twist pitch after cabling [mm]	18±1.5	15.0±1.5
	Critical current 10T / 1.9K	>515	
	Critical current 9T / 1.9K		>380
	n-value at 7T / 4.222K	>30	>30
	Width of hysteresis loop at 0.5T/1.9K	<(30mT)±4.5%	<(23mT)±4.5%
	Thickness of coating [µm]	1	1
	Broken filaments after sharp bend test	<1%	<1%
	Nr. of turns unwinded in springback test	<2.5	<3
cable			
	Number of strands	28	36
	Cable dimensions		
	Mid thickness at 50Mpa [mm]	1.900±0.006	1.480±0.006
	thin edge [mm]	1.736±0.006	1.362±0.006
	thick edge [mm]	2.064±0.006	1.598±0.006
	width [mm]	15.1±0.02	15.1±0.02
	Transposition pitch [mm]	115±5	100±5
	Keystone angle (degree)	1.25±0.05	0.90±0.05
	Aspect ratio (width/mid-thickness)	7.95	10.20
	Critical Current I_c [A] 10T / 1.9K	>13750	
	Critical Current I_c [A] 9T / 1.9K		>12960
	I_c of extracted strand at 1.9K [A]	>505 at 10T	>360 at 9T
	dI_c/dB [A/T]	>4800	>3650
	Variation of I_c of the strands in cable	<±2%	<±2%
	Crossing contact resistance per contact	~15µΩ	~40µΩ
	Contraction after heating to 190°C in 1h	<0.15%	<0.15%

Table 1.2-1: Strand and cable characteristics for the LHC main magnets;

characteristics [CERN 97] are listed in Table 1.2-1. The LHC project will require a considerable fraction of the annual world production of niobium and monopolize a great part of the world-wide superconductor manufacturing capacity between 1999 and 2004. The quality control of the series production consists of a broad range of electrical, dimensional and mechanical tests (I_c-, magnetization-, RRR-, R_c-, dimensional-, dilation-, strand-cross-over-, copper to superconductor ratio-, sharp-bend-, spring-back-, eddy-current-tests) which should guarantee that the final product corresponds to the demanding technical specifications (e.g.: [CERN 97]). The R&D-work in the course of conductor development included many topics. One of them, the "Minimum Quench Energy", is the subject of this thesis. The following describes the main characteristics of the superconducting cables for the LHC magnets with particular emphasis on their impact on superconductor stability.

To prevent shorts between adjacent turns in the magnet, the cables have to be insulated. The insulation (Figure 1.2-1) must safely withstand a turn-to-turn voltage of 75V, be robust in order not to break during winding and curing and be sufficiently porous to let the superfluid helium carry away the heat generated in the cables during operation.

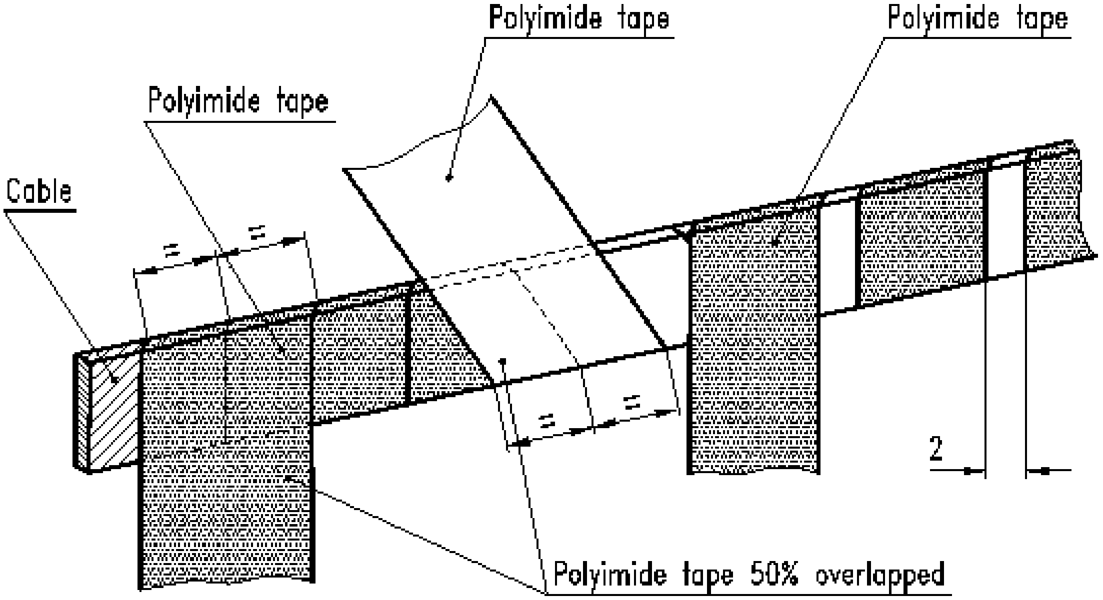

Figure 1.2-1: The superconducting cables are insulated with two wraps of polyimide tape. This technique makes the insulation permeable to superfluid helium. In case of a magnet quench the insulation between the turns and to ground has to withstand high electric fields. Furthermore it has to mechanically sustain high pressures (~40Mpa) and low temperatures (1.9K).

The different sources of heat load on the conductors during normal operation will be separately discussed in chapter 1.2.1. The steady state heat transfer characteristic of different types of insulation-materials and schemes have been evaluated experimentally and theoretically [Baudouy 94]. This work concluded that the insulation should be porous to superfluid helium via small channels which appear for example when the insulation tape is wrapped only with partial or without overlap. During curing under pressure the polyimide insulation flows into the outer interstices between the strands (see Figure 1.1-3).

The LHC-magnets are wound from Rutherford-type-cables to obtain high packing factors, hence low inductance and high overall current density (Figure 1.2-2). Such cables are formed by flattening a hollow tubular cable comprising 28 strands for the dipole inner layer cable and 36 strands for the dipole outer layer cable. Flat NbTi cables can be compacted to filling factors of about 90% without significant damage. The degradation of critical current after cabling is only of a few percent. During the rolling the dimensional control [Adam 96] is important in order to achieve the desired field uniformity in the magnet. The strands in a Rutherford cable are fully transposed with a transposition length (cable pitch) which is usually 6-8 times the cable width. Apart from the fact that the cables have to be designed such that they can carry the transport current density necessary to obtain the required magnetic field plus a safety margin to account for the normal heat load deposited during normal operation (see 1.2.1), various other electromagnetic phenomena may interfere in the proper use of these cables in accelerator magnets. Different types of induced currents can be excited in that particular cable configuration, which differ with respect to the part of the conductor through which they flow [Verweij 95].

- *“Persistent Currents in the filaments (partially) shield the interior of the filaments against external field. The magnitude of these currents depends on the field strength and field history but, in first approximation, not on the field sweep rate*.” On the single strand level these persistent currents cause the quasistatic magnetization which can disturbingly interfere in magnet performance during injection (at 0.58T) (Wolf 92). They can be effectively reduced (but never eliminated) by decreasing the filament diameter.
- *“Interfilament coupling currents (IFCCs) are induced by an external field variation and flow between and in the filaments of a strand. The magnitude of the IFCCs increases with twist length of the filaments and decreasing resistivity of the matrix material. The IFCCs have a characteristic loop length equal to the twist pitch of the filaments, exhibit time constants of typically 0.01 to 0.1s and cause the interfilament coupling loss.”* IFCCs are induced in the magnets during ramping (~ 9T in 1200s) and cause dynamic field errors which can be controlled through ramp-rate, plateau-time and eventually through the copper-RRR in the strands.
- *“Interstrand coupling currents (ISCCs) are also induced by an external field variation and flow between and in the strands of the cable. The magnitude of the ISCCs increases with increasing twist length of the strands and decreasing electrical contact resistance. The ISCCs have a characteristic loop length equal to the twist pitch of the strands, exhibit time constants of typically 0.01 to 10s and cause the interstrand coupling loss.*
- *Boundary-induced coupling currents (BICCs) are mainly induced by variations of the field-sweep rate and the contact resistance along the length of the cable. BICCs can flow in and between strands of a cable and also in and between the filaments of the strand…The loop length and the characteristic time of the BICCs can be several orders of magnitude larger than those of the ISCCs. The additional power loss caused by the BICCs is dissipated in the contact resistance between the strands…”* (quoted from [Verweij 95]).

ISCCs and BICCs cause the so called dynamic field-errors during magnet-operation (snap- back and decay at injection, [Bottura 97]). They can be controlled by specifying the transverse contact resistance R_c between the strands in the cable (the adjacent contact resistance R_a plays a minor role because the magnetic field is mainly perpendicular to the conductor broad face (Figure 1.1-7)). In order to limit the field errors during ramping, the minimum allowed values for R_a and R_c are ~1 respectively 10µΩ per contact [Verweij 94]. A R&D program was launched to find a suitable coating of the strand which guarantees the specified value of R_c even after storage of the cable, curing and long-time performance of the magnets [Richter 97]. For field quality reasons there would be no upper limit of R_c - the upper limit of R_c is imposed by stability considerations: in case of an accidental quench of one or a few strands in the cable the current should easily distribute to neighboring strands allowing the initially quenched strands to recover; during current transfer excessive heating in the inter-strand-contacts should be avoided [Wilson 97b].

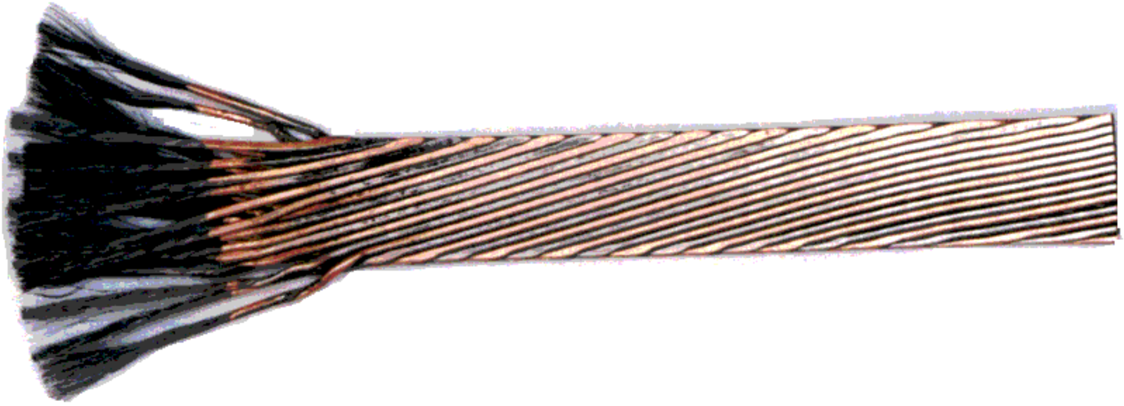

Figure 1.2-2: Inner-layer superconducting "Rutherford-type-cable" wound of 28 strands; At the left end of the sample the copper has been etched away to reveal the twisted NbTi filaments.

The contact resistance influences as well the steady state current distribution in the strands of the cable, which is mainly determined by the joint resistance of the strands in the cable. An inhomogeneous current distribution has not only major consequences on the field quality but as well a major impact on stability: The strands carrying more than the average current are more vulnerable to quench and therefore may reduce the overall stability of the cable. Since variations of the joint resistance are difficult to control a more homogeneous current distribution can be obtained by reducing the contact resistance between crossing and adjacent strands [Verweij 97].

A brief consideration of the dipole magnet cross-section (Figure 1.1-5) reveals that there is not much space left for helium. Its low viscosity allows the superfluid helium to circulate nevertheless between the helium supply tubes and the coils. Undoubtedly as much helium as possible is needed in the vicinity of the coils and in the voidage inside the cables for stability purposes. Some work [Depond 98] has been dedicated to the evaluation of this volume with the aim to find cable-dimensions which suit the primary requirements of current-density and field quality and create the biggest possible space for helium. A rough comparison of the enthalpy per unit volume of superfluid helium (between T_b=1.9K and T_λ=2.17K) and of the NbTi/Cu composite (Cu/Sc-ratio=1.6, between T_b=1.9K and current

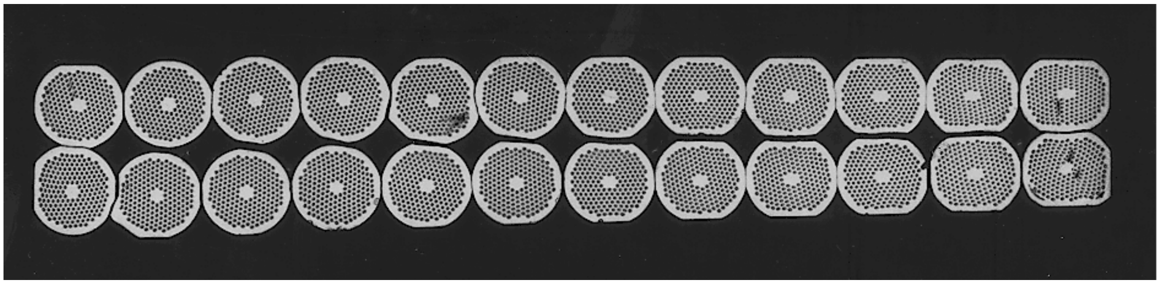

Figure 1.2-3: Cross-section of Rutherford-type cable (here prototype with 24 strands); The deformation of the strands at the thin edge is clearly visible. The Rutherford-type cable has the biggest possible packing factor with the conductor occupying approximately 90% of the total cable volume. During curing the polyimide insulation flows into the outer interstices between the strands. Helium is believed to fill the voids inside the cable.

sharing temperature T_{cs}(8T,410A)=3.25K) gives 0.236 J/cm^3 to 0.00141J/cm^3. Even if only 5% of the entire cable volume is filled with helium the heat removal capacity of the helium is still 10 times the heat absorption capacity of the conductor. In practice the considerable cooling reserve represented by the liquid helium may not always be used to its full extent. The heat generated in the cable has to find its way to the helium. Therefore the cable design has to consider as well the proportion of cooled surface and the heat transfer coefficient. Helium volume and cooled surface-fraction will play a dominant role in the ongoing text.

In the course of superconducting cable R&D some other types of cables have been developed and tested, like for example the “core-cable” featuring a thin stainless-steel foil to reduce thermal contact between crossing strands combined with partial soldering to ensure good electrical contact between adjacent strands (Adam 97), and the porous-metal cable which was an attempt to increase the cooled perimeter of the strands by injecting a fine Cu/solder mixture into the cable [Adam 97]. So far, the ideal cable design, which would provide a small inter-strand resistance for current, a high inter-strand resistance to heat flow and a high helium content with at the same time a high overall current density and mechanical stability, has not been found yet.

However, the main task of conductor R&D was the push for the highest possible critical current densities in the strands (today j_c(1.9K,10T)> 1500A/mm^2). The multifilamentary strand (Figure 1.2-4) consists of NbTi filaments embedded in a copper matrix. The filaments in the strands are twisted in order to reduce the interfilament coupling loss caused by a change in magnetic flux. Together with the subdivision into small filaments this technique serves to reduce the filament magnetization which is the main cause of field distortion at weak excitation (e.g. injection). The filament diameter is specified to 6 and 7µm to reduce magnetization under the permissible threshold [Wolf 92]. Inter-filament spacing has been controlled through magnetization measurements (proximity effect) and metallographical methods during the pre-qualification phase. It has been as well specified to keep the variation of magnetization of the strand within a magnet to less than ±4.5% to keep some dynamic field-errors under the required level [Wolf 92]. Another advantage of the subdivision into fine filaments is the enhancement of stability: If a disturbance causes the temperature of a filament to rise locally beyond the critical temperature, the matrix can rapidly conduct the heat and transfer the current of the filament to adjacent filaments. Formerly technical superconductors often suffered so called flux-jumps, a vicious circle where locally an infinitesimal (accidental) rise in temperature could build up to a quench. The origin of this problem is the predominance of magnetic versus thermal diffusivity in niobium-titanium. This former stability problem could be removed with the multifilamentary design. Unfortunately the subdivision of the superconductor and the embedding in a high conductivity matrix created an new problem: the interfilament coupling currents: By twisting the filaments the interfilament current loops induced by a change of external magnetic field (e.g. during ramping) are given an alternating sign along the strand which significantly reduces the interfilament coupling loss, leveling out the disadvantage of subdivision. To reduce the heat generation caused by the transport current flowing in the matrix, the matrix material (here copper) should be of high purity (high RRR value). This is unfortunately in contradiction with the other stipulation aiming at damping the interfilament coupling currents.

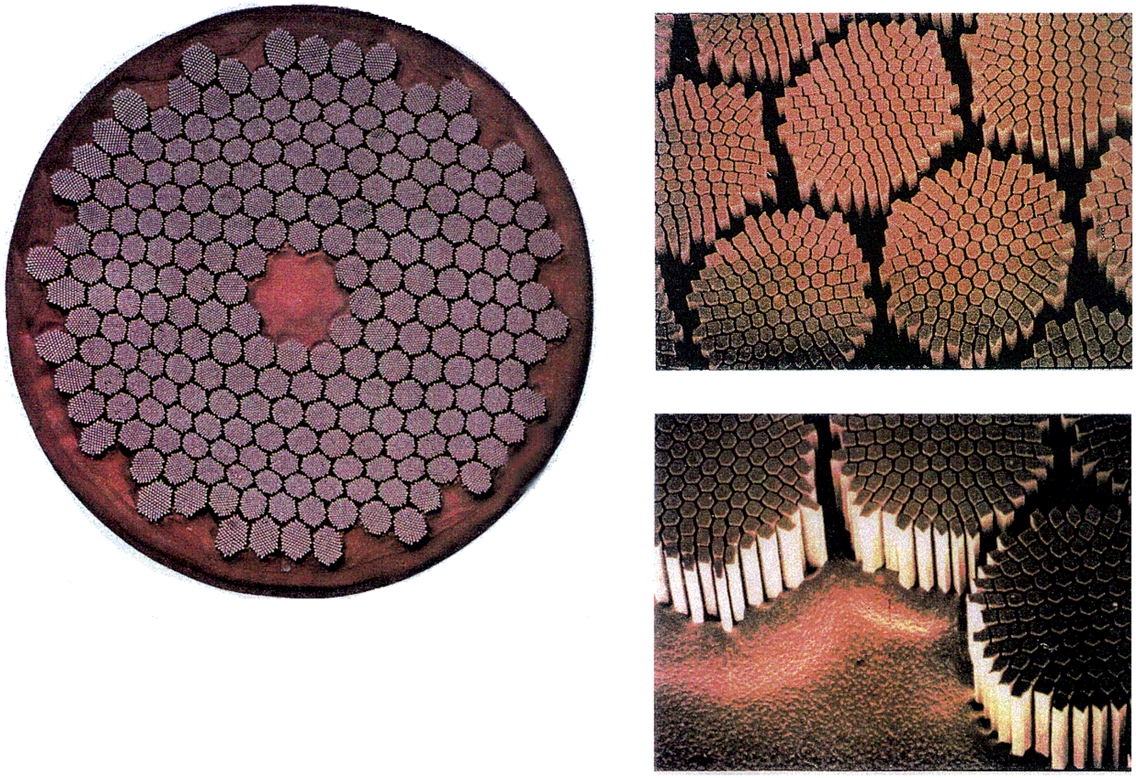

Figure 1.2-4: Micrograph of a double stack superconducting strand with bundled NbTi-filaments in Cu-matrix (∅ 1mm). This is not an LHC-type strand.

A common lay-out of the cross-section of an LHC-strand consists of the following three concentric layers:

- a central core of copper
- a ring filled with many thin filaments embedded in a copper-matrix
- an outer shell of normal conducting material.

The outer shell is required to facilitate the wire production. The purpose of the normal-conducting core is to maintain the required Cu/Sc ratio for stability. The values for the copper to superconductor volume ratio λ (as listed in Table 1.2-1) are a well-balanced choice of current-density-requirements, stability-related considerations [Wolf 94] and stipulations concerning the maximum permissible voltage during magnet quench for magnet-protection reasons. The more copper in strand cross-section the better from the stability point of view. A simple stability criterion [Stekly 65] relating worst case cooling (cooling through a layer of vaporized helium) to critical heat generation (all the current in the copper but T_{cond}<15K) would give in the present case of an inner cable strand a ratio of 3.3/340 kW per unit of cooled surface (assuming a cooled perimeter fraction of the cable in the strand of 15%). The ratio cooling versus heating becomes even smaller if the conductor exceeds 15K, when the copper resistivity starts to rise proportionally with temperature. Another stability criterion (Maddock 69) compares steady state cooling and heating as a function of temperature (Fig. 1-2.5). For a given maximum temperature T_{max} in the process "steady state" stability would be achieved if the integral of (cooling h-heating g)dT between bath temperature T_b and T_{max} is >0. This is definitely not the case in the following plot. In fact this integral would be negative almost from current sharing on! But there are two reason why the plot in the following figure does not say everything about the stability of strands in LHC cables: 1) the cooling to superfluid helium becomes more powerful in transient cases; 2) the strands in a cable behave in a collective way (inter-strand current transfer, increased heat exchange surface through neighboring strands,…etc).

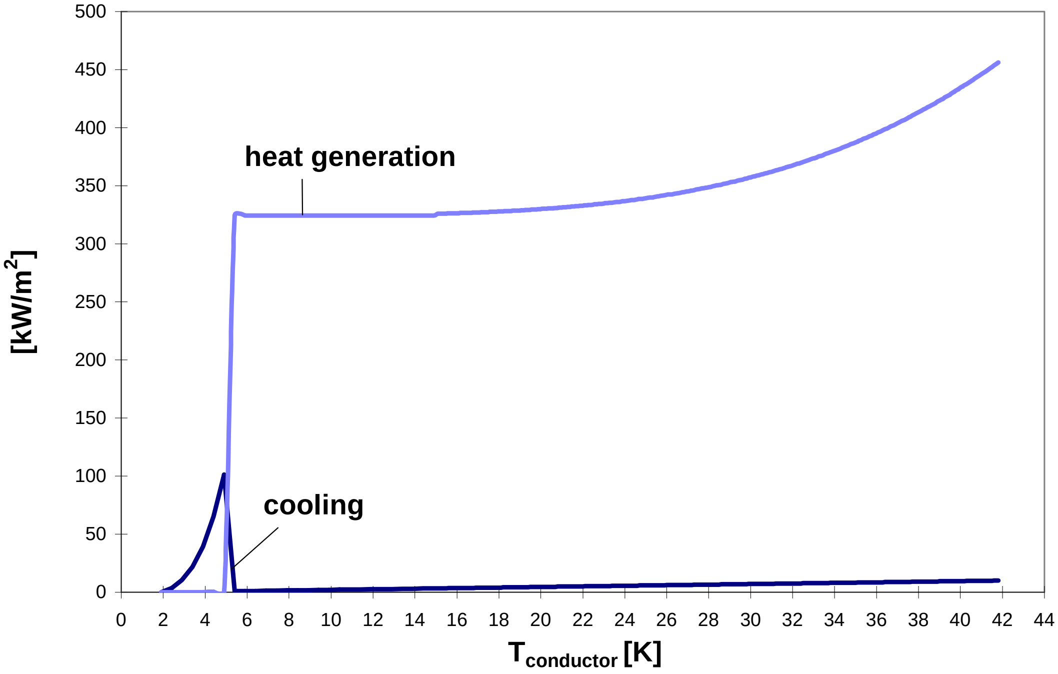

Figure 1.2-5: Comparison of heat generation and steady state cooling per unit of cooled surface to helium for an LHC strand (yellow book design, inner cable strand: I=410A=0.69I_c at 9T/1.9K, cooled perimeter fraction 15%, T_{cs}=2.93K, cooling as described in stability program documentation);

The strands are coated with Staybrite$^{®}$ (95% Sn, 5% Ag). A special oxidation treatment will result in the specified contact-resistance between crossing strands in the cable. The coating has as well a major impact on stability and is therefore an important item of the following work. Another class of strand parameters, the exact dimensions of Cu-core, Cu-shell, local Cu/Sc ratio, single stack/double stack and transverse filament to matrix conductivity (resumed under the name “design parameters”) have been looked at from the stability point of view in the present work. Without giving any further proof (see e.g. [Duchateau 75]) at the moment we consider the effects of the variation of the design parameters to result merely in the “fine-structure” of stability.

1.2.1 Heat load on the conductors during operation

On the average the cables of the dipole magnets will operate at ca. 65% of their critical current at nominal field. This means that the bath temperature T_b (1.9K) will be much smaller than the critical temperature $T_c(B(I),I)$ of the superconductor at given transport current and magnetic field. Unfortunately, as a consequence of beam- and ac-loss the conductor temperature T_{cond} will be above bath temperature T_b. The temperature margin T_c-T_{cond} is crucial for safe and reliable magnet performance and any gain in temperature margin (e.g. through improvement of the steady state cooling through the cable insulation) is a gain in magnet-stability.

The empirical scaling laws of [Lubell 83] estimate the critical temperature of a $NbTi_{46\%}$ superconductor as a function of the field and the current:

$$T_c(B,I) = 9.2\left(1-\frac{|B|}{14.5}\right)^{0.59}\left[1-\frac{I}{\left(C_1 - C_2|B|\right)}\right] \qquad [K] \qquad (1.2\text{-}1\ )$$

where C_1 and C_2 are derived from known $T_c(B,I)$ values. Taking the yellow book magnet design [CERN 95] as a reference C_1 becomes 2970A and C_2=213.5A/T, and at an operating current of 410A per strand and a peak field (inner layer) of 8.81T (at 8.4T central field) the critical temperature can be estimated with (1.2-1) to 3.3K.

Preliminary studies have established the heating power deposited in the cables during normal operation for different types of loss mechanisms: beam loss [Jeanneret 96] and ac loss [Verweij 95]. Continuous beam loss is unavoidable, especially in such high luminosity accelerators as LHC. Some protons will skip out of the beam and release their kinetic energy in the form of hadronic showers in the magnet. Since the protons will hit the beam screen at small, grazing angles the hadronic showers will mainly extend longitudinally along the cables. Beam screen and vacuum chamber will therefore absorb most of the beam loss. Assuming that the heat deposit occurs almost adiabatically the number of incident protons per second multiplied by the energy density deposited by one proton result in the power density deposited in the cable. The energy-loss of the protons distributes radially from a peak value at the inner conductor to smaller values further outside. The heat will be absorbed by the conductor material and radially conducted along the cable and transferred to the superfluid helium. As a result an equilibrium temperature distribution will establish. [Jeanneret 96] estimates the worst case average beam loss in the magnet to be 4.5mW/cm^3 (7-8x10^6 protons/s). A worst case calculation, assuming the heat transfer from the conductors going through a layer of insulation (k~0.01W/m/K), relates this heat generation rate to a temperature rise of 1.12 K. Measurements at CEA ([Meuris 91], Baudouy 97]) indicate that with improved insulation schemes (and derived from that improved heat transfer to helium characteristic) the average temperature rise in the conductor can be reduced to 0.2-0.5 K.

Ac-loss in the magnet occurs mainly during ramping due to ISCCs. Hysteresis loss becomes negligible at high fields. The contribution of the BICCs to ac-loss is difficult to estimate. In any case ac-loss is negligible in comparison to beam-loss. With a ramp-rate $dB_{\perp}/dt$ of 8mT/s and an average cross-contact resistance R_c=10µΩ the ISCC-ramping loss theory predicts 0.05mW/cm^3, which at a reasonable rate of steady state cooling should result in a temperature increase of 0.04K of the cable. Calorimetric measurements on model-magnets show a spread of a factor 10, an average experimental value for hysteresis loss and coupling loss together so far was 0.03mW/cm^3 (personal communication D. Richter CERN/LHC/MMS).

Summing up the worst case values for the two loss contributions the conductor temperature will reach 2.3-3.06K according to different estimates during normal operation. From (1.2-1) the temperature margin can be calculated to be as small as 0.24K. This does not leave much margin for a safe magnet operation.

1.3 Quench Precursors in Prototype Dipole Magnets

Obviously the conductors of LHC - magnets are designed to operate at a B,T,I-point located as far underneath the “critical surface” of the superconducting material as possible (“temperature margin”). The design accounts for the steady state heat load emanating from beam- and ac-loss as indicated in chapter 1.2.1. Superconducting magnets quench not only when they are operated above the critical current of their cable (“short-sample limit”). As shown for example in acoustic emission experiments [Iwasa 92], as a consequence of the extreme working conditions (stress, low temperature), the mechanical structure of high field magnets continuously generates an electrical background “noise”. Some of these to a certain level unavoidable mechanical disturbance peaks may be strong enough to cause a quench of the magnet (“premature quench”). Another common phenomenon in superconducting magnets is “training”, the fact that the quench field of a magnet gradually rises from quench to quench until a quench field is reached which is given by the intersection of the load-line B(I) relation and the I_c(B) relation (“short sample limit”). Training is believed to be caused by the emergence of mechanical disturbances originating in mechanical imperfections of the magnet structure. Once the energy level of disturbance related to the repositioning of conductors and other mechanical parts stays under a certain threshold (the threshold of what we define here as stability) training stops and the magnet performance does not change anymore. Some of the LHC prototype magnets have shown training-quenches at magnetic fields smaller than the nominal field. It is not reasonable to build an accelerator with several thousand superconducting magnets that need to be trained each time they are put into operation. Training and degradation in superconducting magnets of many different types has been the subject of an impressive amount of publications. Ways have been found to build so called “cryostable” conductors [Stekly 65], which through an extensive use of copper-stabilizer prevent any local quench to spread to the rest of the magnet. Unfortunately this technology is not applicable to LHC-main magnets because it would suffer the drawback of any normal-conducting magnet: too small overall current densities. All these efforts have not yet raised a general view of the phenomenon: the approach to magnet stability remains that of trial and error and one can never be sure that a successful design is not “over-stabilized” which can be relevant to the cost of the system.

Although the experimental evidence is somewhat weak in this area, there are some indications about quench precursors in LHC magnets. Figure 1.3-1 shows the quench precursor in a 1m LHC test dipole. *A spike, thought to be movement of the conductor, is followed by a resistance which grows, starts to recover and then grows again. Duration of the spike is ~½msec. and the resistive voltage at the first peak corresponds to a normal zone length of ~60mm. Thus this quench seems to have been triggered by a short pulse affecting a small volume."* (quoted from [Wilson 97]); A huge series of experiments on prototype LHC dipole magnets, many of them showing strong training, revealed only a small number of "spike-triggered" quenches. It has not been clarified yet if the quench precursors have simply not been recorded because of a lack of temporal resolution of the measurement-system or if the quenches were caused by "distributed" (in time a space), and thus invisible disturbances. However, even when a spike appears it is very complicated to distinguish the ohmic "disturbance"-contribution in it from the inductive voltage following current redistribution. It is mainly that difficulty which has so far rendered any further "disturbance" analysis on prototype magnets impossible. Furthermore disturbances may travel through the magnet as mechanical shock waves triggering quenches in locations far from the disturbance origin.

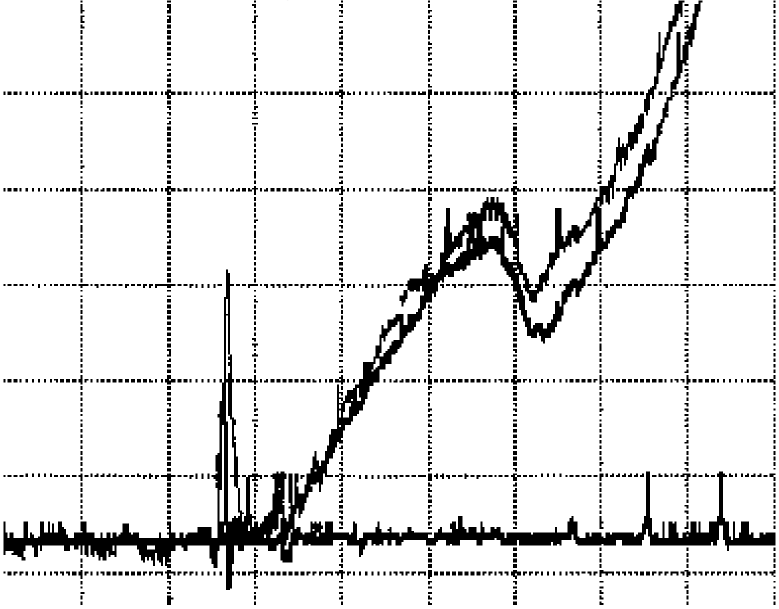

Figure 1.3-1: Quench precursor in the LHC model dipole "MFISC", scale 2 msec/div. horizontal and 2 mV/div. vertical. [A. Siemko CERN/MTA private communication]

1.4 Scope of the thesis

As indicated previously a consequence of the huge Lorentz-force acting on the conductors during magnet operation is that very small effects like the displacement of e.g. a strand in a cable may cause a disturbance strong enough to quench this strand and in the following the cable and the magnet. A simple calculation [Leroy 97] shows that a strand displacement of 0.6µm on a comparably short length could trigger an energy release of approximately 100µJ. This range of energy has been established as capable of triggering quenches in LHC-strands in the course of the present work. Before going further let us resume how a quench occurs in a strand (Figure 1.4-1):

The trouble starts with a localized disturbance followed by a release of energy inside the windings. The bigger the device, the more likely are releases of energy and the more varied the character of the disturbances. The immediate consequence of a disturbance is a local rise in temperature. This temperature rise may be huge even for small disturbances because the specific heat of metals at superconductor operating temperatures is very small.

The multifilamentary composite will react to any temperature excursion exceeding the so called current sharing temperature with current-sharing, hence some of the transport current in the filaments will spill over to the normal-conducting matrix. In most of the cases (except for the so called adiabatic case or in case of very high superconductor-content) the consequences of the temperature excursions of this range can be withstood with a modest amount of cooling to the surrounding cryogen, resulting in the recovery of the superconducting state. If the maximum temperature does not reach the current sharing temperature (corresponding to current density and magnetic field), the extra heat is removed into the surroundings through cooling and conduction, and the coil performance is not seriously affected. If the maximum temperature exceeds for example the critical temperature, a normal zone is created within the coil winding. In the normal zone there is additional Joule heating $j^2\rho$, j being the current density and ρ the resistivity in the normal conducting composite. In this case the composite acts like a heat amplifier reacting to external heat with an "intrinsic" heat generation. The strength of Joule heating due to current transfer to the matrix can only be reduced via enhancement of the Cu/Sc ratio ("cryostability"). In the present case the Cu/Sc ratio is small and it cannot be extended to any desired value. At the same time heat is conducted along the conductor and to the coolant. Especially in transient cooling to superfluid helium the cooling can become extremely powerful. Therefore the environment of the conductor strongly interferes into stability, making the single strand or a strand in a cable two completely different cases (Of course an additional feature of the multi-strand cable is that of inter-strand current transfer!). For a small enough normal zone, cooling and heat conduction will remove more heat than is created, with the result that the normal zone shrinks and disappears again. If the normal zone is too large, more heat is produced within than can be removed by cooling and heat conduction. The zone will heat up and spread, and a coil quench results. The critical size and peak temperature of the normal zone created in the dynamics of intrinsic and external heating versus cooling is a function of many parameters. However as M.N. Wilson states it in [Wilson 91] it is firstly related to the shape of the initial disturbance: *"The first step in designing for stability should be the question 'what are we stabilizing against?'. Wipf* [Wipf 78] *has advanced the idea of a disturbance spectrum, i.e. the whole range of possible energy inputs afflicting a magnet. Continuous disturbances, i.e. steady state heat loads from poor joints, cryogenic losses,..etc, can be troublesome but they can usually be avoided by careful design…. One is thus left with the more troublesome and less predictable transient disturbances. Apart from flux jumping, which may be eliminated by fine subdivision, very little is known about the nature of these disturbances. They are generally thought to be mechanical in origin but it is not even clear whether they are predominantly localized to a point or distributed over a large volume."*

The spectrum of disturbances Wilson refers to, covers everything from steady-state and spatially distributed disturbances (e.g. ac-loss) to transient - small extent events (e.g. local conductor movement). For example in spatially distributed disturbances heat conduction from the sides of the warm zone will not intervene, whereas the cooling characteristic of e.g. liquid helium will strongly differ between transient- and steady-state-cases.

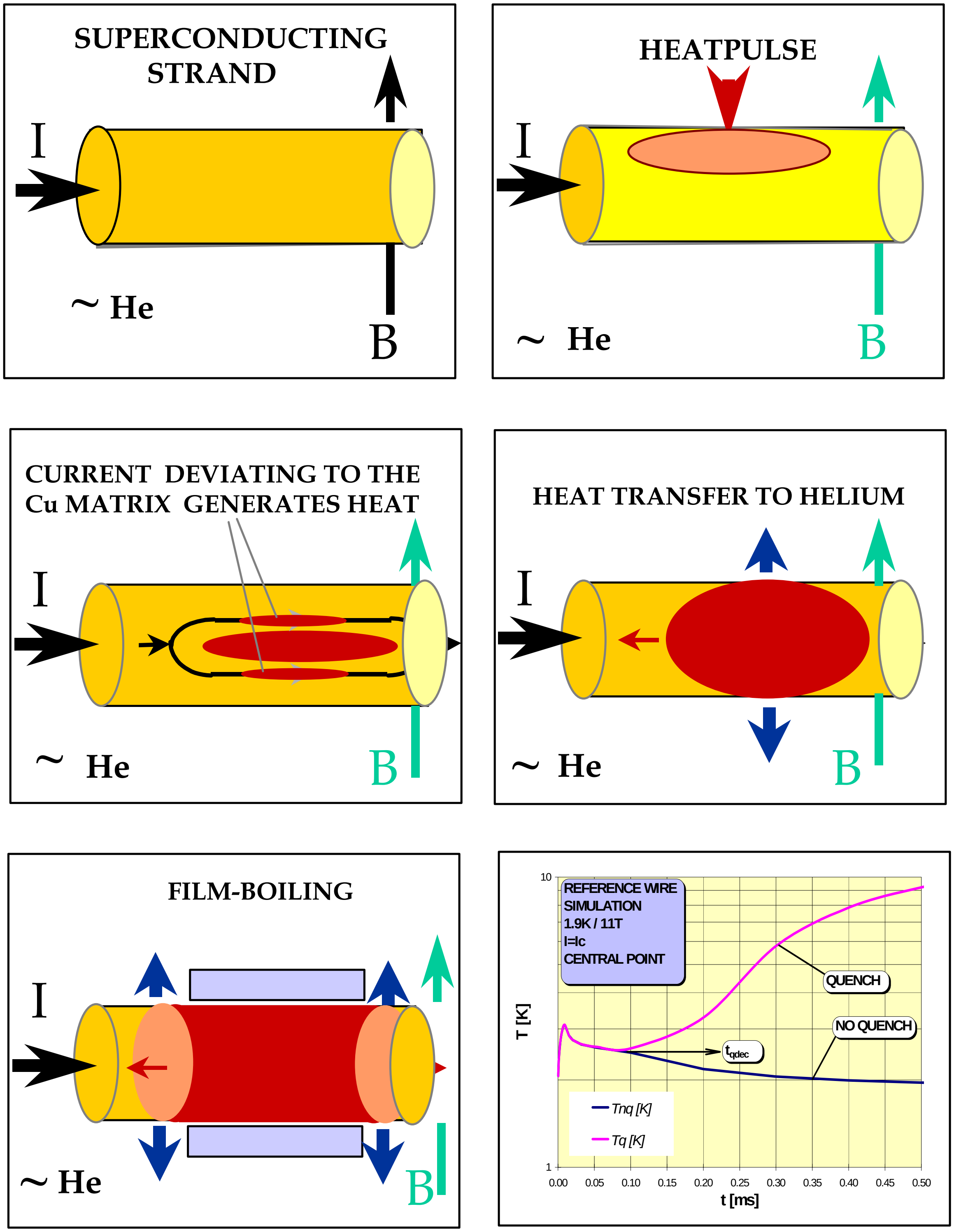

Figure 1.4-1: Schematic illustration of the quenching process;

Within the frame of the LHC project a program has been initiated at CERN intending to raise the understanding of conductor-stability in superconducting accelerator magnets with respect to short, transient disturbances. By investigating the “stability” of the conductors, thus raising a quantitative estimation of the stability threshold (which can eventually be improved) gives an indication of the level to which the mechanical background noise in the magnets has to be reduced. The task was split into two, one group working on the single strand to provide the understanding of the basic element and another group concerned with the more complex case of the (Rutherford-) cable consisting of a certain number of strands. Furthermore the project comprised collaborations with groups at BNL, DRAL and TU Twente.

The experimental approach to stability of LHC-conductors has been defined as the measurement of Minimum Quench Energy MQE (which is that energy input, of short duration applied to a small volume of a superconducting wire under operation conditions, which is just sufficient to trigger a quench) using an electrical graphite-paste heater technique [Seo 96]. In a MQE process small quantities of energy of approximately 100µJ are deposited in a small conductor-volume during a very short time (~10µs) involving huge power densities of the order of 10W/mm^3. In the aftermath of such a pulse the multifilamentary type of strand will locally react with strong Joule heating of the transport current in the normal conducting matrix in the 50mW/mm^3 power range. Since the quench decision time is of the order of ~1ms the heat quantity deposed in the strand due to current sharing will in general be of the same order as the initial heat pulse. The normal zone created in the aftermath of the initial heat pulse will either grow or shrink according to the interaction of heat generation, cooling to the cryogen and heat conduction along the strand. Other teams in the collaboration have used different heater techniques and/or chosen other types of disturbances. The scope of this thesis was to characterize LHC prototype strands by their MQE and to investigate the effect of the main strand parameters (such as the matrix RRR, the Cu/Sc ratio, the coating, the billet design and the cooling) on MQE..

1.5 Nomenclature

The following table (Table 1.5-1) contains the symbols used in the following.

SYM	UNIT	MEANING	SYM	UNIT	MEANING
x	[m]	space coordinate along the wire	x_{ini}	[m]	characteristic (half-)length of initial heat pulse
a, r	[m]	(wire, filament,..)-radius or radial coordinate	z	[m]	cartesian space coordinate transversal to the wire axis or longitudinal coordinate in cylindrical coordinates
d	[m]	diameter (wire, heater, channel, filament,..)	L	[m]	cold boundary length or characteristic length or channel width
D	[m]	heater diameter or diffusivity	w	[m]	channel width (=length)
p	[m]	cooled perimeter	l	[m]	length of voltage tap
r_s	[m]	radius of current saturation in filament	f	[m]	cooled perimeter fraction or pinning force density
R_m	[m]	cold boundary radius in Wilson’s MQE formula	R_g	[m]	MPZ radius in Wilson’s MQE formula
MPZ	[m]	length of MPZ	l_{MPZ}	[m]	length of MPZ

V_{ini}	[m^3]	initially heated volume	δ	[m]	penetration depth in general or parameter in dynamic heat transfer limit
A	[m^2]	surface of wire cross-section	A_{sc}	[m^2]	superconductor surface in composite
A_{Cu}	[m^2]	copper surface in composite	v		voidage
λ		Cu/Sc volume ratio	n		transition exponent or exponent of Gaussian or exponent in general
D_{therm}	[m^2/s]	thermal diffusivity	D_{mag}	[m^2/s]	magnetic diffusivity
ρ	[Ωm]	electrical resistivity	ρ_{Cu}	[Ωm]	Cu resistivity, normalized on Cu cross-section
ρ_0	[Ωm]	fiducial sc resistivity, normalized on total wire cross-section	ρ_{Comp}	[Ωm]	Cu resistivity, normalized on total composite cross-section
β	[J/m^3/K^4]	Debye parameter in c_p	γ	[J/m^3/K^2]	Sommerfeld param. in c_p
c_p	[J/m^3/K]	volumetric specific heat	L_0 (L_0’)	[WΩ/K^2]	(modified)Lorentz constant
k	[W/K/m]	thermal conductivity	k_r	[W/K/m]	radial heat conductivity in spherical or cylindrical coordinates
k_z	[W/K/m]	longitudinal heat conductivity in cylindrical coordinates	α^2		k_r/k_z
B	[T]	(perpendicular) magnetic field	μ_0M	[T]	magnetic polarization
t	[s]	time	t_{post}	[s]	end of post-heating
τ	[s]	turbulence onset time, helium II	t_K	[s]	relaxation time
t_{ini}	[s]	duration of initial heat pulse	t_R	[s]	recovery time
t_{qdec}	[s]	quench decision time	$t^{*(II)}$	[s]	burn-out time in transient heat transfer to helium II
$t^{*(I)}$	[s]	burn-out time in transient heat transfer to helium I			
α		Stekly number or proportionality coefficient in turbulence onset time formula	β		stability parameter in dynamic stability theory or geometric constant
T_b	[K]	bath temperature	T	[K]	temperature
T_c	[K]	critical temperature	T_{cs}	[K]	current sharing temperature
T_s	[K]	conductor-surface temp.	T_0	[K]	fixed boundary temperature
ΔT	[K]	difference betw. T_s and T_b	T_{sat}	[K]	saturation temperature
T_λ	[K]	lambda temperature	T_{smax}	[K]	maximum surface temperature
I_q	[A]	quench current	I	[A]	current
I_t	[A]	total transport current	I_c	[A]	critical current
i		reduced current I_t/I_c			
j_t	[A/m^2]	tot. current density, normalized on total wire	j_{sc}	[A/m^2]	current density in sc, normalized on total cross-

		cross-section			section
j_{Cu}	[A/m^2]	current density in Cu, normalized on total cross-section	j_c	[A/m^2]	critical current density, normalized on sc cross-section
j_s	[A/m^2]	switching current density, normalized on total cross-section	f	[A/m^2/T]	pinning force density
V	[V]	voltage	v_l	[V/m]	voltage per unit length lower branch
v_h	[V/m]	voltage per unit length upper branch	v_q	[m/s]	quench propagation velocity
V_{qi}	[V]	voltage on strand at tap i			
q_{ini}	[W/m^3]	initial heating power density per unit volume	q	[J/m^3]	heat density per unit volume
g	[W/m^2]	heat generation density per unit surface or gravita. acceler. on earth	g_c	[W/m^2]	heat generation density at critical current per unit surface
$g_c i^2$	[W/m^2]	critical heat generation p.u.s.	U	[J]	potential energy
Q_{ini}	[J]	initial heat	Q	[J]	heat
MQE	[J]	minimum quench energy	e_B	[J/m]	magnetic energy per unit length
e, e'	[J/m^2] [J/m^3]	energy per unit surface or per unit volume			
e*	[J/m^2]	general critical energy per unit surface transferred to cryogen	e_t	[J/m^2]	total heat per unit surface transferred to bath
$e^{(I/II)}$	[J/m^2]	limiting energy per unit surface in helium I and helium II	$e_{Cl}^{(I)}$	[J/m^2]	energy limit for heat transfer to helium I in open channel
$e_{cCl}^{(I)}$	[J/m^2]	energy limit for heat transfer to helium I in closed channel	$e_{Sl}^{(I)}$	[J/m^2]	dynamic energy limit in helium I ("Schmidt limit")
$e_{SS}^{(II)}$	[J/m^2]	dynamic energy limit in helium II in second sound state	$e_{GM}^{(II)}$	[J/m^2]	dynamic energy limit in helium II in Gorter-Mellink state
$e_{Cl}^{(II)}$	[J/m^2]	energy limit for heat transfer to helium II in open channel			
K_{SL}	[J^2/m^4/s]	Schmidt Constant in transient helium I heat transfer	K_{SS}	[J^2/m^4/s]	Proportionality constant in burn-out time formula in helium II (second sound state)
K_{GM}	[J^4/m^8/s^3]	Proportionality constant in burn-out time formula in helium II (Gorter-Mellink state)			
h	[W/m^2]	heat flux per unit surface	q	[J/m^2]	heat or heat flux p.u.s.
h_{nc}	[W/m^2]	convection heat flux p.u.s.	h_{nb}	[W/m^2]	nucleate boiling heat flux p.u.s.
h_K	[W/m^2]	Kapitza heat flux p.u.s.	h_{fb}	[W/m^2]	film-boiling heat flux p.u.s.
$h_c^{(I)}$	[W/m^2]	critical heat flux p.u.s. in helium I	h_0	[W/m^2]	incoming heat flux p.u.s.
$h^{*(I)}_{sub}$	[W/m^2]	NBM in subcooled	$h^{*(I)}$	[W/m^2]	nucleate boiling

		conditions			maximum NBM in helium I
$h_R^{(I)}$	[W/m^2]	minimum recovery heat flux p.u.s. in helium I	$h^{*(I)}_{sat}$	[W/m^2]	NBM in saturated conditions
$h^{*(II)}$	[W/m^2]	burn-out steady state heat flux p.u.s. in helium II	$h_c^{(II)}$	[W/m^2]	critical heat flux p.u.s. in helium II
h_{post}	[W/m^2]	post heating flux per unit surface			
a	[W/K^n/m^2]	general heat transfer coefficient	a_{fb}	[W/K^n/m^2]	film-boiling heat transfer coefficient
a_K	[W/K^n/m^2]	Kapitza heat transfer coefficient			
n		Kapitza heat transfer exponent	m		Gorter Mellink exponent
f^{-1}	[W^3/K/m^5]	heat conductivity function in turbulent helium II	K	[Wm$^{1/3}$/K$^{1/3}$]	heat conductivity function in turbulent helium II according to Dresner
R_K	[Km/W]	thermal Kapitza resistance	$R^{(I)}_{nc}$	[Km/W]	thermal resistance of helium I in natural convection regime
$R^{(I)}_{nb}$	[Km/W]	thermal resistance of helium I in nucleate boiling regime	R_{fb}	[Km/W]	thermal resistance of helium in film boiling regime
ρ / ρ_{tot}	[kg/m^3]	total density	ρ_s	[kg/m^3]	density of superfluid component
ρ_n	[kg/m^3]	density of normal component	ρ_v	[kg/m^3]	density of vapor phase
ρ_l	[kg/m^3]	density of liquid phase	s_m	[J/K/kg]	entropy per unit mass
s_{ms}	[J/K/kg]	entropy per unit mass of superfluid phase in helium II	s_{mn}	[J/K/kg]	entropy per unit mass of normal phase in helium II
η	[Ns/m^2]	viscosity	C_p	[J/K/kg]	isobaric specific heat per unit mass
c_p	[J/K/m^3]	isobaric specific heat per unit volume	c_v	[J/K/m^3]	specific heat per unit volume at constant volume
Pr		Prandtl number	Ra		Rayleigh number
λ	[J/kg] [J/m^3]	latent heat per unit mass or per unit volume	λ'	[J/m^3]	effective latent heat
A	[sm/kg]	Gorter-Mellink parameter	D_{GM}	[m$^{4/3}$/s]	apparent diffusivity of helium II in Gorter-Mellink regime
σ	[Pa]	surface tension	p	[Pa]	pressure
p_{atm}	[Pa]	atmospheric pressure	p_{sat}	[Pa]	saturation pressure
θ		Heavyside function			

Table 1.5-1: Summary of the symbols (all magnitudes in SI units) used in the following text.

2. STABILITY OF SUPERCONDUCTORS - LITERATURE SURVEY

In the development of technical superconductors stability has always been a key issue: from the flux jump problem, the dynamic stability theory, Stekly's and Maddock's work on cryo-stabilization to today's investigations of the Minimum Quench Energy. This chapter first introduces historical stability concepts which have successively entered strand design to improve stability in the past. Today's understanding of superconductor stability is summarized under the label "standard model of stability".

A second part deals exhaustively with heat transfer to helium I and helium II in steady state and transient conditions. The properties of normal liquid and superfluid helium are recapitulated. Heat transfer correlations for steady state and transient cooling are presented and explained. The models for cooling to pool-boiling or superfluid helium, which will be subsequently used, are explained in detail. A third part relates mile-stone articles related to the stability of strands, cables and magnets. Especially in what refers to complex systems like magnets there were only few teams investigating stability issues directly on the magnets. Instead many groups investigated sources of quenches in magnets. Other subjects which received special attention, and which are mentioned here, are the quench propagation velocity (for magnet protection reasons) and the optimum copper to superconductor ratio question. A final chapter presents several analytical approaches to the calculation of the quench energy of a superconducting strand.

2. STABILITY OF SUPERCONDUCTORS - LITERATURE SURVEY

2.1 Introduction

Today's design of technical LTc superconductors (especially NbTi and Nb_3Sn) is the result of almost half a century of constant progress in production and design. Stability has always been one of the key issues in applied superconductivity. [Wilson 83, chapter 7] and [Dresner 95, chapter 1&3] presented excellent historical reviews of the subject. Stability investigations in the past 20 years have been related to big-scale applications of superconductivity for high energy physics, fusion science, SMES systems, magnetic levitation, etc.. . The following reviews publications related to general stability concepts, liquid helium cooling and stability investigations on superconducting strands, cables and magnets. Since the Minimum Quench Energy is related to local, transient disturbances, distributed perturbations (AC-loss) or steady state heat load (heat generation in bad joints) have been disregarded here as well as the stability of cable in conduit conductors.

2.1.1 Flux Jump

The first type of instability in technical superconductors to be identified and resolved was flux jumping. The concepts developed to cope with flux jumps evolved into today's stability theory. A flux jump is the sudden and dissipative rearrangement of magnetic flux in the superconductor resulting in a quench. A flux jump can be triggered by a local, infinitesimal temperature rise. The rise in temperature reduces the critical current and forces the shielding- and transport-current (which according to the Critical State Model CSM flow with critical current density) distribution to flatten over the superconductor cross-section. The current redistribution results in a change of magnetic flux inducing dissipation through flux flow resistance in the superconductor. At this point the vicious circle of flux jump closes if the heat dissipated in the flux jump cannot be removed effectively and therefore causes a further rise in temperature. The energy released in a flux jump is the magnetic energy of interaction of the magnetic moment caused by the shielding currents in the superconductor and the magnetic field in the superconductor ("hysteresis energy"). The heat generated by the deviated transport current in the matrix material following a local disruption of the superconducting state is not counted as disturbance energy. A rough estimation of the energy density released in a flux-jump can be calculated from $e=B^2_{mag}/2\mu_0$. In a typical LHC strand (which is stable against flux jumps) with a polarization $\mu_0 M$ of ~1mT at 8T the energy density calculated from $B^2_{mag}/2\mu_0$ would be $0.5 J/m^3$, which applied to a small length of conductor (1mm) gives 10nJ. This disturbance energy is negligible compared to the scale of MQE and can be neglected in an MQE experiment. In superconductors susceptible to flux-jumps these energies maybe an order of magnitude larger but they never reach the scale of MQE.

The remedies against flux jumps are manifold: reduction of the energy dissipated in the process through the reduction of magnetization and the reinforcement of thermal stability. Both concepts involve the fine subdivision of the superconductor in a matrix with a high thermal conductivity. The adiabatic flux jump theory (valid if $D_{therm}=k/c_p < D_{mag}=\rho/\mu_0$) first presented in [Swartz + Bean 68] predicts that a filament will be stable against flux jumping as long as the local heat generation due to flux jump is smaller than the local enthalpy margin $c_p(T_c-T_b)$ of the superconductor. The heat dissipated in a flux jump is proportional to j_c and the filament diameter. Since it is not useful to reduce j_c the only free parameter is the filament diameter. A rough calculation for a hypothetical mono-filamentary LHC strand [CERN 95] with a critical current density of 1.786×10^9A/m^2 at peak field 8.81T/1.9K and the enthalpy reserve of NbTi between T_c=5.4K and T_b=1.9K according to [Swartz 68] indicates that the filament diameter would have to be smaller than 50µm to avoid flux jumping. The adiabatic model of Swartz and Bean does not account for the benefit of thermal stabilization through a conductive matrix. Unfortunately the multi-filamentary design does not necessarily prevent from flux jumps because the filaments are electrically coupled through the conductive matrix, with the characteristic distance for flux jumping becoming the composite radius rather than the filament radius. Fortunately it is possible to reduce coupling by twisting the filaments. Although twisting is fully effective in homogeneous, external fields it is totally ineffective with respect to the self-field. In twisted multi-filamentary conductors the self-field generated by the transport current therefore becomes the major source of flux jumping. [Duchateau + Turck 75] presented very accurate calculations (dynamic stability theory) for the stability parameter β of twisted and stabilized (D_{therm}>D_{mag}) conductors including the self field effect. They showed that β could be raised by some orders of magnitude from the lower adiabatic limit $\pi/4$. A typical LHC strand, assuming a steady state heat transfer rate to helium of 50kW/m^2, can reach β=170 at 9T. Following [Duchateau + Turck 75] with an average specific heat of a Cu/Sc-ratio=1.6 composite of 1550J/K/m^3 and a composite normal state resistivity of $9.2\times10^{-10}\Omega$m at 9T and average composite heat conductivity of 115W/K/m, the reduced degraded current $i=I/I_c$ becomes 0.85. Experience has shown that theoretical predictions are still pessimistic and filamentary composites generally do better than expected. According to [Klimenko 92] this discrepancy can be explained by the transition to the normal state which is in reality smooth rather than jump-like, as in Duchateau’s model. Thus, superconducting strands as designed for LHC should not suffer flux-jumps. Nevertheless the dynamic stability theory combined with AC-loss considerations (e.g. [Mints 82]) could still have a significance for “premature quenching” in critical current measurements [Ghosh 97].

Today “stability” evokes the recovery to the superconducting state from temperature excursions by far exceeding the critical temperature. This work deals with short perturbations in the range of 100µJ per mm^3 of conductor, the instabilities related to flux-jumps involved perturbations in the 10nJ/mm^3 range. In terms of power the MQE heat pulses reach up to some 10W/mm^3 during 10µs, whereas the intrinsic Joule heating due to current sharing is approximately 50mW/mm^3 (but acting during a much longer time). The paradigm of today’s stability research is cooling to the surrounding cryogen, whereas before it was the transverse and longitudinal heat conductivity of the stabilizing matrix.

2.1.2 Stekly Criterion and Cold End Recovery

[Stekly 65], with his coworkers were the first to build superconducting magnets that recovered the superconducting state after a normalizing perturbation. Using boiling helium as coolant they arranged for cooling to unconditionally exceed Joule heating by adding copper to the conductor until the worst case Joule heating was less than the worst case cooling. This concept of cryo-stability is illustrated in Figure 2.1-2, were the steady state heat transfer characteristics of pool boiling helium I is plotted against the heating per unit of cooled surface as a function of the temperature difference (T_s-T_b). Further details on the heat transfer characteristics of liquid helium I and II are given in chapter 2.2. A hint to the tremendous impact of helium on stability is that the specific heat of both helium I and helium II at 1atm can reach values of 4000-6000J/kg/K, which is 4 orders of magnitude bigger than that of copper or NbTi. Given a high heat exchange coefficient between the conductor and the helium, the helium can act as a very efficient thermal reservoir able to absorb a fairly large amount of heat [Claudet 90]. Equation (2.1-1) resumes the Stekly criterion $\alpha i^2<1$, with $i=I_{tot}/I_c$, where α the Stekly number is the ratio of worst case heating versus worst case cooling and ρ_{Cu} is the copper resistivity, A_{Cu} the Cu cross-section in the composite, d the wire diameter, f the cooled perimeter fraction, a_{fb} the film-boiling heat transfer coefficient and (T_c-T_b) the difference between bath- and critical-temperature. As can be seen in equation (2.1-1) α becomes smaller for increased copper fraction, respectively copper to superconductor ratio.

$$\frac{(I_{tot}^2\rho_{Cu}) \big/ (A_{Cu}\pi df)}{a_{fb}\left(T_c - T_b\right)} = \alpha i^2 < 1 \qquad (2.1\text{-}1)$$

At a given Cu/Sc ratio the Stekly number α can be reduced only by decreasing the total transport current density. Here appears the major disadvantage of cryo-stability: the low overall operating current density. A cryo-stability criterion which penalizes less the current density is the Maddock criterion [Maddock 69]. As shown in Figure 2.1-2 the three part heating curve is now allowed to cross the cooling curve, to such an extent that the areas under the curves between T_b and T_{smax} are equal ("Equal Area Theorem"). This guarantees that any transient temperature profile (as a consequence of e.g. a thermal perturbation) in the conductor with $T<T_{smax}$ will flaten out again with the edges of the normal zones propagating inwards ("cold end recovery"). The mathematical expression of cold end recovery (equation. (2.1-2)) can be obtained from the steady state heat balance equation describing the problem (further discussion in chapter 2.1.3) and states that the integrated difference between heat transfer h and the heat generation g (all in W/m^2) should be zero.

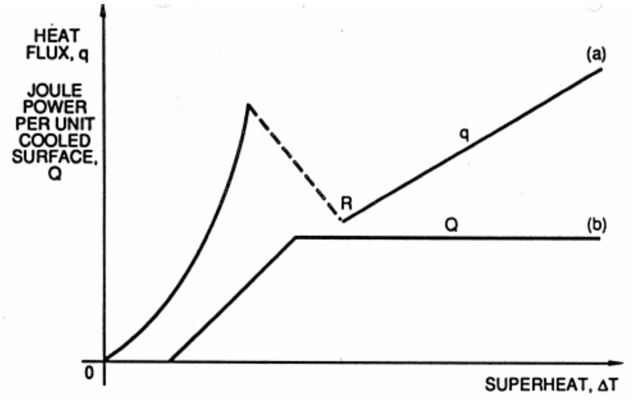

Figure 2.1-1: Cooling(q) versus heating(Q) in a Stekly-stable configuration. Steady state cooling to pool-boiling helium I, simplified 3-part Joule heating.[Dresner 95].

$$\int_{T_b}^{T_{s\,\max}} (h-g)kdT \ge 0 \qquad (2.1\text{-}2)$$

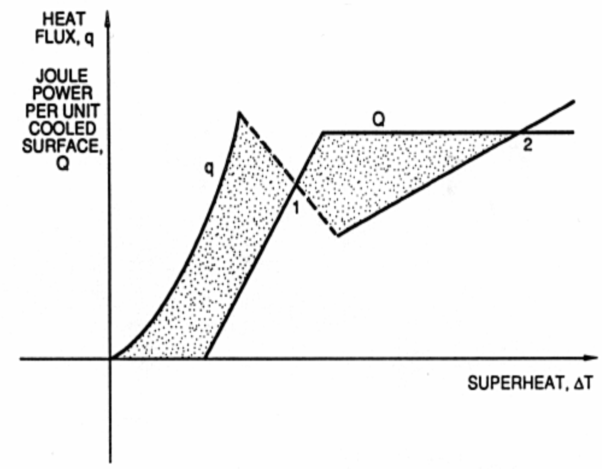

Figure 2.1-2: Cooling(q) versus heating(Q) in a Maddock-stable case. Steady state cooling to pool-boiling helium I, simplified 3-part Joule heating. [Dresner 95]

"In the … case of pool boiling liquid helium, the original Stekly theory demands an ohmic heat generation (per unit area of cooled surface) of less than 2kW/m^2 and the Maddock theory demands less than 3kW/m^2. These theoretical values have been checked by embedding heaters in magnet windings and have been found to be essentially correct." (quoted from [Wilson 78]); A strand as specified for the LHC main magnets has a αi^2~410 and a maximum heat generation of roughly 300kW/m^2 and therefore operates far from cryo-stability. However, it has to be emphasized that both criteria are conservative because they are based on steady-state cooling characteristics. The present work being dedicated to the stability versus transient disturbances has revealed higher stability margins than those indicated above.

2.1.3 "The Standard Model of Stability"

"The Standard Model of Stability" describes the thermal perturbation of a superconductor cooled by liquid helium by means of the one-dimensional heat balance equation (HBE):

$$0 = \frac{\partial}{\partial x}\left[k(T)\frac{\partial T}{\partial x}\right] + I_t^2\,\frac{r(I_t,T)}{A} + q_{ini} - h(T,q)\frac{p}{A} - c_p(T)\frac{\partial T}{\partial t}\;\left[\frac{W}{m^3}\right] \qquad (2.1\text{-}3)$$

Table 2.1-1 describes the parameters used in the 1-dimensional HBE (2.1-3).

T(x,t)	Temperature distribution in the wire [K]
I_t	Total current [A]
r(I,T(x,t))	Total wire resistance per unit length [Ω/m]
A	Cross-section surface of wire [m^2]
h(q(x,t),T(x,t))	Heat flux density to the cryogen [W/m^2]
p	Wetted perimeter 2πaf [m]
f	Cooled perimeter fraction ∈[0,1]
a	Radius of wire [m]
c_p(T(x,t))	Specific heat of composite [J/m^3/K]
k(T(x,t))	Heat conductivity of the composite [W/K/m]
q(x,t)	Cumulative heat transferred from conductor surface [J/m^2]
q_{ini}(x,t)	Initial heat load power density [W/m^3]

Table 2.1-1: Nomenclature of the 1-dimensional heat balance equation;

The HBE is normalized on a unit volume of conductor (W/m^3). The first term is the classical heat conduction term of the Fourier-type. Then comes a series of three source terms: the Joule heating in the normal conducting matrix, the initial (external) heat pulse and with a negative sign the cooling to helium. The last term describes the diffusion of heat in the conductor related to its specific heat. The functions describing the electrical behavior of the composite superconductor (the resistivity-function) and the cooling function as well as the material parameters k and c_p can be of any degree of complexity. The external heat pulse can take any shape in space and time. Some authors ([Wilson 83], [Amemiya 94]) have investigated the two- and three-dimensional versions of the HBE, but the solutions of (2.1-3) are already sufficiently complex in the one-dimensional (isothermal cross-section) case. Analytical solutions exist only for extremely simplified cases [detailed discussion in Dresner 95]. [Malinowski 93] adds a time derivative of heat flux to the Fourier term to account for thermal relaxation of heat conduction:

$$\vec{q} = -k\left(T\left(\vec{r},t\right)\right)\vec{\nabla}T(\vec{r},t) - t_k \frac{\partial \vec{q}}{\partial t} \qquad \left[\frac{W}{m^2}\right] \tag{2.1-4}$$

This new term brings along additional complexity which may not be necessary in the usual applications of this formula. Discrepancies between the solutions of the HBE with the additional term (2.1-4) and the one in (2.1-3) occur only in the ns-time range which is much smaller than the µs-time range discussed in this work.

The most important factor for stability in (2.1-3) is the heat transfer function h. Numerous experimental and theoretical studies have been conducted to elucidate heat transfer from metallic surfaces of all kinds to helium in all its states (A summary of this work can be found in [Van Sciver 86]). Especially heat transport in turbulent helium II is a highly complicated problem and it is governed by a non linear heat balance equation. Many publications deal with heat transport in helium II, from reviews in [Van Sciver 86], [Khalatnikov 65], to some sophisticated numerical simulations in [Kitamura 97]. The heat balance equation in turbulent helium II is:

$$c_p \frac{\partial T}{\partial t} = \vec{\nabla}\left(K\left(T\right)\left(\vec{\nabla}T\right)^{1/3} \right) \qquad \left[\frac{W}{m^3}\right] \tag{2.1-5}$$

where K is the temperature and pressure dependent apparent thermal conductivity which goes through a maximum at 1.9K. Derived from (2.1-5) [Van Sciver 91] proposed an appropriate definition of the effective thermal diffusivity of turbulent helium II:

$$D_{GM} = \frac{K}{c_p \Delta T^{2/3}} \qquad \left[\frac{m^{4/3}}{s}\right] \tag{2.1-6}$$

Despite the exceptionally high apparent thermal conductivity of helium II, the impact of the difference between helium I- and helium II-cooling on superconductor stability is not as big as one would expect. In fact the advantages of transient cooling in helium II are partly compensated by the decrease in specific heat of the superconducting composite.

Mainly due to the fact that the decision to work in superfluid helium is always accompanied by the claim for higher current densities (= rise in heat generation if Cu/Sc-ratio unchanged) and higher magnetic fields (=rise in heat generation as a consequence of a rise in matrix resistivity) the stability margin in helium II often turns out to be smaller than in helium I. Therefore only at identical worst case heat generation helium II will be a much better choice as cryogen than helium I. [Kobayashi and al 77] were the first to report enhanced transient cooling in helium II.

The challenge of stability-theory is to link the superconductor and the helium-cooling problems. The approach chosen in this work is presented in detail in the stability program documentation. Here, as in the majority of the cases in literature, the helium and the superconductor problem are de-coupled using a parametrization of the cooling function elaborated in independent heat transfer experiments published in literature. Unfortunately this approach suffers from the disadvantage that the independent helium experiments may not be simply transposable to the stability case when the experimental set-ups are not identical (in what refers to heater-surface and helium volume geometry). The ultimate goal from the theoretical point of view would be to calculate the electrical and thermal behavior of a composite superconductor in helium with a 3D finite element model, calculating simultaneously the electrical and thermal properties of the superconductor and the thermal properties of the helium in contact with the wire. For sure this task would require huge computing capacity and in what refers to the details of current sharing in the superconductor (thermal contact between filaments and matrix, electrical model of current sharing, ..etc) and to the heat transfer coefficient to helium the model will continue to rely on the same type of models as those used in simpler 1D approximations.

2.1.4 MQE and MPZ

By virtue of varying the initial heating power (at given perturbation profile in time and space) the solutions of (2.1-3) can be used to differentiate between cases which quench and cases which recover. The pulse-energy Q_{ini} which marks the bifurcation between quench and recovery is called Minimum Quench Energy (MQE) in the limit of δ-like (in time and space) disturbances. The MQE uniquely stands for the dynamic interaction of a multitude of parameters mentioned above: heat transfer properties of the wire surface, local aspect of helium volume, heat conduction in helium, onset-time of burnout, transverse and longitudinal heat conduction in the sample, heat generation due to current sharing, specific heat of the different materials in the composite, shape of initial heat pulse, ..etc. [Wipf + Martinelli 72] and [Wipf 78] suggested the existence of a limiting steady state temperature profile whose enthalpy content can be considered as the MQE. The length over which this equilibrium temperature profile extends is called Minimum Propagating Zone, MPZ. The MPZ profile, according to [Wilson 78], is that solution of the steady state HBE (2.1-3), with cooling and heating functions of arbitrary degree of accuracy, which obeys the boundary conditions $(dT/dx)_{x=0}=0$ and $T(\pm\infty)=T_b$. One might wonder if, even under perfectly reproducible experimental conditions, MQE or MPZ could ever be reproducible and thus representative magnitudes? Investigating the character of the different possible solutions to (2.1-3) [Dresner 95, p.207-212] showed on the basis of a simplified HBE, that the MPZ is unstable and that it unambiguously separates the quenching initial conditions from those that recover: The solutions of the 1-

dimensional partial differential HBE with temperature independent parameters (2.1-7) (g stands for heat generation, initial heating is supposed to have stopped) obey the ordering theorem. The ordering theorem says that when one solution (temperature) starts out bigger it always remains bigger.

$$c_p\left(\frac{\partial T}{\partial t}\right)=\frac{\partial}{\partial x}\left[k\left(\frac{\partial T}{\partial x}\right)\right]+\left(g-h\right)\frac{p}{A} \qquad \left[\frac{W}{m^3}\right] \tag{2.1-7}$$

The immediate impact of this theorem is that solutions whose initial state is everywhere greater than MPZ continue greater than MPZ and solutions whose initial state is everywhere less than the MPZ continue less than the MPZ. As already mentioned the MPZ is an unstable, limiting state, like a pencil balanced on its tip, which does not withstand the slightest perturbation. This concept, although tempting at first glance, reveals to be dubious: Each set of source terms has its "own" specific MPZ profile. Therefore an MPZ profile calculated with a steady state cooling function couldn't possibly apply to a transient cooling problem. Among the multitude of spatial temperature shapes crossed in time which is the one that has to be compared to the MPZ profile? The one just at the end of the pulse, the one at quench decision time (to find the quench decision time the problem has to be in any way solved independently of the MPZ concept)? Experiments and numerical simulations show that the temperature rises during and falls after the pulse to reach the quench decision plateau. Comparing a temperature profile at $t<t_{qdec}$ to the MPZ profile will lead to a wrong conclusion. In most of the cases the temperature profiles will cross the MPZ profile and the crossing profiles cannot easily be classified into quenching and recovering ones by mere comparison with MPZ. Furthermore the critical energy related to the MPZ, namely its enthalpy content, does not include the heat transferred to helium all along the process. Therefore this MQE criterion is only applicable in the limit of infinitely short quench decision times. For a realistic range of t_{qdec} (50µs-1ms) the MPZ enthalpy content strongly underestimates the MQE.

2.2 Heat Transfer to Liquid Helium

2.2.1 Heat Transfer

A heat transfer experiment consists in heating a surface with arbitrary orientation, exposed to a bath or a duct (length L, diameter d) containing helium, from inside and measuring the temperature difference between the bath T_b and surface T_s as it varies with the heat flux h [W/m^2]. Numerous variables affect the result of this experiment (bath temperature, pressure, surface orientation, physical characteristics of the heated surface, the frequency of heat flux). Though a typical measurement consists in finding ΔT of h the situation reverses in engineering applications, where the heat flux is determined from a calculated or measured temperature difference. The relation between h and (T_s-T_b) is called heat transfer correlation. Anything running on a very small time scale (µs-ms) is considered to be transient. Some phenomena well known in steady-state heat transfer, like convection and bubble formation, do not occur in the transient case. The steady state heat transfer mechanisms are often less efficient than those dominating on the short time-scale, making transient cooling a more powerful tool for cooling. The following chapters give a brief summary of the heat transfer characteristics for steady state and transient cooling in helium I and helium II, preceded by a compilation of the thermodynamic properties of liquid helium.

2.2.2 Helium Properties

The following series of figures resumes the most important helium properties at atmospheric pressure and between zero and ten Kelvin (data from [Cryopac]).

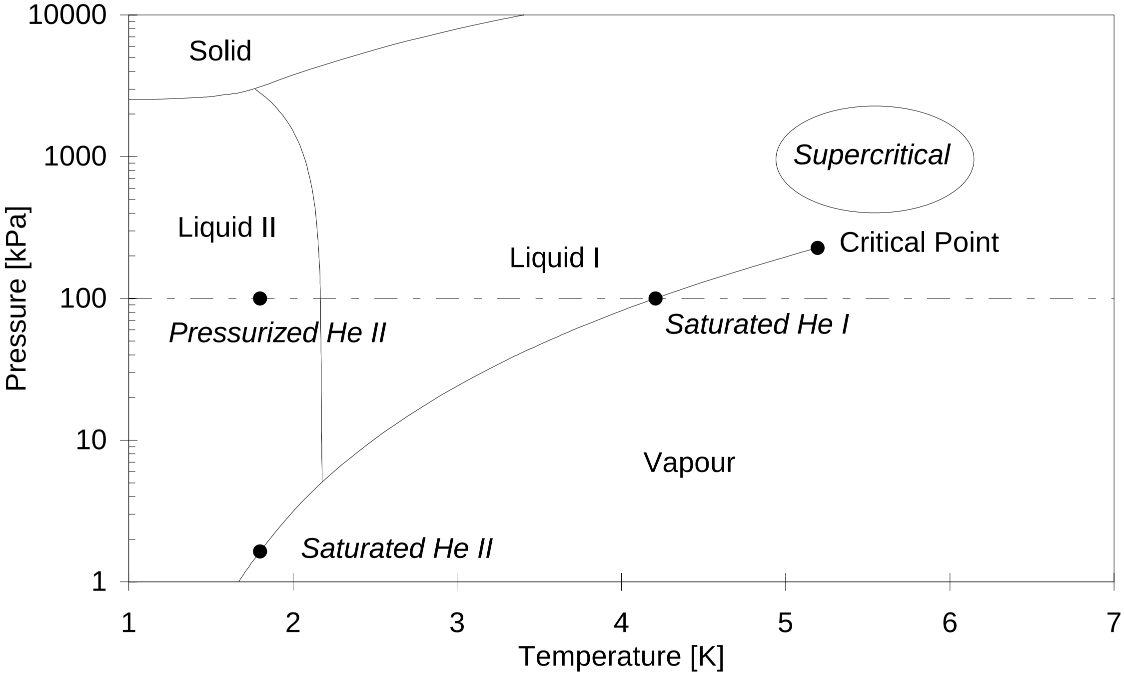

Figure 2.2-1: Helium phase diagram; Operating points: (4.2K, 1atm) and (1.9K, 1atm).

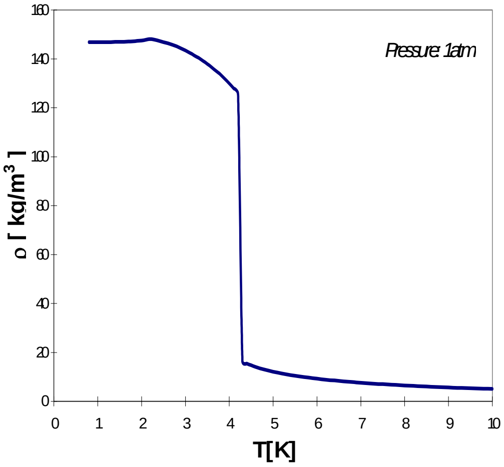

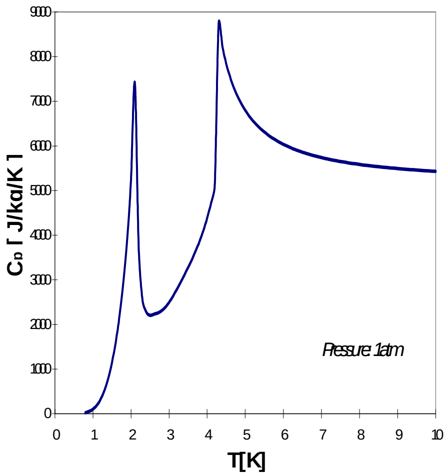

Figure 2.2-2a): Helium density as function of temperature at 1atm. Based on this graph the helium density is ~ 147kg/m^3 for $T<T_{\lambda}$, ~ 125kg/m^3 for liquid helium I and ~ 17kg/m^3 for gaseous helium.

b): Isobaric specific heat of helium as a function of temperature at 1atm.

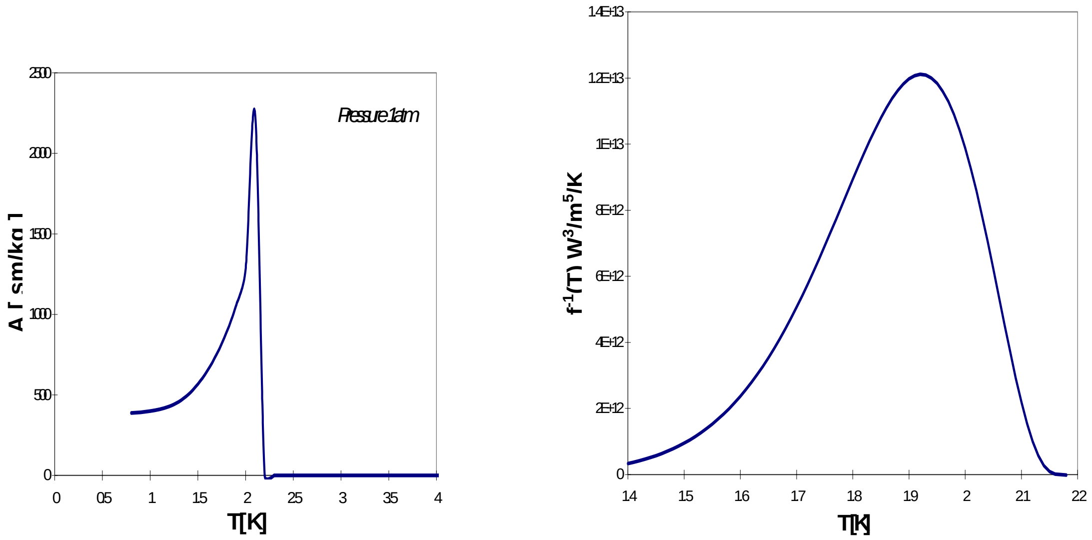

Figure 2.2-3a): Gorter-Mellink parameter A of helium II at 1atm. b): Heat conductivity function for turbulent helium II at 1atm [Van Sciver 86]. The maximum is at 1.92K.

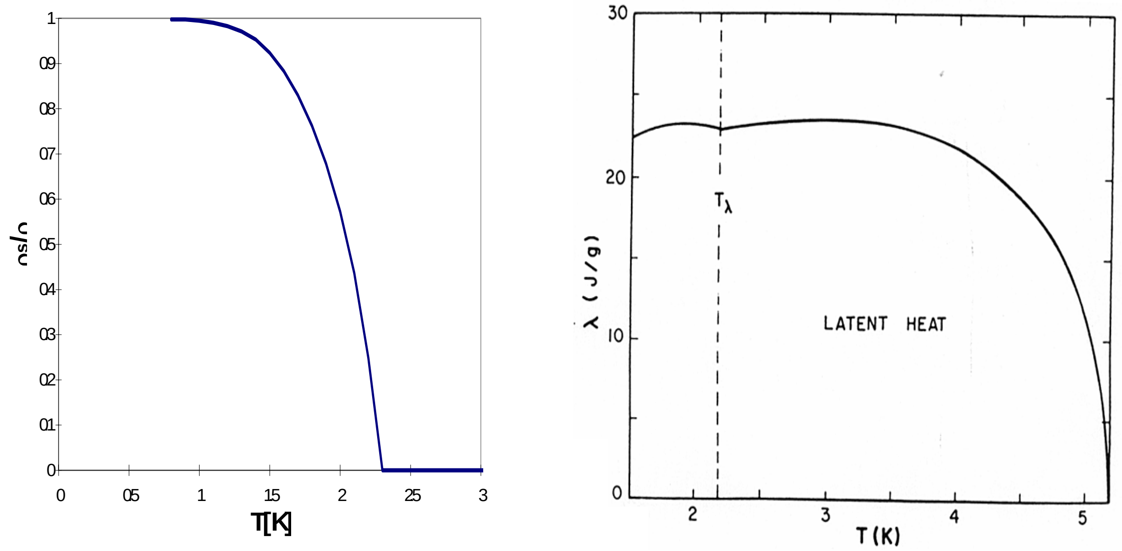

Figure 2.2-4 a) Superfluid versus total density as a function of T. Although ρ is approximately constant for T<T_λ, ρ_s and ρ_n are strongly changing functions with a maximum at 1.95K. b) Latent heat of vaporization of helium [Van Sciver 86].

The most important figures we will deal with in the following are gathered in Table 2.2-1 for helium I at 4.2K, 1atm and in Table 2.2-2 for helium II at 1.9K, 1atm:

ρ [kg/m^3]	C_p [J/kg/K]	k [W/m/K]	D [m^2/s]	σ [J/m^2]	λ [J/kg]
125	4747	0.01867	$3.126\cdot10^{-8}$	150	$2.05\cdot10^{4}$
		≈ Const		$370-7.9\cdot10^{-6}T^{7/3}$	$2\cdot10^{4}(1-(T/5.2)^{2})$
η [Ns/m^2]	Ra	Pr	ρ_V [kg/m3]	C_{pV} [J/kg/K]	k_V [W/m/K]
$3.2824\cdot10^{-6}$	1200	1.15	16.9	9780	0.01
≈ Const					$\propto T^{1/2}$
D_V [m^2/s]	η_V [Ns/m^2]				
$2\cdot10^{-6}$	10^{-6}				
	$\propto T^{1/2}$				

Table 2.2-1: Properties of liquid and gaseous helium at 4.2K, 1atm. The subscript v refers to the vapor phase. If possible analytical expressions for the temperature dependence are added. [Van Sciver, 86]

ρ [kg/m^3]	C_p [J/kg/K]	K [W/m$^{5/3}$/K$^{1/3}$]	D_{GM} [m$^{4/3}$/s]	η [Ns/m^2]	C_p [J/K/m^3] at T_λ
147.1	5030	$1.2\cdot10^{5}/20$	0.084	10^{-6}	$4\cdot10^{6}$
	$117\cdot T^{5.6}$	$1.04\times10^{5}\tau^{5.7}(1-\tau^{5.7})$ $\tau=T/T_\lambda$	$\Delta T^{-2/3}$		

Table 2.2-2: Helium properties at 1.9K, 1atm. [Van Sciver 86]

2.2.3 "Kapitza-like" Heat Transfer

The Kapitza resistance opposes heat transfer through the interface of two dissimilar materials. It strongly decreases with temperature ($\sim 1/T^3$) and is noticeable only at cryogenic temperatures. Theoretical approaches therefore predict the lower (acoustic mismatch theory, [Khalatnikov 65]) and upper limit (phonon radiation limit) for the Kapitza conductance coefficient a_K, but the agreement with measurement is poor. Eventually, this is related to an underestimation of the electron's role in the heat transmission from metallic surfaces ([Challis 62]). Formerly defined as the thermal conductance in the limit of vanishing ΔT [Kapitza 47] at T<1K, it regroups today a multitude of partly unexplained phenomena (among them certainly as well the original effect) causing a temperature discontinuity at the boundary between metal and liquid helium when crossed by strong heat flux. No significant change was observed in the range between vapor pressure and atmospheric pressure and there is no detectable explicit time dependence of the boundary conductance down to the millisecond time scale [Seyfert 80b]. On the other hand metallurgical condition and surface state of the sample affect the Kapitza resistance. To some extent imperfection and contamination of the surface reduce it. In general soft metals have higher Kapitza conductance coefficients a_K than hard metals, magnetic field and coatings or "dirty" surfaces enhance it [Kashani 85]. "*Moreover, a certain scatter of data from samples of practically the same type is a generally observed effect. It is in particular attributed to small variations of the surface condition which are almost impossible to control.*" (quoted from [Seyfert 80b]); Experimental values for the Kapitza conductance of copper at low heat fluxes range between $0.4T_s^3$ to $0.9T_s^3$kW/m^2/K. A practical heat transfer law in the Kapitza regime is given in (2.2-1), some of the values for a_K and n of Cu surfaces found in literature are given in Table 2.2-3.

$$h_K = a_K\left(T_s^n - T_b^n\right) \quad \frac{W}{m^2} \tag{2.2-1}$$

a_K [W/m^2/K^n]	n	Comment	Source
130-200	4	untreated	[Schmidt 81]
180	4	no special treatment - only at low ΔT<0.6K	[Gentile 80]
490	2.8	no information available	[Seyfert 81]
105	2.7	no information available	[Goodling 69]
458	3.5	oxidized in atmosphere for one month	[Kashani 85]
518	3.7	oxidized in air at 200°C for 40min.	[Kashani 85]
764	3.4	50-50 PbSn solder coated (25μm)	[Kashani 85]
735	2.1	GE7031 varnish coated	[Kashani 85]
670	1	electropolished OFHC Cu	[Taneda 92]
710	1	PVF-coated (~14μm) OFHC Cu	[Taneda 92]
840	3.5	?	[Shiotsu 92]

Table 2.2-3: Values of Kapitza conductance fit coefficients for copper;

The Kapitza conductance of several other materials has been reported in literature: e.g.: a_K=2000W/m^2/K^n, n=4 for Pt-Co [Shiotsu 96], a_K=840W/m^2/K^n, n=3.5 for Au-Mn$_{0.25}$ [Shiotsu 92], a_K=2240W/m^2/K^n, n=2.72 for stainless steel [Taneda 92],..etc. [Denner 77] measured the Kapitza resistance of lead, copper and nickel, but unfortunately only at T<1.4K. [Schmidt 75] investigated the Kapitza boundary resistance between niobium and copper and niobium-tin and copper: "*At 4K, filaments 6μm in diameter, show a temperature discontinuity at the NbTi/Cu boundary, which is already as large as the temperature difference in the filament itself.*". Therefore the Kapitza resistance between filament and matrix may as well play a certain role in stability considerations of multifilament conductors.

2.2.4 Helium I

2.2.4.1 Steady State Heat Transfer in Pool Boiling Helium I

Helium I has a rather small thermal conductivity (and large specific heat), suggesting that conduction heat transport is of little significance to the overall heat transfer picture. Particularly in the steady state, heat transport is dominated by density driven convection. Conduction merely occurs in a thin layer adjacent to the heater, henceforth inducing convection or bubble formation. In the transient case conduction becomes the dominant heat transport mechanism in helium I. The heat transfer process in helium I can be regarded (in the electro-thermal analogy) as a heat flow through a sequence of thermal resistors: the Kapitza resistance at the boundary between the solid and the helium and the thermal resistance of the helium bulk, where R_{nc}, R_{nb}, R_{fb} are the thermal resistors associated with the different heat transfer regimes in helium I (Table 2.2-4). The switching between these three regimes is related to critical heat flux densities. A simplified but widely used approach is to relate the temperature drop over the whole chain to the resistance of the largest contributor. In steady state helium I heat transfer the most resistive part is the helium. The Kapitza resistance can be neglected (example: $R_K:R^{(I)}_{nc}\approx1:1000$, $R_K:R^{(I)}_{nb}\approx1:100$, $R_K:R^{(I)}_{fb}\approx1:1000$). The heat transfer correlations in steady state helium I boiling are given in (2.2-2), (2.2-3) and (2.2-6). The nc-correlation (2.2-2) is taken from classical hydrodynamics and describes heat removal by density driven convection currents (Bénard convection). C is an empirically determined parameter, n ≈0.3, L is the heater dimension, Ra the Rayleigh number (Table 2.2-1).

REGIME	*L/k=R THERM. RESIST.m²K/W*	*CRITICAL HEAT FLUX DENSITY W/m²*
Natural convection nc	≈0.002	$h_c^{(I)}\approx10 W/m^2$
Nucleate boiling nb	$\approx2\cdot10^{-5}(T_s-T_b)^{-3/2}$	$h^{*(I)}\approx(5-15) kW/m^2$
Film boiling fb	≈0.004	-

Table 2.2-4: Steady state heat transport regimes in boiling helium I. The thermal resistance R is calculated from L/k with k taken from the heat transfer correlation h=kΔT. The switching from one regime to the other occurs when h has reached the critical values given in column three. Data from [Schmidt 81] and [Van Sciver 86].

$$h < h_c^{(I)} \qquad h = C\frac{kRa^n}{L}\left(T_s - T_b\right) \approx 500\left(T_s - T_b\right) \tag{2.2-2}$$

With h increasing beyond the critical heat flux $h_c^{(I)}$ bubbles of helium vapor form at preferred sites on the surface until the nucleation sites get fully activated. Bubble detachment creates macroscopic turbulence with cold liquid rushing down to cool the surface. At the same time natural convection even if somehow perturbed persists. [Caspi 84] showed that the free convection heat transfer can be maintained to considerably higher heat flux with increased subcooling. A derivation of the nucleate boiling heat transfer correlation from basic principles accounting for the latent heat of the helium within the bubble, the energy required to superheat a new layer of liquid that replenishes the layer taken away with the departing bubble and the nc-term includes too many unknown parameters. According to [Van Sciver 86] the most accepted phenomenological correlation has been presented by [Kutateladze 52]:

$$h_c^{(I)} \le h < h^{*(I)} \qquad h = 1.9\cdot10^{-9}\left[g\left(\frac{\rho_l}{\eta_l}\right)^2\right]^{0.3125}\left(\frac{p\chi}{\sigma}\right)^{1.75}\left(\frac{\rho_l C_{pl}}{\rho_v\lambda}\right)^{1.5}\left(\frac{k_l}{\chi}\right)\left(T_s - T_b\right)^{2.5} \tag{2.2-3}$$

where the subscripts l and v refer to liquid and vapor, λ to the latent heat in J/kg, σ the surface tension of liquid helium in N/m^2, η_l the viscosity, $g=10m/s^2$ and $\chi=(\sigma/\rho_l/g)^{1/2}$. At 4.2K and 1atm the coefficient of proportionality becomes $58kW/m^2/K^{2.5}$, in vague agreement with experimental values (for Cu surfaces) of $10kW/m^2/K^{2.5}$ [Schmidt 81].

The steady state Nucleate Boiling Maximum (NBM) $h^{*(I)}$ according to [Van Sciver 86] is:

$$h^{*(I)} = 0.16\lambda\rho_v^{1/2}\left[\sigma g\left(\rho_l - \rho_v\right)\right]^{1/4} \qquad (2.2\text{-}4)$$

(2.2-4) can be seen to rise (λ) in subcooled conditions [Verkin 80]. The maximum nucleate boiling heat flux $h^{*(I)}$, calculated from (2.2-4), is 8.5kW/m^2 at 4.2K / 1atm., but experimental values vary within a greater range (indicated in Table 2.2-4). The NBM is heater orientation dependent, with surfaces facing upwards giving higher values than surfaces facing downwards. [Iwamoto et al 96] studied heat transfer from a 18×76mm copper plate, varying the orientation and the treatment of the heat transfer surface. They found that the oxidation of the heat transfer surface improved the NBM and the minimum recovery heat flux MRF (transition to free convection when coming from higher flux). The NBM was highest when the copper plate faced upwards (7.5kW/m^2). Interesting phenomena occurred with the plate in the vertical position when half of the sample surface was oxidized: Once the polished part had run into film boiling the heat flow was deviated to the oxidized half until $h^{*(I)}$ was reached there as well. This gave rise to a double transition involving two $h^{*(I)}$. This effect could not be reproduced in the horizontal position where the vapor film immediately extended over the whole surface, due to reduced convection. [Iwamoto et al. 94] varied the amount of helium in contact with the heated surface (d=2-3mm channels). They (and many others, e.g. [Schwall 80], [Guo 97]) observed that the channel geometry degraded the steady state critical heat flux at any orientation of the plate but in particular in the horizontal position. This could be explained by the accumulation of vapor during nucleate boiling (vapor locking). Just for one orientation (-15° from the horizontal position) the channel geometry enhanced $h^{*(I)}$ because the expulsion of vapor resulted in a forced flow of the liquid/gas mixture through the channel (thermo-siphon effect). In general a degradation of the heat transfer properties in channels is observed [Van Sciver 86], the effect of channel size (length and width) on nucleate boiling being explained by vapor filling of the channel. [James 70] observed that the critical steady state heat flux in channel cooling correlated well with (depth)/$(\text{length})^{1/2}$, thus decreasing at smaller channel depth (width). [Iwamoto 98] points out the decrease of h*(I) with sample length noting that free convection around the surface interferes stronger in heat transfer when the heated surface becomes smaller. [Caspi 84] reports the following formula for the increase of critical steady state nucleate boiling heat flux as a function of subcooling:

$$\frac{h*^{(I)}_{sub}}{h*^{(I)}_{sat}} = 1 + 0.198\left(\frac{\rho_v}{\rho_l}\right)^{3/4}\frac{c_p\left(T_{sat}\right)\left(T_{sat} - T_b\right)}{\lambda} \qquad (2.2\text{-}5)$$

where λ is the latent heat of vaporization in J/m^3.
At still higher heat fluxes, the nucleate boiling bubbles get large and detach at such a rate that they become unstable and coalesce into a continuous vapor film. The best known film-boiling heat transfer correlation was presented in [Breen and Westwater 62] (2.2-6). The proportionality constant in (2.2-6) is 300-1000W/m^2/K according to the choice of D. The pronounced diameter effect has been found as well in experiments [Brentari 65].

$$h \geq h^{*(I)} \qquad h = \left\{ 0.37 + 0.28\sqrt{\frac{\sigma}{gD^2}} \right\} \left\{ \left[\frac{g^3}{(\rho_l - \rho_v)\sigma} \right]^{1/8} \left[\frac{k_v^3 \rho_v \lambda`}{\eta_v (T_s - T_b)} \right]^{1/4} \right\} (T_s - T_b) \qquad (2.2\text{-}6)$$

where λ` is the effective latent heat given in (2.2-7) and D the heater diameter.

$$\lambda` = \frac{\left[\lambda + 0.34 C_{pv}(T_s - T_b)\right]^2}{\lambda} \qquad (2.2\text{-}7)$$

[Holredge 71] experimentally confirmed the use of (Kutateladze- and) Breen/Westwater-correlation for horizontal cylindrical heaters. In many practical cases, however, a more conservative heat transfer coefficient may be used with values between 170 and 280W/m^2/K [Schmidt 81]. Taking the heat flux back to smaller values the recovery of nucleate boiling heat transfer will occur at the recovery heat flux $h_R^{(I)}$ which is approximately $0.35h^{*(I)}$ [Van Sciver 86] and explicitly given in (2.2-8).

$$h_R^{(I)} = 0.16 \lambda \rho_v \left[\frac{g\sigma(\rho_l - \rho_v)}{(\rho_l + \rho_v)^2} \right]^{1/4} \qquad (2.2\text{-}8)$$

[Schwall 80] reports that in narrow channels the steady state heat transfer to helium I lacks hysteresis ($h_R^{(I)} \sim h^{*(I)}$).

2.2.4.2 Transient Heat Transfer to Pool Boiling Helium I

Early reports in [Steward 78] and [Iwasa 78] indicated an improved heat transfer characteristic for transient cases. [Sakurai 96] reports an increase of a factor 10 in the critical heat flux between transient and steady state heat transfer. For very short times, that is, Δt<1ms, the heat transfer process turns out to be controlled mainly by Kapitza conductance because it is worse than pure conduction in helium I, the only contributor to transient heat transport. Transient conduction can be sustained up to a heat flux by far exceeding the steady state NBM, but restrictions related to critical times and critical energies impose the limits of this highly efficient state. Transient heat transfer is usually investigated with fast thermometers in pulsed source or step heat flux experiments.

[Schmidt 81] believes that transient heat transfer in HeI is governed by Kapitza resistance and another not well understood heat flux independent contribution giving rise to a moderate temperature gradient between solid and bath ($\Delta T_0 \sim 0.2$K). The temperature offset has been reported as well in [Steward 78]. [Sakurai 88] speaks of “quasi steady nucleate boiling”. When the amount of heat transferred to the helium reaches a (energy- or time-) limit film-boiling ensues. The burn-out limits are functions of the helium properties only. Film-boiling is triggered when the energy transferred into the heated helium-volume has provided the latent heat of vaporization λ(J/kg) associated to it. Hence the critical energy depends on the penetration depth (δ) of heat (Table 2.2-5).

t [ms]	0.001	0.01	0.1	1	10	100	1000
δ [μm]	0.2	0.6	1.8	5.6	17.7	56	180

Table 2.2-5: "Penetration depth" of heat in pool-boiling helium I versus time.

In small (L=1-100μm) open channels and for heat fluxes moderately above NBM the heat transfer will take advantage of the full heat absorption capacity of the channel and run into the so called channel limit, which according to [Iwasa 77] is given by 0.7λL because the evaporation will cause a fraction of the liquid to be pushed out of the channel (2.2-9).

$$e_{Cl}^{(I)} = 0.7 \cdot 2..5 \cdot 10^{6} \cdot L \quad \left[\frac{J}{m^{2}}\right] \tag{2.2-9}$$

In small closed channels even a heat flux below NBM (acting long enough) will vaporize sufficient helium during nucleate boiling to raise the pressure in the channel to critical [Schmidt 88]: The constant Const in (2.2-10) ranges between 3.7(calculation) and 5.3(measurement). Above critical pressure film-boiling ensues without any further heating.

$$e_{cCl}^{(I)} = Const \cdot 10^{4} \cdot L \quad \left[\frac{J}{m^{2}}\right] \tag{2.2-10}$$

[Schmidt 88] reports that a small vapor fraction (~10%) in closed channels improves transient heat transfer because the high compressibility of the vapor compensates the pressure rise due to evaporation. In long channels or in an open bath and for particularly high heat flux it is likely that the channel limits are out of reach because massive heat input occurs into a thin (δ<<L) layer. Following [Schmidt 78] the dynamic critical energy ("Schmidt-limit") can be deduced from the energy needed to evaporate a superheated layer with a thickness δ (diffusion length). By virtue of the diffusivity D of helium I [Schmidt 88] calculated λδ assuming a constant heat flux and obtained a law (2.2-11) which conveniently reproduces his own step-heat-flux experiments [Schmidt 78].

$$e_{Sl}^{(I)} = \frac{6.9 \cdot 10^{5}}{h_{K}} \quad \left[\frac{J}{m^{2}}\right] \tag{2.2-11}$$

(2.2-11) is in quantitative agreement with measurements on a thin brass foil [Tsukamoto 85]. The constant in (2.2-11) K_{SL} is $D(\rho_l\lambda)^2 = 2.8\cdot10^5 J^2m^4/s$ at 4.2K/1atm (see Table 2.2-1 for the helium properties).[Lezak 86] explains the factor 2 difference between the calculated value and Schmidt's data by the fact that film boiling sets in at partial (e.g. 50%) coverage of the surface with vapor. The above mentioned formula for K_{SL} shows a bump-like temperature dependence reaching a maximum at 3.5K. However, the success of (2.2-11) shows that transient burn-out in helium I can be better described by a simple diffusion model than by the assumption of some minimum stable film thickness based upon steady state hydrodynamic calculations as formerly attempted (e.g. [Holmes 82]). Nevertheless, as Lezak states it, the diffusion model turns out to be less accurate at lower heat flux, when burn-out time increases and macroscopic convection and turbulence appear. In optical measurements of transient heat transfer to helium II [Tamada 94] estimated the critical energy of bubble formation to be $5\times10^4/h_K$ J/m^2 which seems reasonable referring to (2.2-11) because bubble formation precedes burn-out. The important consequence of (2.2-11) is that the total energy transferred before onset of film-boiling decreases with increasing heat flow. That means that a decrease of the heat flow, e.g. by a thin insulation layer may be advantageous in some cases because it prolongs the duration of the nucleate boiling regime [Chandratilleke 89]. Resuming transient heat transfer to helium I [Filippov 90] suggested the use of a so called mode map plotting h or ΔT (=(T_s-T_b)) as a function of time (like that in Figure 2.2-5**)**: Bubble formation onset time and film boiling onset time divide the h/t plane into the lower conduction and the upper film boiling part. An additional time condition divides the plane into the left transient and the right steady state part. The steady state region can be shaped in layers using the critical heat flux $h_c^{(I)}$ and $h^{*(I)}$ to separate convection from nucleate boiling and film-boiling. A more refined picture, as suggested by [Filippov 90} would then contain fine-structures along the boundaries between the different regimes.

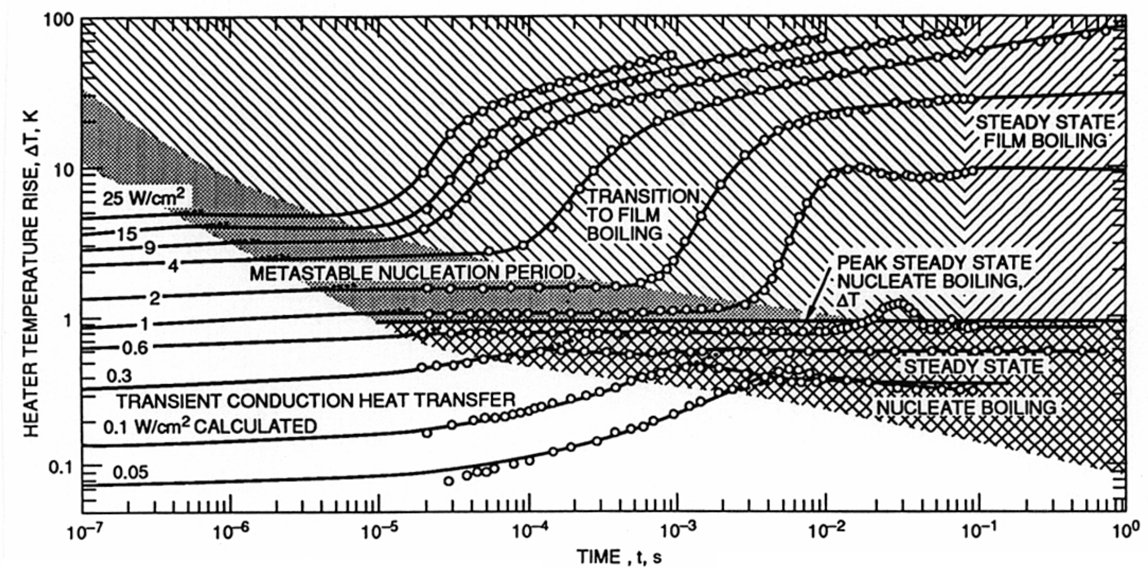

Figure 2.2-5: Heat transfer correlation map in helium I: $\Delta T(t)$ curves for varying step heat flux. Upper right corner steady state film-boiling, lower left corner transient "Kapitza-like" heat transfer. [Steward 78].

Many authors have investigated the effect of the heater surface condition on the heat transfer characteristic. Successful solutions often rely on an increase of active surface (e.g. fine copper pins bonded to the surface [Ogata 91], multi-layered porous structure pins [Hakuraku 87], grooves machined into the heater surface [Ogata 82], porous metal coating [Baynham 81],….). Another approach which mainly concerns steady state heat transfer to helium I consists in roughening or oxidizing the surface to increase the number of potential nucleation sites to improve heat transfer in the nucleate boiling regime (e.g. [Ogata 82]).

2.2.5 Helium II

Below T_λ (=2.17K at 1atm.) helium enters the superfluid phase, characterized by a complete lack of viscosity and unique heat transport properties. The apparent thermal conductivity is several orders of magnitude greater than in metals. Derived from that the heat transfer correlation for steady-state and transient heat transfer in subcooled helium II is determined by Kapitza resistance, unless film-boiling occurs. But unlike bulk thermal conductivity in a metal, heat transport in helium II is subject to various restrictions.

2.2.5.1 Heat Transport in Helium II

The two-fluid model describes heat transport in helium II as a friction-less counter-flow process where a normal fluid component (the normal fluid entropy density $s_{mn} \approx s_{m\lambda}$, normal viscosity η_n, normal density ρ_n, superfluid density ρ_s) transport entropy and temperature to the cold sink, whereas the superfluid component (viscosity η_s=0 , superfluid entropy density s_{ms}=0) flows back, such that there is no net mass transport involved in the process [London 54, Wilks 87]. Strictly speaking the 2-fluid model is a macroscopic model of a “real” Bose gas at T close to zero, having a fraction in the condensed state (superfluid) and a spectrum of excited states (normal component). When the heat flux in the helium II bulk becomes such that the counter-flow process occurs at a “critical velocity” the helium II becomes turbulent. The stipulation that critical velocities associated to the superfluid, the normal and the relative motion of both components mark the transition from the ideal to the turbulent state has to be added to the 2-fluid model. The transition is not well described in literature, but it is established that each component is thought to contribute to the transition with a change in behavior (laminar to turbulent flow for the normal component, appearing of vortex-tangle in superfluid component) when its critical velocity is reached. The qualitative picture of helium II above the critical velocities (usually some cm per second) is that of a liquid with turbulence distributed in an array of vortex lines each bearing a quantum of circulation h/m_{He}. The success of the 2-fluid model lies within the fact that the characteristics of helium II can be derived from normal hydro-dynamics. Equation (2.2-12) gives the heat transfer correlation [Landau 59] for the ideal (Landau-) regime, where β is a geometrical constant (β~10-20) and d the channel diameter. A special feature of the conductivity function in the ideal regime is its strong diameter dependence, with the helium getting less conductive as the diameter increases.

$$h = \frac{d^2 (\rho_n s_{mn})^2 T}{\beta \eta_n} \left| \vec{\nabla} T \right| \qquad \left[\frac{W}{m^2} \right] \tag{2.2-12}$$

The calculation of the heat transport equation in turbulent helium II is also based on 2-flow fluid-dynamics, with the additional assumption that there is a viscous drag between the normal fluid and the vortices (2.2-13).

$$\left| \vec{\nabla} T \right| = \frac{\beta \eta_n}{d^2 (\rho_n s_{mn})^2 T} h + \frac{A \rho_n}{\rho_s^3 s_m^4 T^3} h^3 + ... \qquad \left[\frac{K}{m} \right] \tag{2.2-13}$$

The first term of (2.2-13) is the same as the one developed for the viscous flow of non-turbulent helium II (2.2-12). The second term describes the mutual friction interaction. It lacks diameter dependence and goes as the cube of the heat flux and therefore largely dominates (2.2-13). A(p,T) (Figure 2.2-3) is the experimentally obtained Gorter Mellink mutual friction parameter, which has been introduced in (2.2-13) through a phenomenological approach to the force acting between vortices and normal flow [Vinen 81]. The following figure resumes the heat transport correlation in helium II.

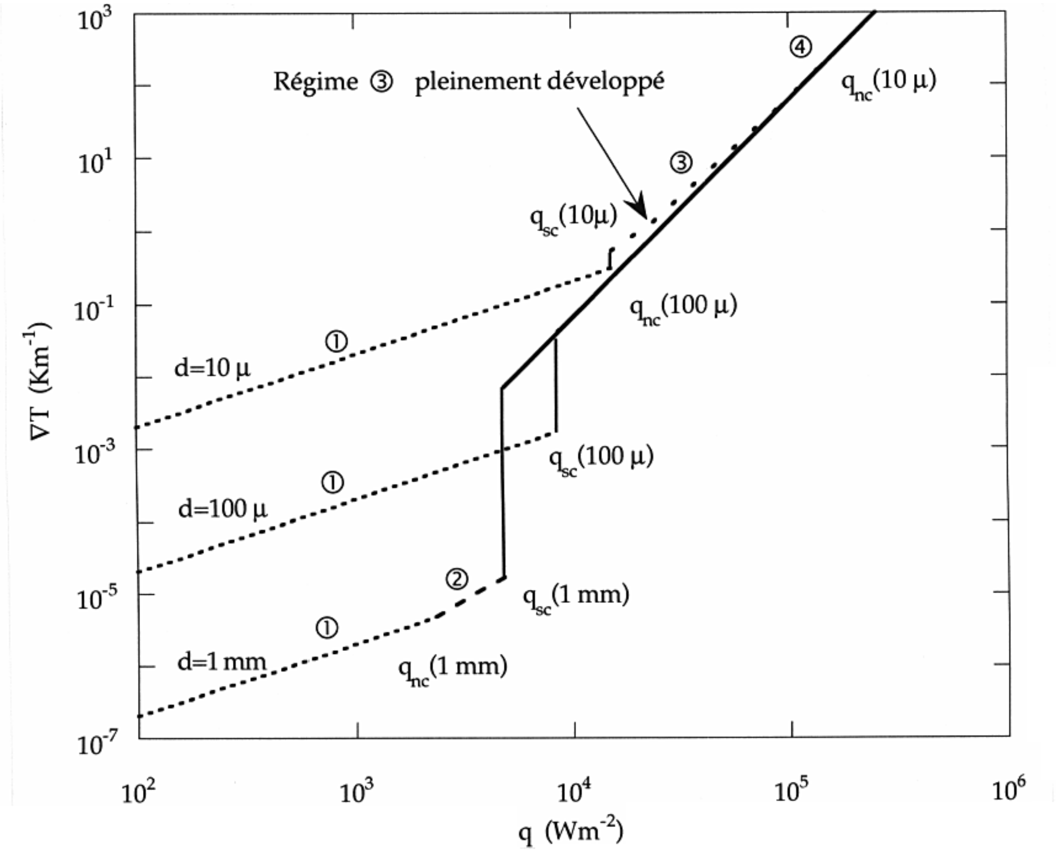

Figure 2.2-6: Regimes of heat transport in superfluid helium II: ❶: ideal regime for different channel diameters (10, 100, 1000µm), ❷: normal turbulence appears, ❸: turbulence in the superfluid appears, ❹: fully developed turbulence in normal and superfluid; Figure taken from [Baudouy 96];

The thermal bulk resistance (slope in $\Delta T(h)$) in superfluid helium is small. Therefore the heat transfer correlation of surface cooling to superfluid helium is always determined by the interface Kapitza resistance. This was verified in many experiments, among them [Gradt 90]. A heat flux higher than the critical steady state heat flux or a heat flux smaller than the critical steady state heat flux into a restricted volume of helium can trigger film boiling. It has been found that the onset of film boiling is not only related to the volume of helium available but also to the magnitude of heat flux and the geometry of the helium volume (number, size and shape of “channels”). In an engineering correlation the steady state heat diffusion equation (2.2-13) is [Van Sciver 86]:

$$\frac{dT}{dr} = f(T)h^m\left(\frac{r_0}{r}\right)^m \qquad \left[\frac{K}{m}\right] \tag{2.2-14}$$

At atmospheric pressure the conductivity function $f^{-1}(T,p)$ (Figure 2.2-4) goes through a maximum at 1.9K. The factor m is usually 3. (2.2-15) is a phenomenological fit for f^{-1}:

$$f^{-1}(T,1atm) = \frac{\rho^2 s_{m\lambda}^4 T_\lambda^3}{A_\lambda}\left[\left(\frac{T}{T_\lambda}\right)^{5.7}\left(1-\left(\frac{T}{T_\lambda}\right)^{5.7}\right)\right]^3 \qquad \left[\frac{W^3}{Km^5}\right] \tag{2.2-15}$$

The Gorter Mellink regime can be sustained as long as the helium II in the channel has not reached T_λ in any point. The critical steady state heat flux $h^{*(II)}$ may therefore be obtained from (2.2-14) with (2.2-15) by integrating between T_b and T_λ and from x=0 to x=L.

$$h^{*(II)} = \left(\frac{2}{r_0}\int_{T_b}^{T_\lambda}\frac{dT}{f(T)}\right)^{1/3} \qquad \left[\frac{W}{m^2}\right] \tag{2.2-16}$$

At 1.8K and L=1mm $h^{*(II)}$ in (2.2-25) becomes 150kW/m^2, which is remarkable. The critical heat flux depends on the geometrical properties of the channel and the boundary conditions of the heat flux problem. For very long channels, the steady state peak heat flux is low because the allowable temperature gradient is smaller than in short channels (always assuming that the end of the channel is kept at T_b). [Kobayashi 96] reports that $h^{*(II)}$ decreases with decreasing ratio of channel diameter and channel length L. The steady state critical heat flux from round wires decreases proportional to $d^{-1/3}$ (see (2.2-16) with wire diameter d (e.g. [Shiotsu 96]: from 30 to 20 kW/m^2 for d=0.1 and 1 mm). Van Sciver (81) reports that much higher steady state peak heat currents could be obtained if the channel was divided by filling it with a large number of fine tubes (experiment in saturated helium II). This effect was later confirmed as well in [Tsuruga 91]. Other $h^{*(II)}$ measurements: [Van Sciver 79]: 5.2kW/m^2,L~1m , [Seyfert 82]: 3.5kW/m^2, L~1cm (both at SVP, 1.8K), [Van Sciver 80] 40kW/m^2,L~1cm), [Bon Mardion 79] 40kW/m^2, L~1cm ,[Shiotsu 92] 30kW/m^2 (all at 1.9K, subcooled at 1atm). On the other hand [Warren 82] reports that $h^{*(II)}$ is bigger in an open bath environment (e.g. 100kW/m^2 at 1.8K, subcooled) than in a moderately restricted geometry. Since not only $h^{*(II)}$ but also many other helium II parameters reflect the geometry dependence of f, a geometry independent heat flux was defined: $h \rightarrow hL^{1/3}$. The critical heat flux increases significantly with enhanced subcooling (e.g. [Goodling 69], [Ibrahim 78], according to [Chen 87] it increases proportionally to the enthalpy difference between the two helium states). Whenever $h^{*(II)}$ is exceeded under subcooled conditions, a double transition takes place: First creating a film of liquid helium I, followed by film-boiling, bringing all helium states close to the heat transfer surface. In steady state heat transfer experiments the transition to helium I can be seen as a rapid jump in surface temperature preceding the temperature jump due to onset of film boiling [Chen 87]. The steady state critical heat flux in a 1-dimensional approximation (and not for cylindrical samples as in (2.2-16)) is [Van Sciver 86]:

$$h^{*(II)} = \left[\frac{1}{L} \int_{T_b}^{T_\lambda} \frac{s_m}{A\rho_n} (\rho_s s_m T)^3 dT \right]^{1/3} \qquad \left[\frac{W}{m^2} \right] \tag{2.2-17}$$

2.2.5.2 Transient Heat Transfer to Subcooled Helium II

A diffusion-like model has been shown to describe transient heat transfer to helium II effectively. The transient temperature profile is available through numerical solutions of the heat conduction equation, taking the Landau- or the Gorter-Mellink proportionality factor as an effective conductivity. In addition this method yields the (critical) energy needed to trigger film-boiling. The most striking aspect of transient heat transfer to helium II is that a heat flux by far exceeding the steady state critical heat flux $h_c^{(II)}$ (and $h^{*(II)}$) can be sustained (Figure 2.2-7). This stems from the finite time it takes the dissipative mechanisms causing the limiting heat flux to appear.

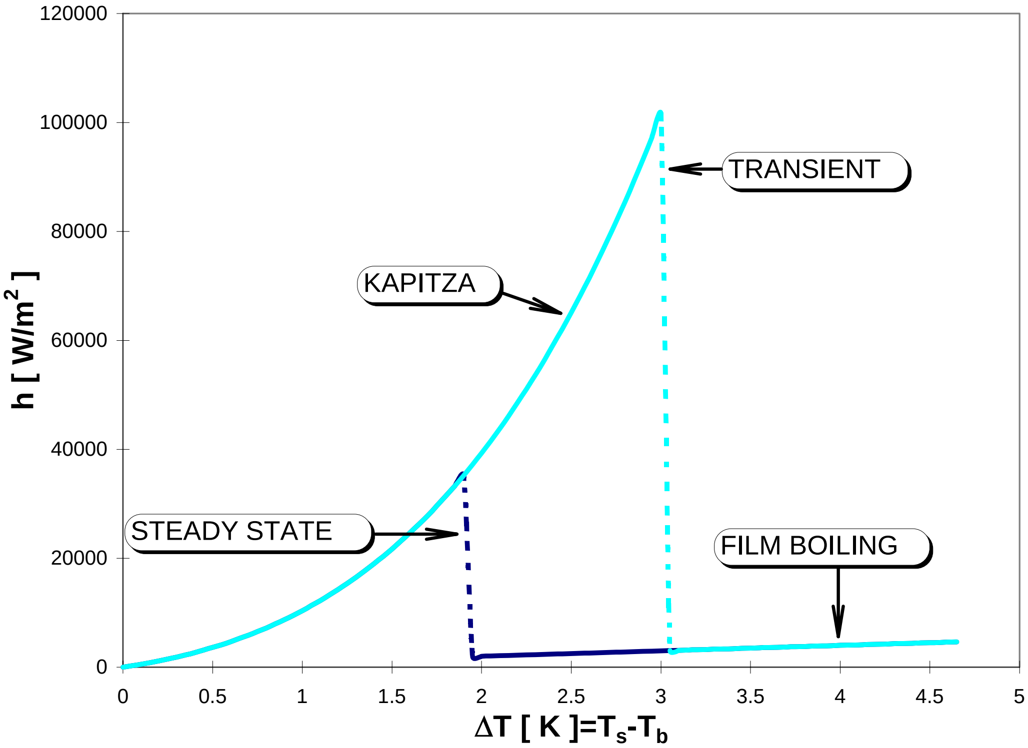

Figure 2.2-7: Comparison of steady state and transient heat transfer in helium II at 1.9K and 1atm. Kapitza regime (a_K=180W/m^2/K^4) before burn-out and film boiling (a_{fb}=1000W/m^2/K) after burn-out. Limiting heat flux in steady state is 35kW/m^2 (arbitrary); Gorter-Mellink limit: $e_{GM}^{(II)}$=800J/m^2, with h_{Kmax}=100kW/m^2 (arbitrary) and film boiling onset time of 8ms for the transient case.

The heat diffusion equation in turbulent helium II is a nonlinear partial differential equation given in (2.1-5). Dresner has solved this equation for constant properties (T-independent c_p and K) with the "method of similarity solutions" for two boundary conditions:

a) a half space with clamped heat flux at the free face and
b) a half space with clamped temperature at the free face.

The clamped flux problem corresponds to experiments, where a step heat pulse was applied to a long channel (~10m) containing helium II and an array of temperature sensors measured the time dependent temperature gradient in the helium [Van Sciver 79]. [Dresner 82] calculated the solution of the turbulent superfluid diffusion equation (2.1-5) (with constant properties) and found for the temperature of the helium layer next to the heater (2.2-18):

$$T(0,t) = T_b + 0.8339 \frac{h^2}{\sqrt{\overline{c}_p}\left(\overline{K}\right)^{3/2}}\sqrt{t} \qquad [K] \tag{2.2-18}$$

where K is Dresner's temperature dependent helium II heat conductivity function (much alike $f^{-1}(T)$) related to the Gorter-Mellink friction parameter A (given in (2.2-19) together with a fit from [Van Sciver 86]).

$$K = \rho_s s_m T\left(\frac{s_m}{A\rho_n}\right)^{1/3} \approx 1.04\cdot 10^5\left(\frac{T}{T_\lambda}\right)^{5.7}\left(1-\left(\frac{T}{T_\lambda}\right)^{5.7}\right) \qquad \left[\frac{W}{m^{5/3}K^{1/3}}\right] \tag{2.2-19}$$

Computing burn-out time $t^{*(II)}$ from (2.2-18) with the condition ($T(0,t^{*(II)})=T_\lambda$) gives the burn-out formula $t^{*(II)} \sim h^{-4}$:

$$t^{*(II)} = 1.438\cdot \overline{K}^3 \overline{c}_p \left(T_\lambda - T_b\right)^2 \frac{1}{h^4} \qquad [s] \tag{2.2-20}$$

The proportionality constant K_{GM} ($t^{*(II)}=K_{GM}/h^4$) calculated from (2.2-20) with the following average material properties (at average temperature T_{av}, taken from [Van Sciver 86]) for subcooled helium II at T_b=1.8K: $T_{av}=(T_\lambda+T_b)/2$=1.99K, c_p(2K)= 8.36×10^5J/K/m^3 and K=24152W/m$^{5/3}$/K$^{1/3}$ is 12×10^{17} W^{4}s/m^8. The experimental values in [Van Sciver 79] vary between 9-11$\times10^{17}$ W^{4}s/m^8. Dresner's calculated data converge to Van Scivers experimental data when the deterioration of Kapitza-like heat transfer begins not at T_λ but at slightly lower temperatures. [Van Sciver 79] came to a quite similar theoretical result with a phenomenological model, assuming an exponentially shaped temperature profile with an adjustable peak temperature T_{s0} down the channel ((2.2-21), δ is the penetration depth).

$$\Delta T(x) = T_s - T_b = \left(T_{s0} - T_b\right)e^{-\frac{x}{\delta}} \qquad [K] \tag{2.2-21}$$

Assuming that δ, h_{K0} (see Figure 2.2-11) and $c_p\approx$const, makes T_{s0} linear in time. Integrating the enthalpy $e=c_p\Delta T(x)$ between zero and x, with $\Delta T(x)$ from (2.2-21), transforming e in [J/m^3] to e' in [J/m^2] and taking the time derivative gives de'/dt [W/m^2].

Substituting de'/dt into the heat current equation $h=h_{Ko}-de/dt$ (describing the heat path in the helium as a simple nod with a resistor and a capacitance in parallel) together with $h_{K0}=\delta c_{paverage}(dT_{s0}/dt)$ (conservation of energy) gives an expression for the heat flux density in the helium bulk (2.2-22).

$$h(t,x) = \rho \bar{c}_p \delta \frac{dT_{s0}}{dt} e^{-\frac{x}{\delta}} = h_{K0} e^{-\frac{x}{\delta}} \left[\frac{W}{m^2} \right] \qquad (2.2\text{-}22)$$

Substituting h(t,x) from (2.2-22) into the heat transport equation in the GM regime ((2.2-13) without the first term) produces a heat transport equation with an explicit time and space dependence of dT(x,t)/dx. The critical time can be obtained by solving the so found equation for h_{K0} and integrating over temperature between T_b and T_λ on one side, between zero and δ on the other and by dividing through h_{K0}. The criterion of burn-out is in fact again that the hot end of the channel reaches T_λ. The result quoted from [Van Sciver 79] is given in (2.2-23).

$$t^{*(II)}_{GM} \approx \frac{3\rho \bar{c}_p \left(T_\lambda - T_b\right)}{h_{K0}^4} \int_{T_b}^{T_\lambda} \frac{\rho_s^3 s_m^4 T^3}{A \rho_n} dT \qquad [s] \qquad (2.2\text{-}23)$$

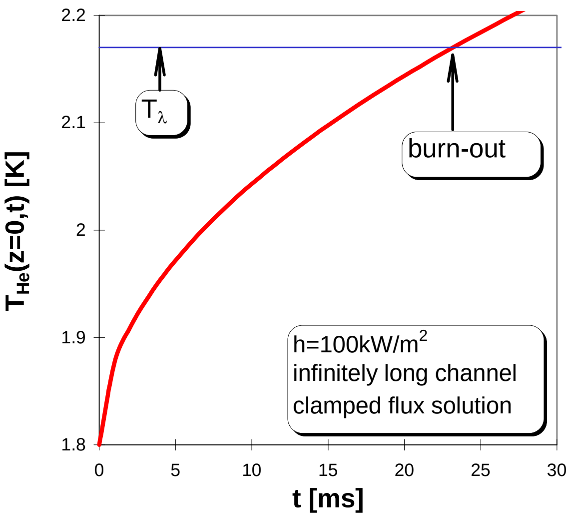

Figure 2.2-8: Transient temperature at the hot end of an infinitely long channel (one-dimensional) with turbulent helium II at an incoming heat flux of 100kW/m^2 calculated according to [Dresner 82] with (2.2-18). T_b=1.8K, K=24150W/m$^{5/3}$/K$^{1/3}$, c_p=8.36×10^{5}J/m^3/K; From this plot burn-out time can be estimated to 23ms.

(2.2-6) overestimates the experimental results by a factor 2, but nevertheless predicts the correct functional dependence between h_{K0} and $t^*_{GM}{}^{(II)}$. Using the same argument as before (Kapitza heat transfer starts to deteriorate at $T<T_\lambda$), the quantitative discrepancy can be corrected. Van Sciver's experimental data have been confirmed in the following by [Seyfert 80,82] ($t^{*(II)} \sim 9.26\times10^{18.6}/h^{4.4}$s), who used a channel geometry given by the annular space between two ~10cm long concentric stainless steel tubes, and [Nemirovskii 89] (K_{GM}=9-15×10^{17}W^{4}s/m^8). The heaters in the experiments discussed above had a long time constant (e.g. [Seyfert 82]: ~3ms), giving the helium the time to fully develop the turbulent regime. Later experiments aiming at a smaller time scale revealed details of the initial stages of transient heat transfer to superfluid helium. [Shimazaki 95] used a high precision superconducting temperature sensor (time constant ~ µs) to measure transient

temperature profiles in helium II. He found that at low heat flux (~50kW/m^2) transient heat pulses are transported rapidly (~20m/s) through the fluid in a second sound wave pattern. Above a critical heat flux (here ~300kW/m^2 during ~200µs at 1.95K) a thermal boundary layer with high peak temperature (e.g. 1.9K+70mK at h=400kW/m^2) formed in the vicinity of the heater. The thermal boundary layer consists of a tangle of turbulence vortices whose formation absorbs a considerable amount of the incoming heat (e.g. thickness 5mm 2ms after the pulse at 400kW/m^2, 1.9K). The boundary layer slowly (~1m/s) diffuses into the bulk ("secondary temperature rise"). The stronger the incoming heat pulse the higher the fraction of energy absorbed in the first helium layer to form turbulence or to evaporate the liquid. For example in the case of 1.95K, h=300kW/m^2 (t_{ini}=200µs) the branching ratio of second sound, turbulence and evaporation is 20/40/40. In this case turbulence first appeared during the pulse but at lower heat flux (e.g. 50kW/m^2) the formation of turbulence takes longer (some ms). [Iida 96] observed that the second sound wave is usually preceded by a normal pressure wave (first sound) which propagates through the helium at velocities 10 times higher than the speed of second sound (recorded with a laser holographic interferometer). Numerical calculations [Rao 96] of transient heat flow in helium II based on the basic hydrodynamic equations of the two-fluid model showed the heat flow patterns found in the experiments of [Shimazaki 95], [Iida 96] and [Katsuki 95]. The importance of second sound in transient heat transfer has been shown as well in experiments made by [Wang 90,95] and [Gradt 88,90]. Based on the method of [Gentile 80] in which a thin monofilamentary superconductor is used as temperature sensor and heat source at the same time, [Gradt 88,90] made film boiling onset time measurements in helium I and II (at saturated vapor pressure (SVP) and subcooled). He found for turbulent helium II (K_{GM}~5.31×10^{18}W^{4}s/m^8 at T_b=2K) and observed the second sound limit at short times (<100µs) where $t^{*(II)}$ is $\propto 1/h^2$ (with a proportionality constant 2×10^7W^{2}s/m^4 at T_b=2K). [Wang 90] studied the film boiling onset time $t^{*(II)}$ of subcooled superfluid helium at various temperatures and bath pressures using a RhFe wire (∅ 51µm) as heater (rise time ~10µs) and temperature sensor to which he applied step current pulses. Like [Gradt 90] he performed his measurements rather in an open bath environment than in a narrow channel geometry. He confirmed that different heat transfer regimes (Second sound / Gorter-Mellink) generate different burn out times. Applying the same phenomenological model Van Sciver proposed to calculate $t^{*(II)}$ in [Van Sciver79] to a case where the helium was in the second sound regime (linear heat transfer correlation) he found a $1/h^2$ dependence of $t^{*(II)}$. His experimental results for the second sound burn-out time are $t^{*(II)}_{SS}=2.44\times10^{11}/h^{2.7}$ at 1.9K/1atm and $t^{*(II)}_{SS}=4.4\times10^{12}/h^{2.94}$ at 2K/1atm. [Nemirovskii 89] measured a K_{SS} between $0.025\cdot10^7$ to $2.5\cdot10^7$ J^2/s/m^4. [Gradt 90] reports $K_{SS}=2.025\cdot10^7$J^2/s/m^4.

Nemirovskii (as well as [Van Sciver 95]) suggests in his review article [Nemirovskii 89] that an even finer subdivision into different regimes is necessary to describe transient heat transfer to superfluid helium. What has been so far identified as second sound should be considered as vortex-free Gorter-Mellink (friction but no thermal barrier in the form of vortex-tangle) whereas the former Gorter-Mellink regime reveals to be in fact a Gorter-Mellink state after turbulence onset. The pure second sound regime is restricted to very small under-critical heat flux ($h_c^{(II)}$~100 W/m^2) only. At very high heat flux and small times the non turbulent Gorter-Mellink regime becomes highly non linear ("shock-waves”). A new classification brings along new transitions between different regimes, increasing the complexity of the problem. On the other hand it could help to explain the spread of results for example for the burn-out time constants found by different experimenters, unaware of operating in different varieties of superfluid helium. To explain the temperature wave patterns in helium II under the effect of very strong heat pulses [Nemirovskii 94] proposes a model based on the hydrodynamics of superfluid turbulence (HST) which aims at a proper description of the formation of vortex tangles and their interaction with heat flux. The onset time of turbulence τ marks the transition between the two “families” of heat transfer regimes, the laminar and the turbulent. It depends on heat flux [Vinen 57].

$$\tau = \alpha(p,T)\frac{1}{h^{3/2}} \qquad [s] \qquad (2.2\text{-}24)$$

Vinen reports α~9.10^{4}sW$^{3/2}$/m^3 in subcooled helium II at 1.8K, which gives 90ms for h=10kW/m^2. [Wang 95] has deduced α(p,T) from the change of slope of t*$^{(II)}$(h) at various pressures and temperatures and obtained 4·10^{4}sW$^{3/2}$/m^3 at 1.9KI/1atm.

$$\alpha(T,p) = \left[1 + 0.2235\ln\left(\frac{p}{p_{atm}}\right)\right]\left[-136.7 + 329.8\frac{T}{T_\lambda} - 193\left(\frac{T}{T_\lambda}\right)^2\right]10^6 \qquad \left[\frac{W^{3/2}s}{m^3}\right] (2.2\text{-}25)$$

Related to the Gorter-Mellink heat conductivity function f^{-1}(T,p), the curve in (2.2-25) shows a pronounced maximum at 1.9K/1atm.Wang found as well that α is smaller for open bath than for fine channel cases. Burn-out time t*$^{(II)}$ can be transformed into a limiting energy density e$^{(II)}$, hence the maximum energy per unit surface which can be transferred to the helium at a given heat flux rate. As a first approximation both sides in the burn-out time correlation are multiplied by the momentary heat flux to obtain (2.2-26).

$$e_{SS}^{(II)} = \frac{K_{SS}}{h} \qquad e_{GM}^{(II)} = \frac{K_{GM}}{h^3} \qquad \left[\frac{J}{m^2}\right] \qquad (2.2\text{-}26)$$

Heat transfer experiments in short channels revealed the “channel limit” to transient Kapitza heat transfer [Seyfert 80c]. In closed channels a heat flux below or moderately higher than steady state critical heat flux gradually heats the helium in the entire channel to transition temperature. The effect of channel limit can be seen in plots of the critical energy as a function of heat flux (e.g. figure below): At high heat flux the curves representing different channel lengths join into one curve (GM-limit) whereas at low flux the smaller channels show much smaller limiting energies than the big channels. The channel limit is the enthalpy difference of helium II between bath temperature and transition temperature (e.g. T_λ), which gives 2.36×10^{5}J/m^3·L at T_b=1.9K for subcooled helium II (1atm.) and 2.85·10^{5}J/m^3·L for T_b=1.8K/1atm. [Seyfert 82].

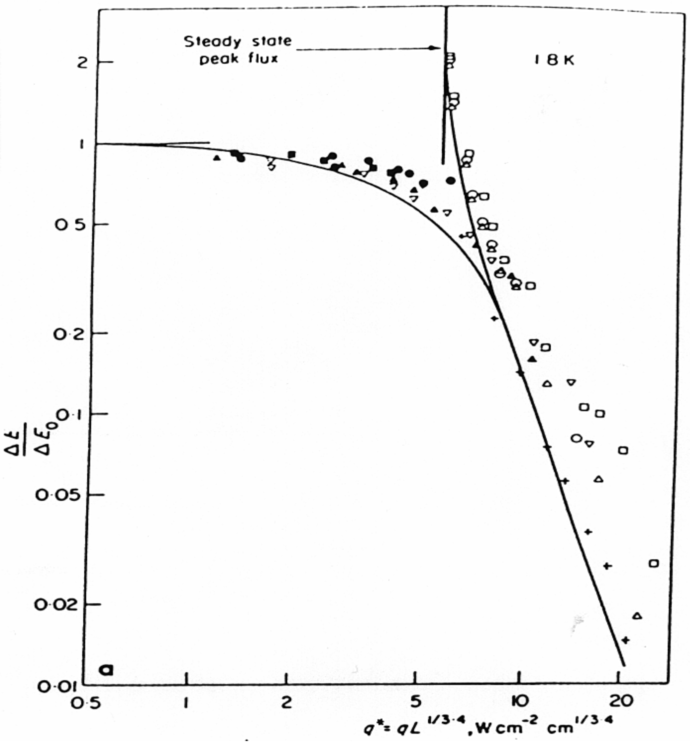

Figure 2.2-9: Fraction of enthalpy used by step heat pulses in Kapitza regime at 1.8K in different channels. Light squares and circles: L=4cm (open, vertical), open triangle: L=4cm, horizontal; filled triangles: closed, L=1cm, filled circles L=0.2cm, filled square: L=0.1cm, all vertical and closed, + and - [Van Sciver 79] L=901cm.

The clamped temperature problem describes partial recovery from burnout in the presence of steady heating as investigated by [Seyfert et al 82]. Inspired by the case of a superconductor driven normal by a short pulse, they considered a situation in which after a heat pulse q_{ini} (stopping at t_{ini}) follows a steady power per unit surface h_{post} (post-heating). They were interested in the maximum value of q_{ini} in Joule per unit of heated surface that permits recovery of the superconducting state for a given h_{post} (stopping at t_{post}) when the helium II near the heated surface has been vaporized during the initial pulse. At t_{ini}, when the heating power has been reduced to h_{post} the helium I (or vapor) is believed to partly condense back to helium II. It is assumed that a vapor layer of negligible thickness remains at the heater/channel interface. According to [Gentile 81] film-boiling usually propagates with ~25mm/s along the channel. With respect to that number the vapor film in Seyfert's experiments could not have had the time to extend to more than 50µm.This thermal barrier has its temperature locked at T_λ and hitherto affects the post heating flux h_{post}. [Dresner 84] calculated the similarity solution of the superfluid diffusion equation for the boundary condition: $T(z=0,t)=T_0(<T_\lambda)$:

$$T(z,t) = T_b + \left(T_0 - T_b\right)\left[1 - \frac{\sqrt{\left(T_0 - T_b\right)}\,z\left(\bar{c}_p \big/ \bar{K}t\right)^{3/4}}{\left(\frac{8}{3\sqrt{3}} + \left(T_0 - T_b\right)z^2\left(\bar{c}_p \big/ \bar{K}t\right)^{3/2}\right)}\right] \qquad [K] \qquad (2.2\text{-}27)$$

T_0 is the temperature to which the hot side (z=0) of the infinitely long channel is locked. The gradient (with respect to z) of (2.2-27) raised to the power 1/3 and multiplied by the conductivity function K(T) (Gorter-Mellink heat conduction law in superfluid helium as used in (2.1-5)), is the instantaneous heat flux $h(z=0,t) \sim t^{-1/4}$ into the helium. According to the model of [Seyfert et al 82] the maximum heat pulse Q_{ini} still permitting recovery after burnout is related to the post heating power h_{post} by the balance of the areas emerging in a plot of h_{ini} (initial heating power density which integrated over the pulse-time and heated surface gives Q_{ini}) h and h_{post}. The balance of areas represents the fact that the sum of initial and post heating power cannot be bigger than the heat flux given in a helium channel with the hot end locked at $T_0 \sim T_\lambda$. The algebraic statement of this balance of areas together with the expression for the heat flux results in a function for the critical energy:

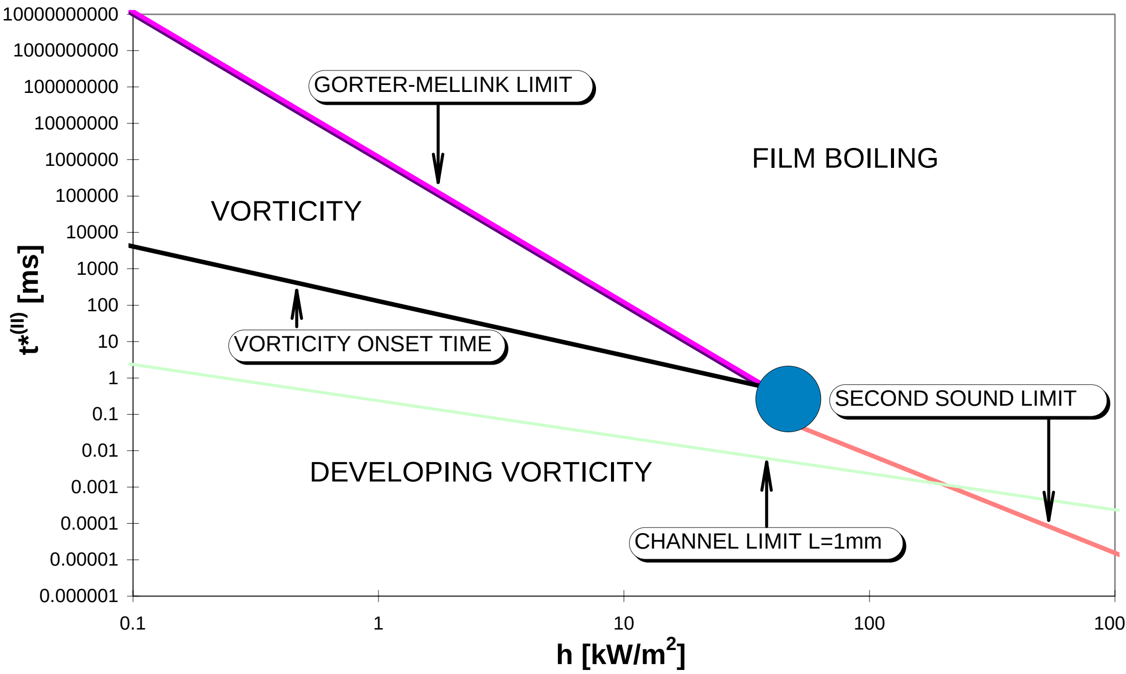

Figure 2.2-10: Schematic diagram of transient heat transfer regimes in subcooled helium II (1.9K, 1atm): burn-out time $t^{*(II)}$ versus heat flux h. The t/h plane is divided into three parts: developing vorticity ($t<\tau$, [Wang 95]), vorticity (between τ and GM burn-out limit - [Nemirovskii 89]) and film boiling (above GM-limit and SS-limit - [Wang 90]). For $h<0.1\mathrm{kW/m^2}$ burn-out time becomes infinite - pure SS heat-conduction. For illustration purposes the "channel-limit" CL [Seyfert 82] of a 1mm long channel is shown.

$$e_c = \int_0^{t_{post}} h\,dt - h_{post}\left(t_{post} - t_{ini}\right) = \frac{1}{4}\bar{K}^3 \bar{c}_p \left(T_\lambda - T_b\right)^2 \frac{1}{h_{post}{}^3} \qquad \left[\frac{J}{m^2}\right] \tag{2.2-28}$$

Using the same average helium properties ($c_p \sim 8.36\times10^5 \mathrm{J/m^3/K}$ and $K \sim 24153 \mathrm{W/m^{5/3}/K^{1/3}}$) as in the clamped flux problem (2.2-28) yields $e_c = 2.15\times10^{17}/h_{post}{}^3\ \mathrm{J/m^2}$. The calculated values agree with the experimental results published in [Seyfert 82] and [Pfotenhauer 86]. Seyfert noticed that in both helium I and helium II recovery was always possible when the post-heating flux was smaller than the critical steady state heat flux. In helium II recovery was still possible for post-heating amplitudes above the steady state limit when e_c and h_{post} fulfilled relation (2.2-28). Pfotenhauer experimentally tested Seyfert's quench energy model on a solenoid wound of a SMES-conductor. A second phenolic cylinder, fitting inside the first (which holds the sample), defined an annular space which was then filled with helium. The heat transfer to helium happened from the inner face of the conductor through a thin phenolic layer with time constants quite close to those observed in Seyfert's experiments. The heated surface was facing perpendicular to the helium-channel axis as in Seyfert's set-up. 10ms heat pulses were applied to the outer face of the conductor along one complete turn by means of a stainless steel ribbon heater while the conductor was operating in magnetic field carrying a huge transport current. Additionally Pfotenhauer's measurements revealed a discrepancy of the data from (2.2-28) in the limit of high post heating (Joule heating in the normal conducting matrix). As later confirmed by [Dresner 89] this behavior is indicative of the fact that at large post heating the length scale appropriate for the one-dimensional heat flow model switches from the half channel height to the channel width. Seyfert's/Dresner's stability model, which will summarily be discussed in 2.4, is only valid in the limit of long channels, when channel limit does not interfere in the process. Another insufficiency of this model is that it determines the heat flux only from the helium point of view. The heat conductance of helium II is very large - it could be that the heat flux predicted with (2.2-27) cannot cross the thermal resistance at the heater/coolant interface unless the surface temperature of the heater (superconductor) is very high (eg. above the current-sharing temperature T_{cs} of the superconductor). To account for the "Kapitza limit" [Dresner 89] the post heating has to remain smaller than the Kapitza-like heat transfer correlation between T_b and T_c.

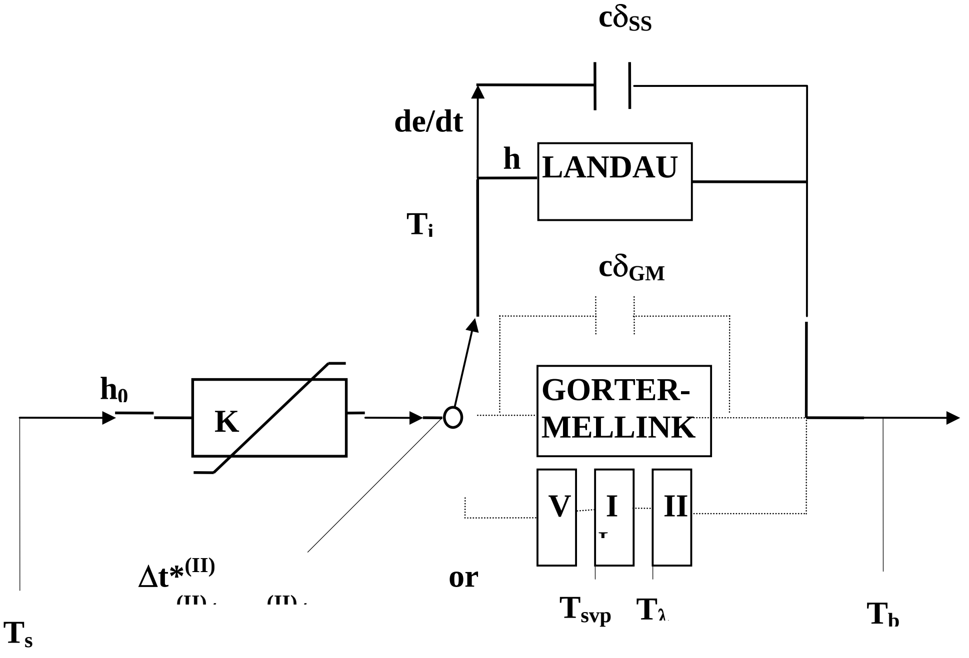

Figure 2.2-11: Thermal model of transient heat transfer to subcooled helium II. In the transient case the limit heat flux densities $h_c^{(II)}$ and $h^{*(II)}$ can be exceeded by far the critical energies $e_{SS}^{(II)}$ (Second Sound limit) and $e_{GM}^{(II)}$ (Gorter-Mellink limit), that determine the boundary between Kapitza heat transfer and film-boiling. These critical energies are related to the total energy needed to raise a certain volume of helium to T_λ. The amount of volume heated during transient heat transfer depends on the diffusivity of the helium, which varies between different regimes (second sound or GM). Heat absorption by the bulk is represented in the model by capacitors, where $C_{therm}=c_p$·penetration depth in [J/K/m^2]. The heat transfer correlation is assumed to be dominated by the Kapitza term before, by film boiling after burn-out.

2.2.6 Film Boiling

The Breen and Westwater film boiling heat transfer correlation (2.2-6) is linear in ΔT. The measured film boiling heat transfer coefficients a_{fb} scatter significantly: [Schmidt 81]: a_{fb}=250W/K/m^2, [Iwamoto 98] a_{fb}=300W/K/m^2, [Frederking 65]: a_{fb}=200-300W/m^2/K and on the upper end of the scale e.g. [Lyon 65]: a_{fb}=2000W/m^2/K. Film-boiling in helium II is accompanied by a three phase transition bringing the two liquid and the vapor phase in close proximity to the heater: [Chuang 82] observed that at low heat flux (h<10kW/m^2) the three phase transition can extend in time when nucleate boiling in the helium I can transfer the heat without break-down. However at high heat flux the nucleate boiling phase becomes shorter. Furthermore in transient cases considerable superheating occurs (for example 0.2K [Irey 84]). There are two film boiling modes in helium II: noisy and silent boiling, where the former has weaker heat transfer properties [Kobayashi 79]. For larger hydrostatic pressures and at lower temperatures, exclusively noisy boiling appears. [Katsuki 95] used visualization methods (Schlieren- and shadow-graphs) to investigate film boiling. He could distinguish between three stages of film boiling, namely precursor nucleate boiling, film boiling and noisy film boiling. Precursor nucleate boiling, that is the appearance of isolated bubble nucleation sites, appears long before burn out. Interestingly Katsuki observed two different patterns of onset of film boiling : for heat flux h<100-200kW/m^2 the precursor nucleation sites expand to overlap adjacent sites whereas at higher flux the initial number density of boiling sites is larger and film boiling appears after a further increase of nucleation sites. Similarly to Katsuki [Pavlov 87] pointed out that with increasing heat flux rate dh/dt, bigger fractions of the channel switch to film boiling simultaneously. The film boiling heat transfer coefficient reaches its maximum when the heated surface stands vertically [Iwamoto 96]. [Schmidt 81] observed that in vertical cooling channels the liquid circulates due to the thermo-siphon action induced by the ascending bubbles. According to [Iwasa78] the transient film boiling correlation departs from the steady state correlation by a factor proportional to dh/dt to account for the heat absorption of the gas. This improvement of film boiling heat transfer in transient conditions (Breen Westwater being the steady state asymptote) has been reported as well in [Giarratano 79]. Another instructive investigation concerns the time of recovery after burnout. [Filippov 92] found a strong correlation of vapor film thickness δ and recovery time (δ~mm for some kW/m^2). [Hilal 79] presented an interesting method to measure the vapor fraction in a delimited helium volume by means of a capacitance bridge. With a resolution of 0.25 pF the vapor fraction can be measured to 1% accuracy.

2.3 Superconductor Stability

	ρ [kg/m^3]	**c_p [J/K/m^3]**	**k [W/K/m]**	**D=k/c_p [m^2/s]**
He1 l [2] **(4.2K, 1atm)**	125	2.1×10^5	0.02	~10^{-7}
He g [2] **(4.2K,1atm)**	16.9	5×10^3	~0.01	~$2\cdot10^{-6}$
He2 [2] **(1.9K,1atm)**	147.1	7.4×10^5	1.2×10^5	6×10^{-10}
Cu RRR=100	9000 [5]	903/*248* [8]	660/*299* [8]	0.73/*1.2*

(4.2K/*1.9K*)	8920 [8]			
Epoxy (4.2K/*1.9K*)	300 [5]	3000[5]/*300* [6]	0.07/*0.04* to $7x10^{-4}$ / *$4x10^{-4}$* [1]	$2.3x10^{-5}$ / *$8x10^{-7}$*
Carbon (Graph.[3] element.[4]) (4.2/*1.9K*)	1537 [4]	215/*8*[3]	10^{-3} / *$2.5x10^{-4}$* [3]	$5\cdot10^{-6}/3\cdot10^{-5}$
Kapton type H	1420 [8]	21926 / *14174* [8]	0.009 / *0.009* [8]	$4x10^{-7}$ / *$2x10^{-4}$*
Nb(46.5%Ti) (4.2/1.9K)[8]	6020	229644 / *20930*	0.1077 / 0.0246	$5x10^{-7}$ / *$1.2x10^{-6}$*

Table 2.3-1: Characteristics of materials used in superconducting magnets; References: [1] "*Polymer properties at room and cryogenic temperatures*", G. Hartwig, Plenum Press 1994, [2] "*Helium Cryogenics*", S.W. Van Sciver, Plenum Press, 1986, [3] "*Kryogenni technika*", J. Jelinek, SNTL-Nakladatelstvi, 1982, [4] "*Handbook of Chemistry and Physics*", [5] "*Superconducting Magnets*", M.N. Wilson, Clarendon Press 1983, [6] Calculated from C_p(4.2K) with T^3 law, [8] Magexec, material data bank "http//supermag2.kek.jp:80/~programs/magexec/"

2.3.1 Stability of Strands

[Seo 96a] introduced the graphite paste heater, reaching for the first time the sub-mm / µs range of perturbation space. MQE measurements in pool-boiling helium I on strands with rectangular cross-section (~1×2mm) to which a $1mm^2$ large, 20µm thin carbon paste layer, covered by a 0.1mm thick copper foil and insulated with epoxy has been pressed with a GFRP clamp revealed a decrease of almost one order of magnitude compared to a former heating wire technique. The innovative aspect of the graphite paste (a graphite emulsion in epoxy) is its low temperature resistivity, which is in such a range (that of semi-conductors) that 1-100W of heating power can be generated with only moderate (~1-10A) heater currents in very small heater volumes ($<0.001mm^3$). A hint towards the success of the graphite paste technique is that it has as the first ever yielded MQE values that are of the same order as theoretical calculations [Seo 96a]. In the past attempts to measure MQE by using resistive heaters (coils of Constantan wire, wrap of resistive sheets,..) have always yielded high values since the thermal time constants of the heater-sample system was usually large and not well controlled. Therefore many former measurements have to be considered rather as quench energy QE than as MQE (see fig. 4.1-1 and 4.1-2), among them the ceramic heater technique presented in [Yoda 91]. A numerical analysis performed in [Senba 96] shows that for a stainless steel tape heater with polyimide surface insulation, strongly pressed against a flat conductor and insulated from the helium, less than 10% of all input power eventually reaches the sample during a transient heat pulse. This can be explained by heat absorption in the large heat capacity of the organic heater material and the insulation.

[Nick et al. 79] conducted a QE study on a 2.5×1.4mm copper/niobium-titanium superconductor (CuSc ratio=5) in pool-boiling helium I at 4.2K/4T using a 50µm manganese wire, wound over 2mm length of sample and insulated from the bath with a drop of Stycast®, as a heater. Their observation that the QE stays constant for t_{ini}<1ms has been confirmed many times since. (Strictly speaking MQE(t_{ini}) goes through a slight minimum: [Fujiwara 94] suggested that the minimum reflects the transition from transient to steady state stability.) In general the agreement of their numerical model (taking into account the finite rise time of the initial heat pulse) based on a numerical solution of the one-dimensional HBE with three part Joule heating and transient heat transfer (as suggested in [Schmidt 78]), with experiment in what refers to quench propagation velocity and MQE gave following wind for all future applications of the standard model of MQE and helium heat transfer. It is particularly noteworthy that their model parameters are almost the same as those used in the here discussed stability program. Small differences between parameters used in [Nick 79] and those used in the present program concern the heat conductivity k (modified Lorentz-constant $L_0'=2.5L_0$ instead of $1.3L_0$ here) and the Kapitza heat transfer ($h=5\times10^4T^2$ W/m^2 [Nick 79] and here $h=180(T^4-T_b^4)$W/m^2). They used as well Schmidt's limit for transient heat transfer to pool boiling helium I. Minimum propagating current measurements were performed to determine some steady state heat transfer parameter from the Maddock stability condition (2.1-2). [Tsukamoto 85] investigated the effect of matrix/Sc ratio and matrix-type (CuNi or copper) on stability in pool-boiling helium at 4.2K. The particularity of this work consisted in separate transient heat transfer measurements on a 30µm thin, 6mm wide brass foil heater having a AuFe/Cr thermocouple attached to it. The so found heat transfer data (a_K~45W/K^4/m^2, $t^{*(I)}=3.16\times10^7\cdot h^{-2.5}$), together with a three part Joule heating and a 500µs/1cm perturbation were fed into the one dimensional HBE (see e.g. (2.1-3)), which was solved numerically for various different Cu/Sc ratios and matrix materials characteristics (Cu, CuNi). The results, namely that in the high current region a conductor (fixed diameter) gains more in stability by decreasing I/I_c (by decreasing the Cu/Sc ratio) than by decreasing the matrix resistivity, have been confirmed since.

The study of AC-loss and quench current degradation showed evidence that the cooling conditions and an increase in matrix resistivity (adding Ni) reduce the quench current [Tsuda 94]. This has been claimed already in [Tsukamoto 85]. The effect of the "design parameters" was studied by [Fujiwara 94] on large (d~20mm) high current LHD cables with Al/Cu matrix. In one sample the NbTi/Cu composite was close to the surface and a large Al or Cu section in the central part whereas in the other the superconducting filaments where bundled in the core surrounded by a thick stabilizer layer. In conductors of these dimensions the isothermal assumption fails and the cross-section design has a noticeable impact on MQE. Calculations, simulating the effect of heat pulses of different shapes (t_{ini}~20ms-1s) in pool-boiling helium I, showed that the configuration with the superconductor located close to the surface had higher MQE, also when the pulse was released on the surface of the sample. This was confirmed by [Anashkin 81].

In various papers on stability tests the existence of stable normal conducting zones was reported. From a theoretical point of view it is a surprising effect because any stationary solution of the HBE is believed to represent an unstable equilibrium. In experiments where GF10 spacers partly covered the heat transfer surface of a sample [Meuris 81] concluded that variations in the cooling along the sample cause stable normal zones. Stable solutions of the HBE appear when connecting uncooled and cooled zones.

Some stability studies claim that coatings like Formvar, Enamel,.. are profitable for stability because they reduce the heat flux from the sample and therefore help to delay burn-out (e.g. [Chuang 80], [Seo 96]). Although not of particular interest for the present work one should mention as well the studies on cryo-stabilized conductors. The items of interest in cryo-stabilized conductors are the dynamics of recovery (time constants), the peak temperatures during current sharing, rather than transient cooling or stability (O. Christianson, Z.J.J. Stekly, L.R. Turner, S.T. Wang, R.W. Boom,..)

2.3.2 Stability of Cables

Major “stability-issues” in Rutherford cables are:

- strand to strand, crossing and adjacent, electrical and thermal contact resistance
- mutual inductance between strands, time constants of current redistribution
- helium volume in the cable, average cooled perimeter of the strands in the cable
- single strand stability
- transport current distribution in unperturbed state
- self field effects

Shintomi et al. at (KEK) studied the stability of SSC, RHIC and LHC conductors, with particular emphasis of the effect of the cross-contact resistance R_c. In agreement with [Collings 97] it was found that un-coated (Cu-matrix) strands give R_c values which can strongly fluctuate with different heat treatments, pressure cycles , etc. According to [Collings 97] Ni-plated strands showed a reproducible contact resistance after different heat treatments. Using 3mm long carbon paste heaters, they investigated the response of 3-strand Rutherford cables to 10ms heat pulses into one strand. [Kim 96] ([Tsuda 96]) found that a high R_c (matrix resistivity) due to a CuMn-barrier or CuNi matrix reduces MQE because it causes a non-uniform current distribution among the strands in the cable (and stronger Joule heating). Of tremendeous importance for stability is that the MQE experiments on cables at KEK showed that the current transfer from the perturbed strand occurs very fast. Based on that observation the main stability parameter in a Rutherford type cable will be related to the question whether the transport current of the quenched strand can be carried by the neighboring strands without in turn quenching them [Kim 98c]. Interestingly Shintomi et al. made the following observations: Heat transfer between neighboring strands increases MQE only at high currents. Small contact heating (as given by a small R_c) raises MQE only at low currents (3-strand simulations in [Amemiya 95]). [Wilson 97 a,b,c,d] found a so called “kink” in MQE curves, which signals the transition from a single strand behavior at high currents to a collective behavior at a transport current below the kink. Wilson believes that the position of the kink (that is the transport current at which the slope of MQE(I) significantly changes is mainly related to the cooling performance. Wilson tested different cable prototypes in the hope to push the kink to very high currents. One cable prototype was the partially soldered, resistive core cable, where the contact resistance is unisotropic: high in transverse direction to reduce eddy-currents (malign to field quality) and low to adjacent strands for stability purposes. Unexpectedly experiments at BNL revealed that the gain in MQE at high currents was small, whereas as expected the MQE at low currents was lower than that of a similar unsoldered, bare LHC-type cable without core. Reactivating an old DRAL concept, the porous metal cable ([Baynham 81]) , Wilson experimentally found a strongly increased MQE over the whole current range (kink shifted to high currents) which he explained by the increase in cooled surface. Although several attempts have been made to reproduce these results since, no significant increase in MQE has been found in new LHC-cables filled with different types of porous metal (small grain Ag or Cu powder mixed with solder) [Kim 98b].

The stability of CIC-conductors for fusion applications operating in flowing, supercritical (~3atm.) helium and exposed to distributed disturbances (in the form of a high sudden (~1ms) current pulse superimposed on the transport current) was investigated by [Lottin

83]: The MQE versus transport current curves at 4.2K shows a clear kink (=sudden strong rise), the curve at 1.8K two distinct kinks, which according to the authors mark the sudden participation of helium heat transfer below a threshold transport current. It is rare that QE- measurements operate with cooled perimeter fractions big enough to reveal the above mentioned effects.

2.3.3 Stability of Magnets

A huge number of publications (e.g. [Tsukamoto 88], [Superczynski 89], [Gavrilin 96],..) show the success of the ‘standard model” of stability in explaining the experimental behavior (quench current, quench propagation velocity, average temperature rise in winding at a given AC-loss, quench energies) of potted magnets in pool-boiling helium I. Another important fraction of articles (e.g.: [Romanovskii 90]) refers to quench protection (hot spot temperature, time constants,..) of various types of magnets (mainly operating at 4.2K). Thermal disturbance and quench propagation in pool boiling pancake coils have been visualized with a high speed camera by [Aihara 94].

A reference paper promoting the operation of superconducting magnets in superfluid helium (related to Tore Supra) is [Claudet 79]. This paper points out that the reduction of operation temperature below T_λ does not only result in a gain in peak field for conventional NbTi-superconductor, but also in a gain in stability. He experimentally underlined latter statement with heat pulse experiments on a test-coil. A theoretical study in [Baynham 83] came to similar conclusions. Furthermore E. Baynham proposed to operate a future 10T dipole rather at 1.8K with NbTi technology than at 4.2K with Nb_3Sn. One statement from [Baynham 83] has revealed utterly correct: *“From stability analysis it seems likely that severe training could be experienced in a NbTi, 10T magnet designed to operate at 1.8K.*” [Eckels 89] is just one among many who claim that the MPZ theory or the MQE of the single conductor is correlated to the training and quenching of the magnet. Unfortunately these statements often go without proof.

[Chechetkin 90] calculated that for statistical reasons the maximum permissible thermal background noise in superconducting magnets should be ten times smaller than the MQE of the single magnet conductor.

2.3.4 Conductor Motion and Other Sources of Quenches in Magnets

“Disturbances which drive the superconductor to the normal state in the magnet may be conventionally split into two groups. First are quantitatively predictable disturbances, like plasma current disruption in tokamak magnets or AC-fields in AC magnets. Second are those of mostly mechanical nature and they are very sensitive to details of (the) *manufacturing procedure. These are to some extent inherent to all magnets…. Appropriate technology can limit* (the) *probability of such a disturbance, but there is still no technique to estimate the* (strength) *of such a disturbance in advance. That is why the level of stability chosen for a conductor by a magnet-designer is a matter of intuition.”* (quoted from Klimenko 92).

[Devred 89] discussed the quench behavior of SSC prototype magnets in terms of conductor motion and frictional energy release. Finding that conductor displacements of the order of 10µm yield enough heat to quench the magnets, he suggested to apply higher prestress during assembly of the magnets. Conductor-limited quenches (degraded Ic during “accidents”) could be identified through their strong correlation with temperature ($I_c=I_c(B,T)$). [Iwasa 92] reports that acoustic emission (AE) and voltage analysis of SSC-dipoles showed that the perturbations were mainly related to short length conductor movements (involving disturbance energies in the 10-100µJ range). [Ghosh 89] reported that training in SSC cables during I_c-measurements were indeed caused by conductor motion (both cable and single wire). Their interesting experimental result that cables with higher Cu/Sc ratio (~1.5) were less likely to train than those with a lower Cu/Sc ratio (~1.2) triggered a big discussion about the optimum Cu/Sc ratio in SSC cables. This result hints towards a correlation between MQE and stability versus disturbances generated during I_c-measurements. Several authors indicate that premature quenches in strands may be related to “micro-yielding” in the superconductor (e.g. [Schmidt 77]). This idea has not been pursued any further since.

In the simplest approximation, with half of the energy stored in the bending (with 2L the length of conductor deformation) of the conductor the disturbance energy due to conductor motion in a perpendicular magnetic field B_z is given in (2.3-1). From the analysis of the perturbations on real scale high current density magnets (see e.g.: [Tsukamoto 90]) Tsukamoto et al. concluded that conductor motion is the major source of quenches in superconducting magnets. [Takao 97] successfully showed (on Tristan magnets), that assuming irregularities in conductor dimension and insulation thickness to follow a gaussian distribution (with known standard deviation), a statistical statement about the number of locations with a poorly supported length exceeding the critical length (related through (2.3-1) to a MQE) and thus about an approximate number of training quenches can be made.

$$W_{condmot} = \frac{(B_z I)^2 L^5}{45 E I_{dy}} \quad [J] \qquad I_{dy} = \pi d^4/64 \; [m^4] \tag{2.3-1}$$

A reference article for the correlation of conductor motion and quench in big scale magnets (Tristan Insertion Quadrupole Magnets) is [Ogitsu 91]. By means of so called quench antennas he measured the disturbance energies causing quenches and found an order of magnitude comparable to the energy release by wire motion and conductor-MQE (t_{ini}~100µs, E~1mJ/mm^2). Interesting experiments in the context of wire-motion and quenching can be found in [Ninomiya 96] who investigated the quench of magnets triggered by the impact of a weight onto a wave guide (“impact hammer”) equipped with a strain gauge to measure the mechanical impact energy.

A recent publication [Seo 97] promotes the use of water as filling material in coils - MQE measurements on ice-potted strands showed that the high thermal conductivity of ice compared to epoxy helped to diffuse and therefore reduce thermal perturbations emanating from out-or inside the wire. Many quenches in LHC prototype magnets were traced back to bad joints and defects in the mechanical support of the winding [Pugnat 97]. The quench signatures are more often smooth bumps than spikes (disturbances rather distributed than local). Using quench antennas, it has been observed that mechanical perturbations sometimes travel through the magnet until they hit a weak spot, where they finally trigger a quench [Siemko 95].

2.3.5 Quench Propagation Velocity

Once a normal zone has started to grow, it will continue to expand under the combined actions of heat conduction, ohmic heating and heat transfer. It was experimentally found that, when the initial transients have died away, the normal/superconducting boundary continues to propagate at a constant velocity. By timing the flight of the normal-superconducting front between two voltage taps the quench propagation velocity is relatively easy to measure. The quench propagation velocity can be computed from the HBE. [Tsukamoto 79] already noted that in general measured velocities are smaller than calculated values. This is related to the influence of (transient) heat transfer on the propagation velocity. The success of any numerical calculation is therefore strongly linked to the adequacy of the chosen heat transfer model. The sensitivity of v_q to the heat transfer mode has yet tempted several authors (e.g. [Lottin 79]) to calculate heat transfer coefficients indirectly from numerical calculations of v_q. Unfortunately, especially in transient cases, there is not only one cooling parameter, making this procedure unreliable. [Lottin 79], for example, had to artificially increase (factor 2 at 7T) the heat conductivity to achieve reasonable results.

[Wilson 83] presents an analytical expression for the quench propagation velocity which can be found from a “traveling wave” solution of the HBE (2.3-2) with simplified step-heating $g_c i^2 \theta$ (θ being a step-function) and linear heat transfer $a\Delta T$ with adequate boundary conditions:

$$c_p\left(\frac{\partial T}{\partial t}\right)=\frac{\partial}{\partial x}\left(k\frac{\partial T}{\partial x}\right)+\theta\left(T-T_s\right)\frac{I_c^2\rho_{Cu}}{AA_{Cu}}i^2-a\frac{p}{A}\left(T-T_b\right)\qquad\left[\frac{W}{m^3}\right]\qquad(2.3\text{-}2)$$

$$T\left(x,t\right)\Rightarrow T\left(X=x+vt\right)\rightarrow k\frac{d^2T}{dX^2}-vc_p\frac{dT}{dX}+\left(g-h\right)\frac{p}{A}=0\qquad\left[\frac{W}{m^3}\right]\qquad(2.3\text{-}3)$$

The HBE in the traveling wave parametrization (2.3-3) has the boundary conditions: $T(X=0)=T_s$, where T_s is the temperature at which the heat generation model jumps from zero to $g_c i^2$, and $T(X\rightarrow\pm\infty)=T_b$ or T_{max} for the right and left hand side solutions (T_{max} is the maximum temperature at x=0 ($T_{max}-T_b=g_c i^2/a$). The neglect of current sharing always leads to an underestimation of the propagation velocity because current sharing adds additional Joule heating below T_c. Therefore the transition temperature T_s should not be T_c but rather halfway between T_c and T_b, According to [Altov 73] v_q calculated from step-like heating tends to converge to v_q calculated with three-part Joule heating in the adiabatic limit ($\alpha\rightarrow\infty$). Left and right hand side solutions can be linked by imposing the continuity of heat flow at the interface X=0 between these regions. At this stage an expression of the type v_{qlim} ($=vp\delta t^{*1/2}/A$ in helium I) can be added to the continuity of heat flux from left to right at X=0 to account for transient heat transfer effects. The propagation velocity in (2.3-4) can be split into an adiabatic part and cooling corrections, with u standing for steady state and w for transient cooling,

$$v_q = \frac{I_c i}{A c_p}\sqrt{\frac{k\rho_{Comp}}{(T_s - T_b)}}\frac{(1-2u)}{\left[uw^2 + w + 1 - u\right]^{1/2}}\left[\frac{m}{s}\right] \quad u = \frac{a(T_s - T_b)}{g_c i^2} \quad w = \frac{q_{\lim}}{c_p (T_s - T_b)} \qquad (2.3\text{-}4)$$

where ρ_{Comp} is the composite resistivity ($=\rho_{Cu}(1+\lambda)/\lambda$) and T_s the temperature at which Joule heating jumps from zero to its maximum value, q_{lim} is a critical energy per unit volume. The adiabatic quench propagation velocity (the first 2 terms in (2.3-4)) in [Pukhov 97] is slightly different, bearing a factor 2 and the square-root of i . The adiabatic quench propagation velocity formula can be corrected for temperature dependent properties, with $k=L_0T/\rho_{Comp}$ and $c_p \sim T^3$ [Dresner 95] computes:

$$v_q^{adia} = \frac{I_{tot}}{A}\sqrt{L_0 T_s}\left[c_p(T_s)\int_{T_b}^{T_s} c_p(T')dT'\right]^{-1/2} \quad \left[\frac{m}{s}\right] \qquad (2.3\text{-}5)$$

Dresner uses $T_s=T_c$. A simple expression derived from the diffusivity of the potting material ([Dresner 95]) can be used as a correction term for the adiabatic v_q accounting for heat transfer to the potting (superscript pot), which usually is between 0.7 and 0.8.

$$f_{pot} = \frac{1}{\left[1 + \left(\frac{4c_p^{pot}A}{I_{tot}d}\right)\sqrt{\frac{k_{pot}k}{c_p^{pot}c_p L_0}}\right]} \qquad (2.3\text{-}6)$$

[Devred 88] presented correction factors for the adiabatic quench propagation velocity for the cases of current sharing, temperature dependent properties and heat transfer to the potting material. Unfortunately the formulas for the correction factors are complicated and by far too voluminous to be presented in this context.

Similarly to Wilson [Dresner 95] proposed a solution of the problem in the cooled condition (step-heating, linear heat transfer, temperature independent k and c_p), except that the transition temperature for step heating in his version is $T_s=T_b+1-i/2$:

$$v_q = \frac{1}{c_p}\sqrt{\frac{apk}{A}}\frac{\alpha i^2 - 2 + i}{\sqrt{\left(1 - i/2\right)\left[\alpha i^2 - \left(1 - i/2\right)\right]}}\left(1 + \alpha^{-1.45}\right) \quad \left[\frac{m}{s}\right] \qquad (2.3\text{-}7)$$

where the last factor is an empirical correction factor found from comparison with experiment. Analyzing (2.3-7) correctly shows the adiabatic form (first two terms in (2.3-4)) in the limit $\alpha \to \infty$. Furthermore for $i(\alpha i+1)<2$ v_q crosses zero as required by the cold end recovery theory. The additional empirical factor became necessary since theoretical curves proved to be several times steeper than experimental curves. According to Dresner this difficulty is not eliminated by use of three-part boiling curve and temperature dependent properties. It is rather related to the inadequacy of linear (steady state) heat transfer coefficients and may be corrected by a more adequate implementation of transient cooling. Besides linear cooling [Kupferman 92] introduced a more accurate heat generation function by solving the coupled electrical problem simultaneously with the thermal problem. His formalism, which originally described highly stabilized conductors, can be used in the limit of small matrix fraction and states a dependence of v_q on i of the type $i/(1-i)^{1/2}$. [Willig 78] presented a formalism for the quench propagation velocity with temperature dependent properties and steady state cooling characteristic.

$$v_q = v_0 \frac{\left(\frac{I}{I_{Mad}}\right)^2 - 1}{\sqrt{\left(\frac{I}{I_{Stek}}\right)^2 - 1}} \quad \left[\frac{m}{s}\right] \tag{2.3-8}$$

I_{Mad} and I_{Stek} can be deduced from the maximum heat generation fulfilling the Maddock or the Stekly criterion. Willig indicates a way to find an accurate expression for the proportionality constant v_0.

Only a small number of authors have searched for ways to generate analytical formulas for v_q including transient heat transfer. [Casas 89] reports a good agreement between measurements and simulations using an additional cooling term proportional to $aT^2(dT/dt)$ in the HBE to describe transient cooling. But since there seems to be no satisfying physical explanation of that additional cooling term, the coefficient a merely degenerates to a fiddle factor. [Tsukamoto 79] has been successful in reproducing measured data in pool-boiling helium in calculations based on the traveling wave approximation of the one-dimensional HBE by using steady state heat transfer data adding a term of the form a(T)(dT/dt) to the film-boiling term. This term, which has been introduced first in [Iwasa 78], accounts for the latent heat of vaporization of helium absorbed at the front of the expanding gas sheath.

[Dresner 95] points out that the traveling wave approach may not be the only solution to (2.3-2) and not necessarily the asymptotic limit to which non-recovering normal zones tend.

2.3.6 The Effect of Cu/Sc Ratio on Stability

High performance magnets such as the dipole magnets for particle accelerators operate at high current densities. When the basic requirements, such as the overall current density and conductor volume are specified, the fraction of copper stabilizer inside the superconducting cable becomes the next important issue. More NbTi inside the cable implies higher critical current and/or respectively higher critical temperature which results in a higher temperature margin and hence a stability gain. Since NbTi has a bigger specific heat than Cu (almost a factor 7 at LHC operating conditions) an increase in the NbTi fraction increases stability through an increase of enthalpy-margin. A composite with a high superconductor content is therefore less likely to turn normal in the event of a heat deposition. However, this also implies less copper to conduct the heat and any excess current when part of the cable becomes normal. Since those two measures are antagonistic there must be an optimum Cu/Sc ratio for a set of given diameter and overall current density, with respect to MQE.

From theoretical considerations [Elrod 81] found that in NbTi/Cu composites, in adiabatic conditions, the optimum is shifted to a higher Cu/Sc ratio for decreasing heat generation (as later confirmed by [Hassenzahl 89] and [Amemiya 92]) and in cooled conditions the optimum shifts to higher Cu/Sc ratios with enhanced cooling. As [Dresner 95] shows with his analytical MQE formula (see equ.(2.4-18)) there is a clear preference of a lower Cu/Sc ratio. A common feature of many publications is that the experimentally found optimum is usually much larger than the calculated optimum. Measurements on SSC prototype cables presented in [Ghosh 89] have triggered a frantic search for the reasons of the discrepancy between simulations based on the HBE (maxCu/Sc<1) and Ghosh's measurements (maxCu/Sc~1.5). Due to the resemblance of the SSC and LHC strand it can be instructive to study the SSC-team's conclusions on the optimal Cu/Sc ratio as published in [Ng 89] and [Huang 92]: Using three part Joule heating, linear cooling in pool boiling helium I with a dynamic limit (triggering film-boiling), 30µs/~1mm heat-pulse parameters and temperature dependent properties in the numerical solution of the 1-dim HBE equation they computed an optimum Cu/Sc ratio of 1.5 at a rather high transient cooling coefficient of 15kW/K/m^2. Huang concedes that it is the assumption of a rather performing heat transfer coefficient which shifts the optimum Cu/Sc ratio to this rather high value. A former study by [Ng 89] had hopelessly tried to reach this value which had been experimentally indicated in BNL measurements. Since he assumed more conservative linear cooling coefficients (around 2kW/m^2/K) he never reached the experimental values. An interesting side-product of his work was the idea that the copper in the filament region was thinner (<1µm) than its mean free path of electrons at cryogenic temperatures. Therefore the copper between the filaments may not contribute to the thermal and electrical conductivity. Furthermore [Ng 89] investigated the Cu/Sc optimum in SSC type strands in uncooled conditions, showing, as before him [Anashkin 81], that the optimum goes to larger Cu/Sc ratio when the strand is operated at smaller i or with higher RRR matrix material. Ng's explanation was confirmed later in [Amemiya 92] who used Schmidt's model of transient heat transfer to pool boiling helium I in the one-dimensional HBE and found that strong cooling (as given in transient conditions) shifts the optimum Cu/Sc ratio to higher values. He additionally showed that the perturbation profiles and especially the length of the perturbation has a considerable impact on the optimum Cu/Sc ratio, increasing it for smaller perturbation length. [Takao 94] finally presented a theoretical model which reproduced Ghosh's experimental curve [Ghosh 89] of the number of training quenches versus Cu/Sc ratio for SSC test-samples based on a model comparing the disturbances generated by the sample holder to the MQE of the conductor with a given Cu/Sc ratio.

A similar investigation has been conducted by R. Wolf at Cern for the LHC project [Wolf 94]. He used basically the same model as his predecessors at the SSC, that is 1-dim. HBE, three part Joule heating, WF-law for thermal conductivity and a linear type cooling (without burn-out limit) for helium II at 1.9K in a magnetic field of 8.6T. Pulsing the model-strand with 200µs, 2mm heat pulses he calculated the optimum MQE as a function of the Cu/Sc ratio. His conservative approach for the cooling function resulted in optimum Cu/Sc ratios below one. However, Cu/Sc ratios below 1.5 contradict requirements related to magnet quench protection and the mechanical properties of the cable.

[Takao 94] found: "*the influence of Cu/Sc ratio on MQE is not large for Cu/Sc ratios which range from 1 to 2*".

2.4 Minimum Quench Energy Calculations

The standard approach to the analysis of the behavior of technical superconductors versus external perturbations is the solution of the heat balance equation (HBE). Especially in the case of thin conductors the HBE has always been reduced to one spatial dimension. The diffusivity of the matrix material is such that the heat quickly distributes equally over the whole cross-section of the conductor. Stekly's and Maddock's stability criteria were discussed in 2.1. More recent stability models deal with the permissible strength of disturbance from which not "Maddock-stable" conductors can recover. This review presents some of the analytical formulas or simple mathematical models to calculate the quench energy.

2.4.1 The Uncooled Case

The simplest approach to adiabatic stability versus short, transient disturbances is to relate conduction to the sides to the critical (worst case-) heat generation (cooling does not interfere). A characteristic length of this problem certainly is (2.4-1):

$$l_{adia} = \sqrt{\frac{2\bar{k}\left(T_c - T_b\right)}{g_c i^2 \, {}^{p}\!/\!_{A}}} \qquad [m] \tag{2.4-1}$$

The enthalpy content of the triangular temperature profile of the type $T(x)=T_c-(2/l_{adia})(T_c-T_b)x$, with T_c in the center and T_b at $l_{adia}/2$, is an approximation of the adiabatic MQE. A comparison with other adiabatic MQE models shows that this concept overestimates MQE, especially at high currents, because T_{max} is rather T_{cs} than T_c.
[Dresner 85] proposed to split the time dependent HBE into a short time part (2.4-2) with an external δ-like disturbance when $g(T,I)\sim 0$ and a long time part (2.4-4) without disturbance, but $g\sim g_{cs}$. Henceforth the temperature dynamics at the heat pulse center and the heat diffusion from the initially heated region become separate problems.

$$\bar{c}_p \frac{\partial T}{\partial t} = \bar{k}\frac{\partial^2 T}{\partial x^2} \qquad bc: T(t=0, x=0) = T_b + \frac{Q_{ini}}{\bar{c}_p} \tag{2.4-2}$$

The solution of (2.4-2) is given in (2.4-3). Its value at t=0 and x=0 serves as initial condition of the "relaxation" part (2.4-4). Furthermore with some minor modifications it

$$T_1 = T_b + \frac{Q_{ini}}{A\sqrt{\bar{c}_p \bar{k}}} \frac{e^{-\frac{\bar{c}_p x^2}{\bar{k} t}}}{\sqrt{4\pi t}} \; [K] \tag{2.4-3}$$

serves as Ansatz for (2.4-4).

$$\bar{c}_p \frac{\partial T}{\partial t} = \bar{k} \frac{\partial^2 T}{\partial x^2} + g_c i^2 \frac{p}{A} \left\{ \begin{array}{ll} 0 & T < T_b + (1-i)(T_c - T_b) \\ 1 - \frac{1}{i}\left(\frac{T_c - T}{T_c - T_b} \right) & T \geq T_b + (1-i)(T_c - T_b) \end{array} \right\} \quad \left[\frac{W}{m^3} \right] \qquad (2.4\text{-}4)$$

With a separation Ansatz of the type $T(x,t)=f(t)T_1(x,t)$ (2.4-4) can be reduced to a first order differential equation in time. The temperature in the central point T_{cen} according to [Buznikov 96], who investigated the same kind of model, can be calculated from:

$$\frac{dT_{cen}}{dt} + \frac{D}{2t}\left(T_{cen} - T_b\right) = \frac{p}{\bar{c}_p A} g\left(T_{cen}, i\right) \quad \left[\frac{K}{s} \right] \qquad (2.4\text{-}5)$$

where D=1,2,3 the dimension parameter allows to generalize to higher dimensions and g(T,i) is the usual three part Joule curve (like in (2.4-4) with an additional third step at $T>T_c$ $g=g_c i^2$). A solution of (2.4-5) that does not become ±∞ for long times yields the MQE, which in Dresner's notation is the "bifurcation energy" (2.4-6).

$$MQE_{adia} = \pi \frac{\bar{c}_p \sqrt{k} A^{3/2} \left(T_c - T_b\right)^{3/2}}{\sqrt{g_c p}} \frac{1-i}{\sqrt{i}} \qquad [J] \qquad (2.4\text{-}6)$$

Some essential correction factors (2.4-7) to account for finite pulse duration t_{ini} and finite pulse extension $2 \times x_{ini}$ have to be multiplied to (2.4-6). The correction factors can vary between 1 and 5.

$$f_{x\ or\ t} = \frac{2}{\sqrt{\pi}} e^x \int_x^\infty e^{-u} \sqrt{u}\, du \Bigg|_{x = \frac{x_{ini}^2}{16}\left(\frac{g_c p i}{Ak\left(T_c - T_b\right)} \right) \ or \ x = \frac{g_c p i}{2Ac_p\left(T_c - T_p\right)} t_{ini}} \qquad (2.4\text{-}7)$$

[Buznikov 96] calculated the same kind of criterion for the complete three part Joule heating (by adding the condition $g=g_c i^2$ at $T>T_c$ to (2.4-4)) and obtained a slightly modified MQE:

$$MQE_{adia} = \frac{2}{3}\sqrt{2\pi} \frac{\bar{c}_p \sqrt{k} A^{3/2} \left(T_c - T_b\right)^{3/2}}{\sqrt{g_c p}} \frac{1-i^2}{i} \qquad [J] \qquad (2.4\text{-}8)$$

Dresner's correction factors apply as well to (2.4-8).
Dresner's adiabatic MQE can be calculated as well for two and three spatial dimensions [Dresner 85]:

$$MQE_{adia}^{3D} = 6\pi^2 \frac{\bar{c}_p k_r \sqrt{k_z} A^{3/2} \left(T_c - T_b\right)^{5/2}}{\sqrt{\lambda g_c p}} \frac{1-i}{i^{3/2}} \qquad [J] \qquad (2.4\text{-}9)$$

where λ here is the coil packing factor (conductor volume/coil volume) and correction factors can be added in case the initial disturbance is not point-like but distributed. A comparison with measurements of [Scott 81] shows fair agreement.

Two and three dimensional analogues can be found in [Buznikov 96]. [Wilson 83] presented a more sophisticated model of adiabatic MQE for potted coils in which he solves the steady state HBE (2.4-12) in an anisotropic two-dimensional medium (k_r and k_z are the radial and longitudinal temperature independent heat conductivities) to obtain the corresponding MPZ-profile, from which he calculates the quench energy. Again in [Wilson 83] Wilson thinks that the low diffusivity of NbTi causes a temperature difference between filaments and matrix. [Wilson 83] included this "size-effect" in a one-dimensional model by means of a modified heat generation function. The presence of a resistive barrier between filaments and matrix has been theoretically discussed in two limits: the limit of vanishing thermal resistance and effective electrical contact resistance in [Akopov 85] and in the limit of negligible electrical resistance but the thermal contact being insufficient in [Kremlev 67].

2.4.2 The Cooled Case

A simple approach to stability in the cooled case has been presented by [Wipf 79]. He solved a simplified steady state HBE for constant properties, where the heat generation term was of the step-type $\theta(T-T_c)\rho_{Cu}j_{Cu}^2$ and the cooling linear $h=a(T-T_b)$. He introduced a disturbance power q_{ini} through the boundary condition at x=0 ($-k(dT/dx)_0=q_{ini}A/p$) and found the solutions for q_{ini} discriminating between stable and unstable states. The stable states are characterized by the fact that for a positive increase in steady state extra-heating the equilibrium length of normal zone increases, whereas in unstable cases any extra-heating reduces the equilibrium length. Defining the normal length ($x(T>T_c)$) as the MPZ he obtained:

$$x_{MPZ} = x(T = T_c) = -\frac{1}{2}\sqrt{\frac{Ak}{pa}}\ln\left[1-\frac{2}{\alpha i^2}\right] \qquad [m] \tag{2.4-10}$$

In a rough approximation (temperature independent c_p and T_{max}~T_c) the quench energy can be approximated to:

$$MQE_{MPZ}(i) = 2A\bar{c}_p(T_c - T_b)x_{MPZ}(i) \qquad [J] \tag{2.4-11}$$

$$k\frac{\partial^2 T(x)}{\partial x^2} + (h-g)\frac{p}{A} = 0 \qquad \left(\frac{dT}{dx}\right)_{x=0} = 0 \quad T(x=L)=0 \qquad \left[\frac{W}{m^3}\right] \tag{2.4-12}$$

$$h = a(T - T_b) \qquad \left[\frac{W}{m^2}\right] \tag{2.4-13}$$

$$g = g_c i^2 \begin{Bmatrix} 0 & T < T_{cs} \\ \left(1 - \frac{1}{i}\left(\frac{T_c - T}{T_c - T_b}\right)\right) & T_{cs} \le T < T_c \\ 1 & T \ge T_c \end{Bmatrix} \left[\frac{W}{m^2}\right] \quad T_{cs} = T_b + (1-i)(T_c - T_0) \; [K] \tag{2.4-14}$$

$$g_c = \frac{I_c^2 \rho_{Cu}}{A_{Cu}\, p} \quad \left[\frac{W}{m^2}\right] \qquad \alpha i^2 = \frac{g_c i^2}{a(T_c - T_b)} \tag{2.4-15}$$

[Dresner 95] and [Cornelissen 84] calculated an analytical MQE in cooled conditions based on the MPZ concept with the following simplifications: one-dimensional steady state heat balance equation with temperature independent k and c_p (2.4-12), three part Joule heating (2.4-14) and a simple linear heat transfer correlation (2.4-13). The maximum temperature in the center can be calculated analytically when $T<T_c$:

$$T_{\max} = T_b + (T_c - T_b)\left[\frac{1-i}{1 - 1/\sqrt{\alpha i}}\right] \quad [K] \tag{2.4-16}$$

According to the MPZ concept the critical energy for an averaged c_p is:

$$MQE_{MPZ} = 2\bar{c}_p A \int_{-\infty}^{0} (T(x) - T_b)\,dx \quad [J] \tag{2.4-17}$$

In the approximation $T<T_c$ ($\alpha i^3>1$) the quench energy can be calculated:

$$MQE_{MPZ} = 2A\bar{c}_p (T_c - T_b)\sqrt{\frac{\bar{k}A}{\bar{a}p}}\left[\alpha i \frac{(1-i)}{(\alpha i - 1)}\right]\left[1 + \frac{\left(\pi/2 + \arcsin\left(1/\sqrt{\alpha i}\right)\right)}{\sqrt{\alpha i - 1}}\right] \quad [J] \tag{2.4-18}$$

Unfortunately (2.4-18) is extremely sensitive to the choice of the average c_p. Furthermore the limitation to $T<T_c$ is unrealistic. [Jayakumar 87] extended the calculation to $T>T_c$. In this case (for $(2-i)/i^2<\alpha<i^{-3}$, $\alpha<(2-i)i^{-2}$ is the “Maddock limit”) the maximum temperature, (compare to (2.4-16)) is:

$$T_{\max} = T_0 + (T_c - T_0)\alpha i^2\left[1 - \sqrt{1 - \frac{2-i}{\alpha i^2}}\right] \quad [K] \tag{2.4-19}$$

[Jayakumar 87] explicitly stated the calculated temperature profiles ((2.4-20) to (2.4-22)).

$$T(x) = T_b + (T_c - T_0)\left[E e^{x/x_0} + F e^{-x/x_0} \right] \qquad u + v \le x < \infty \tag{2.4-20}$$

$$T(x) = T_b + (T_c - T_b)\left[C\cos\left(\sqrt{\alpha i - 1}\,\frac{x}{x_0} \right) + D\sin\left(\sqrt{\alpha i - 1}\,\frac{x}{x_0} \right) + \frac{\alpha i(1-i)}{\alpha i - 1} \right] \quad u \le x \le u + v \tag{2.4-21}$$

$$T(x) = T_b + (T_c - T_0)\left[A e^{x/x_0} + B e^{-x/x_0} \right] \qquad 0 \le x \le u \tag{2.4-22}$$

where the $u=x(T=T_c)$, $u+v=x(T=T_{cs})$ and $x_0=((kA)/(pa))^{1/2}$. The constants A,B,C,D,E and F together with u and v can be found from the boundary conditions (the gradient of T in x=0 has to vanish, dT/dx has to be equal from both sides at x=u and x=u+v and $T(u)=T_c$ and $T(u+v)=T_{cs}$). Jayakumar suggests that the last boundary condition $T(x\to\infty)=0$ (or $(dT/dx)_\infty=0$) represent just the special case of an infinitely long perturbed zone and replaced it instead by a minimization of the enthalpy integral with respect to the a cold boundary length L ($T(L)=T_b$) computed from the temperature profiles given above. [Seol 94a] gives a review of the modifications induced in the MPZ profile as a consequence of a variation-principle approach to the cold end boundary condition T(x=L)=0.

In a mechanical analogue (2.4-12) can be considered as an equation of motion for a particle of unit mass subjected to a force which is proportional to the difference of heating minus cooling, with the initial condition of zero velocity at x=0 and zero displacement at x=L. By virtue of defining the temperature gradient as a velocity (2.4-12) can be written as an energy balance of kinetic and potential energy:

$$v = \frac{dT}{dx} \to \frac{v^2}{2} = \frac{p}{kA}\int_{T_{\max}}^{T} \left[g(T') - h(T') \right] dT' \quad \left[\frac{K^2}{m^2} \right] \tag{2.4-23}$$

With the definition of a potential energy U(T):

$$U(T) = \frac{p}{kA}\int_{0}^{T} \left[g(T') - h(T') \right] dT' \quad \left[\frac{K^2}{m^2} \right] \tag{2.4-24}$$

the integrated HBE, or energy equation, becomes simply: $(v^2/2)=U(T_{max})-U(T)$. The total energy inherent to the problem derives in fact from $U(T_{max})$. An integration of (2.4-23) considering the definition of U (2.4-24) yields x(T), the implicit steady state temperature profile (trajectory of the particle in the mechanical analogue).

$$x(T) = \frac{1}{\sqrt{2}}\int_{T}^{T_{\max}} \frac{1}{\sqrt{U(T_{\max}) - U(T')}}\,dT' \quad [m] \tag{2.4-25}$$

Since U(T) is an analytical function when cooling and heating are linear ((2.4-25) and (2.4-26)) x(T) (2.4-25) can be evaluated.

$$QE = \sqrt{2}\bar{c}_p A \int_0^{T_{\max}} \frac{(T - T_b)}{\sqrt{U(T_{\max}) - U(T)}} dT \quad [J] \tag{2.4-26}$$

At this stage of the calculation the basic assumption of the MPZ concept as presented above ([Wipf 79], [Dresner 95]) which states that the steady state $T_{MPZ}(x)$ is defined by the boundary condition $T_{MPZ}(x \rightarrow \infty) = T_b$ results in $U(T_{max})=0$. In the case of $\alpha i^3 > 1$ (or $T_{max} < T_c$) the MQE calculated from (2.4-25) would raise Dresner's MQE formula (2.4-18). [Chechetkin 90] minimized the enthalpy content of the MPZ (QE in (2.4-26)) with respect to T_{max} for the condition $T=T_b$ at x=L/2 (with L not necessarily infinite) and found smaller energies than e.g. [Wilson 78], especially at high values of i. [Jayakumar 87] and [Seol 94a] found the same discrepancy pointing out that although they found $T_{max} > T_{max}^{MPZ}$ the enthalpy content of their MPZ was smaller because the temperature was allowed to reach T_b at a smaller length than for the normal MPZ. Furthermore their terminology allows for the consideration of steady state external heating, e.g. in the form of $(dT/dx)_0 \neq 0$. Eventually this could be a way of adapting the steady state MPZ profile to the real temperature profiles after transient disturbances. [Seol 94b] points out that for the same disturbance energy the stability behavior may be different for different disturbance profiles. This has often been observed (e.g. [Ito 91]) and illustrates the insufficiency of the steady state MPZ concept when applied to transient temperature profiles in the aftermath of a strong perturbation. Together with [Chechetkin 90] Seol therefore proposes a more evolved stability criterion based on a plot of a stability functional V versus QE. The stability functional V represents the integrated difference of kinetic and potential energy in the mechanical analogue.

$$V = \int_0^{\infty} \left\{ \frac{1}{2}\left(\frac{dT}{dx}\right)^2 - U(T) \right\} dx = \frac{1}{\sqrt{2}} \int_0^{T_{\max}} \frac{U(T_{\max}) - 2U(T)}{\sqrt{U(T_{\max}) - U(T)}} dT \quad \left[\frac{K^2}{m}\right] \tag{2.4-27}$$

Solving the time dependent HBE numerically for parabolic and rectangular initial disturbances with varying enthalpy content [Seol 94b] traced a quenching / recovery boundary in the V(QE) plane. This boundary obviously did not coincide with a boundary line that could be deduced from the above mentioned steady state considerations.

[Wilson 78] has applied the same concept to a two-dimensional version of (2.4-13). He found the corresponding MPZ profiles numerically and found that they were elliptic in shape and appreciably larger and hotter than the one-dimensional analogs. This is due to an additive conduction term in radial direction.

An approximate theory of "transient stability" can be found in [Wilson 83], which is based on solutions of the space independent HBE:

$$c_p \left(\frac{\partial T(t)}{\partial t} \right) = \theta(t - t_{ini}) q_{ini} + \frac{p}{A}(g(T) - h(T)) \qquad \left[\frac{W}{m^3}\right] \tag{2.4-28}$$

where $\theta(t-t_{ini})$ is the Heavyside step-function which gives zero at $t>t_{ini}$ (end of pulse). Wilson proposes the following iterative procedure: Calculate T(t) from (2.4-28) for the initial condition $T(0)=T_b$ for a given disturbance power q_{ini} and disturbance time t_{ini}. Consider $T(t_{ini})$ as initial condition of (2.4-28) at $t>t_{ini}$ and find the recovery time t_R (defined arbitrarily as $t_R=t(T\sim T_b)$). For a linear form of $h\sim a(T-T_b)$ the total energy per unit surface transferred from the cooled surface e_t is given exactly by:

$$e_t = \frac{Aq_{ini}t_{ini}}{p\left(1-\alpha i^2\right)} \qquad \left[\frac{J}{m^2}\right] \tag{2.4-29}$$

where α is a modified Stekly parameter with a heat transfer coefficient a [W/K/m^2] as taken from above mentioned linear heat transfer correlation (which could be an approximation of a Kapitza-like heat transfer correlation). In an iterative process, with q_{ini} (at a given t_{ini}) as the variable e_t has to be matched with a critical energy taken from an appropriate helium model, e.g. Schmidt limit in the case of helium I or channel limit in the case of a small helium volume. The recovery time t_R in the critical transfer energy (e.g.: Schmidt limit $(t_{ini}+t_R)^{1/2}\sim 900/h$ in seconds, h in W/m^2) can be estimated in a conservative way from the adiabatic recovery limit Y:

$$t_R = \frac{c_p(T_b)A}{ap(1-\alpha)}\left[\ln 3 + \left(26Y^3+30Y^2+24Y-80\right)/81\right][s] \quad Y = \left(1+\frac{4q_{ini}t_{ini}}{c_p\left(T_b\right)T_b}\right)^{1/4} \tag{2.4-30}$$

The disturbance power per unit volume q_{ini} for given t_{ini} that makes e_t smaller or equal to e* is the sought critical energy. (2.4-29) depends not only on a linear heat transfer but also on the hypothetical extrapolation of a current sharing type heat generation function $g=g_c i^2(T-T_b)/(T_c-T_b)$ to temperatures above T_c! Together with the omission of heat transfer along the wire this results in a conservative value for the quench energy. The same type of model has been made easily accessible by [Nick 81]. With the hypothesis that $c_p\neq c_p(T)$ the HBE (2.4-28) at $t>t_{ini}$ can easily be rearranged to give explicitly the recovery time:

$$t_R \approx \frac{c_pA}{pa\left(1-\alpha i^2\right)} \quad [s] \tag{2.4-31}$$

Using an expression for the upper energy limit of heat transfer to helium of the type $e^*=\delta(t)^{1/2}$ (e.g. Schmidt limit in helium I) as a function of time, with the total heat per unit of cooled surface accumulated in the helium e_t from (2.4-29) and the time t_R from (2.4-31) one obtains:

$$MQE = V_{ini}\delta\sqrt{\frac{c_p p\left(1-\alpha i^2\right)}{Aa}} \qquad [J] \tag{2.4-32}$$

Application of (2.4-32) has shown that this model strongly underestimates MQE especially in adiabatic conditions. [Nick 81] suggests that this formula can be fitted to experimental data by choosing an appropriate linear heat transfer coefficient. Interestingly an enhanced heat transfer coefficient reduces the stability margin (via enhanced recovery time) in this formalism. (2.4-32) can be adapted as well to cases of confined conductors (eg. small helium channels) or to superfluid helium cooling by changing the stability criterion: $e_t<e^*_{Cl}$ in the former and $e_t<(K_{GM}t_R{}^3)^{1/4}$ in the latter case.
An extension of Dresner's transient model for adiabatic conditions [Dresner 85] to linear cooling has been presented by [Buznikov 96]. The model follows in general lines the adiabatic model mentioned above with the only difference that a linear cooling term $a(T-T_b)p/A$ is added to the right side of the time dependent HBE in (2.4-4). It has to be mentioned that this concept is an improved version of a stability calculation originally proposed in [Pasztor 78]. There the quench energy criterion is related to a limiting temperature profile created by a δ-like disturbance and calculated from the time dependent HBE without source terms. The resulting temperature profile as a function of the initial energy is known in this case ((2.4-3)). The improvement of [Dresner 85] and [Buznikov 96] lies in the further steps of the calculation in which they seek a recovery criterion in the approximate solution of the time dependent HBE with the disturbance temperature profile as initial condition rather than the almost arbitrary criterion (e.g. heating during recovery < Q_{ini}) proposed in [Pasztor 78]. The correction factors in Dresner's theory (2.4-7) are again refinements of the original idea of [Bejan 78] who corrected the Pasztor/Schmidt model to account for spatially and temporally extended disturbances. Taking into account that the third part at $T>T_c$ of the heat generation function is neglected the model becomes better for moderate pulses at high currents ($i\rightarrow 1$). Furthermore applications of (2.4-33) showed that it strongly depends on the choice of the linear heat transfer coefficient. The transient MQE for the one-dimensional case obtained by [Buznikov 96] is:

$$MQE=\frac{2}{3}\sqrt{2\pi}\,\frac{\bar{c}_p\sqrt{\bar{k}}\,A^{3/2}\left(T_c-T_b\right)^{3/2}}{\sqrt{g_c p}}\,\frac{i(1-i)}{\left(i-1/\alpha\right)^{3/2}}\qquad[J]\qquad(2.4\text{-}33)$$

The simple model of stability of a superconductor cooled by superfluid helium ([Seyfert 82], [Meuris 83], [Dresner 87]) is resumed in (2.2-28), which gives the critical energy deposit per unit surface, which still allows recovery. The model can be roughly adapted to our case if $Q_{ini}=e_c\cdot 2x_{ini}p$ and $h_{post}\sim g_c i^2$ when Dresner's Kapitza limit ([Dresner 87]) is ignored.

$$MQE=\frac{1}{2}x_{ini}\,p\bar{K}^3\bar{c}_p\left(T_\lambda-T_b\right)^2\frac{1}{\left(g_c i^2\right)^3}\qquad[J]\qquad(2.4\text{-}34)$$

[Malinowski 90] solved the time dependent HBE analytically by Laplace transforming the time dependence for constant material parameters, constant perturbation (2_{xini}, t_{ini}), maximum heat generation and a complicated nucleate boiling heat transfer correlation in which he combined a transient term which vanishes at the Schmidt limit and a steady state term (no switch to film boiling). His attempt to define a stability criterion of the type: T_{max}=ConstT_{cs}, with Const deduced from comparison with a numerical solution obtained with a complete steady state heat transfer correlation, three part Joule heating and temperature dependent k,c_p requires complicated calculations and seems to produce only limited convergence with experimental data.

The originality of [Seol 94 a,b]'s concept is the separate calculation of the HBE in the superconductor and the matrix of a simple monolayer or monofilamentary superconductor, coupled through the boundary conditions. In this concept the heat generation in matrix and superconductor can be implemented separately. Furthermore the stability criterion, now related to the superconductor temperature, becomes simply a critical current criterion of the above mentioned type i_{crit}. Unfortunately the model has not been exploited to its outermost leaving us with a lack of conclusions. The heat transfer characteristic was of the simple linear type, an unnecessary simplification. It would be interesting to find out whether these "sandwich"- or monofilament-models are more accurate representations of reality than the one-dimensional composite models.

2.4.3 Long Heater Calculations

The long heater approximation applies when the initially heated region is much longer than a characteristic stability length (e.g. l_{MPZ}). Long heater QE is normally plotted in J/m^3. Simulations show that QE(x_{ini}) starts at a high value (MQE) and with rising x_{ini} rapidly saturates at a lower QE indicating that conduction to the sides at the limits of the heated zone does not interfere in the process anymore, thus justifying the long heater approximation. As expected [Ywasa 79] has reported fair agreement between experiments in pool-boiling helium I and a model based on the space independent HBE (2.4-35) with three part Joule heating, temperature independent c_p and a transient heat transfer correlation.

$$c_p\left(\frac{\partial T(t)}{\partial x}\right) = \left(g(T(t),i) - h(T(t),t)\right)\frac{p}{A} + q_{ini}(t) \qquad T(0) = T_b \qquad \left[\frac{W}{m^3}\right] \tag{2.4-35}$$

Since (2.4-35) is easy to solve numerically, heating and cooling functions of any desired degree of complexity can be implemented. This variation of stability experiments is a good option to investigate the cooling characteristics because heat transfer to helium and (the well known) heat generation are the only players left in the tug-of-war between heating and cooling.

2.5 Conclusions

A review of historical stability concepts revealed how in the past stability related items successively entered the design of superconducting strands: Decomposing the superconductor into fine filaments in a highly conductive matrix to increase the dynamic stability, twisting the filaments to reduce interfilament coupling in external fields,..etc. Showing that “safe” stability criteria like those from Stekly or Maddock are by far out of reach for LHC-type strands, the Minimum Quench Energy becomes the only logical stability concept left. The corresponding “standard model of stability” describes the MQE process in thin conductors with a copper matrix by means of a one-dimensional heat balance equation consisting of a conduction term, a heat generation term due to current sharing, a term representing the initial heat pulse, a heat diffusion term related to the specific heat of the composite and most important the heat transfer term. To provide a sound basis in what refers to heat transfer to liquid helium an exhaustive description of the different modes of heat transfer to helium is given. The transient heat transfer model, used in the following, relies on Kapitza- and film-boiling type heat transfer correlations. The transition between the two regimes is determined by critical energies (enthalpy content of “active” helium volume). The “active” helium volume can either be the helium in a small voidage or determined by the “penetration-depth” of heat in an open bath environment. The penetration depth of heat in helium is proportional to its diffusivity, which obviously differs strongly in superfluid helium from pool-boiling helium I.

A review of articles related to the stability of strands, cables and magnets reveals that the experimental technique was so far not capable to confirm the numerous MQE simulations. Furthermore it seems that so far no sound correlation between stability measurements on conductors and magnet behavior could be established. The obstacle seems to be the difficulty to characterize the quench precursors in real scale magnets. The efforts were either concentrated on the magnets (speculations about eventual sources of quenches in magnets) or the conductors (quench energy measurements) but rarely were these two items linked. This chapter has recapitulated some of the most fruitful attempts to calculate the MQE analytically. These attempts rely either on simplified versions of the basic heat balance equation (neglecting the temperature dependence of the material properties) or use solutions of simpler problems together with a kind of perturbation theory (adding the time dependence to a steady state solution as a correction term).

Introducing the basic concepts of stability with special emphasis on heat transfer to liquid helium and a brief review of former stability investigations serves as a broad basis for the following chapter, which presents the stability model used here. This stability model can be regarded as a synthesis of the above discussed models and experiments.

The stability program calculates the spatial and temporal temperature profile of a one-dimensional model of a strand cooled by liquid helium being exposed to a rapid external heat pulse by solving numerically the corresponding heat balance equation. On the basis of this solution the program calculates the Minimum Quench Energy, the quench propagation velocity, the quench decision time the quench decision length, and many other magnitudes (cooling and heat generation in time and space) related to stability. Thus, the program is not only a powerful means to investigate the effect of different parameters on the MQE but it provides as well detailed information on the MQE process.

This chapter introduces the functions used for the composite heat conductivity, the composite electrical resistivity, the composite specific heat, the heat transfer correlation and the initial heat pulse in the heat balance equation.

A typical MQE process in a LHC-type strand is discussed in detail.

The stability program calculations are compared to calculations based on some analytical models in chapter 2.

A very important part is the comparison of simulated and measured MQE data. Weak and strong points of the model could be elucidated. The comparison as well helps to estimate the fraction of energy lost to the surroundings in an MQE measurement.

Finally a computations of the effect of a variation of the cooling parameters, RRR, Cu/Sc ratio on MQE are presented.

3. SINGLE WIRE STABILITY PROGRAM

3.1 Basic Equations

A multifilamentary superconducting strand cooled by liquid helium is subjected to a perpendicular external magnetic field and charged with a transport current as shown in Figure 3.1-1. The central feature of the following experiment is a punctuate heat pulse, of small extent (0.1-1mm) and short duration (10-100µs), applied onto the strand and denoted Q_{ini} (range: 1-1000µJ).

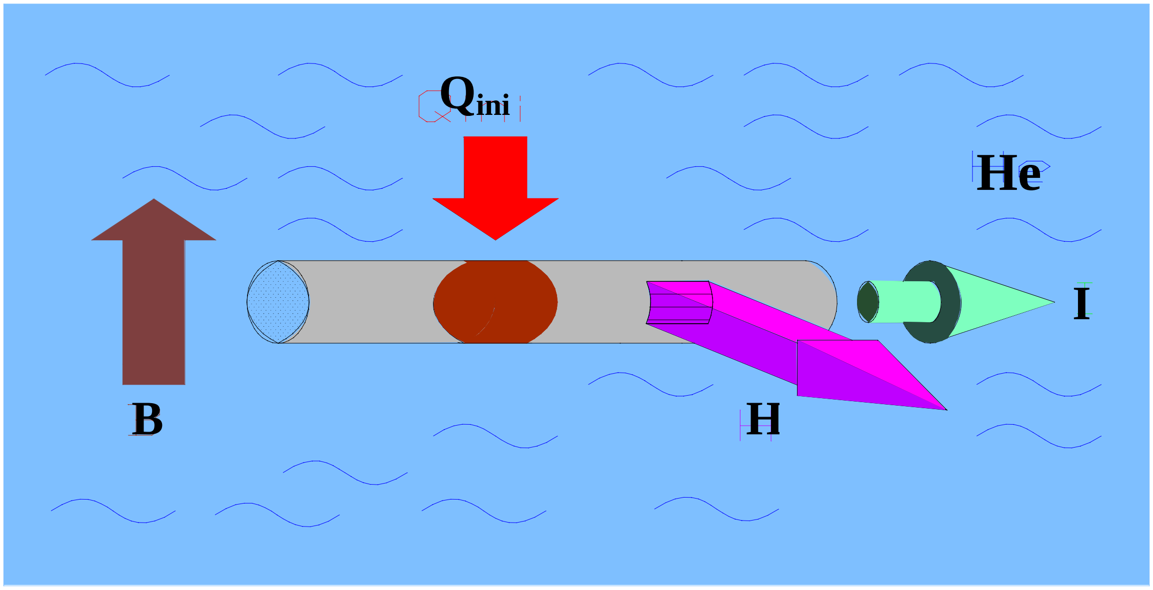

Figure 3.1-1: Sketch of the main parameters related to the single strand stability program.

The stability program, originally developed by M.N. Wilson [Wilson 96 a, b and 97 a, b], calculates the temperature profile of an infinitely long, one dimensional model of a superconducting , multifilamentary strand cooled by liquid helium and submitted to field, current and initial heat pulse, by solving numerically the one dimensional heat balance equation (3.1-1).

$$0 = \frac{\partial}{\partial x}\left[k(T)\frac{\partial T}{\partial x}\right] + I^2\frac{r(I,T)}{A} + q_{ini} - h(T,q)\frac{p}{A} - c_p(T)\frac{\partial T}{\partial t} \qquad \left[\frac{W}{m^3}\right] \tag{3.1-1}$$

In order to calculate h(T,q) in the numerical solution of (3.1-1) an additional equation for the transferred heat surface density q has to be solved (3.1-2).

$$q(x,t) = \int_0^t h(T(x,t'))dt' \qquad \left[\frac{J}{m^2}\right] \tag{3.1-2}$$

$T(x,t)$	Temperature [K]
I	Total current [A]
$r(I,T(x,t))$	composite electrical resistance per unit length [Ω/m]
A	Cross-section [m^2]
$h(q(x,t),T(x,t))$	Heat flux density to the cryogen [W/m^2]
p	Wetted perimeter $2\pi af$ [m]
f	Cooled perimeter fraction $\in[0,1]$
a	Radius of wire [m]
$c_p(T(x,t))$	Specific heat of composite [$J/m^3/K$]
$k(T(x,t))$	Heat conductivity of the composite [W/K/m]
$q(x,t)$	Cumulative heat transferred from conductor surface [J/m^2]
$q_{ini}(x,t)$	Initial heat load density [W/m^3]

Table 3.1-1: Parameters in the basic equations.

The problem has been simplified using the isothermal assumption, which can be justified by a simple comparison of the diffusivity of copper (Table 3.1-2) and NbTi at 4K ($D_{NbTi} \approx 10^{-6} m^2/s$). The ratio of copper and superconductor diffusivity being 10^6 means that it takes as long for the heat to cross a filament as to go round the perimeter of a typical LHC-type strand. The one-dimensional approximation was experimentally validated in former studies (e.g.: [Nick 81]) and in the present work (see chapter 5). It takes conductors with much larger diameters to see the effect of finite heat propagation within the composite cross-section (e.g.: [Fujiwara 94]).

	Cu 4.2K	He 4.2K	Cu 1.9K	HeII GM $1kW/m^2$	HeII GM $10kW/m^2$	HeII GM $100kW/m^2$	HeII SS $d=10\mu m$
D [m^2/s]	0.7	10^{-7}	0.9	16	0.16	0.0016	0.066

Table 3.1-2: Diffusivity D (=k/c_p) of copper and helium at 4.2K and 1.9K. Note that the diffusivity of helium II depends on heat flux h (in kW/m^2) and/or geometrical details (for example channel diameter (d) for the heat transfer to a capillary). GM (Gorter-Mellink) and SS (second-sound) refer to the particular heat transfer regimes of helium II.

The data in Table 3.1-2 indicate that at 4.2K the heat will diffuse much faster through copper than through helium. This supports the idea of dissecting the helium bulk into channels which have no heat exchange along the direction of the wire. This together with the other assumptions used in the model presented in the following is established since [Nick 81]. In helium II the situation unfortunately reverses and the one-dimensional helium model becomes a weak assumption. The heat balance equation (3.1-1) is normalized on a unit volume of conductor, thus it rates in terms of W/m^3. The different source terms in (3.1-1) are the Joule heating in the wire, the initial heat pulse Q_{ini} and with a negative sign the cooling function h. The boundary conditions are that $\partial T/\partial x$ is zero at x=0 and x=l for all times, with l being the length of the calculation interval (therefore the calculation interval has to be chosen long enough to avoid unphysical solutions). The initial condition is that $T=T_{bath}$ for all x. The problem is symmetric around the origin x=0.

The [NAG] Fortran routine D03PHF library is used to solve the heat balance equation numerically. The final data output consists mainly of the wire temperature and the heat transferred to helium in space and time. Quench occurs when the temperature in the central point irreversibly exceeds the critical temperature. The program may

automatically vary some of the parameters and iterate which in the case of varying the initial energy deposit Q_{ini} gives MQE simulations, the main objective of the program. The following presents the calculation of the parameters dealt with in Table 3.1-1. A list of all physical magnitudes required in the calculation is given in the introductory chapter.
The one dimensional approximation does not account for temperature differences between filaments and matrix as a result of poor heat contact between matrix and filaments. The program is a good instrument to simulate the effect of copper content, copper quality (k,ρ), transition number n, coating (Kapitza-conductance), specific heat, wetted perimeter and helium volume (channel length) on stability. It is not possible to simulate the effect of self-field and of the so called “design parameters” (double stack / single stack; dimensions of Cu-core and outer Cu-shell…) on stability.

3.2 The Specific Heat of the Composite

The parameters of the specific heat per unit of volume c_p [J/K/m^3] (3.2-1) , γ (Sommerfeld parameter) and β (Debye parameter) are taken from experiment [Dresner 90].

$$c_p = \beta T^3 + \gamma T \left[\frac{J}{Km^3}\right] \qquad (3.2\text{-}1)$$

The specific heat of the normal (subscript n) composite is calculated from the specific heat of Cu and NbTi weighed with (1-α) and α, where α is the volume ratio of superconductor versus total volume (α=1/(1+λ)) and where ρ is the density in kg/m^3.

$$c_{pn}(T) = \left[\gamma_{NbTi}\rho_{NbTi}\alpha + \gamma_{Cu}\rho_{Cu}(1-\alpha)\right]T + \left[\beta_{NbTi}\rho_{NbTi}\alpha + \beta_{Cu}\rho_{Cu}(1-\alpha)\right]T^3 \left[\frac{J}{Km^3}\right] \qquad (3.2\text{-}2)$$

The specific heat of NbTi in the superconducting state depends on magnetic field. The specific heat of the composite in the superconducting state c_{ps}(T,B) as taken from [Elrod 81] and weighed with α is:

$$c_{ps} = \left[\gamma_{NT}\frac{B}{B_0}\rho_{NT}\alpha + \gamma_C\rho_C(1-\alpha)\right]T + \left[\left(\beta_{NT} + \frac{3\gamma_{NT}}{T_{sc0}^2}\right)\rho_{NT}\alpha + \beta_C\rho_C(1-\alpha)\right]T^3 \qquad (3.2\text{-}3)$$

Parameter	Unit	NbTi$_{(46.5\%)}$	OFHC Copper
γ	[J/K^2/kg]	0.1450	0.011
β	[J/K^4/kg]	0.0023	0.000744
ρ	[kg/m^3]	6000	8960
B_0	[T]	14*	-
T_{sc0}	[K]	9.09	-

Table 3.2-1: Specific heat material parameters as taken from [Dresner 90], * [Dresner 95].

T_{sc0} is the critical temperature of NbTi at zero field, whilst B_0 is a false value for $B_c(T=0)$ to make experiment agree with (3.2-3). The specific heat contributions c_{ps} and c_{pn} are combined in an if-procedure, which assigns c_{ps} to c_p when $T<T_c$ and c_{pn} to c_p, when $T>T_c$. To avoid computing problems the jump during the transition between c_{ps} and c_{pn} is smoothed with a sine-function (3.2-4).

$$c_{pi} = \frac{1}{2}\left[c_{ps}(T,B) + c_{pn}(T)\right] - \frac{1}{2}\left[c_{ps}(T,B) - c_{pn}(T)\right]\sin\left[\frac{\left(T - T_c(B)\right)\pi}{2\Delta T}\right] \quad \left[\frac{J}{Km^3}\right] \qquad (3.2\text{-}4)$$

ΔT is the smoothing temperature interval around T_c. The final c_p function is a three part curve with c_{ps} below (T_c-ΔT), c_{pi} in the interval [T_c-ΔT, T_c+ΔT] and c_{pn} above (Figure 3.2-1).

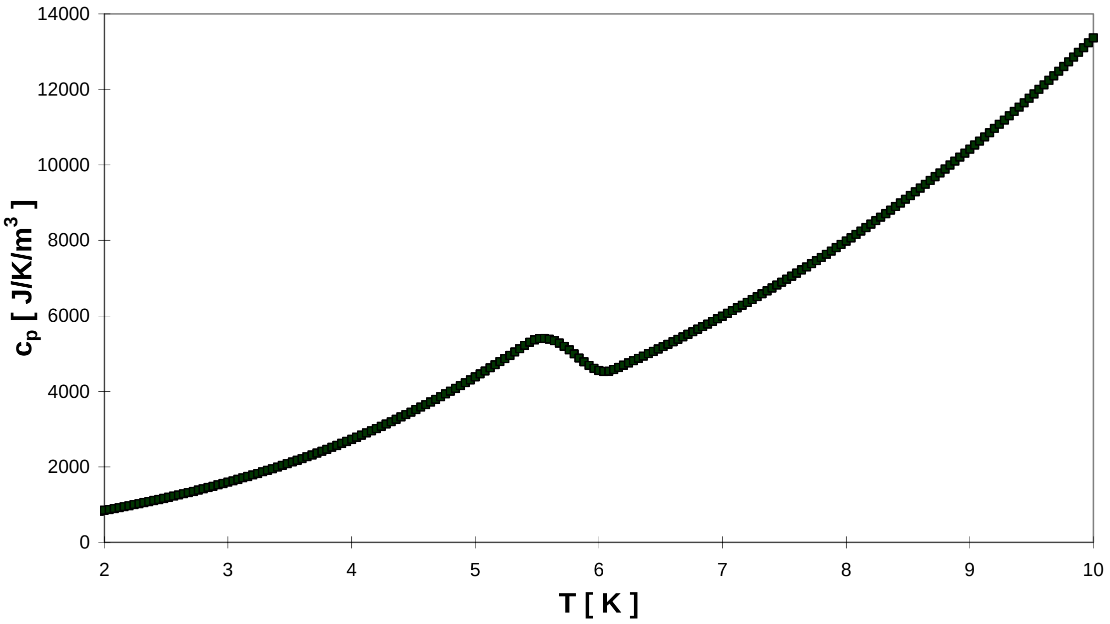

Figure 3.2-1: Specific heat function c_p in [J/m^3/K] as a function of T at B=8T, T_c(8T)=5.766K, ΔT=0.35, Reference wire with λ=1.6;

3.3 The Critical Surface

The critical temperature $T_c(B)$ is needed for quench detection and to locate the jump in c_p. The critical current density $j_c(B,T)$ is the main parameter for the heat generation. A phenomenological expression for B_c of NbTi(46.5%) is given in (3.3-1) [Hudson 81],

$$B_c(T) = K_1\left(1 - \frac{T}{T_{cf}}\right) - K_2\left(1 - \frac{T}{T_{cf}}\right)^{4.5} \qquad [T], \qquad (3.3\text{-}1)$$

where K_1=20.55T, K_2=5T and T_{cf}=9.5K. A less accurate formula for B_c is [Lubell 83]:

$$B_c(T) = 14.5\left(1-\left(\frac{T}{9.5}\right)^{1.7}\right) \qquad [T] \tag{3.3-2}$$

The program calculates $T_c(B)$ from a linear interpolation of (3.3-1). In the range 0-10T this gives the same results as the standard formula [Lubell 83] in (3.3-3).

$$T_c(B) = 9\left(1-\frac{|B|}{14.5}\right)^{0.59} \qquad [K] \tag{3.3-3}$$

J_c can be extrapolated from a known value: With $j_c(B,T)=f/B$ ($f(B,T)$ is the pinning force density) and $f=B_c^m(T)p$ (the pinning curve $p(B/B_c)$) j_c of a known $j_{cal}(B_{cal},T_{cal})$ becomes:

$$j_c(B,T) = j_{cal}B_{cal}\left[\frac{B_c(T)}{B_c(T_{cal})}\right]^{1.8}\left[\frac{p(B,T)}{p_{cal}}\right]\frac{1}{B} \qquad \left[\frac{A}{m^2}\right] \quad , \tag{3.3-4}$$

where $B_c(T)$ is taken from (3.3-1), j_{cal}, B_{cal} and T_{cal} are preferably measured and p/p_{cal} of $NbTi_{(46.5\%)}$ from [Larbalestier 79 + 80] is given in (3.3-5) (b is $B/B_c(T)$).

$$p(B,T) = 4.4\left[b(B,T)+0.03\right]\left[1-b(B,T)\left[1.3-0.3b(B,T)\right]\right] \tag{3.3-5}$$

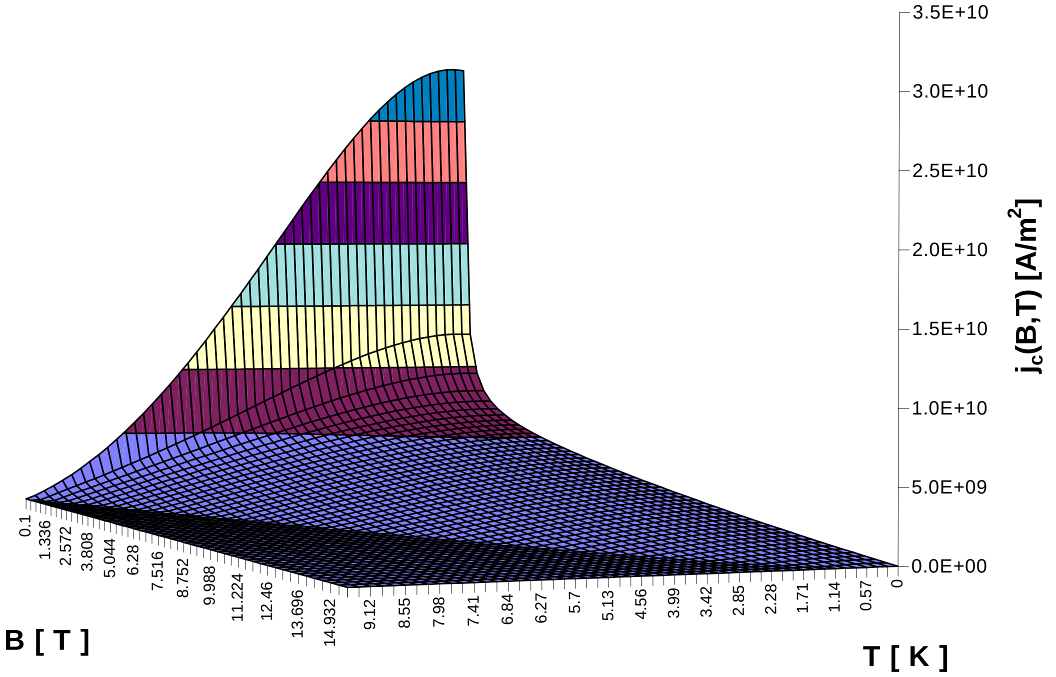

Figure 3.3-1: Critical current density $j_c(B,T)$ of Nb(46.5%Ti). The most important parameters for the calculation are the calibration values: I_{cal}=360A, B_{cal}=8T, T_{cal}=4.23K and from [Larbalestier 79+80]: f_{cal}=0.716J/m^3, B_c(0K)=15.55T, B_c(4.23K)=11.05T, T_c(0T)=9.5K, T_c(8T)=5.77K;

3.4 Resistivity and Heat Generation

3.4.1 Matrix Resistivity

The copper resistivity in the experimental temperature range of 1-20K is assumed to be the sum of residual and magneto-resistivity. The former can be taken from RRR measurements (3.4-1), taken for granted that commercially available copper-specimen have the same room-temperature resistivity of $1.69 \cdot 10^{-8}\Omega\text{m}$ [Meaden 65].

$$RRR = \frac{R_{300}}{R_{10}} = \frac{\rho_{Cu}(300K)}{\rho_{Cu}(10K)} \tag{3.4-1}$$

The magneto-resistive contribution in OFHC copper in a transverse magnetic field is assumed to be linear with field (Koehler's rule) ((3.4-2) [Wilson 83]).

$$\Delta\rho_B = \frac{(7.67 - 2.65)10^{-10}}{10} \left[\frac{\Omega m}{T}\right] \tag{3.4-2}$$

Combining (3.4-1) and (3.4-2) results in (3.4-3).

$$\rho_{Cu}(B) = \frac{1.69 \cdot 10^{-8}}{RRR} + 5.02 \cdot 10^{-11} B \; [\Omega m] \tag{3.4-3}$$

A more reliable ρ_{Cu} can be obtained from measuring the voltage during resistive transitions of the sample. Since no temperature dependence is included in (3.4-3) the formula is not valid above 20K. In general when T_s has locally reached 20K one can reasonably assume that the strand will not recover. The program therefore provides the possibility to set a maximum temperature. Nevertheless a more accurate version of the program (valid up to 40K) could make use of the following formula for ρ_{Cu} [Simon 87]:

$$\rho'_1 = \frac{1.171 \cdot 10^{-17} \cdot T^{4.49}}{1 + \left\{4.5 \cdot 10^{-7} \cdot T^{3.35} \cdot \left[e^{-\left(\frac{50}{T}\right)^{6.428}}\right]\right\}} \quad [\Omega m] \tag{3.4-4}$$

$$\rho'_2 = \left[\frac{1.69 \cdot 10^{-8}}{RRR} + \rho'_1 + 0.4531 \cdot \left(\frac{1.69 \cdot 10^{-8} \cdot \rho'_1}{RRR \cdot \rho'_1 + 1.69 \cdot 10^{-8}}\right)\right] \quad [\Omega m] \tag{3.4-5}$$

$$A = \log\left(\frac{1.553 \cdot 10^{-8} \cdot B}{\rho'_2}\right) \tag{3.4-6}$$

$$a = -2.662 + 0.3168 \cdot A + 0.6229 \cdot A^2 - 0.1839 \cdot A^3 + 0.01827 \cdot A^4 \tag{3.4-7}$$

$$\rho_{Cu} = \rho'_2 \cdot \left(1 + 10^a\right) [\Omega m] \tag{3.4-8}$$

The normal state resistivity of NbTi at 4.2K is approximately $6 \cdot 10^{-7}\Omega$m [Wilson 83]- three orders of magnitude bigger than that of copper. It is therefore a reasonable approach to ignore the normal resistivity of the NbTi-branch. In this approximation the resistivity of the total composite ρ_{Comp} can be calculated from ρ_{Cu} by multiplying with $(1+\lambda)/\lambda = V_{tot}/V_{Cu}$.

$$\rho_{Comp} = \rho_{Cu}\left(\frac{1+\lambda}{\lambda}\right) [\Omega m] \tag{3.4-9}$$

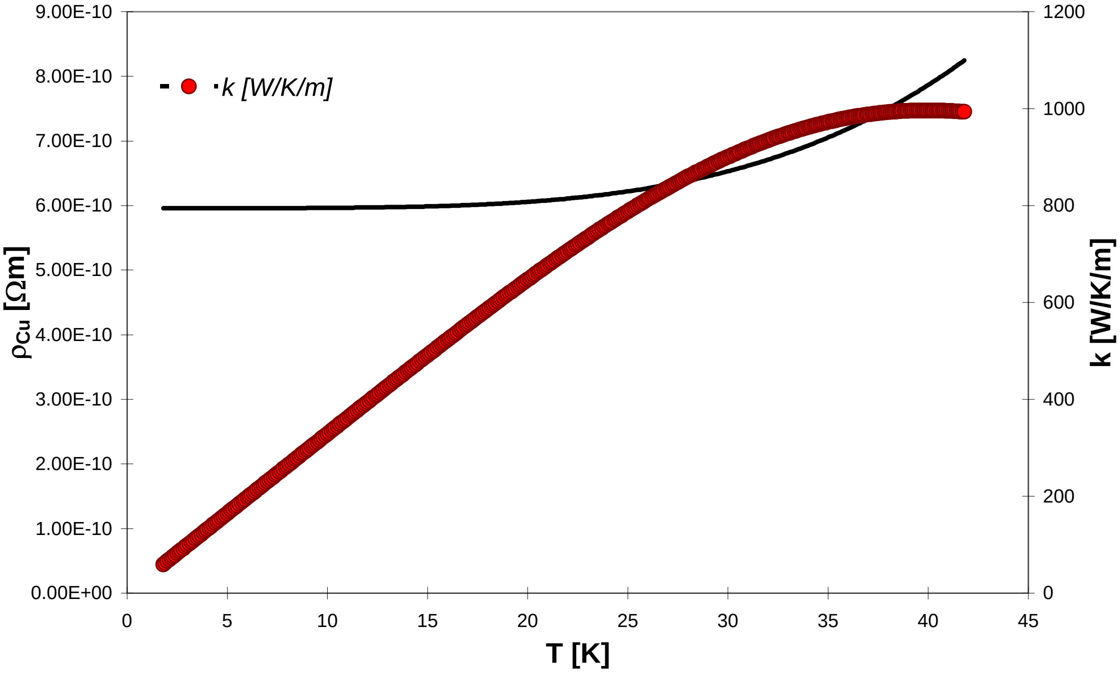

Figure 3.4-1: Temperature dependent electrical resistivity of Cu, calculated with (3.4-8) for RRR=100, B=11T. The resistivity stays constant up to 20K. On the secondary y-axis the heat conductivity of the composite ($k_{NbTi} \approx 0$) calculated from the temperature dependent resistivity with Wiedemann-Franz (modified Lorentz-constant 1.3 L_0 as explained in chapter 3.5). As can be seen in a comparison with Figure 3.5-1 it does not differ too much from the linear k calculated from a constant residual Cu-resistivity.

3.4.2 The Resistivity of the Composite

The usual assumption about the temperature variation of resistance in a superconducting composite is that, above $j_c(T)$, the superconductor carries its critical current and the remaining current flows in the copper. With this assumption, MQE is zero at the critical current - strongly at variance with experiment. However it is well known that superconducting composites do not have a sharp transition at $j_c(T)$, but a progressive one as in (3.4-12). *"To our knowledge, there are no experimental data on the form of $\rho(T)$ at high resistivity - samples usually quench at $\rho \approx 10^{-13}\,\Omega m$."* [Wilson 96].

The equations corresponding to a simple nod with the copper and the superconductor branch in parallel (e.g. Figure 3.4-2) are Kirchhoff's laws ((3.4-10),(3.4-11)) and the power-resistivity law for superconductors ((3.4-12)). (Current density j and resistivity ρ' are related to A_{tot}, for example $\rho'_{Cu}=\rho_{Cu}.(\lambda+1)/\lambda$, voltages v are per unit length of wire.)

$$j_{Sc}\rho'_{Sc} = j_{Cu}\rho'_{Cu} = v \quad \left[V/m\right] \tag{3.4-10}$$

$$j_{tot} = j_{Sc} + j_{Cu} \quad \left[\frac{A}{m^2}\right] \tag{3.4-11}$$

$$\rho'_{Sc} = \rho_0\left(\frac{j_{Sc}}{j_c(B,T)}\right)^n \quad [\Omega m] \tag{3.4-12}$$

Combined, the equations give (3.4-13), which unfortunately has no analytical solution.

$$1 = \frac{j_{Sc}}{j_{tot}} + \frac{\rho_0}{\rho'_{Cu}}\frac{j_{Sc}^{n+1}}{j_c^n j_{tot}} \tag{3.4-13}$$

Therefore an even simpler model has been used in the stability program (Figure 3.4-2). It assumes that ρ follows (3.4-12) at low (subscript l) values and joins smoothly onto the copper line at high currents (subscript h), as shown in Figure 3.4-3.

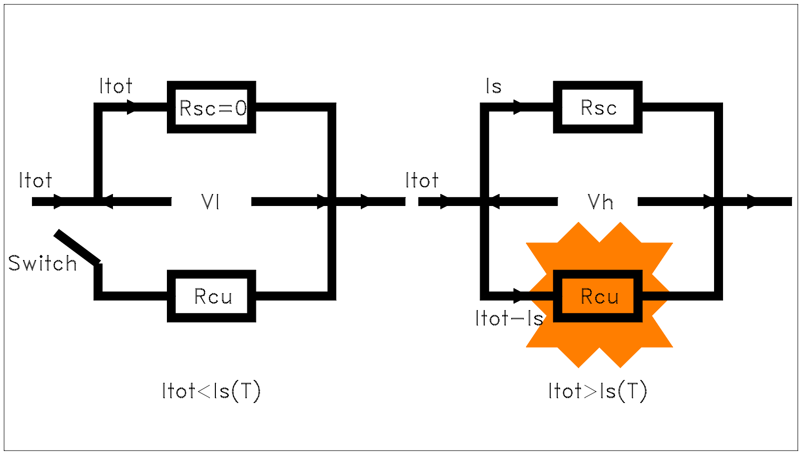

Figure 3.4-2: Network model of a superconducting strand. When I_{tot} has reached $I_s(T)$ the current in excess of I_s spills over to the copper. $I_s(T)$ is bigger than $I_c(T)$, they converge at T_{c0}. The part where heat generation occurs is high-lighted. The superconductor does not contribute to heat generation.

A threshold current $j_s(T)$ ($\geq j_c$), above which all the extra current goes into the matrix is defined as the current where the slopes of v(I) of the lower (3.4-14) and the copper (3.4-15) branch meet ((3.4-16) and (3.4-17)).

$$v_l = j_{tot}\rho_0\left(\frac{j_{tot}}{j_c}\right)^n \quad \left[V\!\!/_m\right] \tag{3.4-14}$$

$$v_h = v_s + (j_{tot} - j_s)\rho'_{Cu} \quad \left[V\!\!/_m\right] \tag{3.4-15}$$

$$\rho'_{Cu} = \rho_0(n+1)\left(\frac{j_s}{j_c}\right)^n \; [\Omega m] \tag{3.4-16}$$

$$j_s = j_c\left[\frac{\rho'_{Cu}}{\rho_0(n+1)}\right]^{1/n} \rightarrow v_s = v_l(j_s) = j_c(T,B)\rho_0\left[\frac{\rho'_{Cu}}{\rho_0(n+1)}\right]^{\frac{n+1}{n}} \left[\frac{V}{m}\right] \tag{3.4-17}$$

$$v_h = j_c\rho_0\left[\frac{\rho'_{Cu}}{\rho_0(n+1)}\right]^{\frac{n+1}{n}} + (j_{tot} - j_s)\rho'_{Cu} \quad \left[\frac{V}{m}\right] \tag{3.4-18}$$

The resistivity of the composite can be calculated by dividing (3.4-14) and (3.4-18) by j_{tot}.

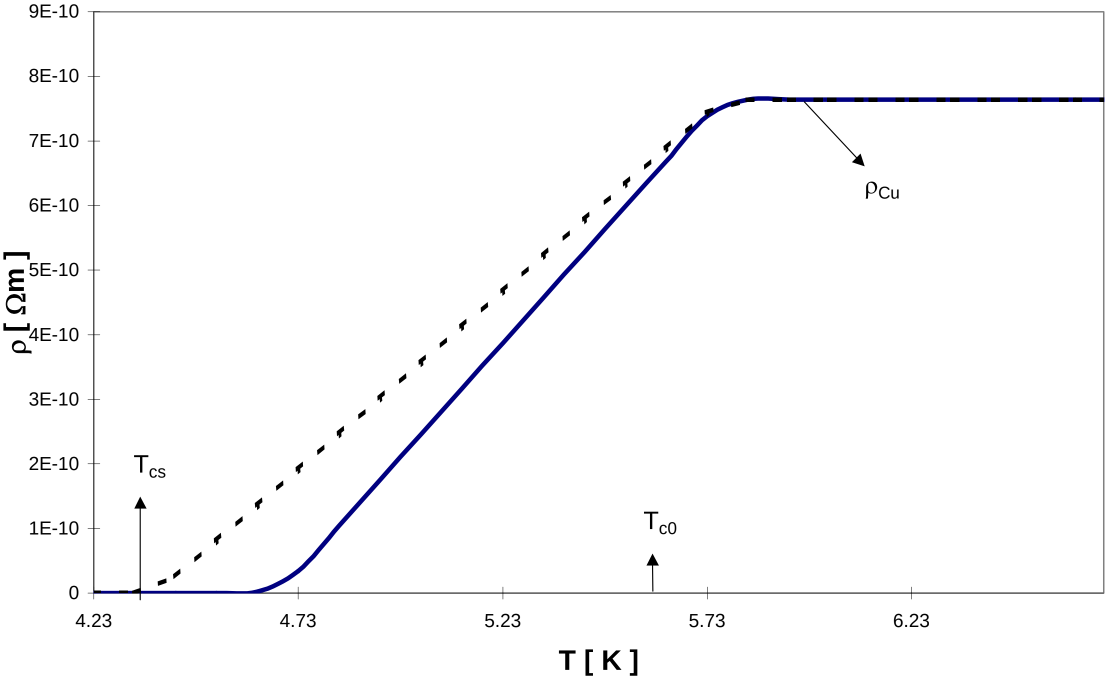

Figure 3.4-3: Models of effective composite - resistivity (reference strand). Continuous line progressive transition as described here ((3.4-14),(3.4-18)), dashed: 3-part-curve-model from

[Wilson 83]. Current sharing temperature T_{cs}=4.384K, critical temperature at zero current T_{c0}=5.766K, bath temperature T_b=4.23K, magnetic field B=8T, transition number n=29, normal conducting composite resistivity $\rho'_{Cu}=\rho_{Comp}=7.64\cdot10^{-10}\Omega m$ (total cross-section) and critical generation $g_c=j_{tot}^2\rho_{Comp}$=100MW/m^3.

The smooth resistive transition used in this stability model can be considered as a novel approach ([Wilson 97]).

3.4.3 The Heat Generation Function

The heat generation function g(T,B,I) is $\rho_{Comp}j_{tot}^2$ and rates in W/m^3. If the total current density is below 0.8j_c g is automatically set to zero. If $j_{tot}<j_s(T)$ g is g_l (3.4-17) and if $j_{tot}>j_s(T)$ g is g_h. In the program code j_s and j_c have to be kept artificially at a small value above zero at T>T_c, so that the heat generation function g stays automatically g_{max}!

$$j_{tot} < 0.8\, j_c(B,T) \qquad g(T,B,I) = 0 \tag{3.4-19}$$

$$j_c(B,T) < j_{tot} < j_s(T) \qquad g_l(T,B,I) = j_{tot}^2\rho_0\left(\frac{j_{tot}}{j_c}\right)^n \quad \left[\frac{W}{m^3}\right] \tag{3.4-20}$$

$$j_{tot} > j_s(T) \;\; g_h(T,B,I) = j_{tot}\, j_c\rho_0\left[\frac{\rho_{Comp}}{\rho_0(n+1)}\right]^{\frac{n+1}{n}} + j_{tot}(j_{tot} - j_s)\rho_{Comp} \quad \left[\frac{W}{m^3}\right] \tag{3.4-21}$$

The critical current density function can be taken from (3.3-4) or as it is actually the case calculated with a simple phenomenological fit from [Wilson 83] (3.4-22).

$$j_c(T) = j_c(T_b)\frac{(T_c - T)}{(T_c - T_b)} \quad \left[\frac{A}{m^2}\right] \tag{3.4-22}$$

A typical heat generation function is shown in Figure 3.6-3. The maximum heat generation at a given transport-current $g_c i^2$ is:

$$T > T_c(B, I = 0) \;\; i^2 g_c = j_{tot}^2\rho_{Comp} \quad \left[\frac{W}{m^3}\right] \tag{3.4-23}$$

3.5 The Thermal Conductivity of the Composite

Most metals and alloys obey the Wiedemann-Franz law fairly well at low temperature. Unfortunately the impact of high magnetic fields on the WF-law is not well established though it is known to be strong (roughly 1-2% increase of the Lorentz-constant per Tesla in a transverse field [Dresner 95]). In spite of this drawback we use WF-law to calculate k from ρ_{Comp}(3.5-1). The thermal conductivity of NbTi is 4 orders of magnitude smaller than that of Cu. Henceforth, heat conduction along the filaments is negligible. The problem of trapped heat within the filament, a phenomenon not accounted for in the stability model, has already been pointed out in chapter 3.1. However, since the program foresees no heat generation within the filaments the simplified approach to restrict heat generation and transport only within the matrix follows at least a self-sufficient logic. In other words the electrical resistivity in the Wiedemann-Franz law is not the two-part function as for the heat generation but simply that of a copper with holes instead of the superconducting filaments. L_0 is the Lorentz-number $L_0=2.45\cdot10^{-8}W\Omega/K^2$.

$$k(T,B)=L_0\frac{T}{\rho_{Comp}(B)}\left[\frac{W}{Km}\right] \tag{3.5-1}$$

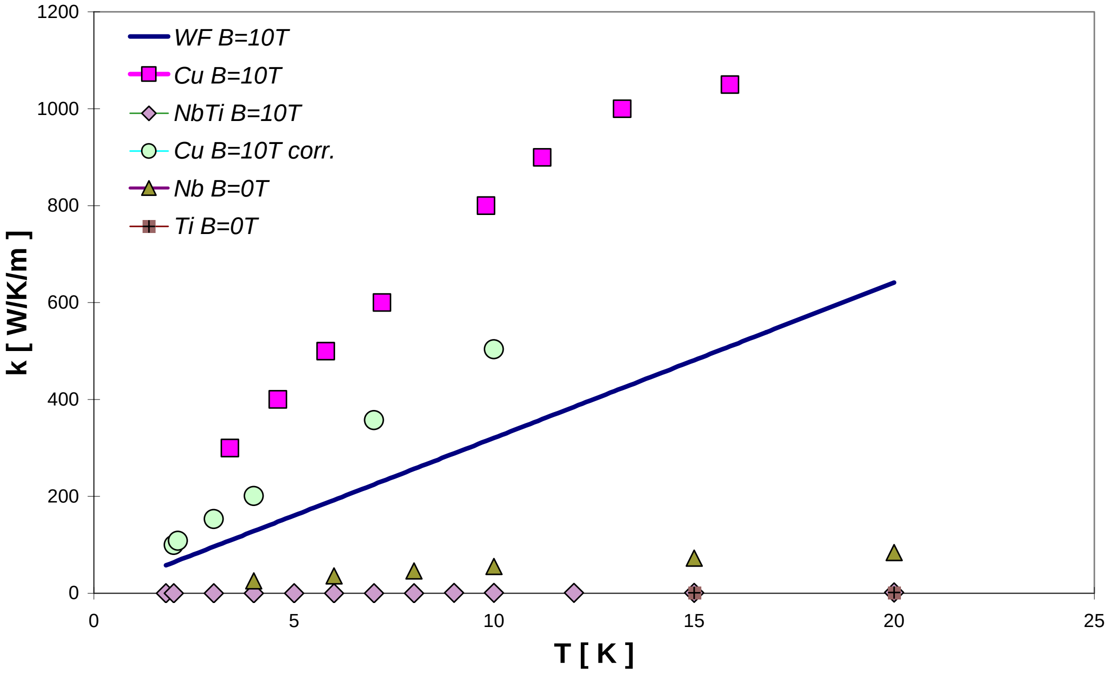

Figure 3.5-1: Thermal conductivity k(T) of Cu, NbTi, Nb, Ti. Upper two curves: measurements on commercial OFHC Cu (RRR≈100) [Arenz 82] and [Iwasa 94]. Latter data for B=0T and corrected for B=10T with $k'=L_B/((L_0/k)+(\Delta\rho_B B/T))$ following a proceeding proposed by Arenz, (L_B-modified Lorentz-constant, $L_{10}=2.835\cdot10^{-8}W\Omega/K^2$), $\Delta\rho_B$ the magneto-resistivity coefficient and k the original data. Full line is a ref-strand calculation $\rho_{Comp}=7.64\cdot10^{-10}\Omega m$ at 8T using WF. Lower curves: NbTi-alloy [Ogitsu], Nb [White 57] and Ti [Tyler 52] at B=0T.

The WF-law can be corrected enhancing L_0 by a factor 1.3 at 10T [Arenz 82]. [Nick 81] used a modified Lorentz-constant of $2.5L_0$ (at 4T) to generate a better agreement between measured and calculated stability data. In any way the (enhanced) WF-law is better adapted to magnetic fields than the standard k fit for Cu in B=0 (3.5-2):

$$k_{Cu}(T,B=0)=\frac{1}{\left[\frac{15.53}{(RRR-1)\cdot24.45\cdot T}+3.35\cdot10^{-7}\cdot T^2\right]}\quad[W/K/m] \tag{3.5-2}$$

3.6 Heat Transfer Function

3.6.1 Transient Heat Transfer to Pool Boiling Helium I

For very short times, that is Δt<1ms, heat transfer to HeI is regulated mainly by Kapitza resistance. In the transient case a heat flux density h ([W/m^2]) by far exceeding the NBM can occur, but restrictions related to critical times or critical energies impose new limits to transient (Kapitza) heat transfer. After burn-out the heat transfer correlation is of the film-boiling type. A Kapitza heat transfer correlation with a term that smoothens the transition to film-boiling is given in (3.6-1).

$$q(x,t) < \min\left(e_{Sl}^{(I)}, e_{Cl}^{(I)}\right) \qquad h_K = 180\left(T_s^4 - T_b^4\right)\left[1-\left(\frac{q}{e_l}\right)^3\right] \qquad \left[\frac{W}{m^2}\right] \tag{3.6-1}$$

The Kapitza coefficient a_K in (3.6-1) is consistent with conservative data from measurements on copper reported in [Schmidt 81] and [Gentile 80].

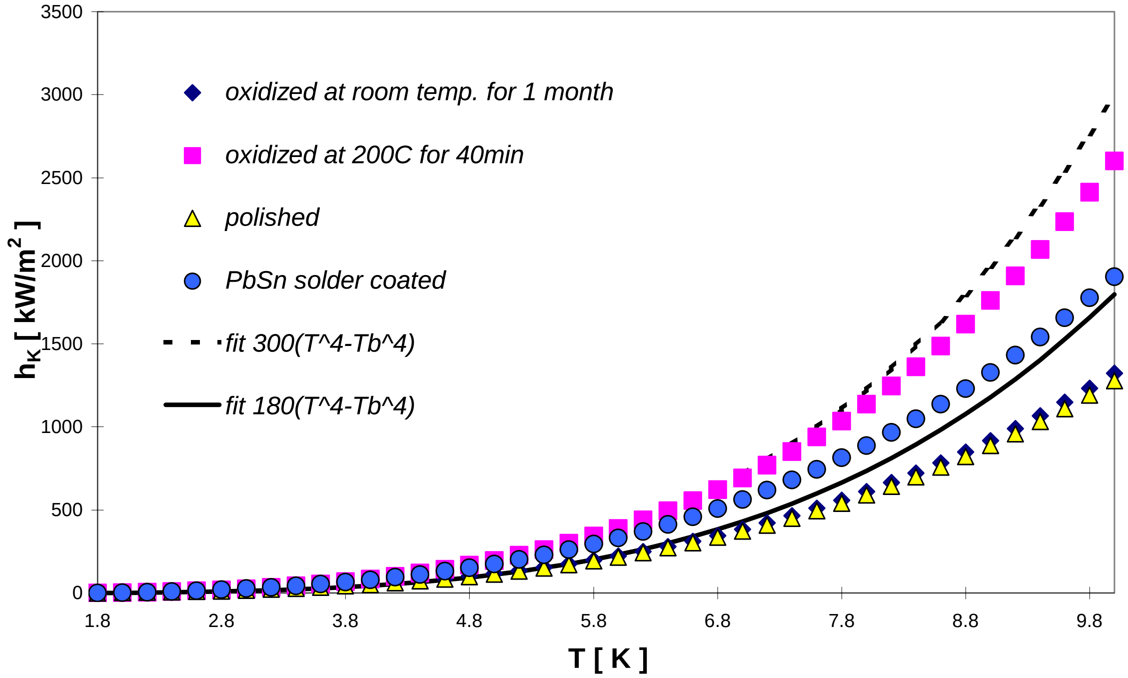

Figure 3.6-1:Measured Kapitza heat transfer correlations from Cu to helium at 1.8K [Kashani 85]. The fit with a_K=180W/m^2/K^4 is supposed to describe best tin coated strands whereas the coefficient a_K=300W/m^2/K^4 fits highly oxidized copper surfaces. Another series of experiments on the same samples published in the same reference indicate that h_K is bigger for the soldered wire than for the highly oxidized one. This shows how confusing experimental evidence is.

Q(x,t) is the cumulative heat transferred from the conductor surface given in (3.6-2).

$$q(x_i,t) = \int_{t_0}^{t} h(x_i,t')dt' \qquad \left[\frac{J}{m^2}\right] \tag{3.6-2}$$

The heat transferred in every mesh-point x_i along the strand has to be taken into account. When the energy density q reaches the limit $e^{(I)}$ ([J/m^2], film-boiling is triggered. Believing that the transition from Kapitza-like- to film-boiling cannot be abrupt, the transition is smoothed by progressively reducing h_K as q approaches the limit e_I (equation (3.6-1)). This limiting factor expresses as well the fact that the Kapitza heat transfer correlation usually flattens for temperature differences exceeding a few Kelvin. An improved version of the program could take into account the temperature rise of the helium in small (<100µm) channels, thus resulting in a further reduction of (T_s-T_b) in the Kapitza-like heat transfer correlation. In a one-dimensional model the wire has to be imagined as a straight line subdivided into a mesh of discrete sections (~1µm-1mm). To each mesh-point a virtual channel of length (height) L (or w) and basis p·Δx is associated (Figure 3.6-2). Actually as a simplification these adjacent helium bars do not communicate. This is a fairly good approximation in helium I because the longitudinal (parallel to the wire) heat transfer within the transient time-scale (µs-ms) is negligible. The length of the channels L and, by virtue of the cooled perimeter fraction f, the width p are optional. To simulate MQE-measurements on single strands in an open bath one has to set L to a big value (mm to cm), so that it does not affect the result. The top of the channels may be open or closed.

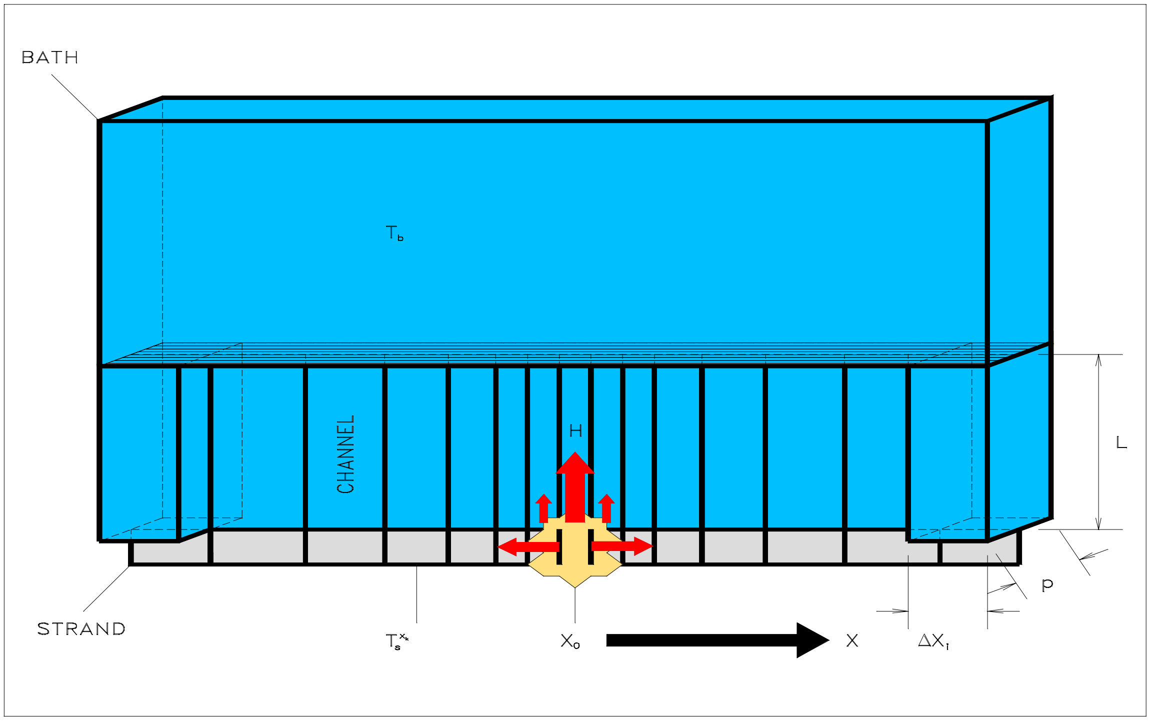

Figure 3.6-2: 1-dimensional cooling model; The strand is divided into length elements (of variable size). Each discrete element $\Delta x_i = x_i - x_{i-1}$ has a helium channel $L \cdot p \cdot \Delta x_i$, which is connected (open channel) or not connected (closed channel) to an infinite bath. The power H_i [W] transferred into each channel is $h \cdot \Delta x_i \cdot p$ (p..cooled perimeter).

As indicated in the basic equation (3.1-1) h can be converted to W/m^3 multiplying with p/A, the mesh size Δx does not appear anymore in (3.1-1). The channel length L cannot be set directly in the program, but it is calculated from the helium volume given as a fraction of strand volume, the so called voidage v with (3.6-3).

$$L = \frac{Av}{p} \qquad [m] \tag{3.6-3}$$

In small (L=1-100µm) open channels and for heat fluxes moderately above NBM the process will consume the full heat absorption capacity of the helium in the channel and run into the so called channel limit, which according to [Iwasa 77] is given by 0.14λL (3.6-4). Iwasa argues that the volume expansion of helium as it changes from liquid to vapor at 4.2K is 7.5-fold and that once enough vapor has been produced to fill the channel the rest of the liquid has been expelled from it.

$$e_{Cl}^{(I)} = 0.14 \cdot 2.5 \cdot 10^{6} \cdot L \qquad \left[\frac{J}{m^2}\right] \tag{3.6-4}$$

In small closed channels even heat fluxes below NBM, when acting long enough will vaporize sufficient helium during nucleate boiling to raise the pressure in the channel to critical [Schmidt 88] (3.6-5). Above critical pressure film-boiling ensues without any further heating.

$$e_{cCl}^{(I)} = 5.3 \cdot 10^{4} \cdot L \qquad \left[\frac{J}{m^2}\right] \tag{3.6-5}$$

In long channels and for particularly high heat fluxes it is likely that the channel limit is out of reach because the heat input is so massive that it triggers film-boiling before heat has spread further than into a thin (δ<<L) layer. By virtue of the diffusivity of helium I [Schmidt 88 and Schmidt 91] has calculated λδ assuming a step-function heat flux and obtaining a result, which conveniently reproduces his own experiments (3.6-6). This value has been confirmed as well in the experiments of [Tsukamoto 85]. Note that the program has to prevent h_K from becoming zero!

$$e_{Sl}^{(I)} = \frac{6.9 \cdot 10^{5}}{h_K} \qquad \left[\frac{J}{m^2}\right] \tag{3.6-6}$$

[Steward 86] experimentally found a slightly different correlation (3.6-7) which is not considered in the current program.

$$e_{Stl}^{(I)} = \frac{1.8 \cdot 10^{6}}{{h_K}^{1.5}} \qquad \left[\frac{J}{m^2}\right] \tag{3.6-7}$$

The smallest of the limits (3.6-4)/(3.6-5)and (3.6-6) applies. Then the heat transfer switches to film-boiling, with a heat transfer coefficient of 250W/m^2/K, which corresponds to typical values reported in [Schmidt 81] and [Van Sciver 86], ranging between 170 and 280W/m^2/K.

$$q(x,t) \geq \min\left(e_{Sl}^{(I)}, e_{Cl}^{(I)}\right) \qquad h_{fb} = 250\left(T_s - T_b\right) \quad \left[\frac{W}{m^2}\right] \tag{3.6-8}$$

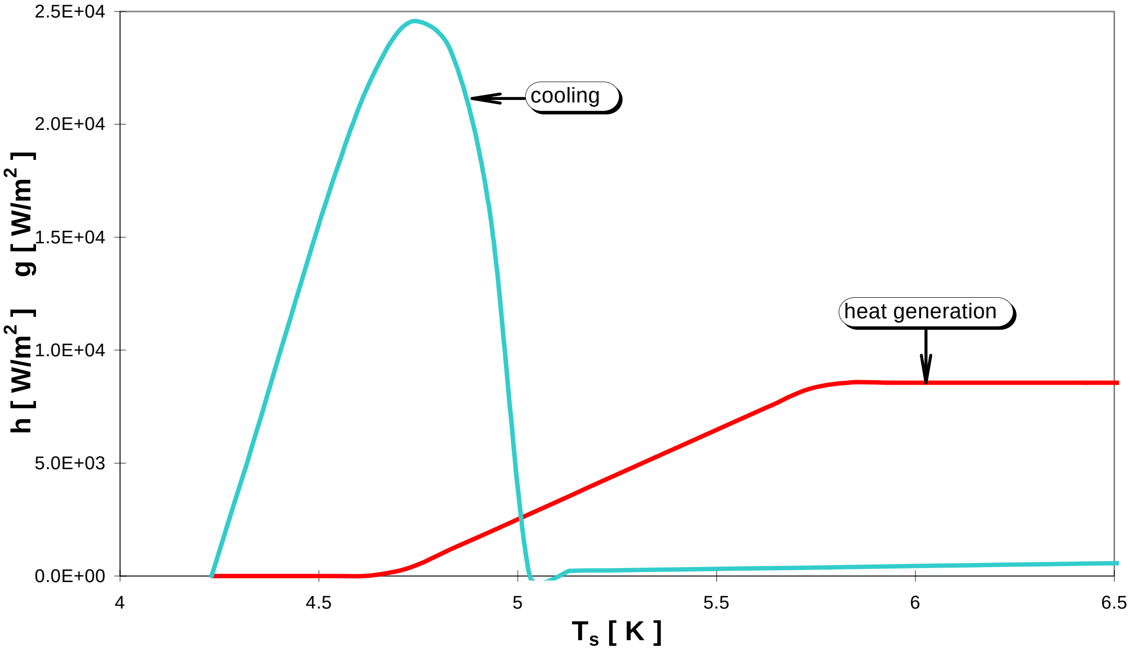

Figure 3.6-3: Comparison of transient cooling to pool boiling HeI and heat generation, reference wire. Heat generation function for I=I$_c$ as described in chapter 3.4.3, converted with A/p to W/m^2. The transient cooling curve shows one particular case (switching from Kapitza-regime to film-boiling at ΔT$_{max}$=0.8K, which is a typical experimental value found in [Van Sciver 86]). Transient cooling function as described in (3.6-1) and (3.6-8).

3.6.2 Transient Heat Transfer to Subcooled Helium II

The transient heat transfer correlation is of the Kapitza-type (3.6-1) before and of the film-boiling type (3.6-8) after burn-out. Burn-out is reached when the transferred heat exceeds the critical energy $e_l^{(II)}$, which is not only a function of heat flux but depends also on the state of the helium II. The $e_l^{(II)}$ data are from experiment. A simple channel limit corresponds to the enthalpy difference per unit volume between T_b and T_λ times L. The value for T_b=1.9K in (3.6-9) is from [Seyfert 82]. Small heat flux (moderately above the critical steady state heat flux) run into Gorter-Mellink limit. An experimental fit for $e_{GM}^{(II)}$ at 1.8K [V.Sciver79] is (3.6-10). [Nemirovskii 89] measured (9-15)·10^{17}sW^4/m^8.

$$e_{Cl}^{(II)} = 2.36 \cdot 10^5 \cdot L \qquad \left[\frac{J}{m^2}\right] \tag{3.6-9}$$

$$e_{GM}^{(II)} = \frac{9.10^{17}}{h_K^3} \qquad \left[\frac{J}{m^2}\right] \tag{3.6-10}$$

Very high heat flux runs into second-sound limit because the critical heat is accumulated in the helium so fast that turbulence cannot appear. The proportionality constant in (3.6-11) is from [Nemirovskii 89] and agrees with [Gradt 90], [Wang 95].

$$e_{SS}^{(II)} = \frac{2.5 \cdot 10^7}{h_K} \qquad \left[\frac{J}{m^2}\right] \tag{3.6-11}$$

The transition from GM to second sound is arbitrarily defined as the point, where the limits cross (3.6-12). In fact this transition is a function of time [Wang 95].

$$h_{Ki} = \sqrt{\frac{9 \cdot 10^{17}}{2.5 \cdot 10^7}} = 190 \frac{kW}{m^2} \tag{3.6-12}$$

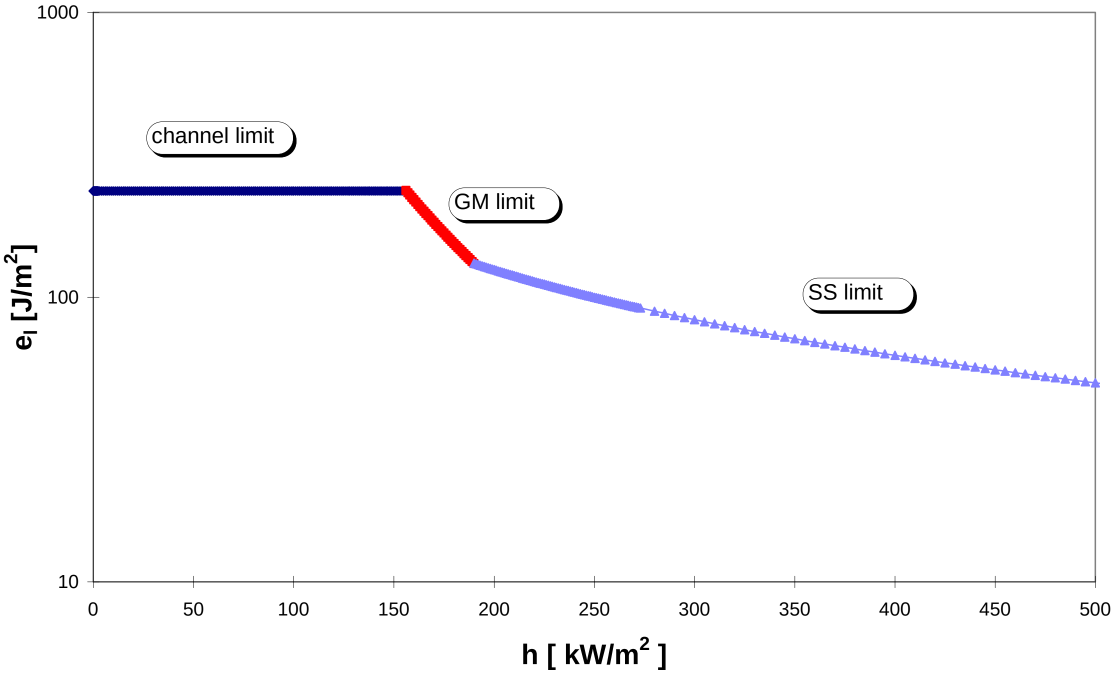

Figure 3.6-4: Energy limit e_l [J/m^2] versus h [kW/m^2]. Channel limit $e_{Cl}^{(II)}$ for L=1mm (236J/m^2), Gorter-Mellink limit $e_{GM}^{(II)}$ and second sound limit $e_{SS}^{(II)}$ as given in (3.6-9), (3.6-10) and (3.6-11). Intersection between Gorter-Mellink and second sound limit at h_{Ki}=190kW/m^2.

The program has a special function to prevent from a recovery from film-boiling, which seems unlikely in the here regarded time-scale.

3.7 The Initial Heat Pulse

The initiating disturbance is a Gauss-shaped power function H_{ini} (3.7-1), extended 1.5X_{ini} to the right and 1.5X_{ini} to the left and with 1.5T_{ini} as full width in time. The program calculates the amplitude of the Gaussian H_{0ini} (3.7-3) according to the total energy Q_{ini} [J] (3.7-2). The exponent n (usually 5-10) fits the Gaussian to various shapes.

$$H_{ini} = H_{0ini} e^{-\left(\frac{t}{T_{ini}}\right)^n} e^{-\left(\frac{x}{X_{ini}}\right)^n} \quad [W] \tag{3.7-1}$$

$$Q_{ini} = \frac{1}{3X_{ini}} \iint H_{ini} dtdx \quad [J] \tag{3.7-2}$$

$$H_{0ini} = \frac{Q_{ini} 3X_{ini}}{\iint e^{-\left(\frac{t}{T_{ini}}\right)^n} e^{-\left(\frac{x}{X_{ini}}\right)^n} dtdx} \quad [W] \tag{3.7-3}$$

$$q_{ini} = \frac{H_{ini}}{V} = \frac{H_{ini}}{3X_{ini} A} = \frac{Q_{ini} e^{-\left(\frac{t}{T_{ini}}\right)^n} e^{-\left(\frac{x}{X_{ini}}\right)^n}}{A \cdot 2 \int_0^{1.5T_{ini}} \int_0^{1.5X_{ini}} e^{-\left(\frac{t}{T_{ini}}\right)^n} e^{-\left(\frac{x}{X_{ini}}\right)^n} dtdx} \quad \left[\frac{W}{m^3}\right] \tag{3.7-4}$$

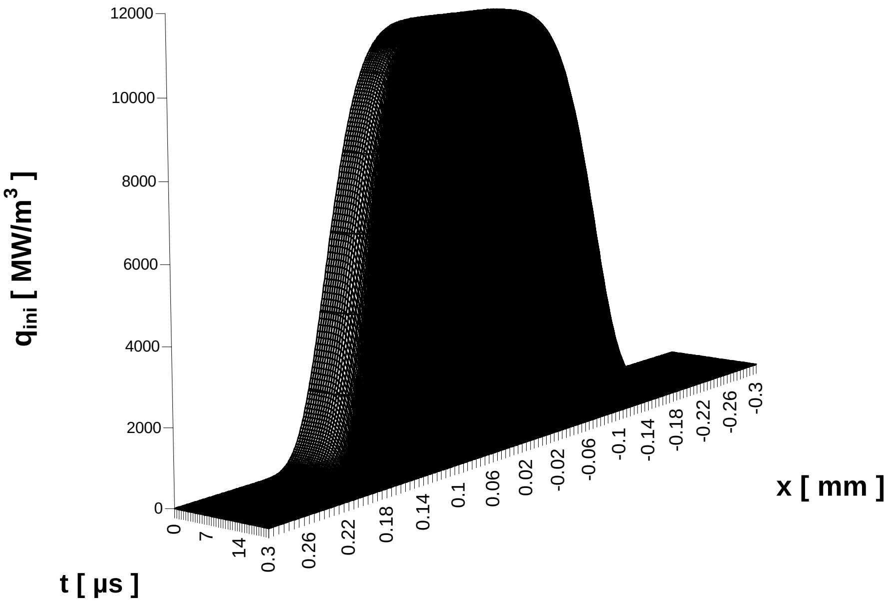

Figure 3.7-1: Initial heat pulse with Q_{ini}=100μJ, T_{ini}=10μs, X_{ini}=150μm (heater-dimension ~ 0.4mm), exponent n=6, reference wire, square pulse, 1MW/m^3=1mW/mm^3! The heat generation in LHC strands due to current sharing is of the order of 50mW/mm^3!

A further step to improve the simulation with respect to the experimental reality would be to include a thermal model of the heater in the program.

3.8 Further Notice on the Program

3.8.1 Fortran Routines

The Fortran code of the stability program consists of nine routines. There are several FORTRAN projects like e.g. 1wiresuperfluid (1wsflongheat, 1wsfTres,..) and 1wirepoolboiling. They differ with respect to some routines. The most important routine apart from the main routine MAIN1HA is PDEDEF1H, which prepares the data for the D03PHF-NAG-library-routine.

ROUTINE	FUNCTION
MAIN1H6	reads the input data from input1h.dat, prints back the input data to inpbak1h.dat, prepares varying space mesh, iterates in space and iterate in time calling NAG-D03PHF partial-differential equation solver, handles the automated quench seeking and the full MQE-curve loop, and prints the output data;
BNDARY1H	to fix boundary conditions
CONDUC1H	calculates k(T)
PDEDEF1H	supplies the functions P_{ij}, Q_i and R_i to the NAG routine D03PHF and therefore uses the subroutines calculating k(T), c_p(T), h(T,q), r(I,T) and q_{ini}.
QINI1H	calculates initial heat pulse profile in time and space
RESWSF1H	calculates total wire resistance per unit length r(I,T(x,t))
SPCHTR1H	calculates specific heat c_p(T,B)
F1SHT	calculates heat transfer function h [W/m^2] for subcooled liquid helium at ~1.9K
F1BHT	calculates heat transfer function h [W/m^2] for pool boiling liquid helium at ~4.2K
NAGLIB	routine D03PHF solves one dimensional heat balance equation for T(x,t) and calculates q [J/m^2].

Table 3.8-1: List of Fortran routines that have to be included in the project. The cooling routines are different in HeI and HeII (F1BHT or F1SHT).

The main routine MAIN1H6 handles the reading and sending of the input data and the quench searching routine. Therefore it features an iteration in time, calling the partial-differential-equation-solving routine D03PHF which solves the heat balance equation (3.1-1) for the whole interval in space. For each time point the D03PHF output consists mainly of the temperature T and the heat transferred to the coolant q. If the maximum temperature has been exceeded the main routine interrupts the calculation and copies the T/q-profiles obtained when the temperature excess occurred onto the array for all further time points. Once D03PHF has solved the problem a part of the main routine determines whether the temperature at the outer end of the wire coincides with the quench (THETQ, usually T_b+2K) or the no quench (THETNQ, usually T_b) criterion. According to the outcome of this test a decreased or increased initial pulse energy (usually half between last quench and last non quench case) is fed into a new calculation round as long as the maximum number of cycles has not been reached or as long as the difference between the quenching and the non-quenching pulse energy is greater than FTOL(usually 1%). If the duration of simulation has been chosen too short to allow for the quench and no quench temperatures in the central point of the wire to be different a “quench undetermined” message appears and the calculation is interrupted. The NAG routine D03PHF integrates a system of linear or nonlinear parabolic partial differential equations in one space variable. D03PHF has been designed for equations of the type (3.8-1) and (3.8-2).

$$P_{1,1}\frac{\partial U_1}{\partial t}+P_{1,2}\frac{\partial U_1}{\partial t}+Q_1=x^{-m}\frac{\partial}{\partial x}\left(x^m R_1\right) \tag{3.8-1}$$

$$P_{2,1}\frac{\partial U_2}{\partial t}+P_{2,2}\frac{\partial U_2}{\partial t}+Q_2=x^{-m}\frac{\partial}{\partial x}\left(x^m R_2\right) \tag{3.8-2}$$

These two partial differential equations ((3.8-1), (3.8-2)) can be adjusted to the basic equations (3.1-1) (heat balance equation) and (3.1-2) (calculation of cumulative heat transferred to helium) with a suitable definition of $P_{i,j}$, Q_i and R_i, supplied in the subroutine PDEDEF1H (Table 3.8-2). The evaluation of the terms $P_{i,j}$, Q_i and R_i is done approximately at the mid-points of the mesh x_i by calling the routine PDEDEF1H for each mid-point in turn. The functions c_p, k, h, and r are calculated by separate routines as indicated in Table 3.8-1. The boundary conditions have to be specified in the subroutine BNDARY1H according to the scheme in (3.8-3):

Function	specified
$P_{1,1}$	c_p
$P_{1,2}$	0
$P_{2,1}$	0
$P_{2,2}$	1
Q_1	$-I^2r/A-q_{ini}+hp/A$
Q_2	-h
R_1	$k(\partial T/\partial x)$
R_2	0
U_1	T
U_2	q
m	0

Table 3.8-2: Functions $P_{i,j}$, Q_i, R_i for NAG

$$\beta_i(x,t)R_i\left(x,t,T,\frac{\partial T}{\partial x}\right)=\gamma_i\left(x,t,T,\frac{\partial T}{\partial x}\right)\qquad i=1,2 \tag{3.8-3}$$

where $\beta_1=\beta_2=1$ and $\gamma_1=\gamma_2=0$. The boundary condition for i=1 fixes zero temperature gradient at the left- and right hand boundaries whereas the second equation is trivial. The system of equations ((3.8-1), (3.8-2)) transforms into a system of 2·NPTS (Number of points in space) ordinary differential equations using the central, three point finite-difference formula. It is then integrated forwards in time using a backward differentiation formula method. NCODE is set to zero and the user supplied routine ODEDEF becomes by default the dummy routine D03PCK.

3.8.2 Discretization

The (constant) time step has to be set by the user (total simulation time of $N_t\Delta t$). The NAG-routine internally varies the space mesh. The space step given in the input sheet defines the output-points. A variable mesh is used to increase calculation speed. The meshing in space is split into two parts, with a close and constant spacing Δx_l from point one to N_l and then a linearly increasing spacing from Δx_l at N_l+1 to Δx_u at N. The size of the calculation length, x_{max} to the left and to the right, can be calculated with (3.8-4).

$$x_{\max} = \Delta x_l\left(N_l - 1\right) + \frac{\Delta x_u - \Delta x_l}{\left(N - N_l\right)}\left[\frac{(N-1)^2}{2} - \frac{N_l^2}{2} - N_l(N-1) + N_l^2\right] \tag{3.8-4}$$

The length x at point j with $j \in (1,N_l)$ is

$$x(j) = \left(j-1\right)\cdot \Delta x_l \qquad , \tag{3.8-5}$$

whereas j with $x \in (0,(N_l-1)\Delta x_l)$ is

$$j(x) = \frac{x}{\Delta x_l} + 1 \qquad . \tag{3.8-6}$$

The length x at point j with $j \geq N_l+1$ is given in (3.8-7).

$$x\left(j\right) = \Delta x_l\left(j-1\right) + \frac{\left(\Delta x_u - \Delta x_l\right)}{\left(N - N_l\right)}\left[\frac{\left(j-1\right)^2}{2} + \frac{N_l^2}{2} - N_l\left(j-1\right)\right] \tag{3.8-7}$$

The index j in the x range $[N_l\Delta x_l, X_{max}]$ is given in (3.8-8).

$$j(x) = N_l + 1 - \frac{\Delta x_l\left(N - N_l\right)}{\Delta x_u - \Delta x_l} + \sqrt{\left(\frac{\Delta x_l\left(N - N_l\right)}{\Delta x_u - \Delta x_l}\right)^2 + \frac{2\left(N - N_l\right)}{\Delta x_u - \Delta x_l}\left(x - N_l\Delta x_l\right)} \tag{3.8-8}$$

The increment in x, Δx is Δxl for $j \in [1,N_l]$, whereas it is

$$\Delta x\left(j\right) = \frac{1}{\left(N - N_l\right)}\left[\Delta x_u\left(j - N_l\right) + \Delta x_l\left(N - j\right)\right] \tag{3.8-9}$$

for $j \in [N_l+1,N]$.

Another version of the program (1wsflongheat) uses a decreasing space mesh instead of an increasing. In this case all terms Δx_u-Δx_l have to be taken as absolute values in above mentioned formulae. A rule of thumb to obtain a reasonable value for N_t and N is to make use of an approximate value for the quench propagation velocity: $x_{max}=v_q t_{max}$.

3.8.3 Automated Quench Seeking

MQE is found by solving repeatedly with different Q_{ini} and finally taking the mean between two pulses ~ 1% apart which either just quench or just recover. Apart from the initial input-value Q_{ini}, the relevant parameters for the automatic quench seeking routine are the fractional change in energy per cycle, the number of cycles per run, a criterion for quench/no quench (which is normally a temperature criterion), the maximum allowable difference between the initial energies of the quench and the no quench case and a maximum temperature option to avoid unnoticed excess of the range of validity of the program. The criterion for quench or recovery is given by the temperature at x=0 of the last point in time exceeding a given value (typically T_b+2K). Therefore one has to take care that the calculation has been pursued far enough in time to distinguish between T(x,t) in quench and no-quench case. The program can calculate a full MQE curve iterating through I_{high} and I_{low} in steps of $0.05I_c$.

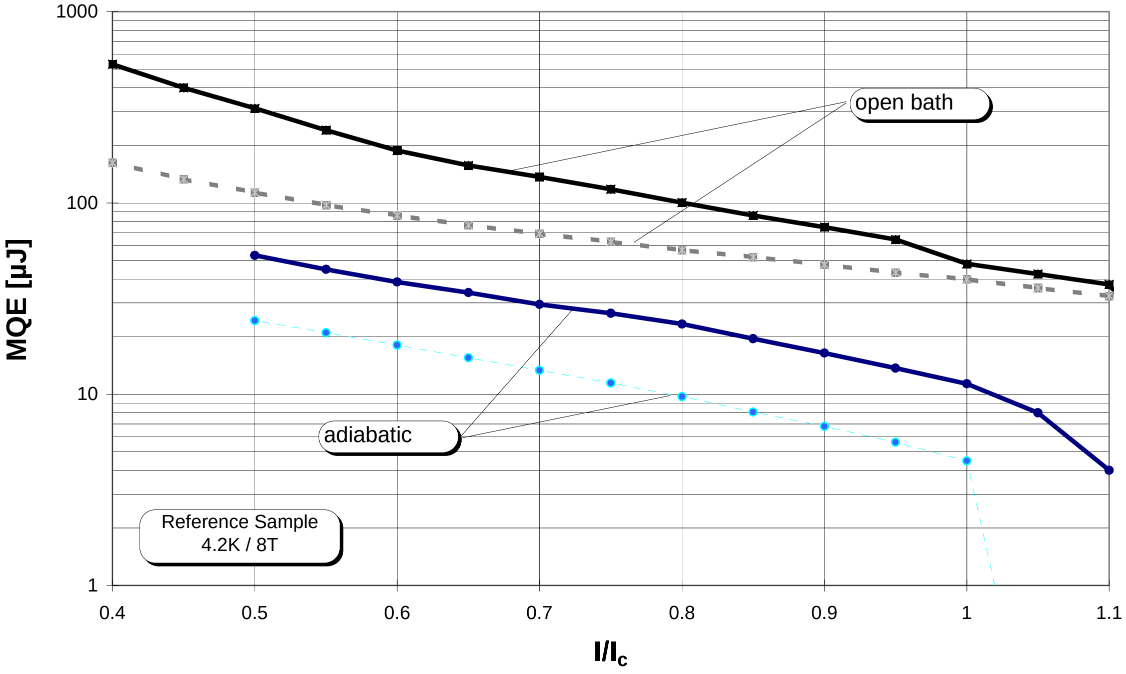

Figure 3.8-1: Comparison Measurement and simulation (dashed) of MQE at 4.2K / 8T, reference sample, I_c≈350A, ρ_{Cu}(8T)≈5.14·10^{-10}Ωm. The general agreement of measurement (uncalibrated!) and simulation is satisfactory, the spread of factor 2 can be explained by loss from the heater to the environment. The experimental case deviates from the simulation stronger with decreasing current because of increased absolute heat loss at higher pulse energy.

3.9 Quench Voltage

An important element in a MQE measurement set-up (Figure 3.9-1) is the array of voltage taps to observe the dynamics of quench and recovery and to monitor quench propagation: there is one voltage tap around the heater, called V_{q1}, and a second adjacent, V_{q2}, both of some cm length (e.g. l=2cm).

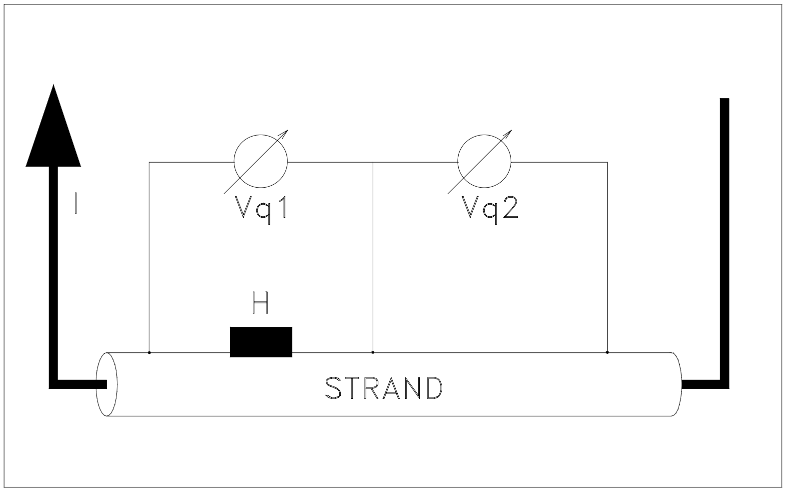

Figure 3.9-1: MQE-voltage taps: V_{q1} voltage over heater H, V_{q2} adjacent voltage tap. V_{q1} is used to detect the quench, V_{q2} is used to measure quench propagation velocity.

The program calculates the quench voltage from the heat generation function g(W/m^3).

$$V_q\left(j_t, T_s\right) = \frac{g\left(j_t, T_s\right)Al}{I_{tot}} = V_q(t) \qquad [V] \tag{3.9-1}$$

$$V_{q1}(t) = 2\frac{A}{I_{tot}}\int_0^{l/2} g\left(j_t(x,t), T_s(x,t)\right)dx \qquad [V] \tag{3.9-2}$$

$$V_{q2}(t) = \frac{A}{I_{tot}}\int_{l/2}^{3l/2} g\left(j_t(x,t), T_s(x,t)\right)dx \qquad [V] \tag{3.9-3}$$

Figure 3.11-8 shows a typical quench voltage simulation for the reference wire (l=2cm). The quench voltage curves contain information about $\rho_{Cu}(B)$ (plateau), v_q (slope) and quench decision time (quench decision length). The struggle of cooling and heating after the initial heat pulse are reflected in the initial part of V_{q1}. As can be seen from the simulation in Figure 3.11-8 the voltage trace reflects that moment of indecision: First the voltage rises as a consequence of the initial heat pulse which together with Joule heating in the matrix causes a strong initial temperature rise (up to 20K and higher). Then, after the end of the pulse, it shortly settles down before it either irrevocably pursues its rise or before it recovers. The initial part of V_{q1} can be characterized by the quench decision time and the quench decision voltage. The quench decision voltage can be converted to a quench decision length (= the length of a normal zone at $T_c<T<15K$ which produces the quench decision voltage), which is an approximation of the MPZ length. Figure 3.9-2 shows the quench decision length of the reference strand in 4.2K/8T conditions (measured and calculated).

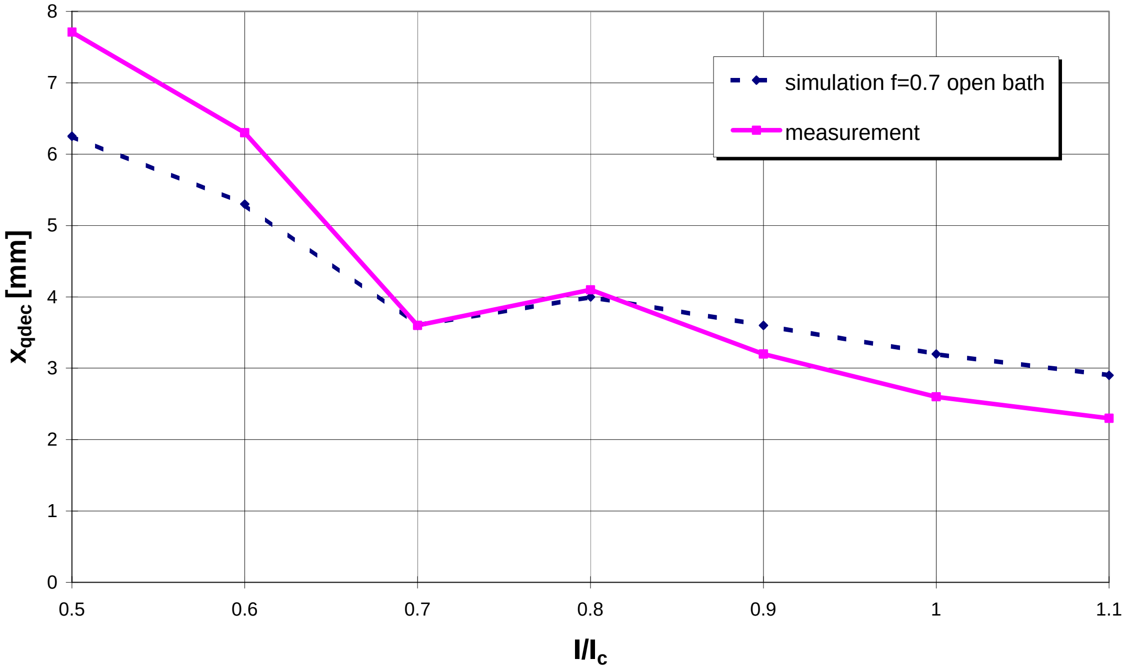

Figure 3.9-2: Simulation (dashed) versus measurement(full line): Reference Wire 4.2K/8T, pool-boiling He I, quench decision length;

3.10 Quench Propagation Velocity

During the first moments after the pulse the temperature profiles are δ-shaped. Going further in time they flatten as a result of heat conduction and cooling. The quench velocity is a rapidly changing function, eventually going through a (negative) minimum. Some mm from the heater and some 100µs after the pulse, the T-profiles become flat Gaussians (Figure 3.10-1). In the quench case they are growing steadily in width and height. The quench velocity has become constant. Therefore v_q has to be measured far from the heater. The quench propagation velocity can be obtained from the slope of $V_{q2}(t)$:

$$v_q = \frac{A_{Cu}}{\rho'_{Cu} I_{tot}} \cdot \frac{dV_{q2}}{dt} \qquad \left[\frac{m}{s}\right] \tag{3.10-4}$$

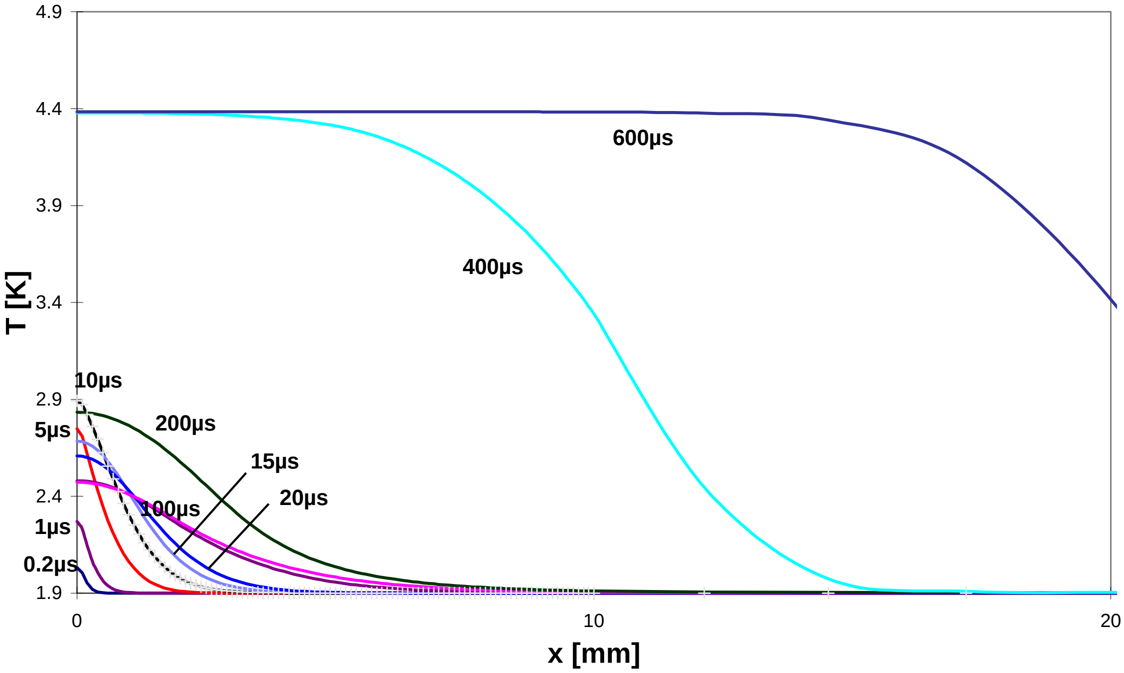

Figure 3.10-1: Temperature profiles in a strand after a quenching perturbation, Reference wire MQE simulation, 1.1Ic, test conditions (f=70%, infinite bath), 1.9K / 11T

In general the correspondence between measured and simulated quench velocities is fair:

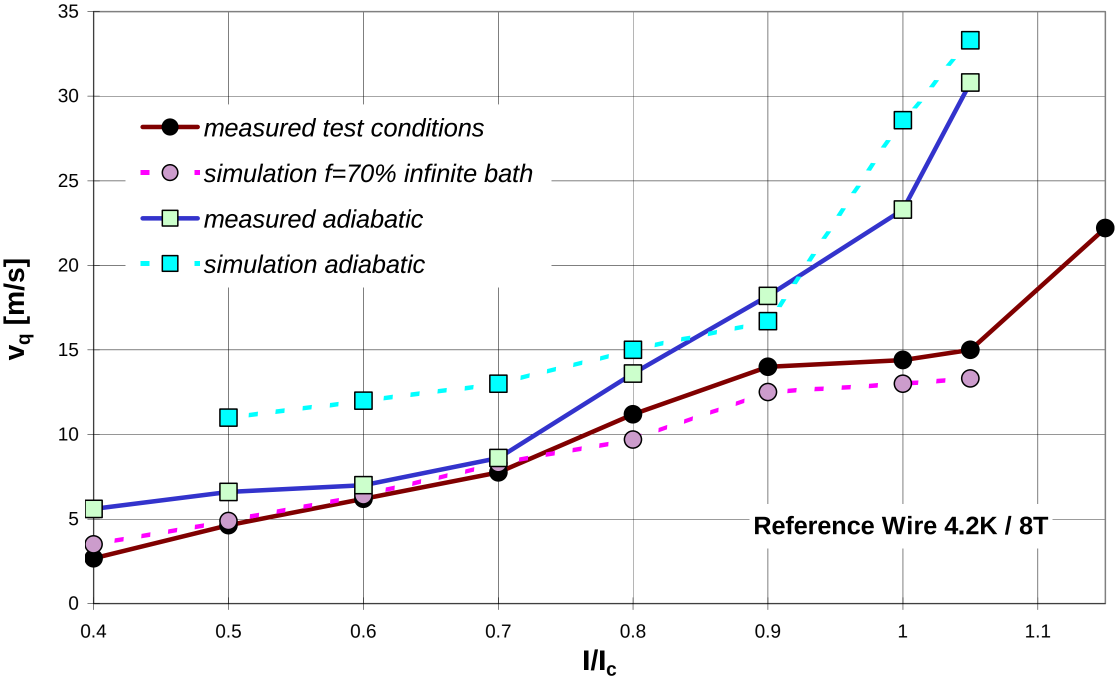

Figure 3.10-2: Comparison measurement / simulation of quench propagation velocity, Ref wire; The agreement of measurement and simulation, especially in pool-boiling conditions is satisfactory.

3.11 Reference Wire MQE Calculations

Of major interest, especially in the definition of the experiment, is the optimal duration of the initial heat pulse. Both experiment and simulation indicate that MQE is approximately independent of pulse time t_{ini} in the range 0-100μs (Figure 3.11-1).

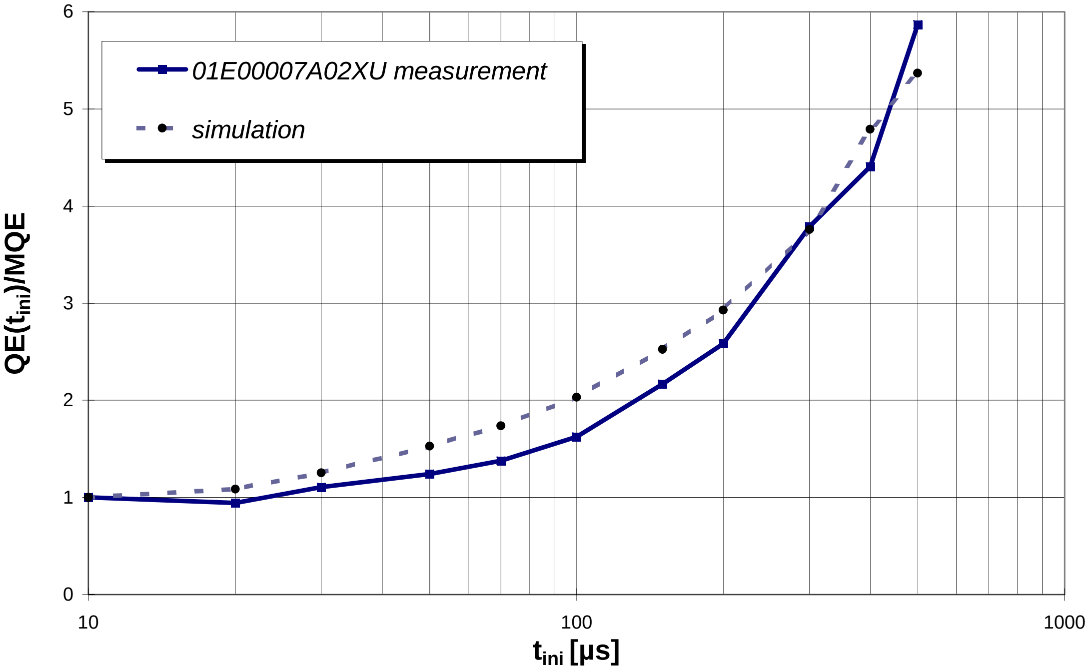

Figure 3.11-1: QE normalized on MQE (=QE(t_{ini}=10μs)) versus pulse duration t_{ini} , comparison between measurement on sample 01E00007A02XU (line) and simulation (dashed). 9T, 1.9K, 0.9I_c (I_c=755..4A), f=0.7, L→∞ ("open bath"), $\rho_{Cu}=5.2\cdot10^{-10}\Omega$m, heater diameter: 300μm

3.11.1 A Model Case

The following presents a MQE simulation for the reference strand (see chapter 4) carrying I_c (=369A) in 1.9K / 11T conditions. The following plots show the program output for T(x,t) and q(x,t) as well as auxiliary functions like cooling h(x,t), heat generation g(x,t), the voltages V_{q1}(t) and V_{q2}(t). The initial energy pulse is Gauss-shaped (n=6) with a duration of t_{ini}=10μs and half pulse width x_{ini}=0.15mm. The cooling parameters were set to open bath values (channel length to 5cm) and cooled perimeter fraction to 70%. The computed MQE is 5μJ. The quench goes through a metastable transition (2×2.5mm). The metastable normal zone expands slowly (~15m/s, compared to the normal quench propagation velocity v_q=60-80m/s). Its temperature is T=4.11K and the equilibrium heat flux h~ 50 kW/m^2. It is just a question of time before the cooling capacity of the cryogen is used up, here approximately 40ms. Figure 3.11-2 shows the simulated temperature profiles in space and time: the just not quenching case recovers during the first few hundred microseconds.

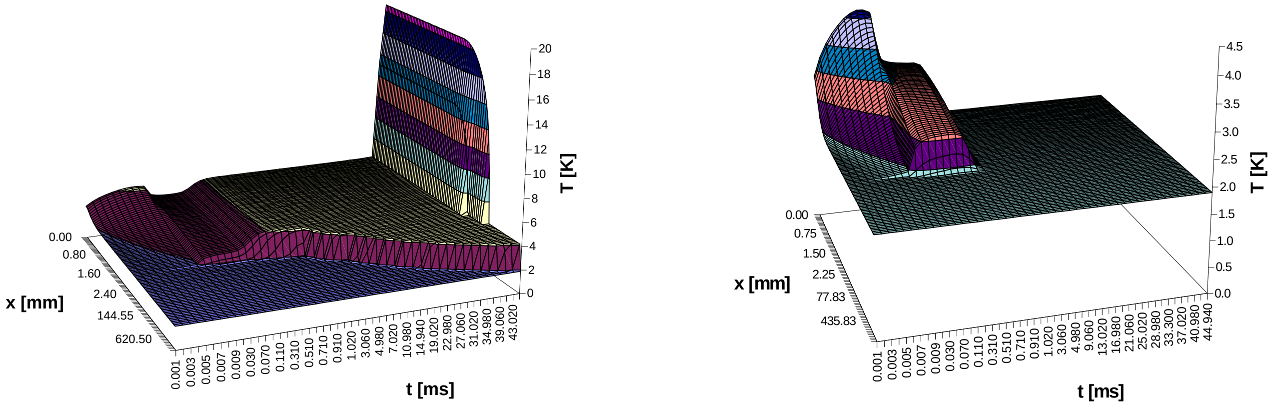

Figure 3.11-2: Temperature profile, Reference strand MQE simulation: quench (left) / no quench (right) case, I_{tot}/I_c=1, T_b=1.9K, B=11T; The initial pulse triggers a normal zone at 4.11K (T_c=4.25K). This normal zone slowly expands. The final temperature rise occurs as a result of the sudden onset of burn-out along parts of the strand. In the non quench case the wire recovers after 700µs.

The plots for the cumulative heat transferred to helium in [J/m^2] in the quench and the no quench case (Figure 3.11-3) show that the recovering case consumes only a negligible fraction of the cooling potential, which means that a much smaller helium volume would have served the same purpose.

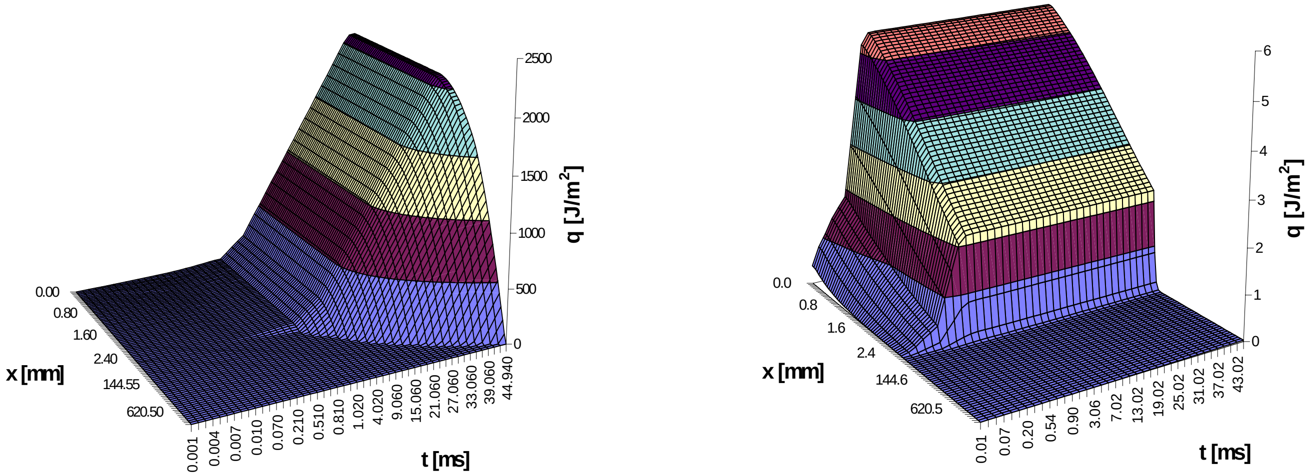

Figure 3.11-3: Cumulative heat transferred in [J/m^2] to helium, quench (left) and non quench (right) case, Reference wire MQE simulation: I_{tot}/I_c=1, T_b=1.9K, B=11T; The rate of heat transferred to the cryogen becomes important during the plateau phase. The initial pulse and the establishment of the metastable normal zone involve only a small rate of heat transfer. The scale of the non-quench plot is a factor 1000 smaller than in the quench case plot.

The heat generation per unit of cooled surface (Figure 3.11-4) goes through a first peak (at ~ g_c=53kW/m^2), then part of the current returns into the superconductor. In the quench case the recovery tendency is of short duration. The cooling curves in Figure 3.11-5 are similar to the heat generation plots. But at the onset of film-boiling in the quench case the cooling goes back to almost zero giving way to the quench.

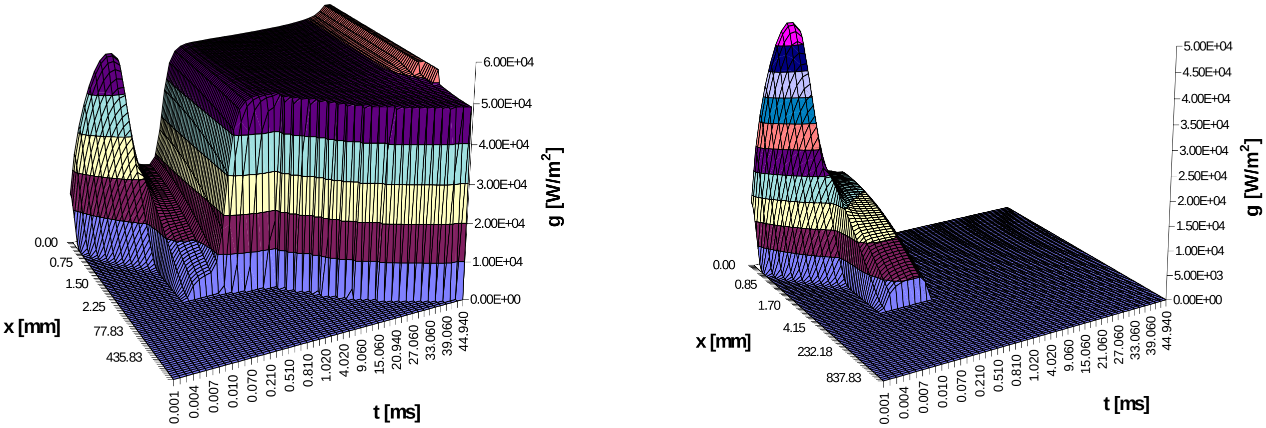

Figure 3.11-4: Heat generation in [W/m^2], quench (left) and no quench (right) case, Ref. strand MQE simulation: I_{tot}/I_c=1, T_b=1.9K, B=11T; A first heat generation peak after the initial pulse the temperature returns to almost T_b. The recovery is short in the quench case: a heating rate of 49kW/m^2 is maintained until burn-out, when the generation rises to its critical value of 53kW/m^2.

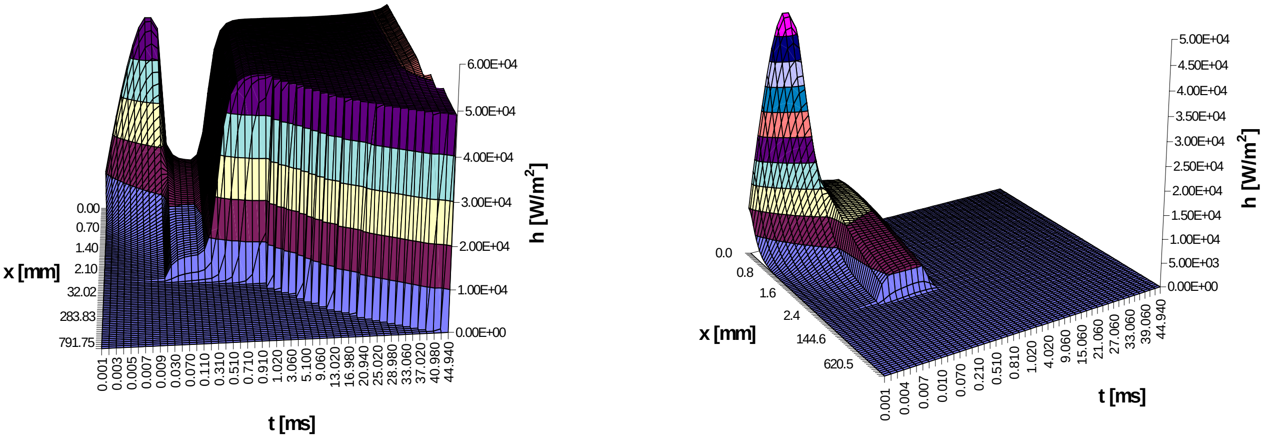

Figure 3.11-5: Cooling in [W/m^2], quench/no quench case, Reference wire MQE simulation: I_{tot}/I_c=1, T_b=1.9K, B=11T; The heat transfer flux during the metastable temperature plateau is ~49kW/m^2. Burn-out occurs after 42ms (film-boiling at ~2-3kW/m^2). The quench propagates with 80m/s.

A particularity of the here presented case is that the strand temperature at the metastable plateau can be explained in terms of the intersection of steady state cooling and heat generation (Figure 3.11-6). Unexpectedly this steady state approach applies successfully to the present situation, where at a heating rate of 49kW/m^2 cooling and heating are in equilibrium at a surface temperature of 4.11K.

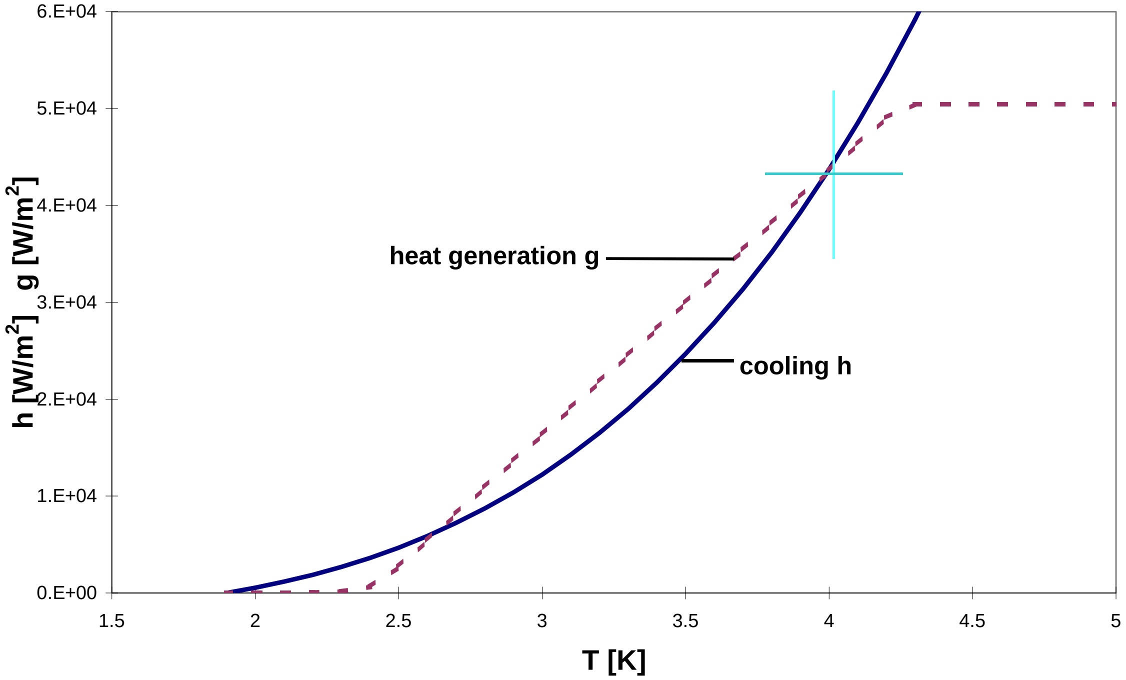

Figure 3.11-6: Reference strand MQE simulation (I_{tot}/I_c=1, T_b=1.9K, B=11T). The metastable plateau occurs when heating and cooling cross at 4K and 44kW/m^2.

The current in the superconducting branch is shown in Figure 3.11-7. Since no inductive phenomena are taken into account I_{sc} immediately shapes to the local temperature.

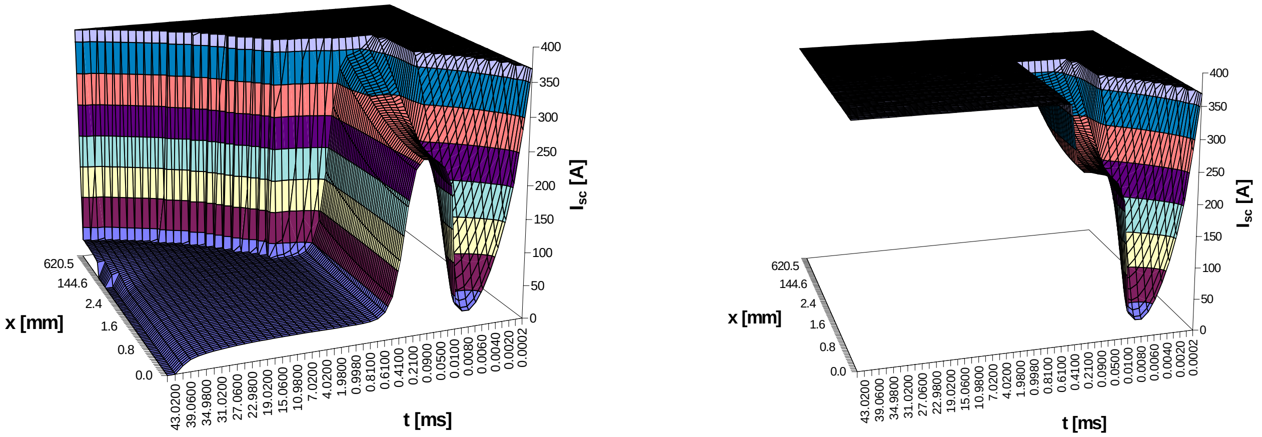

Figure 3.11-7: Current in the superconductor in the reference wire MQE simulation, quench case: I_{tot}/I_c=1, T_b=1.9K, B=11T; The superconductor current during the plateau phase is not zero, but approximately 30A. During the pulse the pulsed region becomes normal-conducting, followed by a partial recovery. Then the temperature is raised again to almost critical.

The superconductor current in the initially heated part drops to zero at t_{ini}. After a short recovery I_{sc} drops again, the last current-fraction escapes the superconductor in the very last moment during the quench. Figure 3.11-8 shows the voltages V_{q1} and V_{q2}. The plot ends at 2.5ms, which is approximately the time at which the metastable plateau has been established over the whole length (±3cm) of tap1 and 2. T_{plat} is just 0.14K below T_c (V_q~V_{qmax}). V_{q1} of the no quench case comes back to zero within 500µs. In the non-quench case the perturbation never reaches V_{q2}.

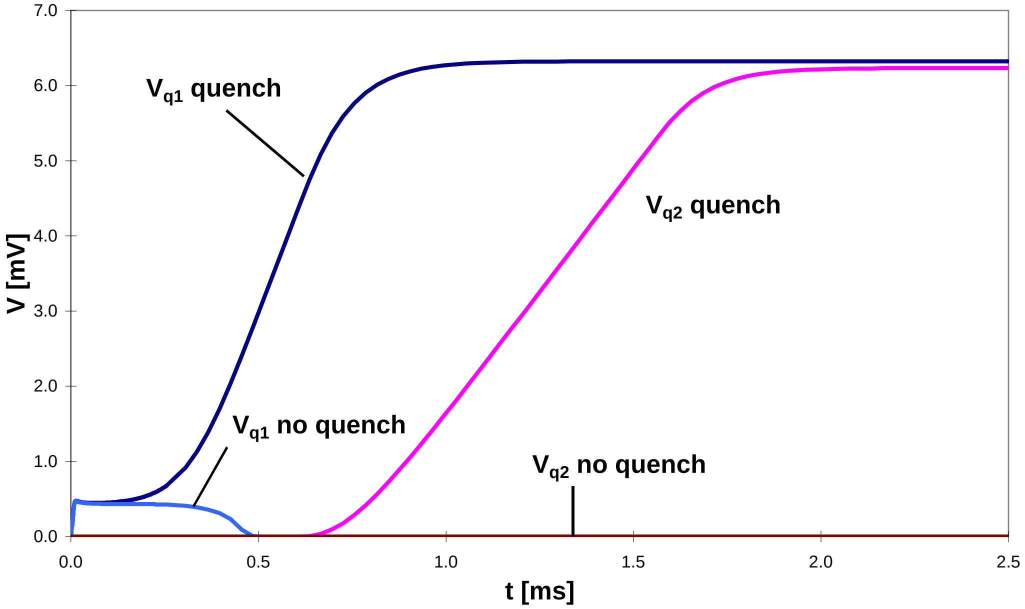

Figure 3.11-8: Voltage on tap1 (central) and tap2 (adjacent), l=2cm, Ref. strand simulation: I_{tot}/I_c=1, T_b=1.9K, B=11T; V_{q1} shows the quench decision process during 200µs.

The next fig. shows the history of heat transfer to helium in the central point (x=0). Film-boiling is triggered when after 41ms the cumulated heat intersects with the GM-limit.

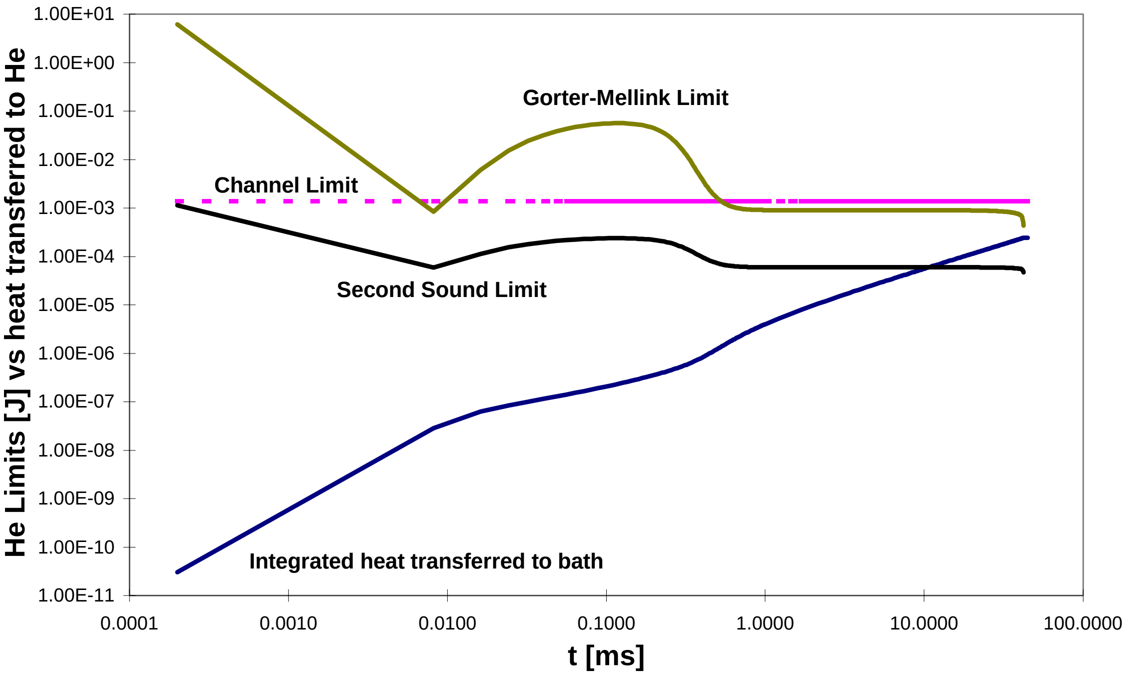

Figure 3.11-9: Limits of transient cooling compared to heat transferred to helium, all in [J], in the central cell (~50µm): ref. strand simulation, I_{tot}/I_c=1, T_b=1.9K, B=11T; Channel limit, being far

out of reach in the present channel (5cm length, base $\pi df\Delta x_l$, V=5.6mm^3, E_{chlim}=1.4mJ); the Gorter-Mellink limit, which triggers burn-out in this particular case after 41ms; the Second Sound limit crossed at t=10.8ms but it doesn't apply because h is smaller than the 190kW/m^2 threshold (see chapter 3.6.2).

3.11.2 Calculation versus Measurements

The agreement of simulation and measurement in the case of pool boiling HeI is fair (see e.g Figure 3.8-1, Figure 3.11-10, Figure 3.9-2, Figure 3.8-1).The discrepancy of ~50% in Figure 3.8-1 can be explained by heat loss in the non-calibrated heater system.

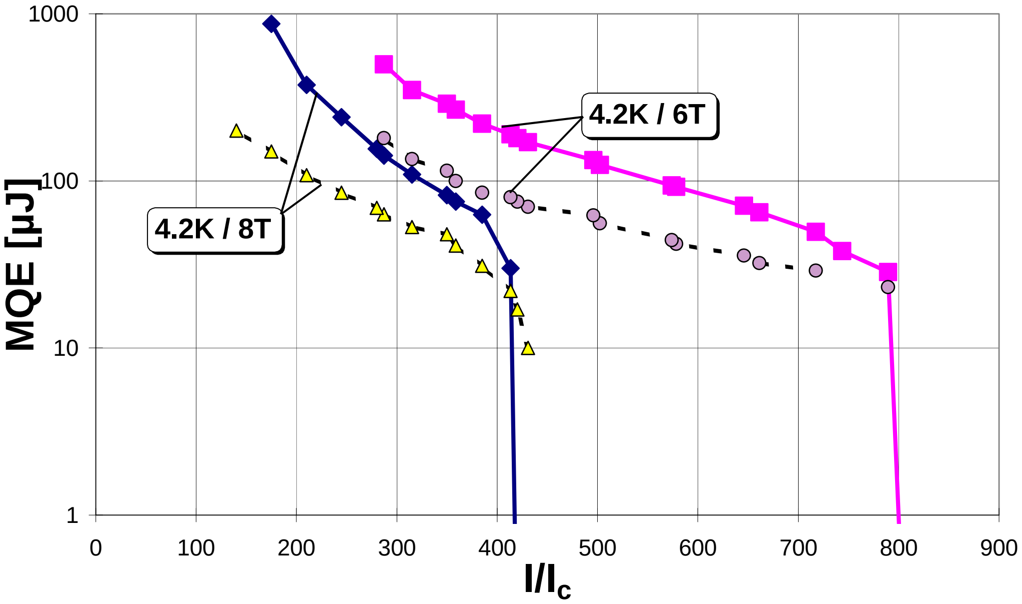

Figure 3.11-10: Comparison measurement (lines) and simulation (dashed), MQE reference strand in open bath conditions in pool boiling HeI at 4.2K, 6 and 8T.

Figure 3.11-12 shows a MQE measurement/simulation comparison for a typical LHC strand at 1.9K/9T. At 1.9K simulations tend to agree less with the measured curves, except for the adiabatic condition, where again the factor 2 difference appears. The simulations fit the measurements in what refers to the onset-current of the superfluid enhancement. This hints towards a good agreement of the model parameters for the heat transfer coefficients (a_K, a_{fb}, f) with reality. The discrepancy is related mainly to the amplitude of the superfluid enhancement. A more detailed analysis (see chapter 3.11.4.1) will show that this is related to an insufficient burn-out limit parameters. As already mentioned in chapters 3.1 and 3.6 this is related to the inadequacy of the 1-dimensional model of heat transfer to superfluid helium. At a heater loss rate of 50 % the agreement of simulation vs. measurement requires increased burnout limits (Table 3.11-1).

	a_K [W/K^4/m^2]	a_{fb} [W/K/m^2]	f [%]	K_{SS} [J^2/s/m^4]	K_{GM} [sW^4/m^8]
standard	180	250	90	**$2.5\cdot10^7$**	**$9\cdot10^{17}$**
proposal	180	250	90	**$50\cdot10^7$**	**$150\cdot10^{17}$**

Table 3.11-1: Parameters for heat transfer to superfluid helium, standard and increased to make simulations agree with measurements.

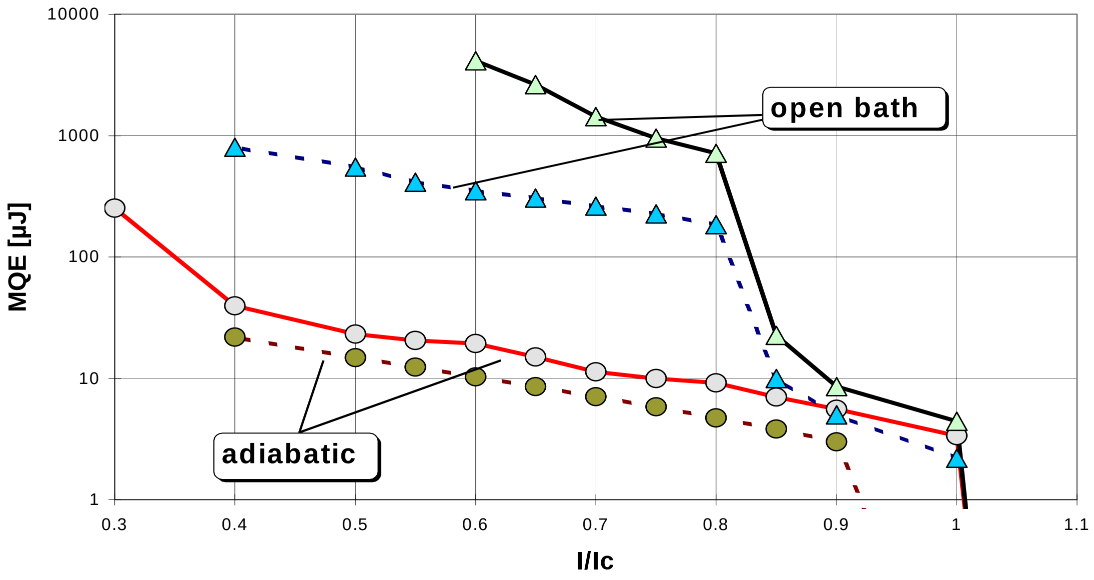

Figure 3.11-11: Simulation (dashed) and measurement (full) of MQE(I/Ic), sample 01B00017A06Y, 1.9K,9T, in adiabatic and open bath conditions. Simulation with "standard" cooling parameters (f=90%, v=∞ (channel length 5cm)) as given in Table 3.11-1. The good agreement of simulation and measurement in superfluid enhancement onset current in open bath conditions hints towards the agreement of model and real heat transfer properties a_K and a_{fb} and/or f. The difference in superfluid enhancement amplitude remains the weak point of the model (see Figure 3.11-12). The heat loss in the experimental system can be estimated from the comparison of simulated and measured MQE curves in adiabatic conditions (~ factor 2 discrepancy).

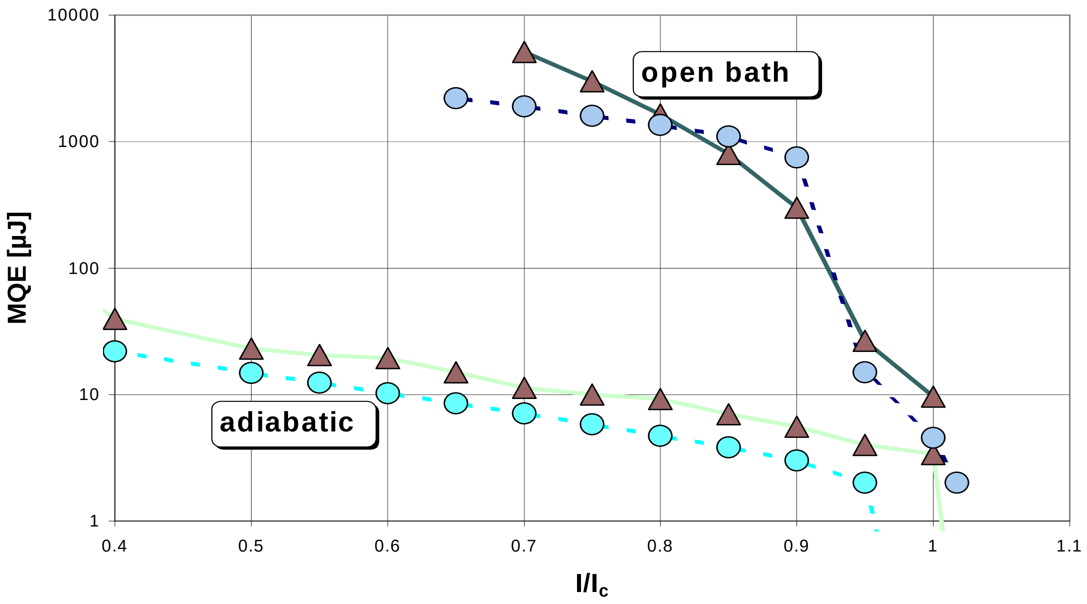

Figure 3.11-12: Measurement (full line) and simulation (dashed), 01B00017A06Y, 1.9K, 9T, adiabatic and open bath conditions. To fit the amplitude of the superfluid enhancement in the simulation to that in the measurements increased burn-out limit parameters had to be used (the heat transfer properties are kept the same as in Table 3.11-1).

3.11.3 Numerical versus Analytical MQE Models

Several analytical and phenomenological approaches to MQE can be found in the literature review (chapt. 2). In the following 2 analytical models are compared to the numerical model for the 1.9K/9T ref. strand case in adiabatic and open bath conditions.

Most of the adiabatic models presented in the literature review ([Buznikov 96], [Dresner 95], [Wilson 83]) have in common that they use averaged material properties (k, c_p). Figure 3.11-13 shows that a suitable choice for this properties (here k~200 W/K/m, c_p~2200J/K/m^3 corresponding to a temperature between T_b and T_{cs}) generates adiabatic MQE curves in accordance with numerical calculations. Therefore, taking into account the agreement of the adiabatic MQE curve generated with analytical and numerical models, the understanding of MQE in the adiabatic case as being roughly the enthalpy content of a hot zone with its hottest part at current sharing temperature, is justified. In the cooled case the analytical models presented in the literature review suffer not only an uncertainty related to the averaging of the material properties but also the inadequacy of the linear heat transfer concept. The comparison of a numerical simulation (1.9K/9T, reference wire, f=0.7, open bath) with the models presented in [Dresner 95] and [Buznikov 96] in Figure 3.11-13 reveals the differences: Dresner's model approaches the numerical outcome with the linear heat transfer coefficient set to 2000W/K/m^2, whereas in Buznikov's model even a 20000 W/K/m^2 is not sufficient to generate a MQE comparable to the numerical model. Whereas the former seems reasonable, taking into account that an average heat transfer coefficient comprises both film-boiling and Kapitza-like heat transfer, the latter is utterly high. Furthermore in Dresner's model the c_p of the composite

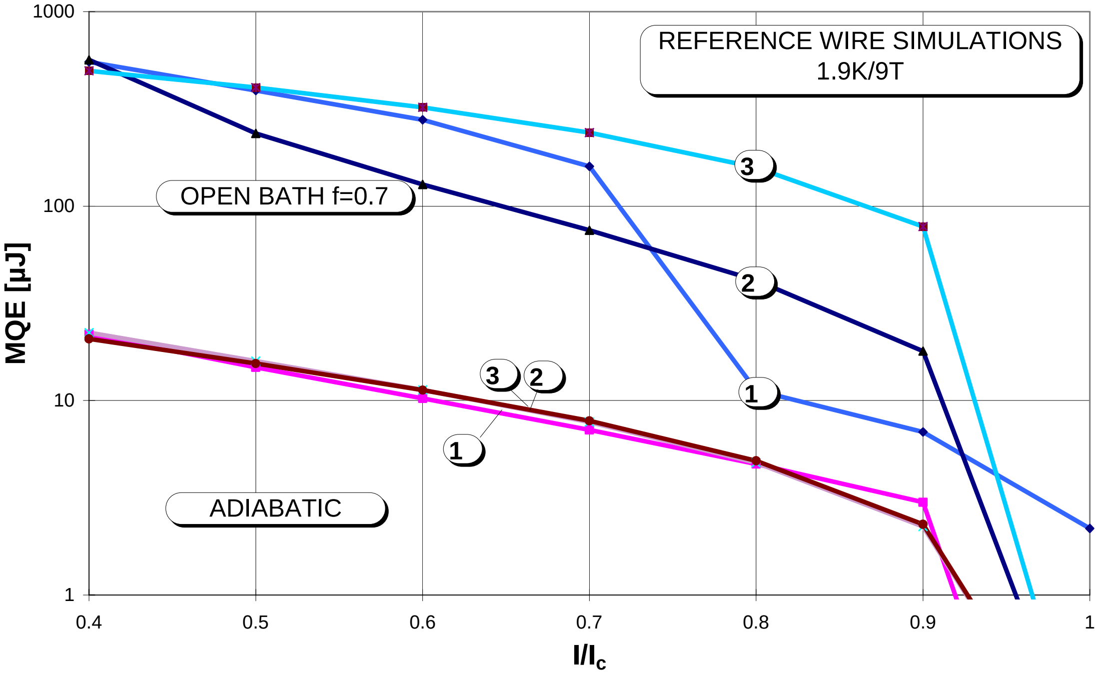

Figure 3.11-13: Comparison of analytical models with numerical MQE calculation. ① numerical stability program as described above; ② analytical model [Buznikov 96] ③ analytical model Dresner [95]; The models are described in detail in the literature review. Whereas the curves agree in the

adiabatic case, the differences in the cooling function have a strong impact on the shape of the MQE curve in cooled conditions.

has been averaged between T_b and 10K, whereas in Buznikov's model an average between T_b and 15K had to be inserted to achieve agreement between the models at low currents (where the analytical models are more reliable). While Dresner's model seems to be based on a valid approximation of the solution of the HBE, Buznikov's model underestimates the MQE, because he extrapolates the current sharing heat generation function to $T>T_c$. Obviously both models do not show the characteristic splitting in high current quasi-adiabatic behavior and low current "superfluid enhancement". This is caused by the fact that there is no unsteady jump from Kapitza-like heat transfer to film-boiling in the analytical models.

Considering the drawbacks, namely the uncertainty related to the use of averaged material parameter like k, c_p and the simplifications in the heat transfer implementation, analytical models are restricted to statements concerning the order of magnitude of MQE. Quench propagation velocity calculations (Figure 3.11-14) with the analytical model in [Dresner 95] require an unnaturally high linear heat transfer coefficient of 25 kW/K/m^2 to agree in order of magnitude with reality. The analytical model is unable to produce the shape of the experimental $v_q(i)$ relation. As indicated before in chapter 3.11.2 the weakness of the numerical model is quantitative rather than qualitative. The analytical model is too rough.

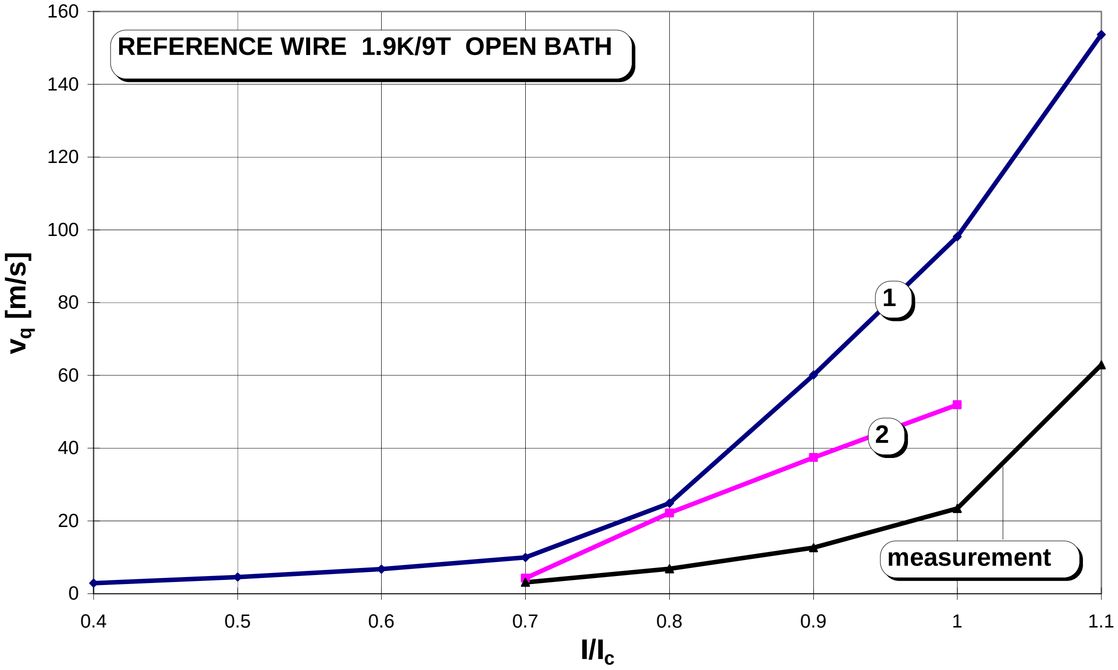

Figure 3.11-14: Comparing ① a numerical simulation with the program described in chapter 3.1 to 3.8 with ② an analytical calculation [Dresner 95] and a reference wire measurement in 1.9K/9T open bath conditions. The discrepancy between the different models and the measurement reveals the insufficiency of the cooling models.

3.11.4 The Effect of Different Parameters on the Minimum Quench Energy

B, T_b, d, A, n, k, c_p, I_c are fixed by LHC strand specification [CERN 95]. The so called design variables are out of the scope of a one-dimensional model. Therefore the parameters which can be varied are Cu/Sc-ratio, matrix-RRR and the variables related to cooling. The following deals with the effect of the these parameters on MQE.

3.11.4.1 Cooling Parameters

A brief look at the heat balance equation (3.1-1) shows that the strongest influence on MQE has to be expected from the cooling term. The MQE curves at 1.9K/9T in Figure 3.11-12 show large differences between the adiabatic and the open bath case (up to 100 times), giving a hint towards what can be achieved by increasing the cooling parameters f and v. MQE simulations in a highly confined environment (e.g. magnet), offering quite modest cooling conditions, give results which are hardly above the adiabatic minimum. A MQE(i) curve of a typical LHC-type strand cooled in an open bath of superfluid helium is characterized by the following parts (see Figure 3.11-12): A high current end which is essentially adiabatic and a lower current part showing superfluid enhancement. In a simplified view the quench energy of these two parts can be considered as proportional to the enthalpy reserve of the composite between T_b and T_{cs} for the adiabatic part and by the enthalpy reserve of the strand plus the enthalpy of the actively participating helium volume in the superfluid enhancement part. The superiority of the specific heat of helium versus that of the composite causes the huge increase of the MQE performance at currents below the superfluid enhancement onset current.

The cooling parameters f (cooled perimeter fraction) and v (voidage) stand for the surface heat transfer properties (Kapitza conductance) and the helium-volume in contact with the wire. The helium volume v is given in % of the conductor volume. In the present analysis f has been varied between zero and 500% of the wire perimeter $d\pi$. Alternatively this parameter-range could be converted to a variation of a_K (Kapitza conductance in $W/K^4/m^2$) at fixed f (e.g.: $f=0.15 \rightarrow a_K \in (0,6000 W/K^4/m^2)$. The idea behind setting f bigger than one, is that there are techniques to increase the active surface of the wire (e.g.: porous metal heat exchanger). One could as well argue that it represents coatings with a strongly varying Kapitza conductance, but a glance at Figure 3.6-1 reveals that the spread of Kapitza conductance is modest for “typical” coatings of strands. The voidage has been set to the following values: 0, 0.02, 0.04, 0.1, 0.5, 1=100%, 2). The channel width L can be calculated from f and v with (3.6-3).

In pool boiling conditions, e.g. at 4.2K/8T the increase of MQE with improved cooling parameters is in the range of 10-20 times the MQE in adiabatic conditions. The helium volume effect quickly saturates (at v~50%) as a consequence of the small diffusivity of helium I. Differently from the case of superfluid coolant the helium volume affects MQE over the whole current range in the same way, i.e. slightly raising the MQE. The results of the simulations suggest that this is caused by the fact that the helium I cases, independently of the current, always run into burn-out (Schmidt-limit) during the pulse. The simulated data for the total heat transferred to helium in the recovery case hardly rises above MQE. At the same time the peak temperatures in the non quench case exceed T_c (reaching up to 16K at $0.4I_c$ in the f=500%, v=50% case) over the whole current range.

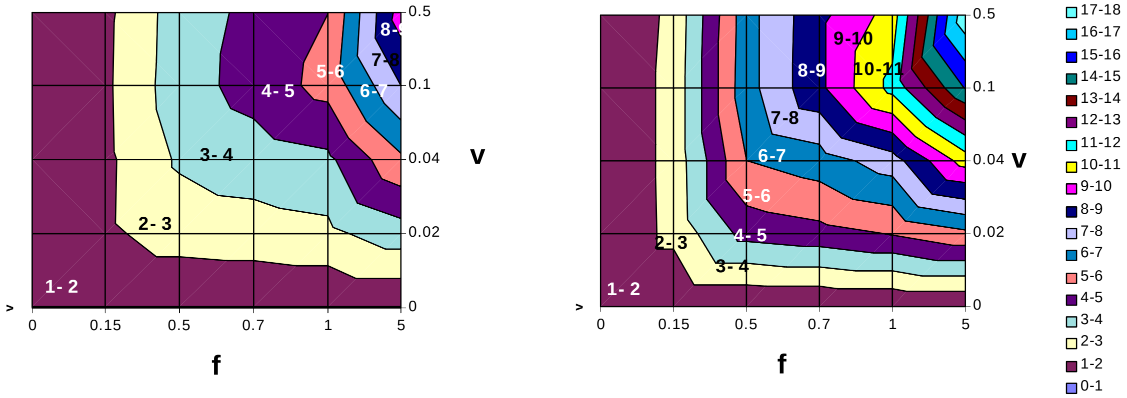

Figure 3.11-15: MQE normalized on the MQE in the adiabatic case as a function of cooled perimeter fraction f (1≡100%) and helium voidage v (1≡100%), reference strand simulations, 4.2K/8T. Left: 0.5I$_c$ case (MQE$_{adia}$=24μJ), right I=I$_c$ case (MQE$_{adia}$=5μJ).

This confirms the understanding of the pool-boiling case as independent of the actual helium volume (as long as v>2%). The effect of the cooled perimeter fraction f (or of the heat transfer coefficient) at a given helium volume is of the same type: a smooth increase in MQE with enhanced f at a given v. One is tempted to simplify by saying that this shy improvement of MQE with increased f comes from an improvement of the film-boiling heat transfer, since in any way film-boiling is triggered almost independently of f during the pulse. Resuming, due to the weakness of cooling at 4.2K other contributors like the specific heat become the determining stabilizing factors. That means, that relatively, variations in RRR or Cu/Sc ratio affect MQE stronger in pool-boiling than in superfluid conditions. Cooling to superfluid involves a totally different scheme! The MQE for different combinations of v and f (resumed in Figure 3.11-18) shows two phenomena which are worth noting. First, the most striking feature, that within the simulated range of voidage the MQE curves for the same f reach basically the same MQE at high currents (I≥I$_c$). Only at low currents curves for the same f but with a different v spread, giving way to the “helium bump”. One could say that while f acts on a MQE curve over the whole current range, v acts on MQE only in the low current range where it sets the height of the superfluid enhancement. Second, the effect of v on MQE saturates above v=200%.

The so called helium bump or superfluid enhancement, which names the fact that an increase in helium volume can push MQE by a factor of up to hundred, can be shifted along the i-axis. The tuning parameter is the heat transfer coefficient (or equivalently the cooled perimeter fraction f). Taking as an example f=50% sets the bump to 0.9I$_c$. Since the effective cooled perimeter f of a strand in a Rutherford cable can hardly be increased beyond 15% and the LHC magnets will operate at ~0.7I$_c$ it is necessary to concentrate the effort on the heat transfer coefficient of the coating. Furthermore this effort is justified only if at the same time there is enough helium to give the superfluid enhancement amplitude (i.e. v>15%).

A series of graphs in Figure 3.11-19) shows clearly the changes accompanying the superfluid enhancement. The bump is characterized by the fact, that recovery is possible even after burnout of some cells during the pulse. This additional degree of freedom explains partly the leap in MQE. At currents higher than 0.9I$_c$ no burnout occurs in the non-quench case. This means that the temperature of the wire has to be kept down to critical or even current sharing. Interestingly T_s is kept below T_c in the present case, independent of v. The energies related to the high current MQE are hardly more than the enthalpy reserve of the wire between T_b and the peak temperature (T_c). The quench case is characterized simply by burnout during the pulse. With superfluid enhancement, the situation changes: recovery is possible even when locally the temperature goes up to 20K. Heat transfer rates correlated to these high temperatures are huge and the presence or missing of helium at this stage makes a noticeable difference. Furthermore the quench decision time increases with decreasing current thus amplifying the positive effect of an increased helium volume. As can be seen in Figure 3.11-19 the ratio of total heat transferred in the recovery case and the MQE pulse energy is normally of 2-4. Only at $0.9I_c$, when the helium bump appears, the ratio becomes 10. This is the result of MQE being kept down to avoid burnout and the surface temperature as well as the quench decision time being large enough to allow for big heat transfer rates. Obviously the helium bump can be seen as well in heat generation plots. Figure 3.11-20 gives the peak heat generation in the non quench case of the ref. strand (1.9K/11T/f=0.5/v=0.5) simulation as a function of transport current. The peak heat generation follows the maximal generation from i=0.4 to i=0.9, all along the “bump” in the MQE curve. Above the bump the generation has to be kept below maximal everywhere to avoid burnout. In the following a figure shows what are the limits applying in the quench cases for two particular f (15% , 70%) and the whole range of helium volumes (here given in terms of channel width). Obviously in the limit of small channels all quenches are triggered by channel limit. The longer the channel the more unlikely the appearance of channel limit.

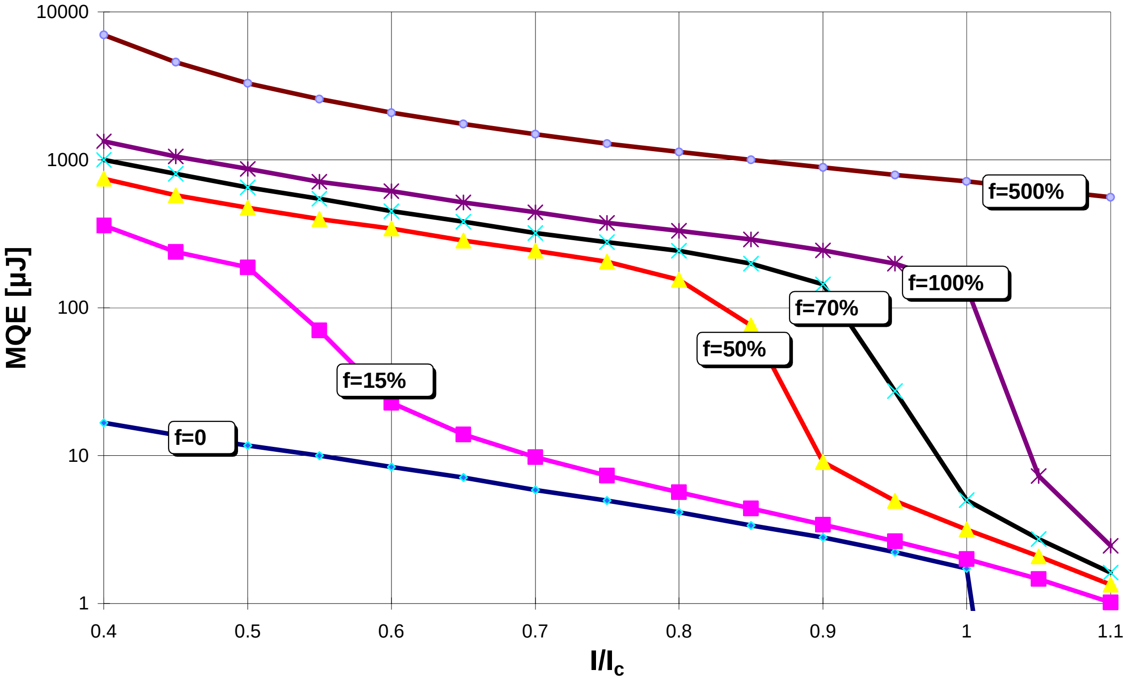

Figure 3.11-16: MQE simulation, Reference Strand, 1.9K / 11T, voidage (reduced helium volume): 200%, Variation of cooled perimeter fraction f. The superfluid enhancement onset current increases with increased f. Apart from the f=5 and f=0 case the curves reach approximately the same MQE at low I/I_c.

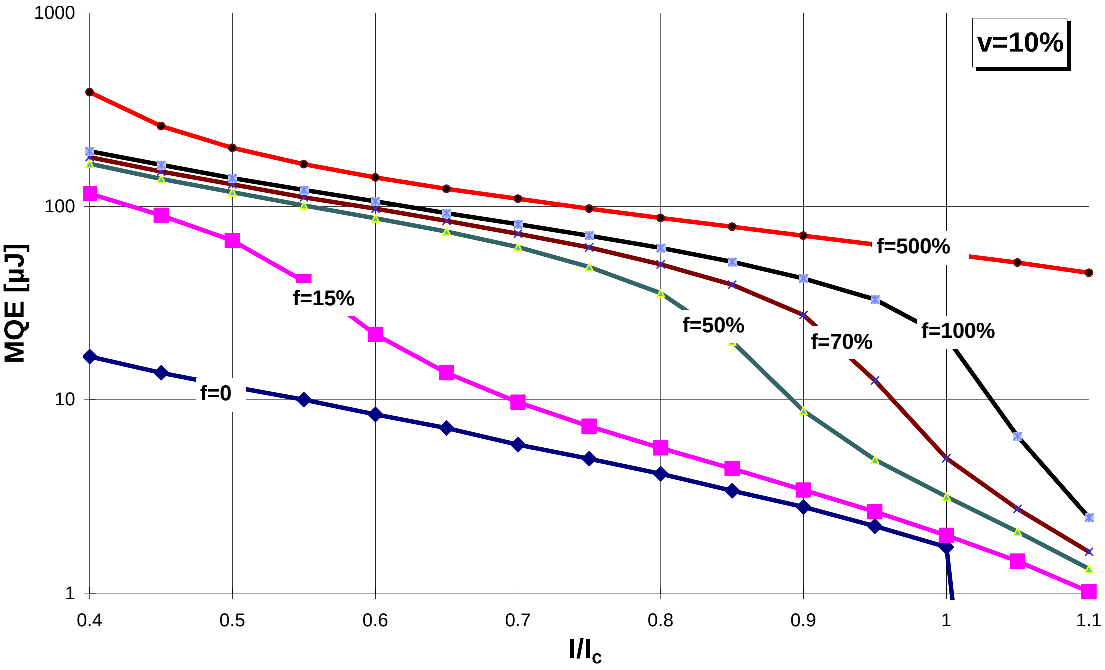

Figure 3.11-17: MQE simulation, Ref. strand, 1.9K/11T, voidage: 10%, Variation of cooled perimeter fraction f between 0-500%. The MQE for a given helium volume join at low (superfluid enhancement) and high I (adiabatic end). F determines the onset of superfluid enhancement.

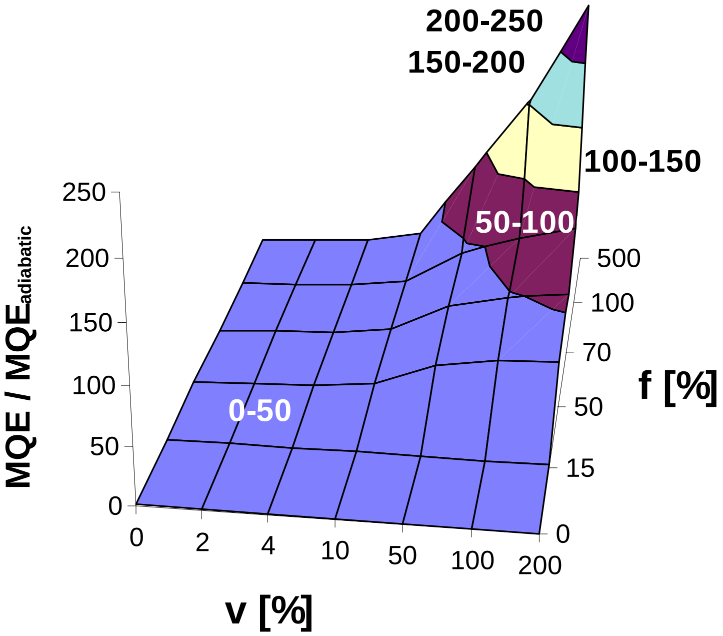

Figure 3.11-18: Effect of cooling parameters on MQE; Reference strand simulation, 1.9K/11T; I= 65% I$_c$, helium volume v in percent of strand volume, cooled perimeter fraction f. The MQE is normalized on its adiabatic value. The superfluid enhancement can raise MQE by a factor of 250 (or more). It appears when f / v are above 50% / 10%. However, even small combinations of v and f can as well take advantage of a 2-10 fold MQE enhancement.

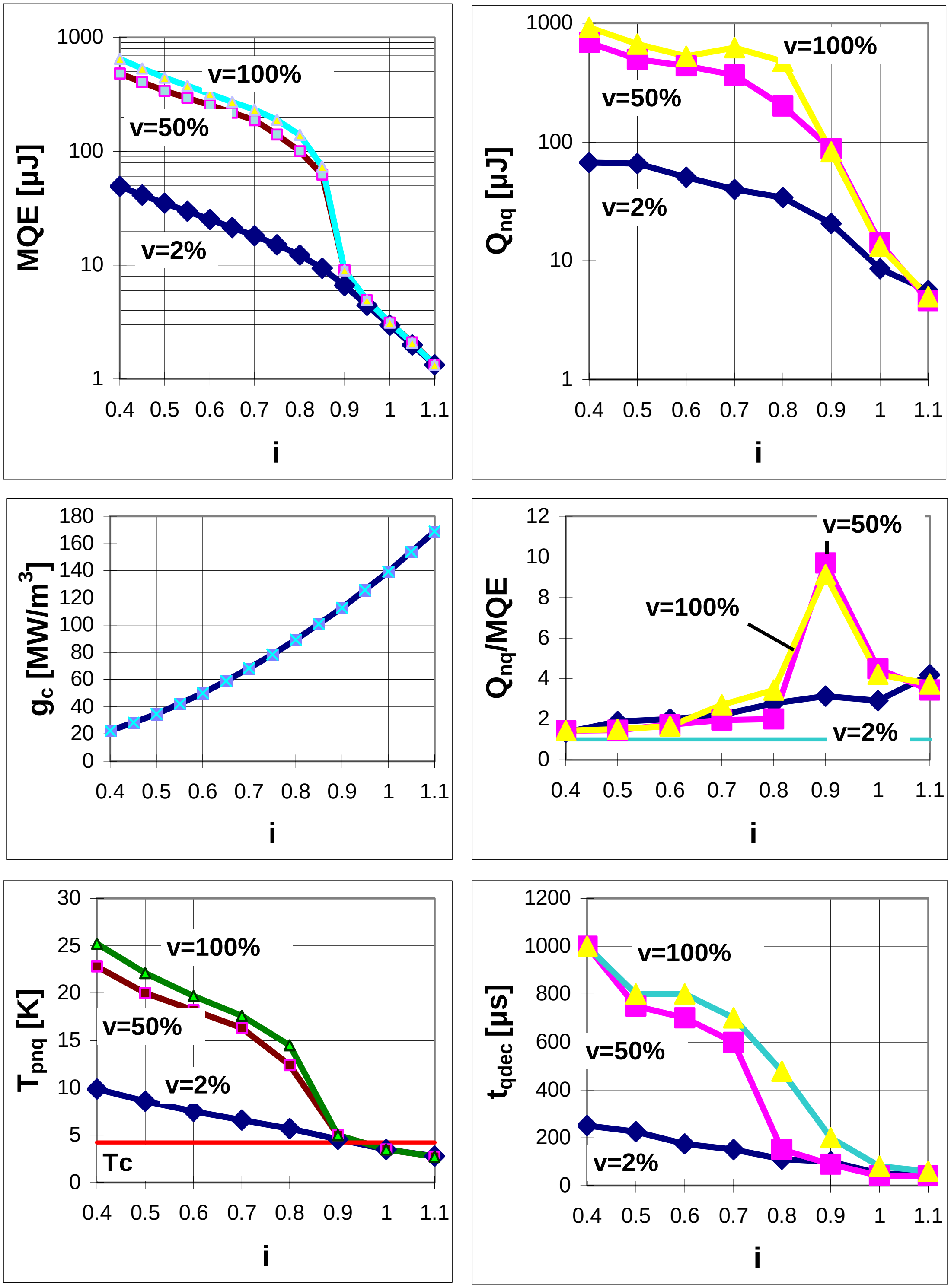

Figure 3.11-19: Analysis of MQE reference wire (1.9K / 11T) simulation-data for f=50% and v=2%, 50% and 100%. The different graphs show : MQE curve, total heat transferred to the helium in the no-quench case Q_{nq} in [J], the maximum heat generation i^2g_c in W/m^3, Q_{nq} normalized on MQE, Peak temperature of the no-quench-case T_{pnq} and quench-decision time for the different MQE points.

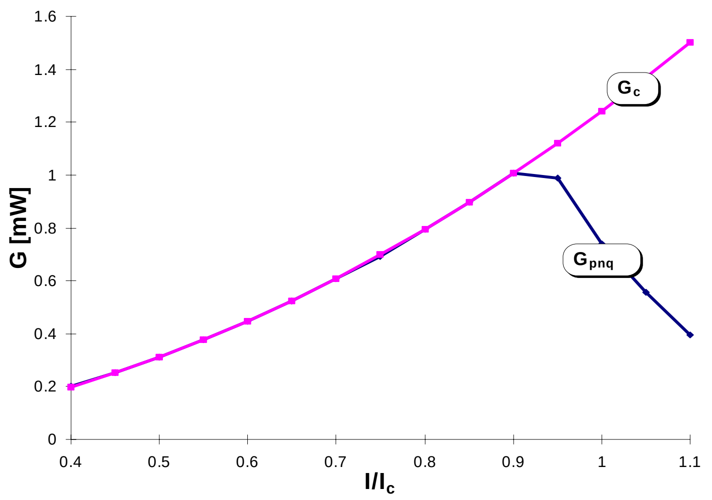

Figure 3.11-20: Peak heat generation in the central cell (l=10µm) at the end of the pulse (t=10µs) in the non-quench case, Reference strand, 1.9K / 11T simulation; f=0.5, v=0.5; The helium bump appears at i<0.9I$_c$. The heat generation follows g$_{max}$ all along the bump. At i>0.9I$_c$ the heat generation is kept below maximum to avoid burnout.

The saturation of MQE at v=200% can be explained by the fact that the dynamic limits have definitely taken over. Unfortunately no pattern has been found so far to relate GM or SS limit clearly to some cooling parameter combinations. In general GM-limit appears first in bigger channels. On the other hand SS limit appears more frequently in channels of medium size. Estimations of the cooling parameters of strands in Rutherford-cables in a LHC dipole magnet [Depond 98] reveals cooling parameters of v~4% and f~15%. Referring to Figure 3.11-18 this means that in the magnet case the strands will not take advantage of the full superfluid enhancement potential.

f=15%	0.4	0.5	0.6	0.7	0.8	0.9	1	1.1
0.0355	CL	CL	CL	CL	CL	CL	CL	CL
0.1775	SS+CL	SS+CL	CL	CL+SS	SS	SS	SS	SS
0.888	SS+CL	GM+SS	GM+SS	GM+SS	SS	SS	SS	SS
1.775	SS+CL	SS+CL	GM	GM	SS	SS	SS	SS

f=70%	0.4	0.5	0.6	0.7	0.8	0.9	1	1.1
0.0076	CL	CL	CL	CL	CL	CL	CL	CL
0.038	SS+CL	SS+CL	SS+CL	CL	CL	CL	CL	CL
0.19	SS	SS	SS+CL	SS+CL	SS+CL	SS+CL	SS	SS
0.3804	SS	SS	SS	SS+CL	SS	SS	SS	SS
50	SS+GM	SS+GM	SS+GM	SS	SS	SS	GM	GM

Figure 3.11-21: Two model cases (f=15% and f=70%) showing which type of limit triggered film-boiling in the reference wire MQE simulations (1.9K / 11T). On the x-axis the reduced current I, y - axis 5 different helium-volumes (v=2%, 10%, 50%, 100%,∞) written here as channel length L in [mm]. There is a clear tendency for channel limit in small channels. In big channels the dynamic limits apply. The bigger the channel and the higher the MQE-pulse (the lower the current) the higher the chance to encounter GM-limit. ("SS+CL" means second sound during the pulse and GM at the quench front.) In fact the SS-limit has a stronger influence on MQE than the GM limit. This can be seen as well in the plot here where the SS limit appears more often than GM.

Nevertheless a modest

improvement of MQE can even be obtained with sub-threshold cooling parameter combinations. Furthermore the modest quantity of helium in the cable together with the capillaries connecting them to the superfluid helium supplies will serve to evacuate the steady state heat load (beam loss, eddy current loss) stuck on the conductor during normal operation.

Eventually it may surprise that the superfluid enhancement appears abruptly. The reason for that can be found in the relation between cooling and heating versus ΔT (e.g. Figure 3.6-3): Coming from a high heat generation the cooling will be to small to allow for strong temperature excursions. But, suddenly at a threshold current the temperature is allowed to exceed the point where heating overrides cooling just because cooling surpasses heating again at an even bigger temperature.

3.11.4.2 Effect of RRR on MQE

RRR values between 100 and 200 are expected to occur after curing of the magnet. The present simulation compares MQE-curves, for RRR=100,170 and 500. The cooling has been set to magnet conditions (f=15%, v=4%), field and temperature to 9T and 1.9K. The RRR variation between 100 and 500 changes the peak heat generation by 25%. Nevertheless the effect of an increase of RRR above 100 is weak. The reason is the saturation of the RRR effect on the electrical resistivity of copper, which becomes essentially determined by the magneto-resistive contribution at RRR>100.

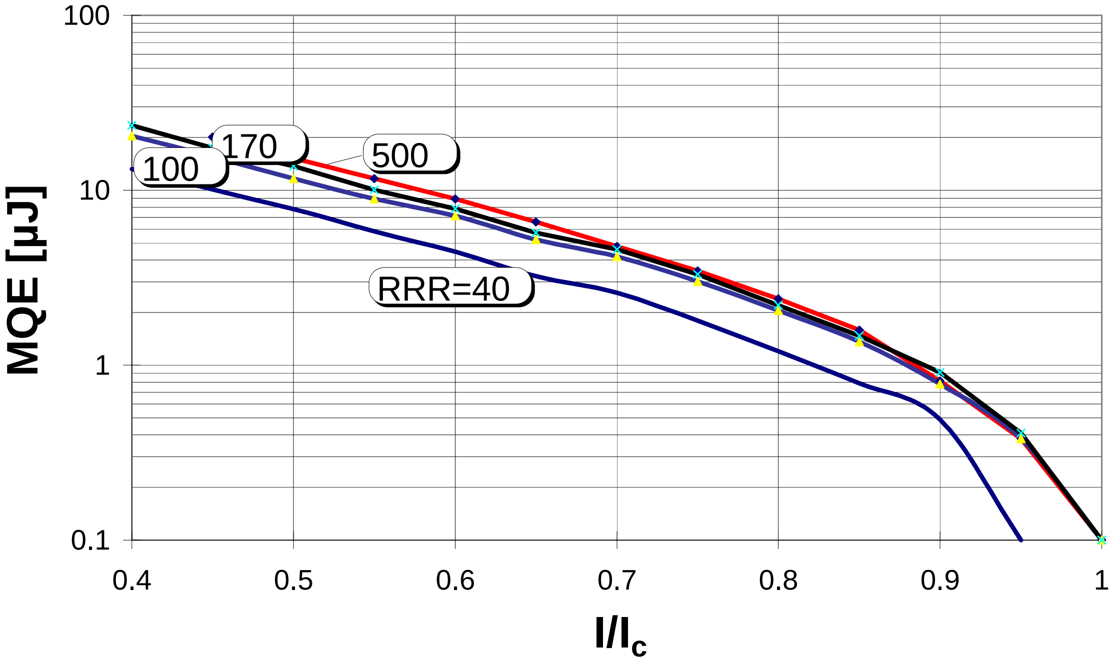

Figure 3.11-22: Effect of RRR of copper on MQE; Reference Strand Simulation, 1.9K / 9T, magnet cooling conditions (f=15%, v=4%). The variation in RRR has a small effect on MQE in the range specified for LHC strands (100 to ∞). On the other hand MQE drops by 50% for a RRR of 40!

An MQE simulation for a copper-type with RRR=40 has been added to illustrate that in these conditions the MQE can be significantly reduced (factor 2).

3.11.4.3 Effect of Copper to Superconductor Ratio on MQE

This is a repetition of a former study presented in [Wolf 94], with the only exception that the present helium model is more evolved. On the basis of the yellow book [CERN 95] parameters for the LHC strand: operating current 411A (≈65%I_c), operating field 8.4T and a fixed wire diameter of d=1.065mm, a reference strand simulation has been performed, where the copper to superconductor ratio λ varied between 3 and 0.5. Increasing the Cu/Sc ratio at fixed d and I_{tot} means going close or above I_c, decreasing the maximum heat generation and strongly decreasing the c_p of the composite at the same time and vice versa. Reducing the superconductor fraction in the composite may result in stability degradation if Ic<I. On the other hand less copper contradicts dynamic stability stipulations (flux jumps). Between those two extremes the MQE(λ) curve shows a maximum at an intermediate Cu/Sc ratio. Simulations (see next figure) show that the optimum depends on the cooling conditions. In reduced cooling conditions (f=15%, v=4%) the simulation shows that the maximum Cu/Sc ratio is slightly below λ=1. This means that for stability purposes it is better to use less copper in the matrix and to go to low values of I/I_c than the opposite. This can be explained by the fact that in quasi-adiabatic conditions stability is defined in terms of the enthalpy margin of the composite between T_b and T_{cs}. T_{cs} and the c_p of the composite increase with increasing superconductor fraction. This situation reverses under very good cooling conditions

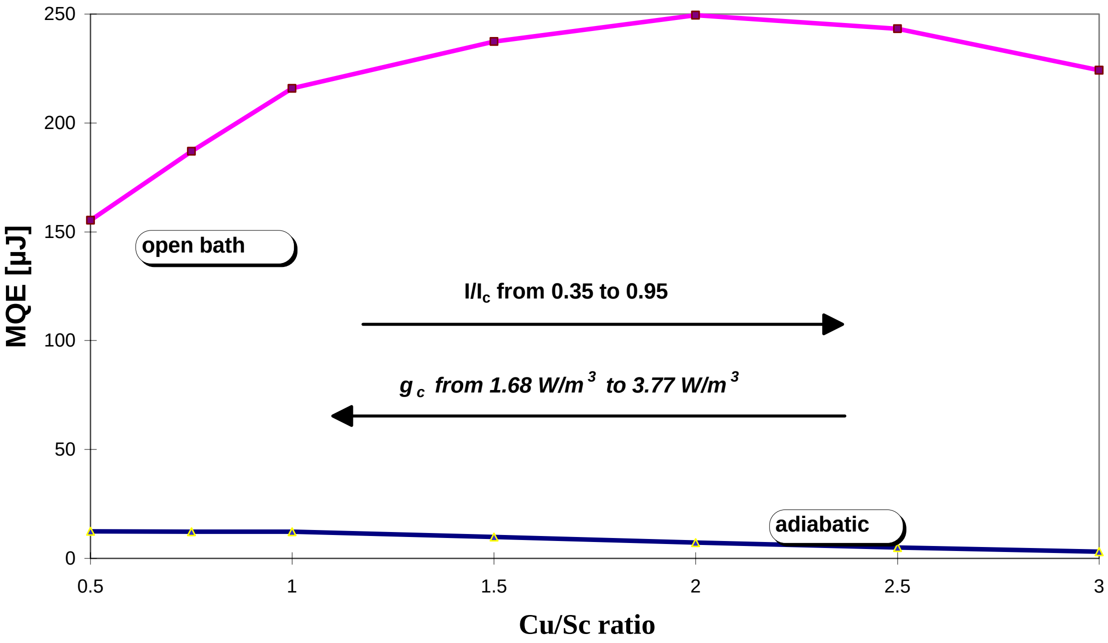

Figure 3.11-23: Effect of Cu to Sc volume ratio λ on MQE, Reference wire (RRR=100) simulation with yellow-book parameters: B=8.4T, I=411A; This result confirms the idea expressed in [Wolf 94] that for stability purposes it is preferable to go further away from I_c than to add more copper in the case of being close to I_c. This simulation has been obtained with f=0.15 and v=0.04 (reduced cooling conditions). With better cooling the maximum is shifted to a higher Cu/Sc-ratio. The highly cooled case corresponds to an infinite bath of helium and f=70%. The arrows indicate the direction of growing maximum heat generation g_{max} or reduced current i.

("open bath"), where the stabilizing effect of the copper is enhanced by cooling. Peak temperatures by far exceeding T_c and current sharing are attained and it is the enthalpy margin of the superfluid helium which becomes the decisive factor. In such conditions it is the composite with the lowest possible heat generation in the matrix which has the better MQE performance. Therefore the maximum shifts to higher λ for better cooling. This result confirms the study presented in [Wolf 94]. The present LHC-strand-prototypes have λ=1.6. Taking into account the reduced cooling conditions in the cable/magnet environment the optimum Cu/Sc ratio for LHC strands should be smaller than one. Unfortunately the copper to superconductor ratio can not be reduced below 1.5 to avoid excessive peak temperatures during the quench of a magnet (quench protection).

3.12 Conclusions

A model based on the one-dimensional heat balance equation was used to calculate the MQE of LHC strands. The basic functions for k, c_p, the heat transfer correlation and the electrical model for current sharing in the strand can be considered the most adequate and realistic found in literature. The electrical strand model uses an extrapolation between the known extremes: power law resistivity at I~Ic and the resistive behavior at T>Tc when all the current is in the copper. Especially the power-law at low heat generation rates introduces a smooth transition compared to the more conventional 3-part Joule heating models. The model of transient heat transfer to helium is based on a Kapitza-like heat transfer correlation with a switch to film-boiling depending on the so called critical energies, related to the dynamic heat absorption capacity of the cryogen in contact with the sample. Being the most crucial part, the model of transient cooling to superfluid helium, was found to be the reason for a slight disagreement between measurements and simulations. The fact that the measurements were not calibrated did not facilitate the comparison of simulation and measurement. But the good qualitative agreement between simulations and measurements in reduced cooling conditions (adiabatic, cooling to helium I) is reason enough to believe that the adiabatic part of the model is reliable. Assuming this, the discrepancy between model and simulation can be declared heat loss, which would then amount to ~50%. This is in agreement with a simple heater-model calculation. The biggest loss contribution in the MQE heater system (chapter 4) is the non negligible quantity of heat which is dissipated from the strand surface into the environment (helium or potting) during the pulse. Since the pulse power is in general three orders of magnitude stronger than the heating power due to current sharing the latter contribution to the above mentioned heat loss is negligible.

The major weakness of the model lies in the assumption that the neighboring helium channels belonging to the finite length elements do not exchange heat. This is a good assumption in poor heat conductors like helium I. In helium II the "longitudinal" heat transport along paths going through the helium becomes noticeable. The model parameters which strongly reflect the thermal diffusivity of the cryogen are the burn-out limits. On the basis of simulation versus measurement comparisons a substantial increase of these parameters has to be suggested. One might argue that the experiments from which the dynamic limits of Kapitza-like heat transfer in superfluid helium (burn-out onset times) are derived represent the real case and not a model case where the bulk helium is dissected into independent "channels". The truth is that all these transient heat transfer experiments worked with step-heat pulses but did not restrict the heating locally, as it is with MQE experiments. Using spatially extended heaters the here mentioned effects were shunted off to the sides ("end effects").

The simulated MQE curves for LHC type strands revealed an adiabatic high current end and a low current superfluid enhancement. Although cooling may be available for all cases it cannot act in the high current adiabatic cases, because the heat generation is so huge that the peak temperatures have to be kept down to avoid a quench. With small temperature differences between sample and bath the cooling rates remain equally small and the cooling negligible. At lower currents, where the maximum heat generation becomes less, the cooling is such that huge peak temperatures by far exceeding T_c can still lead to recovery cases. In these conditions the heat transfer rates become huge and the effect of cooling, especially in superfluid helium, noticeable.

The parameters related to the heat transfer properties (cooled perimeter fraction) were shown to determine the onset of superfluid enhancement, whereas the parameters related to burn-out (helium voidage) were found to affect mainly the amplitude of superfluid enhancement. The enhancement of MQE in superfluid can be 250 fold. Unfortunately the restricted cooling conditions as believed to prevail in the magnet environment make it impossible that the strands take advantage of the full superfluid enhancement. The effect of cooling in helium I was found to be weak. With the diffusivity of helium I being modest it is very common that film-boiling is triggered immediately during the pulse. Therefore there is no enhancement of MQE due to the effect of cooling. The cooling parameters rather have a small, linear effect on MQE over the whole current range.

The simulation of the effect of other parameters, like RRR and Cu/Sc ratio showed, that RRR affects MQE strongly (reducing it) when smaller than 100, showing a saturation above 100 and that the optimum Cu/Sc ratio depends on the cooling conditions. In good cooling conditions the optimum comes close to Cu/Sc~2, in adiabatic conditions it falls below one.

The following chapter describes the MQE measurement technique.

The measurement of the Minimum Quench Energy requires a heater technique which allows to depose short duration, locally restricted heat pulses on the strand. Only recently a Japanese group succeeded to produce low temperature heaters with µs time constants and sub-millimeter size, based on the graphite paste heater technique. Several attempts were made to apply this heater technique to LHC strands (Kapton sandwich heater, clamp heater). Since no way was found yet to calibrate MQE measurements, the reproducibility of the measurements was emphasized to make relative statements about the MQE-difference between different samples possible. The first heater prototypes did not come up to the reproducibility stipulation. Finally the tip heater configuration was found to meet the requirements. It generates a fast heat pulse in a thin graphite paste deposit on top of a small tip that is pressed against the sample with a clamp. The clamp guarantees a maximum of exposure of the sample to the surrounding cryogen. This chapter describes the essential items of heater design, mentioning the difficulties encountered with previous heater prototypes. A brief description of the main components (voltage taps, pulse generator, cryogenic system, sample holder) of the MQE test station is added.
The measurement techniques used by the other teams in the collaboration are discussed and compared to the tip-heater technique.

4. MINIMUM QUENCH ENERGY MEASUREMENT SET-UP

4.1 Defining the MQE-Measurement

Technical superconductors may be characterized by their Minimum Quench Energy (MQE), i.e. the minimum energy pulse needed to trigger a quench. A vast portion of the spatial and temporal disturbance spectrum has so far been covered in quench energy measurements for many different types of low-temperature superconductors. The experimentally most challenging type of disturbance is that of short duration and small extent. The experimental breakthrough to sub-millimeter/microsecond perturbations has only recently been achieved using the electrical graphite-paste heater technique [Kimura 95, Seo 96]. The analysis of training quenches in prototype LHC dipole magnets revealed that some quench precursors were wire movements of short time and affecting a small conductor volume. The Minimum Quench Energy (MQE) is uniquely defined as the smallest energy to quench the conductor in operating conditions (T,B,I) in the limit of a δ-like disturbance. The MQE of a conductor can be found by gradually changing the energy of the external heat pulse until the just quenching and the just recovering cases are found. The purpose of the present experiment being the measurement of the MQE of LHC-prototype- strands, some of the main parameters, magnetic field, temperature, and some aspects of the strand design are set according to the preliminary choices made to fit the LHC-main-magnet-requirements. MQE measurements still remain uncalibrated, although efforts are made to change that deplorable state [Usak 94]. Analytical approaches as well as numerical calculations (see chapter 3) considerably helped in the definition of pulse time t_{ini} and pulse-width x_{ini}: experiment and simulation indicate that MQE is approximately independent of pulse time t_{ini} in the range 0-100µs. Longer pulse-time means lower heating power at the same total energy. Lower heating power results in higher MQE. Eventually quench occurs before t_{ini}. Any “external heat” arriving after quench-decision-time t_{qdec} is meaningless. The effect of increasing x_{ini} above a certain threshold (MPZ) can be explained in the same terms as the increase in t_{ini}. It results in a distribution of the initial heat over a larger volume at lower power rates, thus giving the cooling a better chance to remove the initial heat deposit. Heating beyond the MPZ is as meaningless as heating longer than t_{qdec}. Resuming Figure 1.1-2 and Figure 4.1-2 an experimental pulse duration of 10-100 µs and a heater length of ≤ 1mm could be defined. The following list and table give the reference strand data: ∅ **1.065mm**, ∅ central copper part: 2.15µm, ∅ filament: **7µm**, filament spacing: ~**1µm**, double stack, outer copper layer: 35µm, **SnAg coating**: ~2µm, number of filaments: **8760**, twist pitch: **25mm**, Cu/Sc volume ratio **λ=1.6**;

REFERENCE STRAND	I_c [A]	n	ρ_{Cu} [Ωm]
4.2K / 6T	718	35	$4.25*10^{-10}$
4.2K / 8T	350	25	$5.17*10^{-10}$
1.9K / 9T	740	38	$5.65*10^{-10}$
1.9K / 11T	369	40	$6.57*10^{-10}$

Table 4.1-1: Critical current, n-value and Cu-resistivity of the reference strand (measured); I_c according to the 10^{-14}Ωm A_{tot} criterion. A valid fit for ρ_{Cu} is: $\rho_{Cu}=4.65\times10^{-11}\times B(T)+1.45\times10^{-10}\Omega m$.

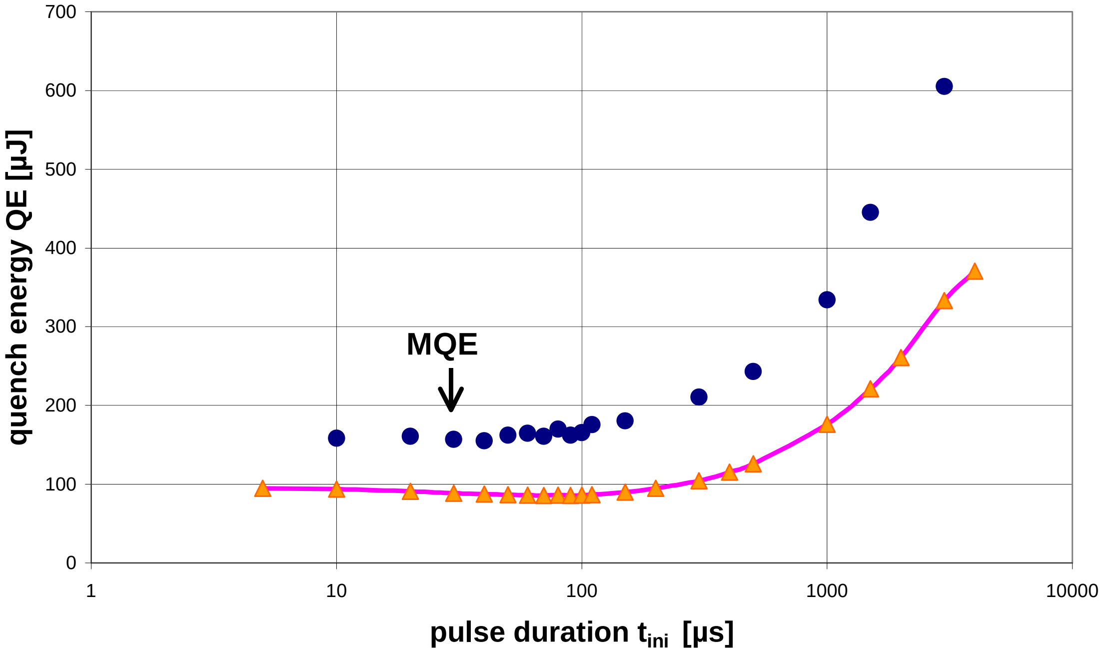

Figure 4.1-1: MQE versus pulse duration, comparison between measurement (dots) and simulation (line). The difference in absolute values of MQE is a consequence of a lack of calibration of the experiment. Sample: reference wire, 8T, 4.23K, $0.7I_c$, f=0.7, $L\rightarrow\infty$, $\rho_{Cu}=4.7\cdot10^{-10}\Omega m$, heater diameter: 300µm, Kapton®-sandwich heater;

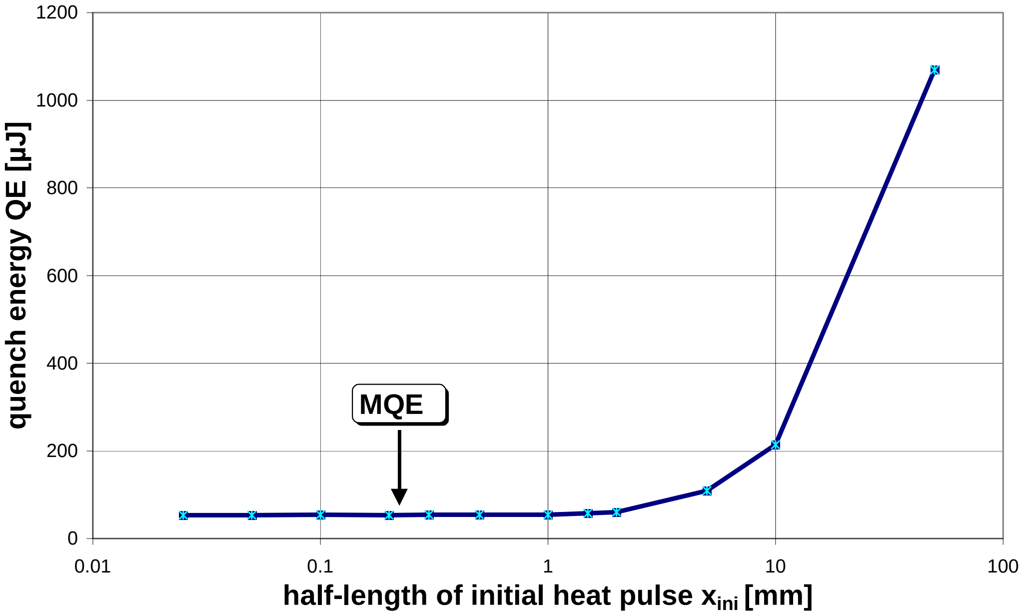

Figure 4.1-2: Simulation of MQE as a function of heater size, reference wire. Note that the heater dimension is approximately $2X_{ini}$. Actually experiments are performed with X_{ini}=0.15-0.3mm. Simulation parameter: $I=I_c$, B=8T, T_b=4.23K, f=0.7, t_{ini}=10µs;

4.2 *Measurement Set-Up*

4.2.1 General Part

The hardware for MQE measurements comprises basically a critical current test-facility with some additional features (pulse generator, voltage taps, heater). The general scheme of measurement is shown in the following figure. The cryostat is split into two baths. The lower bath can be cooled down to 1.9K by pumping liquid helium through a JT valve - heat exchanger circuit (10W max. cooling power at 1.8K). The solenoid (bore: 10cm, length 30cm) is designed for 14T at 1.8K. The sample is wound on a G11 cylinder

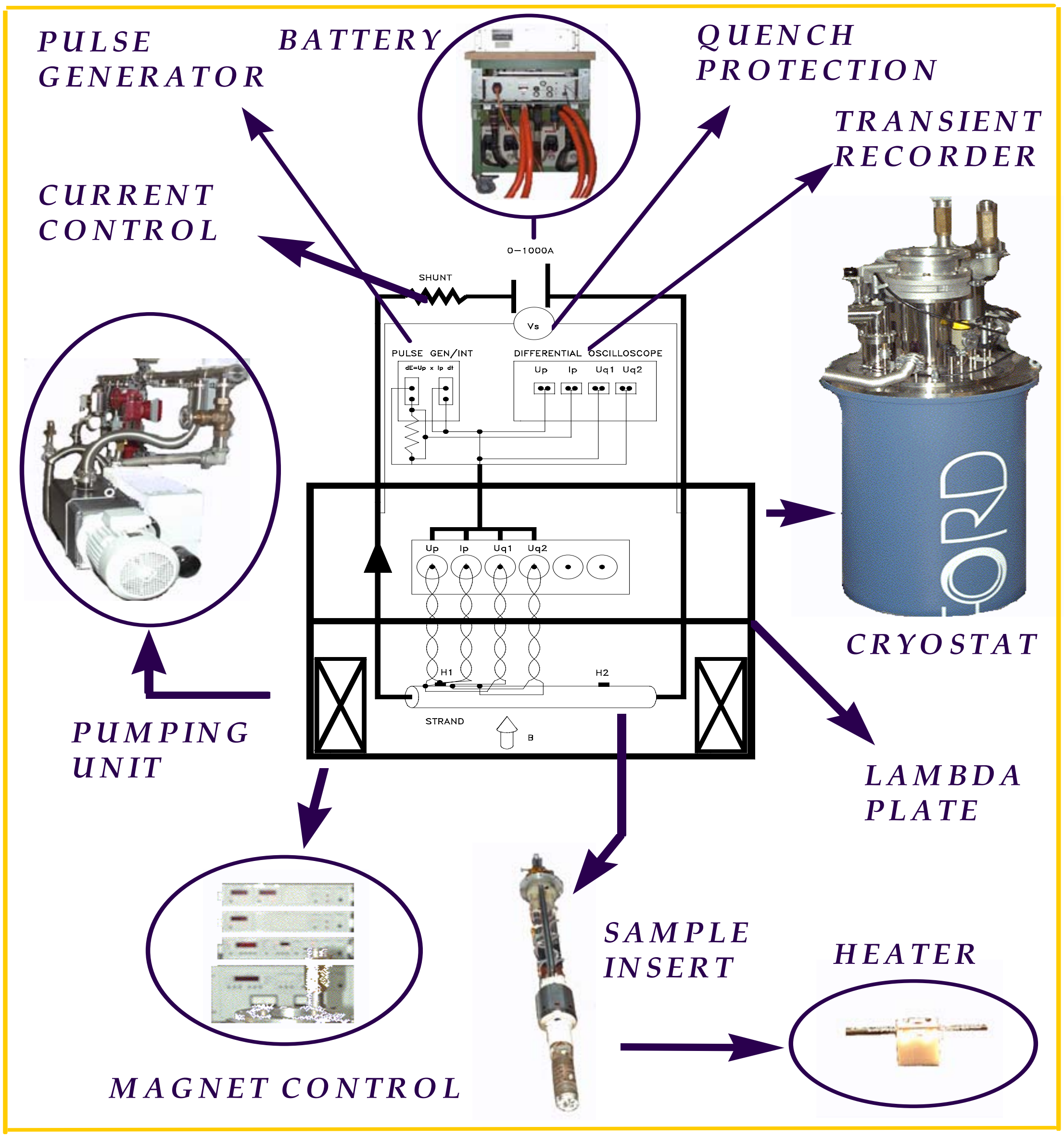

Figure 4.2-1: MQE-measurement set-up - general scheme;

(∅=6cm). The sample is soldered on bottom and top to the in and out current-leads (2000A). A battery power supply (4000Ah/4V) delivers a ripple free current into the sample. A security system automatically opens the circuit when the voltage exceeds 100mV. Three sets of heaters together with 16 pairs of voltage taps are distributed along the sample (1.5m). A pulse generator delivers square pulses (1µs-1ms) of up to 100W into the heater (1-70Ω). Having established temperature and magnetic field the critical and the quench-current are measured. The transport current in the sample is ramped to a nominal value (in the range 40-120%I_c) at a rate of 12A/s. The MQE is determined by applying a series of heat pulses, starting with a roughly guessed energy and gradually approaching the MQE. In the normal case an MQE measurement consists of measuring the minimum quenching heat pulse (at given T, B and I_{trans}) and the maximum non quenching heat pulse. The difference between them can be kept below 1%. MQE is assumed to be the average of these two pulses. After any pulse (quenching or non-quenching) the current is always driven back to zero, because MQE increases following a non-quenching heat pulse because a non quenching pulse results in a more homogeneous current distribution within the wire cross-section and therefore raises MQE. The propagating quenches (or recovery) are detected with a series of neighboring 2cm-voltage taps along the sample, labeled V_{qi}, where i normally goes from 1 to 4. V_{q1} is centered around the heater. Since it covers a length much bigger than the MPZ all the dynamics of quench or recovery can be observed on it. Two important magnitudes have been chosen to represent these dynamics: quench decision time t_{qdec} (defined as the time when V_{q1} in the MQE and the MNQE case split) and V_{qdec} which is correlated to the MPZ-length and directly related to the quench decision length x_{qdec}. These magnitudes can be used to fit simulations to the measurements, eventually hinting towards some of the lesser known parameters (e.g.: Kapitza-conductance, helium volume or specific heat), as done for example in [Iwasa 79]. Unfortunately an accurate measurement of t_{qdec} demands an accuracy in the MQE measurement by far exceeding the normally stipulated 1%! The voltage taps V_{q2}, V_{q3} and V_{q4} as well as the total voltage serve the purpose of monitoring quench-propagation. Normally the quench propagates through the sample at approximately constant speed, independent of the details of quench origin (e.g.: strength of heat-pulse) depending on the heat generation rate (transport current), specific heat and cooling. Any object in contact with the sample may influence quench-propagation through its heat absorbing capacity. Therefore special voltage sensors, namely spring loaded tungsten tips pressed against the wire, were used. The plateau in the quench voltages (e.g. V_{q2max}) can be used to determine the Cu-resistivity because the voltage is given by the transport current flowing exclusively in the matrix, with the temperature still being low enough that the resistivity is still temperature-independent. The measurements are performed on three heaters, the final MQE being the average of these three curves. Quench-propagation velocity v_q, Cu-resistivity ρ_{Cu} and quench-decision length x_{qdec} (≈ MPZ-length) are calculated from the measured data with the following formulas:

$$v_q = \frac{dV_{q2}}{dt} \cdot \frac{A_{tot} \frac{\lambda}{1+\lambda}}{I_{tot}\rho_{Cu}} \qquad \left[\frac{m}{s}\right] \tag{4.2-1}$$

$$\rho_{Cu} = \frac{V_{q2\max} A_{tot} \left(\lambda \big/ 1+\lambda \right)}{I_{tot}\,\ell} \qquad [\Omega m] \tag{4.2-2}$$

$$x_{qdec} = \frac{V_{q1\,plateau} A_{tot} \left(\lambda \big/ 1+\lambda \right)}{I_{tot}\,\rho_{Cu}} \qquad [m] \tag{4.2-3}$$

where *l* is the length of the voltage tap (usually 2cm).

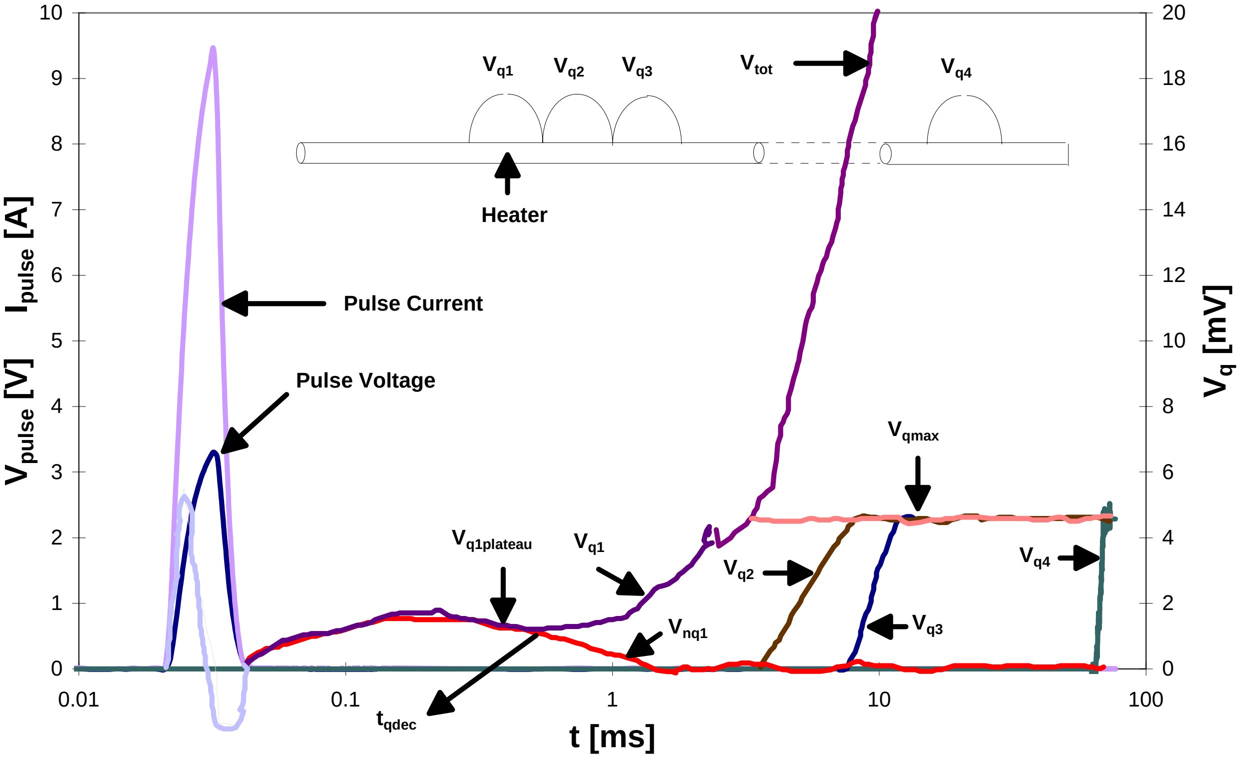

Figure 4.2-2: MQE- measurement-signals; As indicated in the small sketch the voltage along the sample is recorded during quench/no quench. The central voltage tap V_{q1} allows to differentiate the MNQE from the MQE. Furthermore it serves to measure quench decision time t_{qdec} and quench decision length x_{qdec} ($\propto V_{q1plateau}$). The other voltage taps V_{q2}, V_{q3},..etc.., contain several data, like quench propagation velocity ($\propto dV_{qi}/dt$) and Cu-resistivity ($\propto V_{qimax}$). V_{tot} is measured over 80cm of sample.

The standard-deviation for current- and MQE-measurement is within less than 1%. Unfortunately this is negligible compared to the fact that the measurements are not calibrated. The fraction of the deposited heat effectively reaching the sample is unknown and may vary a lot even for similar heaters under the same conditions. MQE re-measured during one measurement run with the same heater stays within less than 5% of the original value. The spread becomes bigger when the heater system has been exposed to a thermal cycle to room-temperature or between different mountings.

4.2.2 Electrical Part

The MQE holder is equipped with 25 voltage taps distributed along the sample (Figure 4.2-3). There are three groups of five 2cm-taps plus heater current and heater voltage connections for the three heaters. The global voltage tap spreads over 80cm.

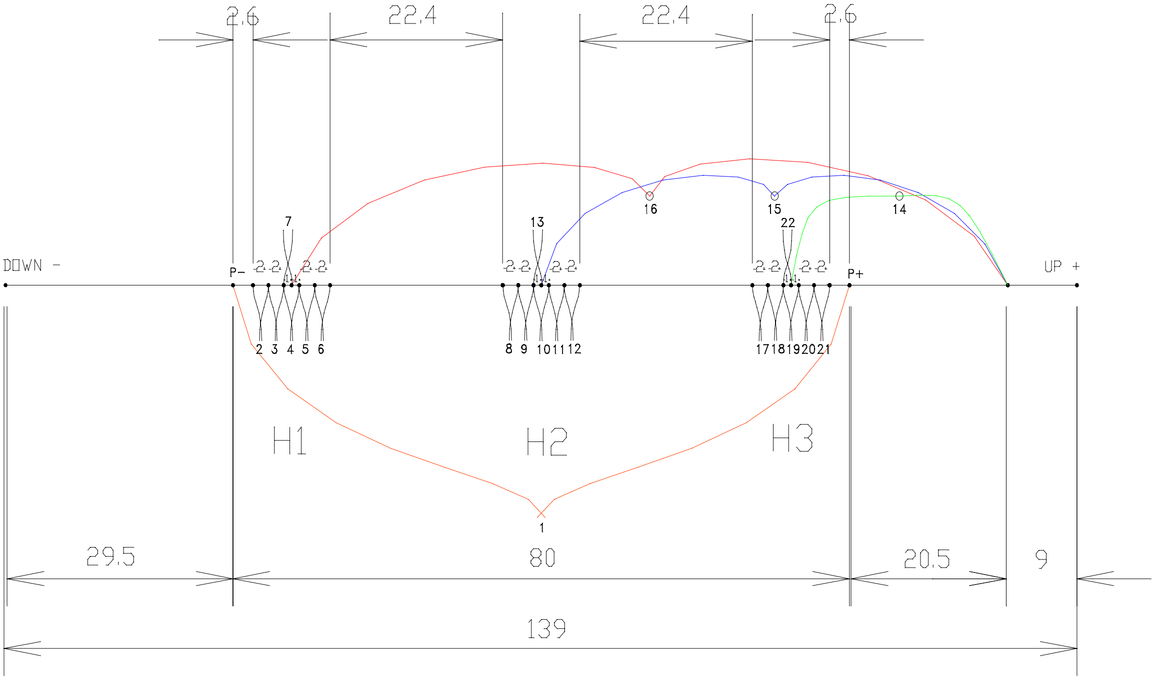

Figure 4.2-3: Distribution of voltage taps along the sample (139cm). V_{tot} is recorded on the 80cm long voltage tap. There are three groups of voltage taps distributed around the three different heaters (H1,H2,H3) locations. Wire pairs 1,13, 22 and 14,15,16 are the voltage/current connections for the heaters. The heaters have a common current return.

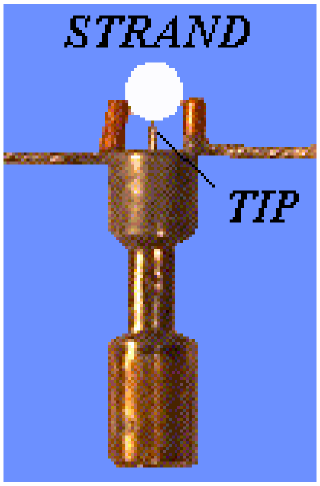

Figure 4.2-4: Spring loaded tungsten pin;

The voltage pick-up (Figure 4.2-4) is a low heat conductivity tungsten tip being pressed against the sample from within the sample-holder. The tip (length: 7.5mm, diameter: 1.2mm, tip diameter: 0.03mm) can move 0.6mm, the back-pressure from the stainless-steel (or alternatively bronze-beryllium) spring is of 140g. The outer hull is made of brass. A 0.5mm diameter Cu-wire is soldered into a groove on two opposite sides of the brass-cylinder. The total resistance of the tip is of approximately 100Ω. The wiring from outside the cryostat to the sample-holder has been optimized to reduce the noise level. Two pin-connector stages allow for the separation of the sample insert from the front end box and of the sample holder from the sample insert.

The following draft presents the sample-insert with the current leads. The transport current is measured in a shunt outside the cryostat.

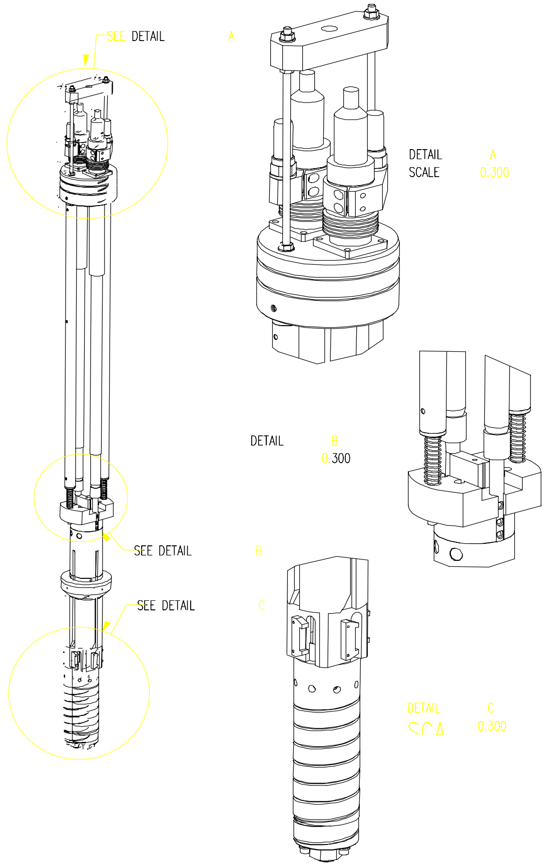

Figure 4.2-5: Sample insert: detail A: Current-leads top-plate connection, detail B: current lead connection between Cu-bars (from top) and superconducting busbars (from bottom), detail C: sample holder;

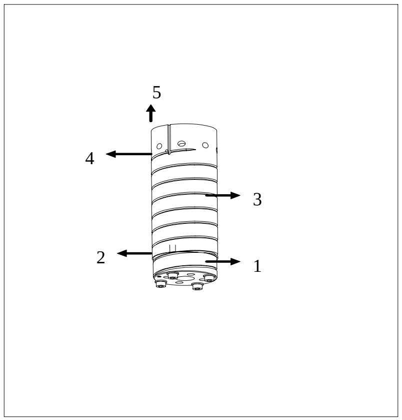

Figure 4.2-6: sample holder 1 copper-block, 2 sample soldered on copper block, 3 sample-groove, 4 solder pin to fix sample, 5 sample soldered on busbar (fixed to sample insert)

The sample is twisted on a cylindrical G11 sample holder (22cm long, ∅ 70mm) into a triangular groove (1.5mm deep, 3mm large) with a spiral rise-angle of 22°. In this configuration the wire is almost perpendicular to the magnetic field. The Lorentz-forces are directed inwards pressing the wire into the groove. Furthermore the sample is wound under high tensile stress (170Mpa) to prevent it from moving during the test. The sample is soldered onto the bottom Cu-piece which is in contact with the central current return. On top the sample is soldered onto the busbar. The solenoidal magnet has a 10cm bore and a field homogeneity of 0.4% along a radial path from the central axis to the inner layer of the magnet. The heaters and associated voltage taps are located around the center of the sample holder, far enough from the current penetration region at the soldered ends. The voltage sensing pin probes are part of the sample holder the contact is established as soon as the sample falls into the groove. The cabling is integrated part of the sample-holder, when mounting the sample holder on the sample-insert some pin-connectors have to be attached. The heaters are clamped to the wire independently of the sample holder to avoid any relative movement between heater and sample. An outer protection hull protects the sensitive heaters from any shock hazard.

4.2.3 Cryogenic Part

The cryogenic system of the MQE-test-station corresponds in principle to that foreseen for the LHC-magnets operating in subcooled superfluid helium at 1.9K / 1atm. The refrigeration scheme has been described first by [Claudet 74]**.** Its features are the separation into lower and upper bath (λ-plate) and an independent cooling device with JT-valve (aspiring liquid helium from the upper bath), heat exchanger in the lower bath and a pumping unit delivering the refrigeration power at 1.9K. Temperature between 1.8K and T_λ can be regulated with a small heating device at constant full refrigeration power. Working in 1.9K subcooled helium II means working at a well defined temperature (± 5mK) whereas in the case of pool-boiling helium I variations in the back-pressure from the recuperation line as well as bath-stratification introduce uncontrolled temperature-variations (±30mK). The lower bath (with magnet, heat exchanger, temperature sensors and sample) contains approximately 15 liter of liquid helium.

4.2.4 Data Acquisition

The estimation of heater-current and voltage requires a time resolution of 1µs. Therefore a numerical oscilloscope with four differential channels, 12bit resolution and MHz sampling rate per channel is used. For all the other voltage measurements a 8-differential channel PC-data-acquisition card device with 100kHz sampling rate per channel, 12-bit - ±10mV resolution is used. The availability of 12 channels provides global control of the measurement-signals.

4.3 Point-Heaters

Inspired by the successful MQE measurements conducted at BNL [Ghosh 97] and KEK [Kim 96] based on the heater technology [Seo 96], M. Wilson suggested this heater technique for the LHC-stability project. The particularity of this heater technique stems from the use of an adhesive graphite paste with a resistivity (some Ωm at 10T/1.9K) in such a range that the heating power (1-100W) can be generated in very small heater volumes, thus reducing the thermal time constant of the heater system to ≤1µs. The range of low-temperature-electrical resistivity represented by this heater paste (graphite emulsion in epoxy) is normally covered by semi-conductors. During the course of the present work attempts have been made to use sputtered Germanium layers as heating element. Although promising this technique had to be abandoned because total control of the various parameters (film-thickness, purity of film, doping concentration, surface layer effects, magneto-resistivity contribution) influencing the thin film-resistivity could not be achieved within the available time. Alternatively ultra-thin metallic tips could be used, but rough calculations following [Tamai 86] indicate that a contact resistance of 1Ω requires a tip-width of less than 10nm. Different heater prototypes based on the graphite paste technology were tested. The guide-line to heater design were the basic stipulations:

- heated strand length < 1mm, heater-volume << 1mm^3,
- range of heater resistance 1-10Ω, as reproducible as possible,
- minimized heat transfer to anything else but the sample;
- minimized physical interference of the heater in the cooling of the strand

4.3.1 Heater-Prototypes

The electrical scheme of the heater-circuit explains often used terms like heater current, heater voltage and heater resistance. The heat pulse is delivered by a pulse-generator /integrator with: V_{max}=40V, $R_{load} \in$(1-70Ω), square-pulse time range 10µs-1ms. The pulse generator is a DC-source with a switch. The pulse energy is estimated from $E=\int V_H(t) I_H(t) dt$ with 1% accuracy. The heater current is measured in a 0.1Ω shunt. The heater voltage comprises the voltage drops in the heater volume, the contacts on both sides of the heater and in a part of the leads to and from the heater. Figure 4.3-2 shows the circuit map of the MQE measurement determined from impedance and RLC bridge measurements.

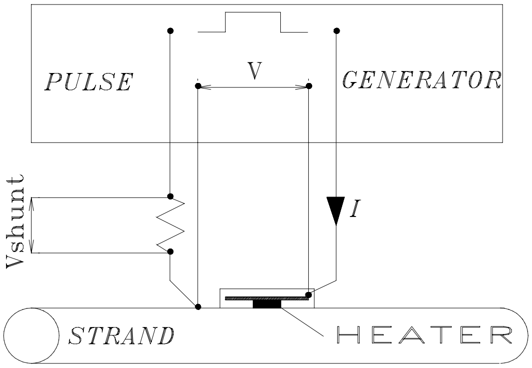

Figure 4.3-1:Electrical scheme MQE heater: 4 point measurement of the heater resistance, The heater current is measured with a 0.1Ω-shunt.

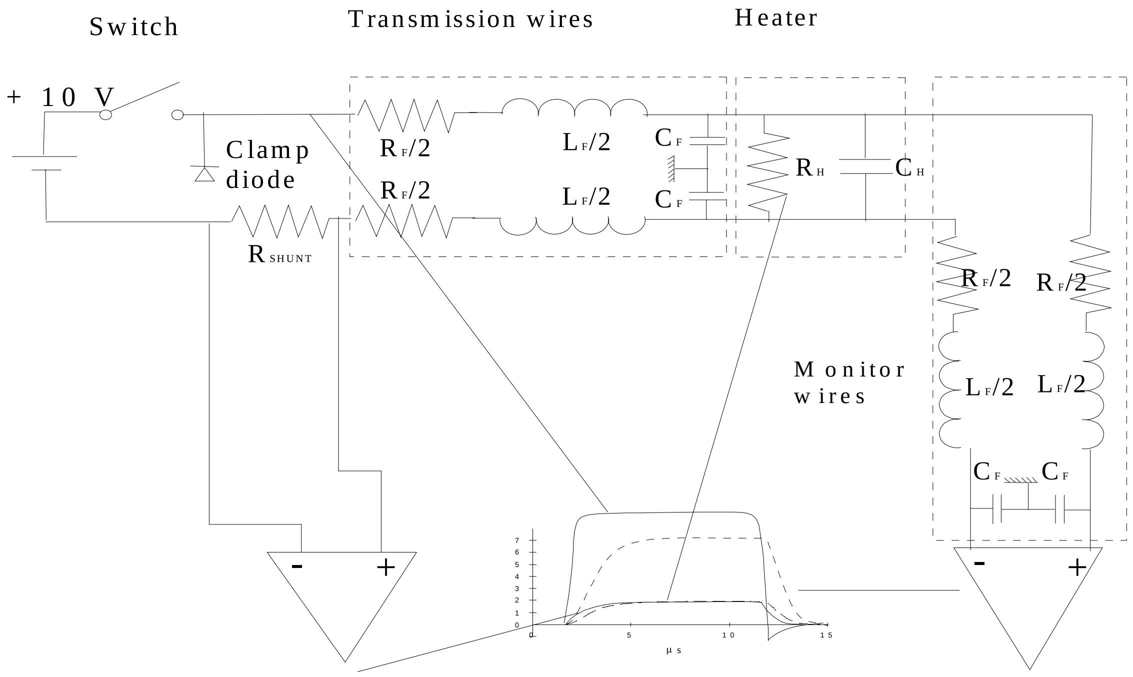

Typical Parameters :
R_H = 3.8 Ω
C_H = 0.1 µF
$R_{F/2}$ = 0.7 Ω
L_F = 7 µH
C_F = 300 pF
R_{SHUNT} = 0.1 Ω

Figure 4.3-2: Heater circuit diagram with pulse generator, heater and monitor wires; The heater can be modeled with the heater resistance R_H (1-10Ω), a parallel capacitance C_H(~0.2µF) and a serial inductance L_H (~1µH) (here included in L_f). U/I pulse shapes simulated with Microcap.

The heater circuit can be represented by a heater resistance R_H (1-10Ω), a parallel capacitance C_H(~0.2µF) and a serial inductance L_H (~1µH). The simulated V_H signal (Figure 4.3-2) shows a weak inductive distortion of the square pulse signal. Measured and simulated pulse-shapes agree well. A very common error occurs when the monitor wire part of the network is not well balanced and therefore V_H not measured differentially (strong negative overshoot in V_{pulse} at end of pulse).

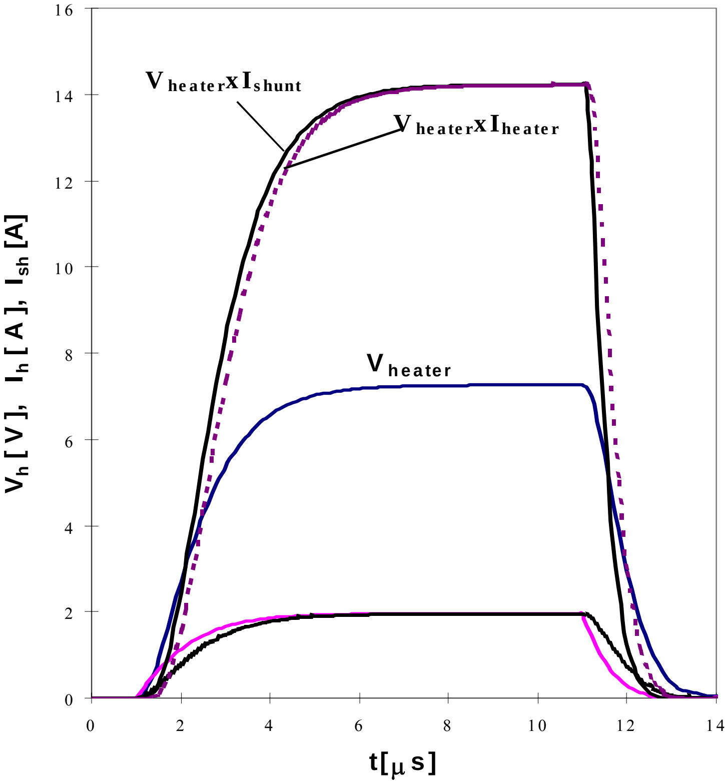

Figure 4.3-3:Simulation showing the error made in the calculation of the heat deposited in the heater when taking I_{shunt} instead of I_H.

The fact that the energy is calculated from I_{shunt} and $V_{H,}$ and that I_{shunt} may be significantly different from the effective I_H had to be analyzed. In fact the problem is not as significant as it appears because the time constants involved (τ~RC, τ~R/L) are in the µs range, which means that any energy stored in C and L is delivered almost immediately at the end of the pulse, hence only slightly modifying the pulse shape, and in what the energy calculation is concerned they are counted anyway in I_{shunt}. Furthermore in the simulation we see that the difference of the power calculated from I_H and V_H and from I_{shunt} and V_H is negligible. The real pulse shape is marked by the change of resistance of the heater bulk during loading: the graphite heater behaves as a NTC resistance at low temperatures, R_H decreases during the pulse.

Another important detail concerning the heater current is the fact that it partially flows along the sample together with the transport current. Normally the pulse current does not exceed a few percent of the transport current. Figure 4.2-2 shows typical voltage signals recorded during a measurement. V_{q1} shows an oscillation in the mV range which is the effect of the time derivative of the pulse current in the sample. Luckily, as a consequence of the skin effect the heater current circuit and the transport current circuit are decoupled. Calculated skin-depths (35µm) are small enough that the heater current remains mainly superficial. Hence the wire section is not necessarily on one potential, the voltage oscillation observed on V_{q1} is just seen by the small heater current, thus not causing significant heating.

4.3.2 Kapton® Sandwich Heaters

The Kapton®-Sandwich-Heaters are inspired by the graphite paste heater design used at BNL. The successful use of this type of heater in MQE-measurements on cables suggested their application on strands. Its disadvantage is a lack of control of almost all parameters.

The Kapton®-Sandwich-Heaters are made of two layers of adhesive polyimide foil of ~20µm. The heater current lead is a thin Cu-strip (0.3mm large, 10µm thick) deposited on the inner side of the back-layer. With a hot tip a hole of ∅0.3mm is punched into the thin top-Kapton® layer. Two thin (∅80µm) varnish insulated Cu-wires are soldered to the end of the Cu-strip. The two layers are then glued together and eventually heat treated at 180°C to close small gaps and capillaries exposing the Cu-strip to superfluid helium. Additionally at the back end, the gap held open by the thin sense wires passing out is sealed with epoxy. The Kapton®-Sandwich is now a thin strip of 1cm length and a few mm width with two thin wires coming out at the back and a small hole on top giving way to the underneath Cu-strip. The little hole is filled with heater paste (Eccobond 60L®). With the paste still soft the heater is mounted on the sample by clamping it between strand and sample holder. The mounting pressure of the strand would maintain the heater in place. A considerable amount of skill had to be developed to mount the heaters correctly without too many trials because the considerable pressure of the wire easily damaged them. Correct mounting means as well resistance control, the preliminary resistance at mounting should not exceed 70Ω. A powerful way of controlling the heater resistance would be a variable pressure. The initial resistance gives an approximate hint of the final resistance after polymerization of the paste. Drying normally lasted at least a day at ambient temperature. During polymerization the resistance dropped. Interestingly the heater had to be pulsed before reaching its final room-temperature value. During pulsing the resistance dropped to some Ω in case it was higher than 10Ω or it stayed at approximately the same value when it had already reached down to 1Ω after drying. The training was independently discovered as well at BNL. Thermal shocks during cool-down and rough operation conditions resulted in the destruction of half of the heaters during testing. Although the heater preparation improved gradually with experience, the MQE measurement results on a test sample revealed a big spread (factor 2) at 4.2K / 8T. Resuming the drawbacks of the Kapton®-sandwich-heaters:

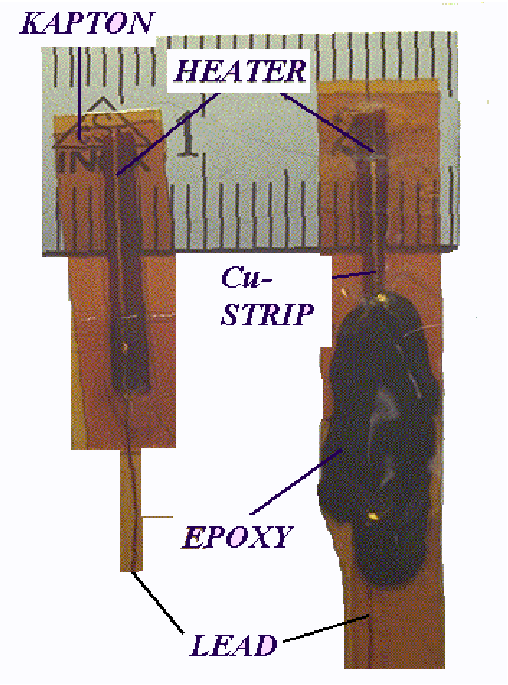

Figure 4.3-4: Kapton®-sandwich-heaters

- no pressure control - no accurate control of resistance
- no visual control of the exact heater position

- highly sensitive to mechanical disturbances
- tedious heater preparation - low efficiency

4.3.3 Clamp-Heaters

By clamping a Kapton® sandwich-type heater to the sample a control of heater resistivity through pressure should become possible. Unfortunately it proved very difficult to actually take advantage of this feature because we could not implement a method to control the position of the heater relatively to the sample. An advanced clamp prototype (Figure 4.3-5) had part of the heater included to reduce complications during mounting.
The clamp consists of an upper and a lower stainless-steel part which clamp the wire by means of two screws equipped with 20N-springs (to compensate for the effect of differential contractions during cool-down) being mechanically independent from the sample holder. The clamp could apply up to 40MPa on the heater. The sample fits into a small groove ($R = r_{wire} + d_{foil}$). The heater-current lead (a 20µm thin Cu-foil) is included into the clamp. A 100µm thin Kapton®-foil is fixed on the lower part with its 0.3mm diameter hole positioned exactly on the Cu-strip in the center of the groove. The little hole is filled with graphite paste and the parts clamped on the sample. Ideally the heater resistance should be controllable through the clamp-pressure. Nevertheless pressure and resistance remained non-correlated because it was difficult to keep the heater in a defined position on the sample. An accurate resistance control was anyway complicated by the decrease in resistance during polymerization and the jump in resistance during the first heat-pulses. First measurements showed no improvement. The clamp method was not pursued further because meanwhile a more advantageous heater prototype had been developed (the tip heater).

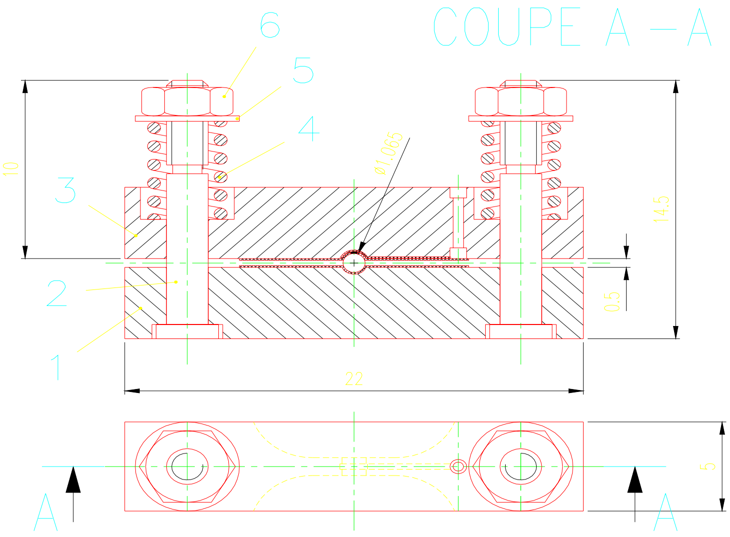

Figure 4.3-5: Clamp heater, side and top view, 1 lower part, 3 upper part, 4 spring, measures in mm

4.3.4 Tip-Heater

The tip heater has been designed and produced by J. Donnier at CERN. It electrically generates a heat pulse in the point where a small tip presses against the sample. The total electrical tip resistance is given by the resistive deposit on top of the heater-tip together with the contact resistance. The main parts of the tip heater are a clamp (to fix the sample position relative to the tip) and a mechanism to press the tip against the sample with controlled pressure. Ideally the total sample surface is wetted with helium and in contact with a bath of liquid helium. The clamp should not thermally interfere in the process, therefore it is made of insulating, machinable glass (Corning's Macor®).

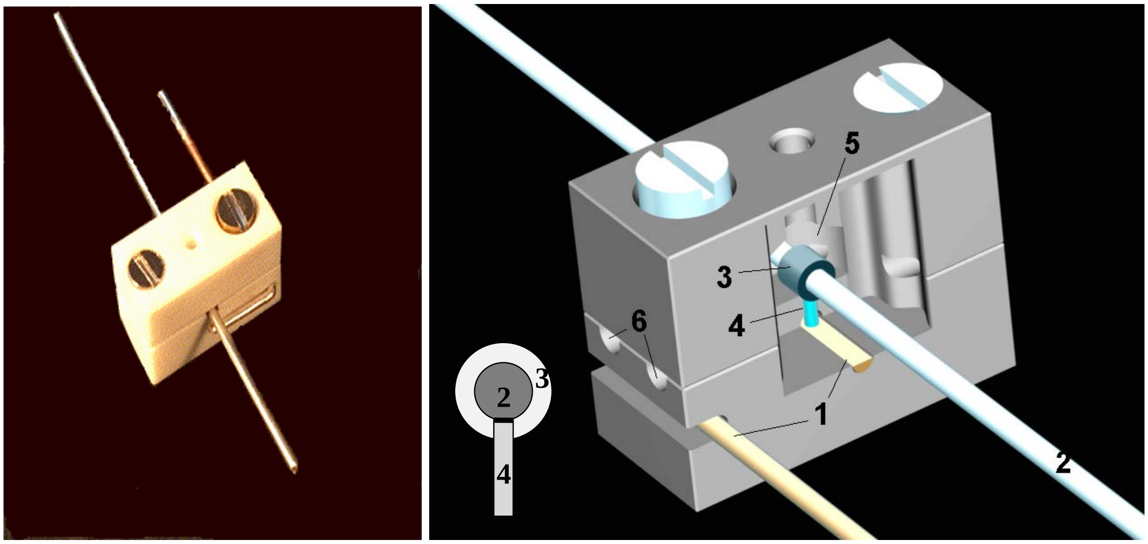

Figure 4.3-6: Tip Heater; Left: photograph of tip-heater clamp (7.5×16×13mm) + strand; Right: drawing of tip-heater clamp with central part uncovered: 1 heater current lead, 2 sample, 3 thermo-sleeve (optional), 4 heater tip, 5 helium reservoir and 6 helium channels. The heater tip is squeezed between sample on top and the heater current lead from below (see small sketch).

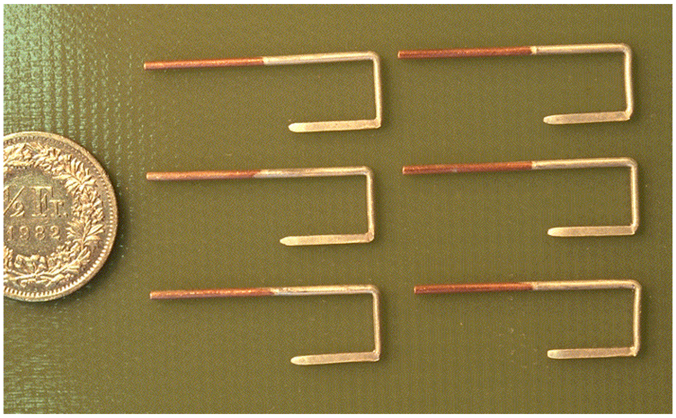

Figure 4.3-7: Tip-heater current leads. The end in contact with the heater tip is filed to half their diameter and silver coated The pressure is regulated by giving the blade a twist (maximum flexion is 0.5mm).

The heater current lead is a u-shaped copper rod, silver plated at the end which presses against the heater tip. It is easily inserted into the lower part of the clamp. The end of the heater-current lead is filed to half the diameter. Therefore it can be bent by this amount (~0.5mm) and generate a maximum pressure of $1\mathrm{N}/A_{\mathrm{contact}}$. At average pressure the contact resistance at the back end of the heater is kept down to some mΩ because both contacted surfaces are relatively big and silver-plated. One end of the heater current lead serves as one pole for both heater voltage and heater current. The second pole for the heater current is a point further away on the sample (see Figure 4.2-3). The tip-heater clamp has been designed to expose the sample to a maximum amount of helium. The distribution of helium can be shown in Figure 4.3-8. The lower part has two cooling channels perpendicular to the sample. Upper and lower Macor® part clamp the wire to the right and the left of the center exactly opposite to the spots where the cooling channels cross underneath the sample. They don't touch the sample in the center, where from the bottom the heater tip points to the wire. In the center the upper part features a dome connected to the top of the clamp through a drilling. The dome (or reservoir) is filled with helium during operation. This way the average cooled perimeter fraction is 90% and the sample is practically in an open bath environment. The pressure on the tip is given only by the flexion of the copper-blade pressing the tip from underneath.

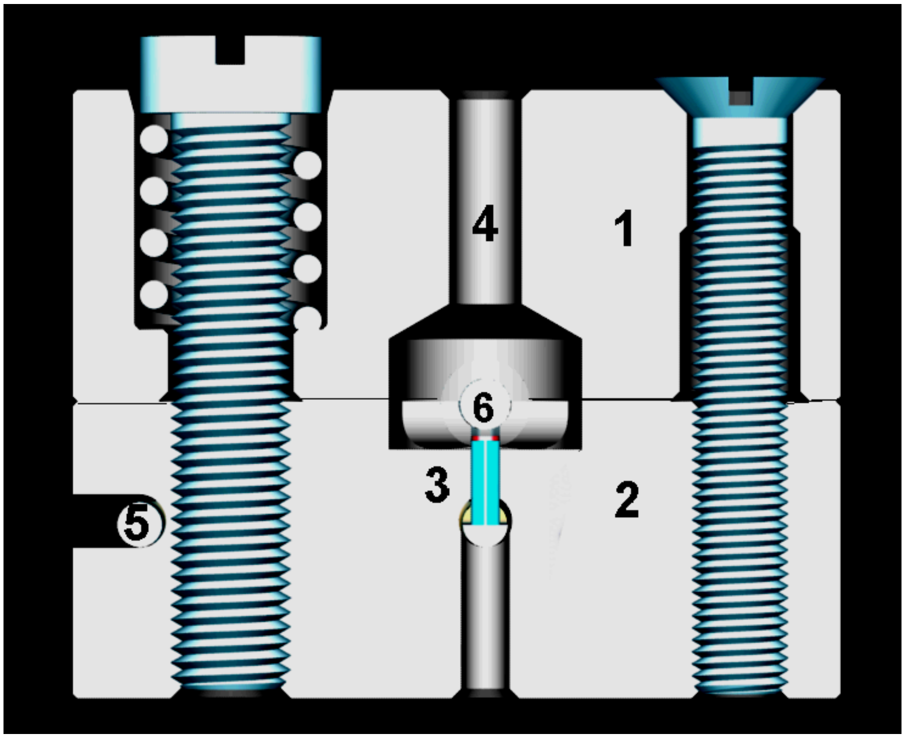

Figure 4.3-8: Tip-heater: cut through the middle plane: 1 clamp upper part, 2 clamp lower part, 3 tip with resistive deposit, 4 helium cavity, 5 heater current lead in lowest position, 6 sample;

The most complicated parts from the experimental- and fabrication point of view were the heater tips. The heater tips are small cylinders, length 1.85mm, diameter 0.6mm. Their complexity arises from the fact that they have to be the right compromise between low heat conductivity and small electric resistivity. At the same time the "active volume" should be as small as possible to reduce the thermal time constant. Figure 4.3-10 lists some of the most promising prototypes which have been developed, ordered from the less to the most successful. The first heater tip material was Graphite. It was believed to be the right compromise between a sufficiently good electrical conductor to conduct the heater current without excessive heat generation along the bulk and enough thermal

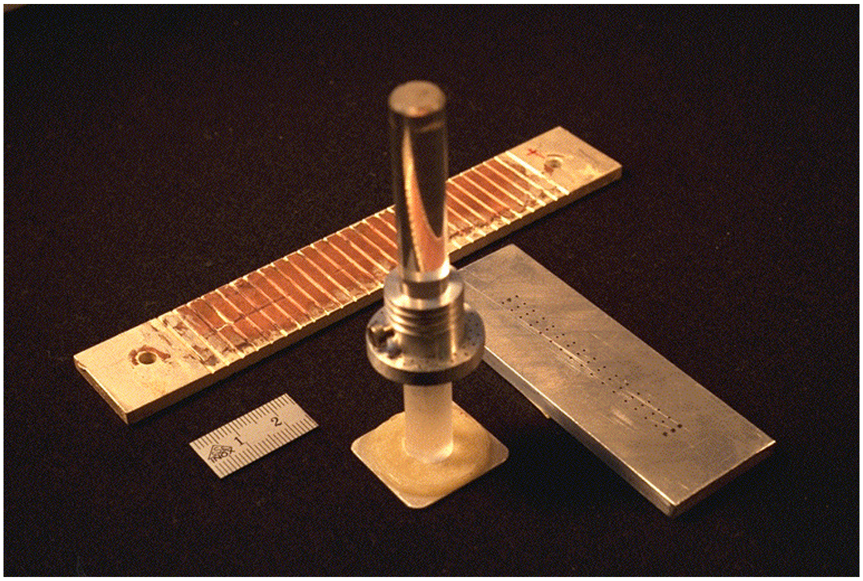

Figure 4.3-9: Tools for the preparation of the graphite heater tips: holder for the galvanic Ag-deposit, plate to file them to the right length, instrument to dissolve undesired Ag-traces from the top of the mines in nitric acid.

insulator to reduce back-heat losses from the hot spot. The back-end of the mine was coated with silver to ensure a good contact to the current lead. The heating was believed to occur mainly in the contact. Unfortunately the heating always occurred along the shaft of the mine giving a (rather stable) resistance of 0.3Ω. Measurements of QE (t_{ini}) clearly showed an increase in thermal time constant. The improved heater-tip prototypes therefore used insulating material (e.g. Macor®) conducting the heater current through a thin coating (type C in Figure 4.3-10). The coating of the small Macor® cylinders demanded a lot of efforts. A reasonably low resistance for painted (paint: Acheson's Electrodag 915RFU) silver films could only be achieved after heat treating (200°C, 1^h) at least two brushed layers (d=10µm). Silver sputtering was successful only after smoothing the edges, chemical cleansing, ultrasound cleaning, cathode beam pre-cleaning in vacuum and magnetron sputtering with a thin (0.1µm) sub-layer of titanium. With this type of conductive coating the resistance of the heater-system without resistive deposit (contacts included) could be lowered to less than 2% of the final value including the deposit. Since the surface ratio conductor/insulator is 1/20 the back-heat-loss fraction is significantly reduced. Different candidates have been tested for the resistive deposit on top. We consider charged epoxy-adhesives as the best choice because they usually have a resistivity in the

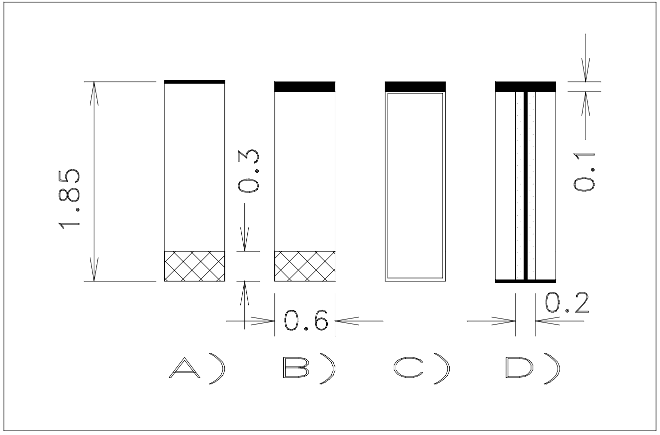

Figure 4.3-10: Heater-tips: A) graphite with silver plated end cap and 1µm Ge deposit on top; B) graphite with silver plated end cap and 100µm graphite paste deposit on top C) Macor® with 10µm silver paint or 3µm Ti/Ag coating and 100µm resistive graphite paste deposit on top; D) (not yet ready) Macor® with 0.2mm hole with 80µm Cu wire soldered on top and bottom to 10µm Cu-foil and with 100µm resistive graphite paste deposit on top; measures in mm;

required range of some Ωm at cryogenic temperatures and high magnetic fields and because they are easily applicable. The most promising materials are Emerson and Cumming's Eccobond 60L® and Epotecny's E300®, both suspensions of graphite in epoxy. The former is unfortunately soft and brittle and only weakly adhesive (although this can be improved by heating to 60°C during application) and the latter requires curing at 200°C and is less viscous. The deposit is polymerized under high pressure (150 bar). The mechanical stability of the deposits are satisfying if excessive shear stress is avoided. The resistive drop occurs only partly in the resistive cap: heater resistance measurements show a factor 2 increase from ambient temperature to liquid helium temperatures. Since this proportionality is observed as well for "naked heaters" (without resistive deposit) it hints towards a strong interference of contact resistance. On the other hand the noticeable effect of magnetic field (again a factor 2 increase) on resistance can only be explained by a resistance-increase of the deposit. Therefore the present heater-tip (type C) seems to work with a well balanced mixture of contact and resistive-layer resistance.

Experiments using a thin insulating thermo-retracting sleeve (~1mm) to reduce the heat loss from the heater revealed that the sleeve strongly modified the experimental results. The sleeve had the effect of excluding heat transfer in the high current MQE part, when the MPZ is shorter than the sleeve length. The sleeve was therefore abandoned.

First test of the tip heater (type C) raised an unprecedented reproducibility of 10% spread between two heaters on the same reference wire sample at 4.2K/8T (Figure 4.3-11).

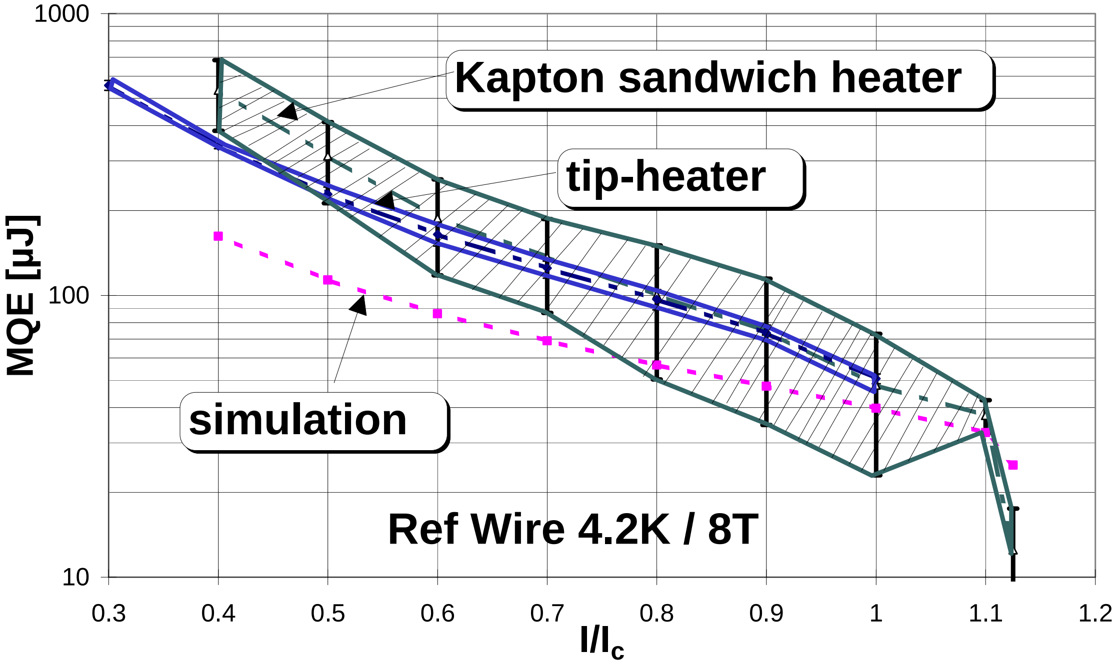

Figure 4.3-11: Comparison of reproducibility of old heater prototype and tip heater in 4.2K / 8T conditions. Reference strand measurements.

At 1.9K/9T the improvement was as well spectacular although it could not be improved beyond the factor 2. The two curves (for two different heaters H1 and H3) shown in Figure 4.3-12 nicely agree at high and low currents whereas they differ in the mid-current range. In simulations this effect occurs for a variation of Kapitza-conductance at equal helium volume An increase in Kapitza-conductance shifts the “helium-bump” to higher currents. The spread between the measurements on two heaters at 1.9K/9T on the same reference strand could be a consequence of a small variation of Kapitza-conductance (10-20%) of the coating at the two heater locations.

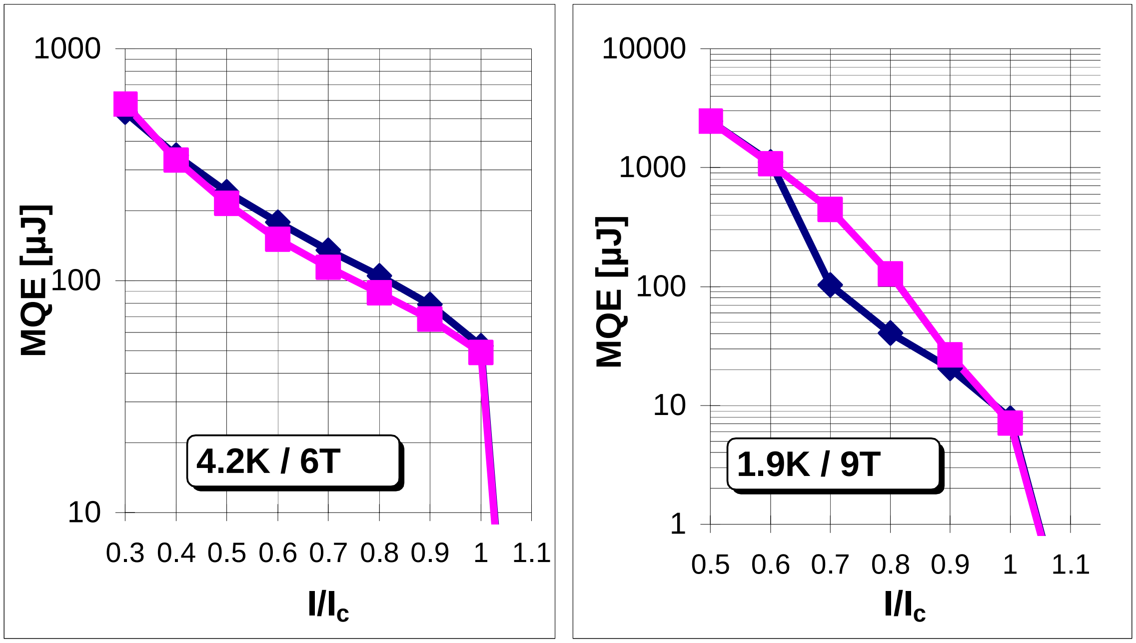

Figure 4.3-12: Macor®-tip test measurement, ref. strand. The reproducibility at 4.2K/6T has reached 10%. The measurement at 1.9K/9T shows an agreement between 2 measurements to a level of 10% at high and low current. The spread of the curves in the mid-current range can be explained by a difference of heat-transfer coefficient.

Without any doubt the MQE-measurements in superfluid helium show the long expected “superfluid enhancement”.

4.4 Collaborations

Other institutions are performing MQE- measurements on cables and strands in the frame of a collaboration agreement with CERN : A.K. Ghosh and W.B. Sampson at BNL and E. Baynham at DRAL perform as well MQE measurement on strands. Since their results will be discussed in the ongoing text it is necessary to introduce the particularities of their measurement set-up.

4.4.1 MQE at BNL

BNL performs MQE measurements at 4.2K/6T and 1.9K/9T. The particularities of the BNL MQE-set-up are:

- the operation in saturated conditions both at 4.2K and 1.9K (pumping on the bath)
- the attempt to reproduce the restricted cooling conditions as prevailing in a cable environment in a magnet.

The BNL heater technique is based on clamped graphite paste heaters similar to the here discussed Kapton®-sandwich heaters. The following fig. shows the BNL MQE set-up.

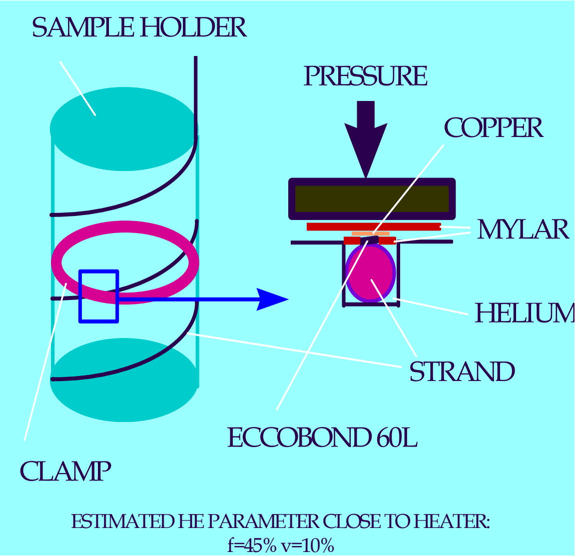

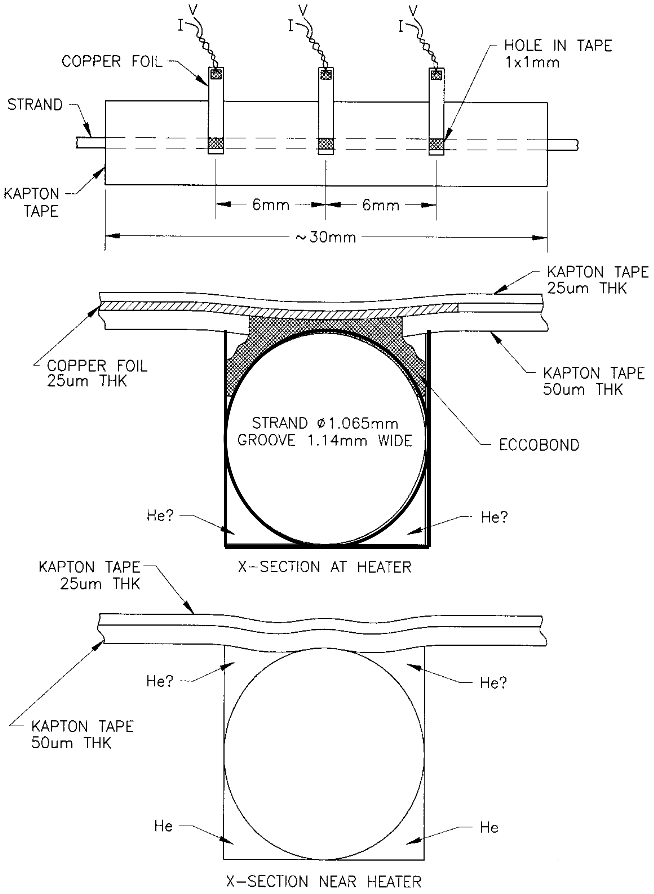

Figure 4.4-1: MQE-measurement set-up at BNL. Three identical heaters are attached to the sample with a aluminum ribbon clamped around the sample holder. The heater consist of three layers: a polyimide layer with a hole punched in it to apply the graphite paste (which flows into the upper right corners), a thin copper foil which serves as a current lead and an outer insulation layer. The heat is generated by a heater current crossing the resistive deposit. The heater current is taken away further on the strand. The strand sitting tightly in the groove is cooled only at the lower corners at the heater location. Measurements have shown that this corresponds to restricted cooling conditions as they might be given in a real cable environment in a magnet.

The reproducibility of the BNL measurements (measurements are performed on two or three heaters at a time) is normally within 10% although measurements with different heaters on the same strand differing by 100% have been observed from time to time. Comparative measurements between BNL and Cern (Figure 4.4-2) showed that BNL operates in close to adiabatic cooling conditions. This can be deduced from the following observations: there is coincidence in the measurements in helium I cooling conditions where the effect of cooling on MQE is small; in superfluid helium the BNL measurements usually yield results of the order of adiabatic or almost adiabatic measurements at Cern. Estimations of the cooling parameters in the BNL set-up are: v~10% and f<45%.

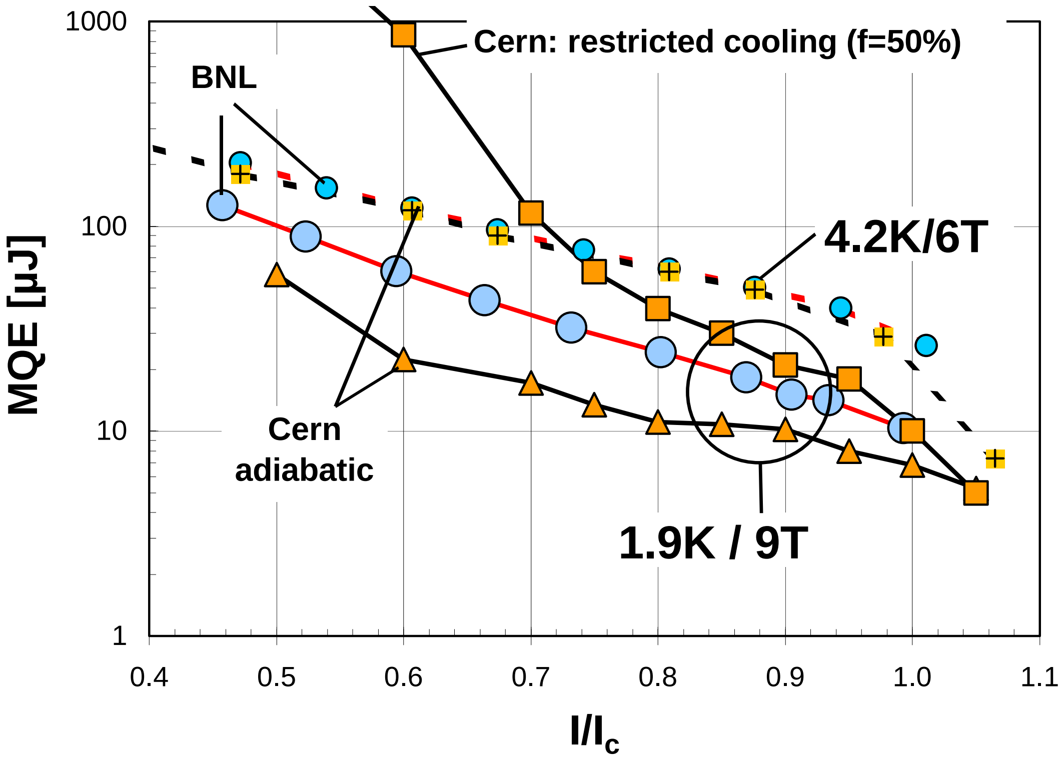

Figure 4.4-2: Comparative measurement Cern (triangles and squares) and BNL (circles), Reference strand. In 4.2K/6T conditions the measurement in adiabatic conditions (using a thermo-sleeve) at Cern yield the same result as the measurement "restricted" BNL cooling conditions. At 1.9K/9T the BNL case lies within 2 cases of restricted cooling conditions tested with the Cern set-up: the lower envelope being the adiabatic measurement, the upper envelope a 50% cooled perimeter (open bath) case.

4.4.2 QEM at DRAL

The RAL Quench Energy Margin (QEM) set-up allows to investigate the stability of strands with respect to spatially long (4cm) and short-time (40µs) heat pulses. Numerical calculations revealed that in this particular setup the effect of heat conduction to the sides can be neglected. This reduces the heat balance equation describing the problem to a simple first order in time differential equation (see chapter 3). The interpretation of the measurement is simplified. Conduction to the side being ruled out, the temperature of the strand becomes determined only by the interaction of cooling from the surface and heat generation within. The main parameter to be investigated with this type of measurement set-up is the effect of the cooling parameters, coating or helium volume.

The RAL-QE set-up consists of a special sample holder with:

-a 10 cm long glass tube with an inner ∅=1mm which contains the sample and helium,

-an outer alumina tube with metallized ends around the glass-tube where the heater coil (4cm long, Cu-wire) is wound and potted in epoxy,

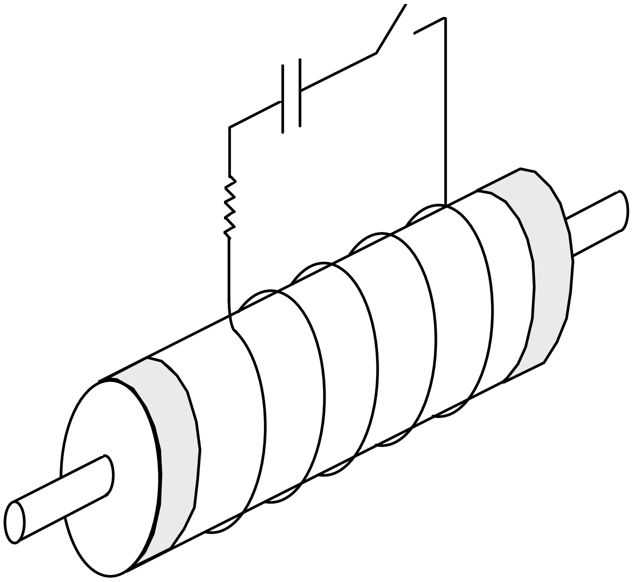

Figure 4.4-3: QEM-set-up at DRAL

-Cu-end-pieces welded onto the metallized ends of the alumina tube to allow for the mounting and soldering,

-an outer mold made of Pertinax to mechanically fix the cylindrical part to the sample insert. The tube diameter being 1mm only “outer layer” LHC strands can be measured (d=0.83mm). The sample fits just into the tube leaving only a thin layer of helium (w~85µm) in contact with the sample. Simulations showed that film-boiling is triggered always by channel limit when working in superfluid helium.

The sample holder can be sealed with solder and the tube evacuated to produce adiabatic conditions.

The current pulse generator consists of a simple combination of switch and capacitor. The capacitor discharge pulse (~10-100µs) triggers a magnet field pulse on the sample causing eddy-current heating in the outer skin (~20µm) of the sample. With a 2D finite element model a relation between charging voltage of the capacitor and heat dissipation of the type

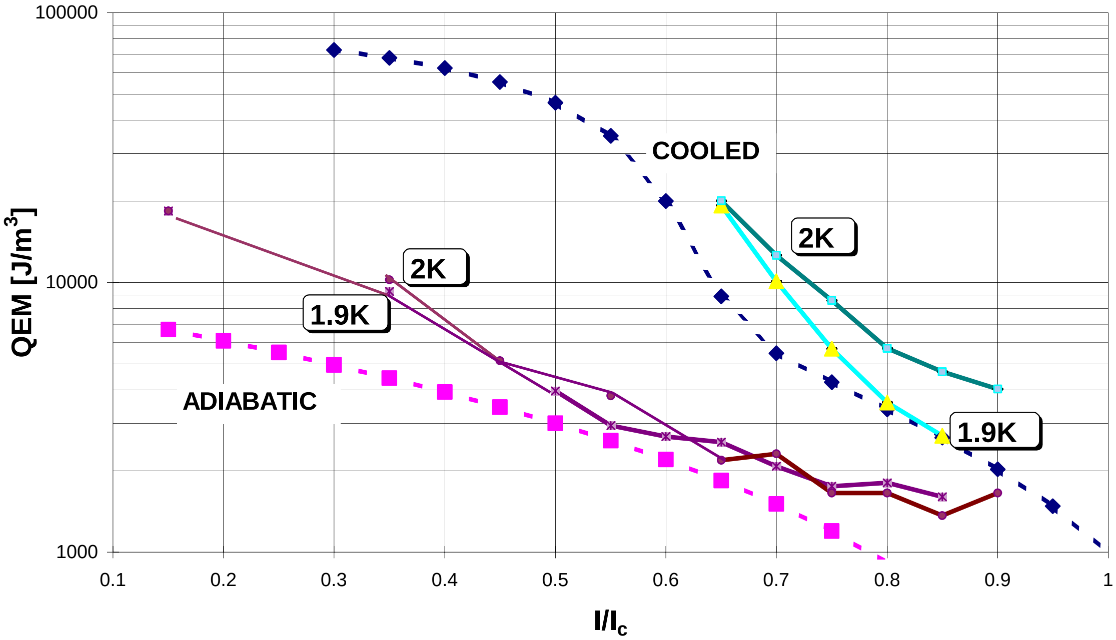

Figure 4.4-4: QE measurement on a test-sample (02B616684A3) in vacuum (lower curves) and cooled conditions at 1.9K and 2K, 8T. The comparison with simulations (dashed) reveals some unexplained spread in the adiabatic case. In cooled conditions the agreement of measurement and simulation is fair (cooling parameters: cooled perimeter fraction f=80%, channel width 85µm).

$E=fV^2$ was established. The pulse time is regulated with an additional resistor in series to the heater coil. A comparison with an adiabatic simulation shows a divergence at low and high currents (Figure 4.4-4), as if the energy calculation was optimized only for intermediate currents. The adiabatic simulation is based on the assumption that the strand temperature has to be kept under current sharing temperature. Simulations with the stability program (chapter 3) compared to the results of the long-heater model ($dT/dx=0$) showed total correspondence confirming that the 40mm heater can be regarded as infinitely long and heat conduction out of the ends is negligible. In fact the heat reaches the ends at ±5cm before quench decision time, but the temperature gradients at the ends are small (due to a small conductor temperature) and therefore heat transfer out through the ends negligible.

The DRAL long heater set-up can be used to investigate the effect of strand coating and helium volume (by partly filling the small volume left empty after the strand has been inserted into the tube with nylon fibers). The volume of helium in contact with the sample is very small (average channel width 85µm) and not equally distributed around the perimeter because the sample can not be kept in a concentric position within the tube. Simulations revealed that it is nevertheless reasonable to represent the helium geometry as a thin layer having as thickness the average over the full perimeter (85µm). Referring to chapter 5 this can be explained by the heat redistribution within the matrix from parts of the perimeter where the process is approaching film-boiling to parts which are still away from it.

Furthermore, by filling the tube with epoxy or other insulating materials, tests of the effect of heat transfer to epoxy on MQE can be conducted.

4.5 Conclusions

With the aim of characterizing the stability of LHC type strands a Minimum Quench Energy measurement technique has been developed. Former heater prototypes suffered from a lack of reproducibility. Finally a tip heater configuration was found to meet the requirements. The heat is generated in a thin graphite paste deposit which is pressed against the sample by means of a clamp. The clamp is designed to expose the sample to the open bath, having an average cooled perimeter fraction of 90%. This is crucial because, with the clamp being ~8mm long the complete MQE process usually takes place within the clamp. By covering the sample with thermo-retracting sleeves adiabatic conditions can be installed. Therefore the Cern set-up is designed to operate in the full range of cooling parameters. Experiments have shown that a set-up like the one at BNL using a “Kapton-sandwich-heater”, based as well on the graphite paste as the heat generating element, operates in strongly restricted cooling conditions like they prevail in a cable environment in a real magnet. The long heater set-up developed at DRAL works with a different concept: aiming at the measurement of the quench energy for the case of a temporarily short but spatially extended perturbation an inductive heater was developed. The long heater case is easy to analyze and emphasizes the effect of the cooling parameters.

The LHC stability project (in collaboration with groups at BNL and DRAL) aimed at the experimental investigation of the influence of various strand parameters, like coating, Cu/Sc ratio, matrix RRR, billet design and cooling, on the Minimum Quench Energy (MQE) of the superconducting strands for the main magnets of the Large Hadron Collider (LHC), designed to operate in superfluid helium at 1.9K, producing magnetic fields of up to 9T.

The experimental technique is based on a graphite paste tip heater described in chapter 4. The analysis of the measurements was facilitated by a theoretical model based on the numerical solution of the heat balance equation describing the MQE process. The model and the results of intensive model-calculations are presented in chapter 3.

Taking advantage of the huge number of different LHC strand prototypes, experimental sets containing samples differing with respect to only a few parameters could be arranged.

In this way the effect of the parameters mentioned above on the MQE could be investigated. The parameters were mainly varied within the narrow constraints of LHC strand specification. Therefore it may not be surprising that the differences in MQE found between different LHC-type samples were not big. Nevertheless in some cases samples with parameter variations exceeding the limits of LHC design have been tested to verify the theoretical predictions of the model and thus confirm the understanding of the MQE process.

Definitely the most important parameter is the cooling: The most striking aspect of repeated measurements on a reference sample is that in open bath conditions the MQE as a function of transport current in superfluid helium can reach hundred times the MQE in adiabatic conditions (i.e. with the sample potted in a low conductivity medium). This extraordinary quench energy performance in superfluid helium has been predicted by many authors (e.g. in [Kobayashi 76]) but never been shown in superconductor stability experiments.

5. MEASUREMENTS AND ANALYSIS

5.1 4.2K versus 1.9K Measurements

The cooling properties of helium I are reduced by its modest heat conductivity (~0.02W/K/m), which is of the same order of magnitude as that of epoxy. Simulations presented in chapter 3 show that the helium I cooling configurations mostly run into film-boiling already during the MQE pulse. Helium I cases are therefore essentially "gas-cooled". Simulations indicate furthermore that a lack of cooling level out differences in MQE. Resuming, MQE measurements on a series of LHC-type strands at 4.2K / 6T were not expected to yield more than merely a statement on the order of magnitude of MQE (see chapter 5.6). The following plots compare the magnitudes related to a MQE measurement (MQE, quench propagation velocity, quench decision length, quench decision time) of a "typical" LHC strand (the characteristics are listed in the following table) at 1.9K / 9T and 4.2K / 6T. All these magnitudes reflect the general tendency of the 4.2K curves being less sensitive to changes in the cooling, whereas the 1.9K cases undergo dramatic changes when switching from adiabatic to cooled conditions.

Stability item	**Strands ID**	**Fil∅ [μm]**	**Stack**	**RRR**	**$\rho_{Cu}\cdot 10^{10}$ [Ωm]**	**Cu/Sc ratio**	**∅ [mm]**	**Coat**	**Ic [A] (1.9K/9T)**	**n (1.9K/9T)**
Comparison between 4.2K/6T and 1.9K/9T	01D95091A19S	7	Single	133	5.8	1.62	1.064	SnAg	786	54

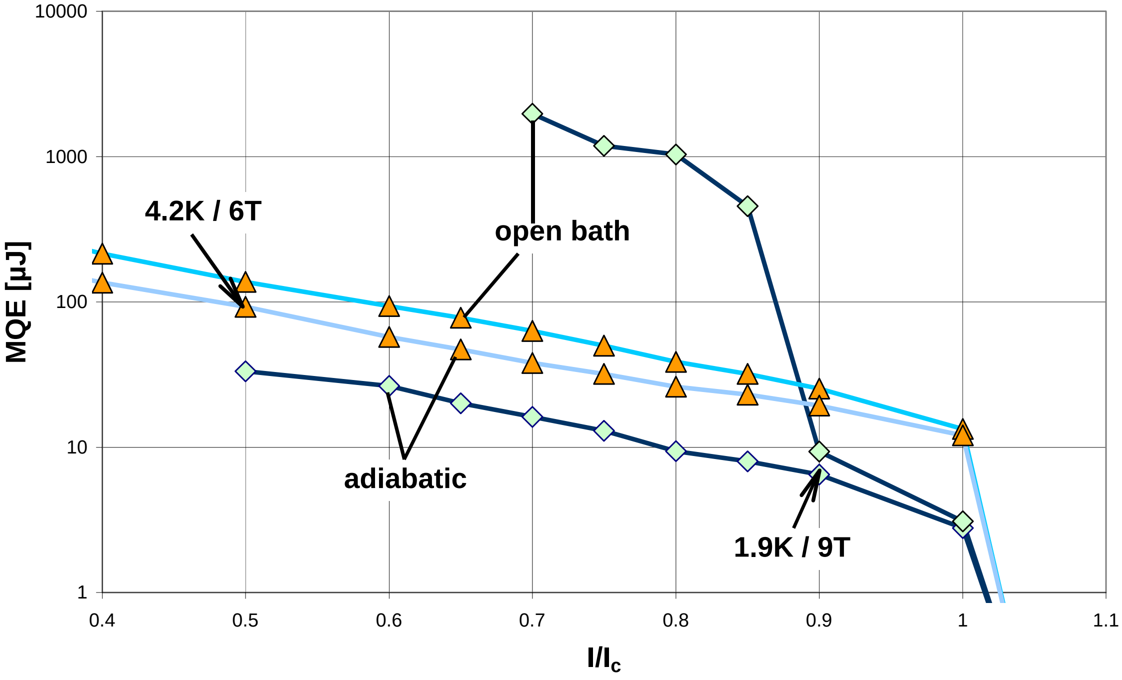

Figure 5.1-1: MQE measurements on sample 01D95091A19S at 4.2K/6T (triangles) and 1.9K/9T(squares) in open bath and adiabatic conditions. As predicted by the numerical model the difference between cooled and adiabatic MQE in helium I at 4.2K is small (< factor 2). This is a

consequence of the poor cooling properties of pool-boiling helium I. Note the characteristic shape of the MQE curve in cooled conditions at 1.9K/9T: adiabatic at the high current end, the "superfluid enhancement" at i<0.9.

Although small with respect to superfluid enhancement the factor 2 increase in pool-boiling HeI cooling has raised a lot of discussions in the past.
At this stage it is interesting to note the difference between adiabatic conditions at 4.2K and 1.9K. The adiabatic 1.9K curve in Figure 5.1-1 clearly reflects the decrease in c_p (~-70% from 4.2K to 1.9K) and the 25% increase in matrix resistivity due to the 3T shift. LHC strands have approximately the same critical current at 4.2K/xT and 1.9K(x+3T).

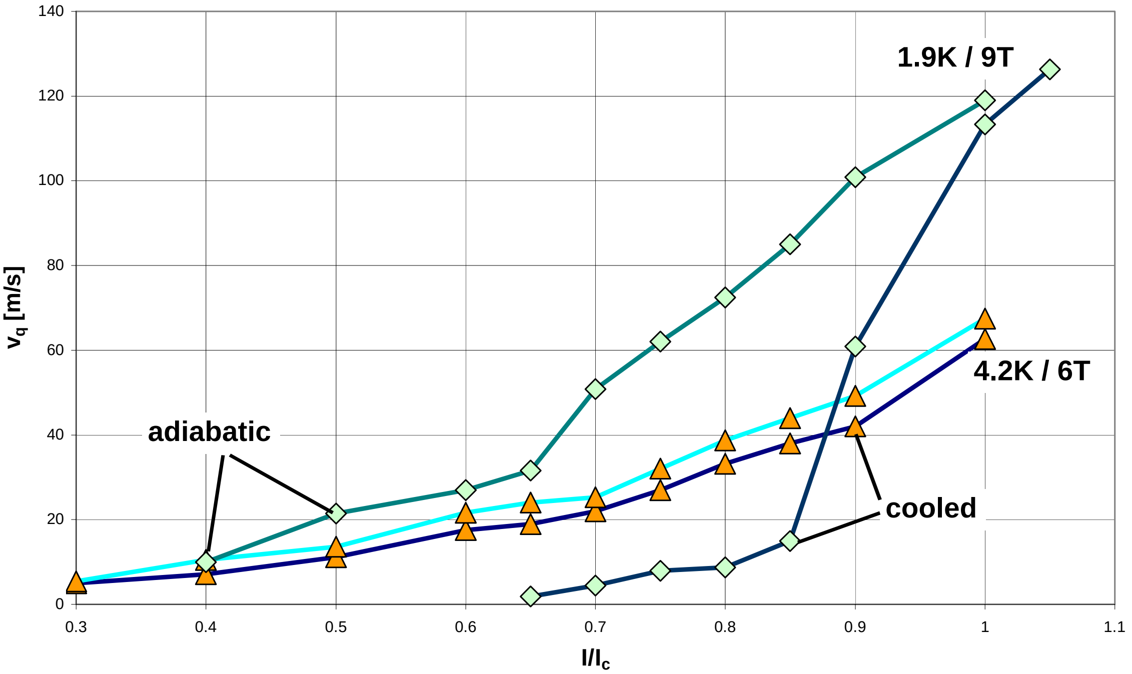

Figure 5.1-2: Quench propagation velocity measurements, 1.9K/9T and 4.2K/6T, strand: 01D95091A19S. The quench propagation velocity data show the same characteristic behavior as the MQE data in Figure 5.1-1: While at high current the cooled and the adiabatic v_q converge, the superfluid enhancement in 1.9K/9T conditions is reflected in the quench propagation velocity as a sharp drop. At high currents the propagation velocity at 4.2K/6T (cooled and adiabatic) is smaller than at 1.9K/9T. This reflects the "adiabatic advantage" of the 4.2K cases (higher c_p, lower matrix resistivity). The difference between the cooled and the adiabatic case is again small at 4.2K.

The following plots do not only serve the purpose of comparing cooling in superfluid and pool-boiling helium but to give a hint of the order of the different magnitudes measured in the course of an MQE measurement: e.g. at 1.9K 9T at $0.7I_c$ (~ operating current of strand in LHC dipole magnet), a LHC-type strand has a (non calibrated) MQE of *3mJ* in cooled and *30µJ* in adiabatic conditions, a quench propagation velocity of *5m/s* / *50m/s*, a quench decision length (proportional to MPZ) of *10mm* / *1mm* and a quench decision time of *1ms* / *50µs* in cooled and adiabatic conditions. The quench decision length is the normal zone length ($T>T_c$) which produces exactly the voltage at quench decision time. At quench decision time the voltage or the temperature profile of the just quenching case and the just recovering case start to diverge. Note, that precise quench decision time measurements usually demand a lot of effort and time (which may not always be justified) because the bifurcation of quench and non-quench voltage moves back and forth by some 50 or 100µs as a response to a change in energy smaller than 1% (required accuracy in the energy measurement). Note as well that the quench propagation velocity measurement is totally independent of the MQE measurement and therefore serves the purpose of confirming the trends found in MQE measurements.

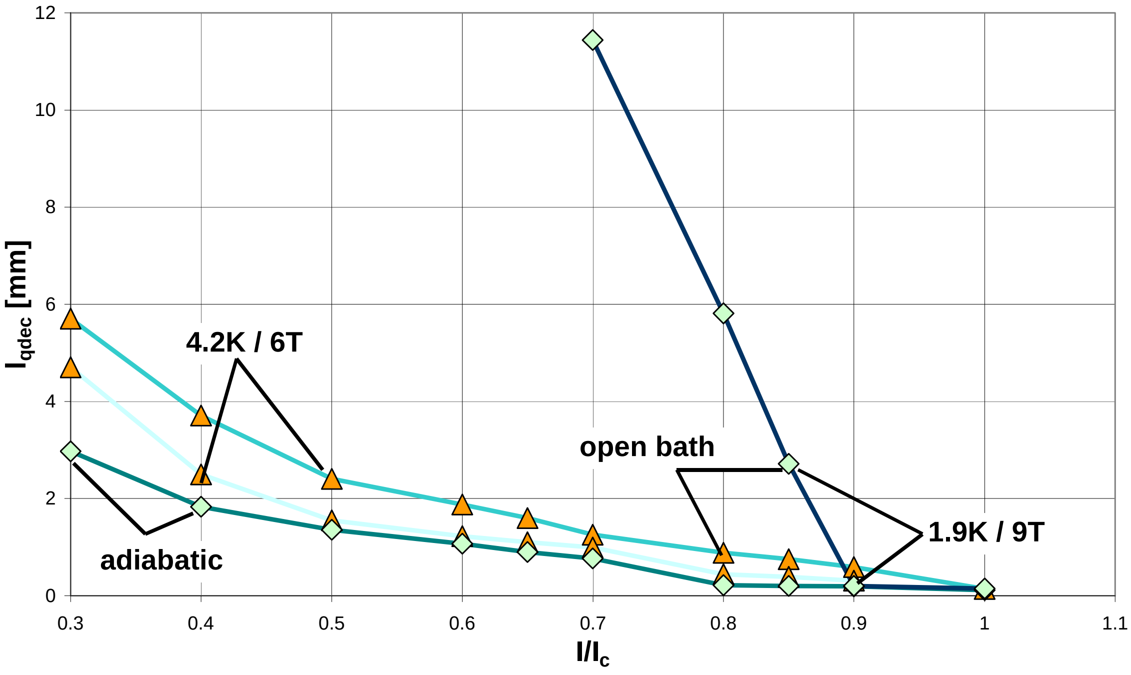

Figure 5.1-3: Quench decision length measurements, 1.9K/9T and 4.2K/6T, strand: 01D95091A19S. The small difference between cooled and adiabatic case at 4.2K can be seen as well in the quench decision length. The superfluid enhancement is reflected in the 1.9K curve as a sharp rise of the quench decision length at i<0.9.

As discussed in chapter 4.4.1 the group at BNL measures the MQE in cooling conditions resembling those in the real magnet. They therefore control the helium volume in contact with the strand as well as the wetted perimeter by mounting the sample tightly in a rectangular groove and covering the groove with the heater. The so obtained cooling parameters are v~10% and f<40% (see chapter 3 for the nomenclature). Using saturated instead of subcooled superfluid, they add another element deteriorating the cooling performance. The comparison of a Cern and a BNL measurement on a reference sample in chapter 4.4.1 shows that the BNL curve ends up close to the adiabatic Cern measurement. We derive from this experimental fact that the strands in an LHC magnet will operate almost in adiabatic conditions. Resuming Figure 5.1-1 to Figure 5.1-4 and taking into account the MQE results found in the restricted cooling scheme of the BNL set-up, LHC magnets operate with a MQE of ~50µJ, a quench propagation velocity of ~40m/s, an Minimum Propagating Zone length of ~1mm and a quench decision time of ~100µs.

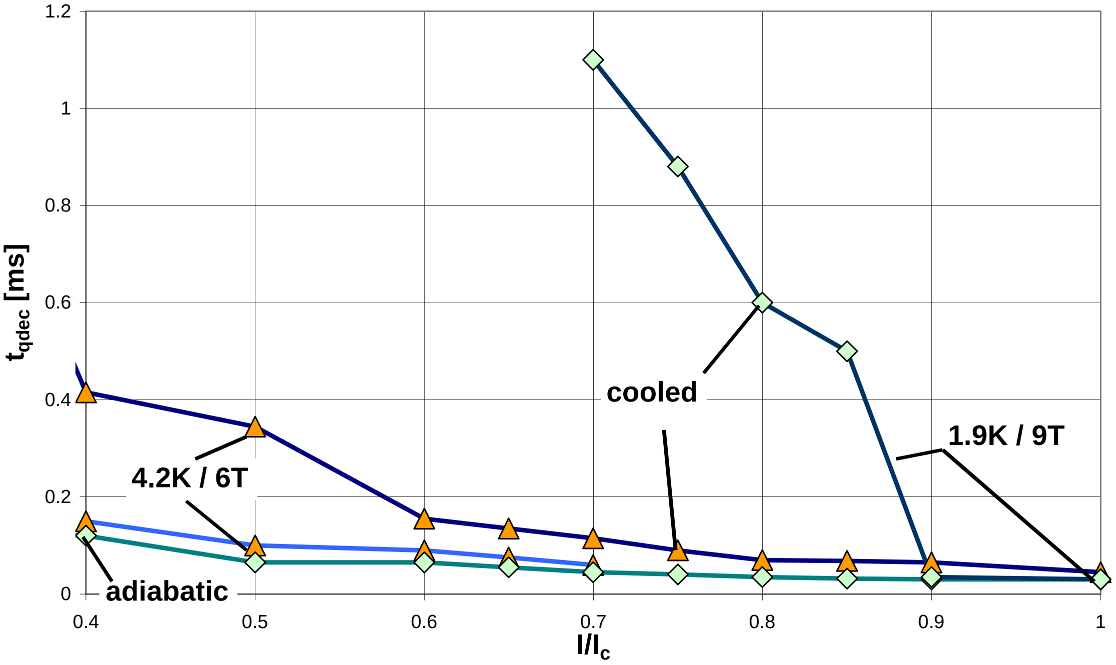

Figure 5.1-4: Quench decision time measurements, 1.9K/9T and 4.2K/6T, strand: 01D95091A19S. The superfluid enhancement is reflected in the 1.9K curve as a sharp rise of the quench decision time at i<0.9.

5.2 Variation of the Cooling Parameters

Undoubtedly the cooling is the crucial parameter for the MQE of superconducting strands. The cooling parameters are related to the rate of heat transfer through f (cooled perimeter fraction which acts as a multiplier of the heat transfer correlation in the heat balance equation describing the MQE process) and to the heat absorption capacity of the cooling volume through v (relative helium volume, normalized on conductor volume). The following tests related to the effect of cooling on MQE were conducted on the reference strand:

- Measurements varying the length of an uncooled zone centered around the heater, using thermo-retracting sleeves of different lengths.
- Experiments involving the variation of the cooled perimeter fraction f by covering portions of the perimeter with an insulator.
- An (indirect) investigation of the effect of helium volume on MQE, varying the temperature of the He-II bath.
- Furthermore the MQE of a strand with and without a (CuNi-) barrier has been measured to evaluate the effect of thermal barriers not on the surface, but within the strand.
- Another series of MQE measurements was dedicated to a sample with different coatings (bare, SnAg, SnNi, CuSn).

5.2.1 The Sleeve Effect

A common feature of the MQE(i) curves of LHC-type strands (Figure 5.1-1) is that at the high current end they are essentially adiabatic (as if uncooled). Below a particular current which may vary the MQE curve changes slope and departs from the “adiabatic” regime. This sudden rise of MQE is denoted “superfluid enhancement” (or bump) because it is related to the extraordinary cooling performance of superfluid helium. There is no such bump in cases cooled by HeI. To confirm the here given interpretation of the bump-like transition of the MQE curve a test series involving the variation of an adiabatic length centered around the heater (1mm, 3mm, “infinitely” long) was effectuated. The sleeve is supposed to suppress the effect of cooling and therefore expected to shift the superfluid enhancement to lower currents. Thermo retractable sleeves of different lengths (with a sealed passage for the heater tip) were used to insulate the central part of the sample along 1mm, 3mm and a few cm (=infinitely long). Consult Fig. 4.3.6 to see an example of measurement set-up with sleeve mounted.
The following table resumes the characteristics of the reference wire used in this test.

Stability item	**Strands ID**	**Fil∅ [µm]**	**Stack**	**RRR**	**$\rho_{Cu}\cdot10^{10}$ [Ωm]**	**Cu/Sc ratio**	**∅ [mm]**	**Coat**	**Ic [A] (1.9K/9T)**	**n (1.9K/9T)**
Cooling parameter	CERN REF 01E	7	Double	127	5.5	1.6	1.065	SnAg	739	38

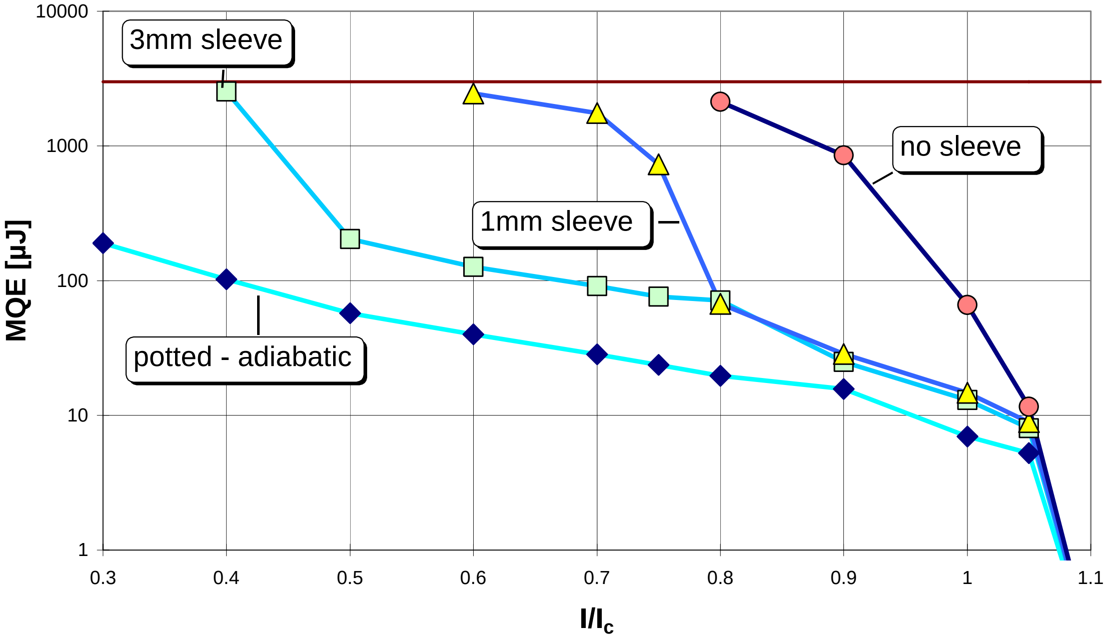

Figure 5.2-1: “Sleeve-effect” on MQE, reference strand measurement, 1.9K/9T. Covering 1mm, 3mm or the whole sample with a thermo-retracting sleeve. The length of the sleeve determines the current at which the MQE changes from the adiabatic to the cooled regime.

The experimental MQE-curves obtained this way (Figure 5.2-1) reproduce the expected pattern, namely a shift of the superfluid enhancement bump to lower currents depending on the adiabatic length. An understanding of the process can be gathered from the quench decision length (Figure 5.2-2): As long as the quench decision length is smaller than the

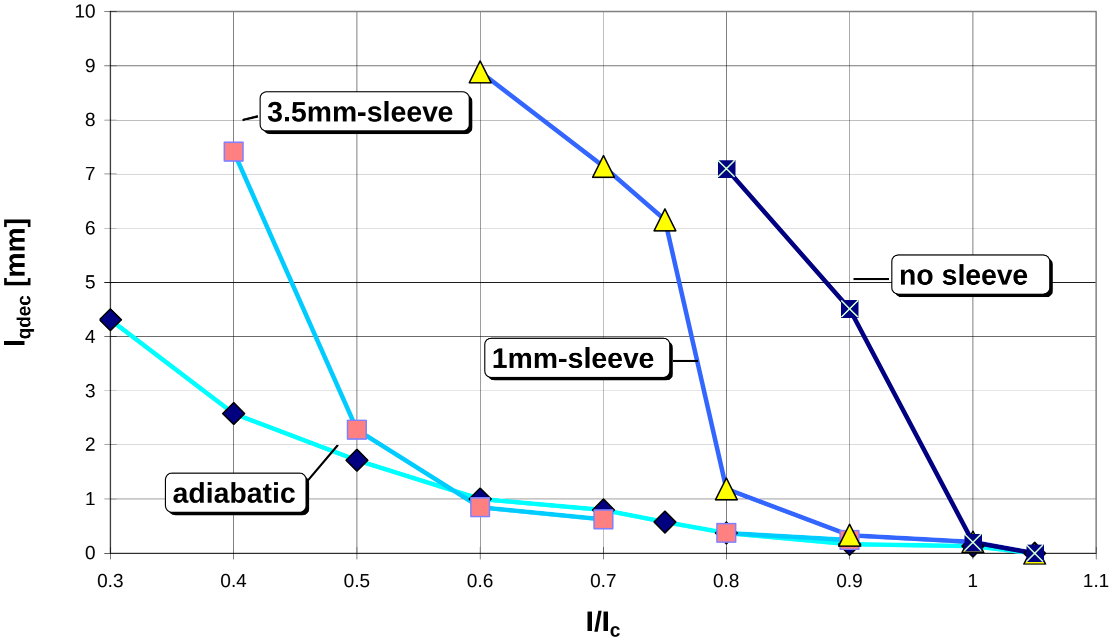

Figure 5.2-2: "Sleeve-effect" on quench decision length, reference strand measurement, 1.9K/9T. The quench decision length is the equivalent length of a normal zone with T<15K in which the transport current generates the measured quench decision voltage. The quench decision voltage is the voltage at quench decision time.

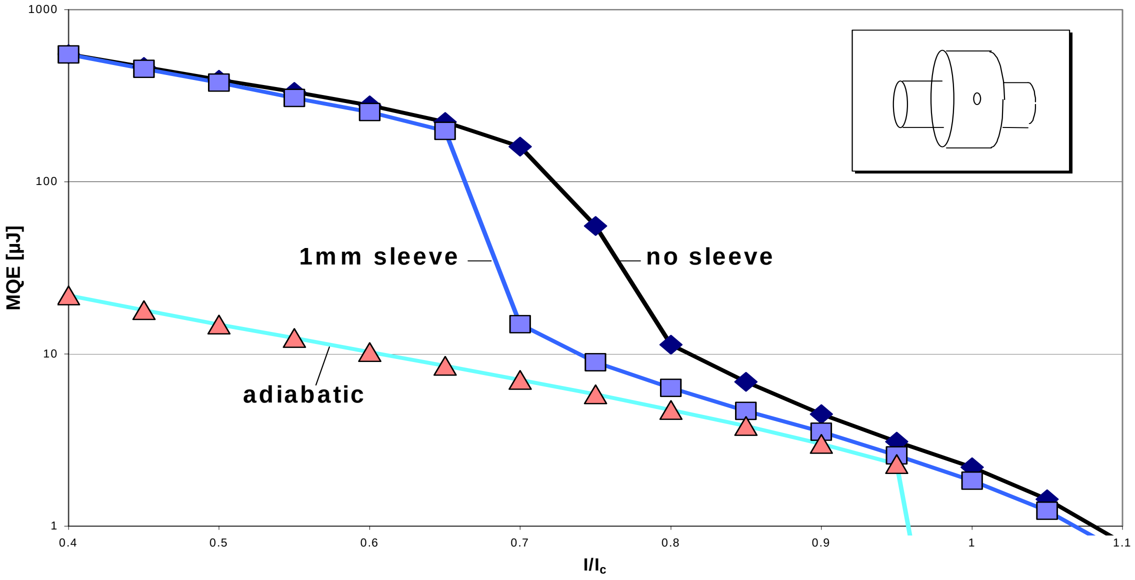

Figure 5.2-3: "Sleeve-effect" on MQE, reference strand simulation, 1.9K/9T. The effect of an adiabatic zone of length ±0.5mm on MQE is to shift the onset of the superfluid enhancement to lower currents. Although the sleeve-effect simulation produces the same pattern (shift of bump to lower currents) as the measurements presented in Figure 5.2-1 the quantitative agreement between simulation and measurement is insufficient. More details on the quantitative discrepancy of model

and measurements can be found in the chapter on the stability program.

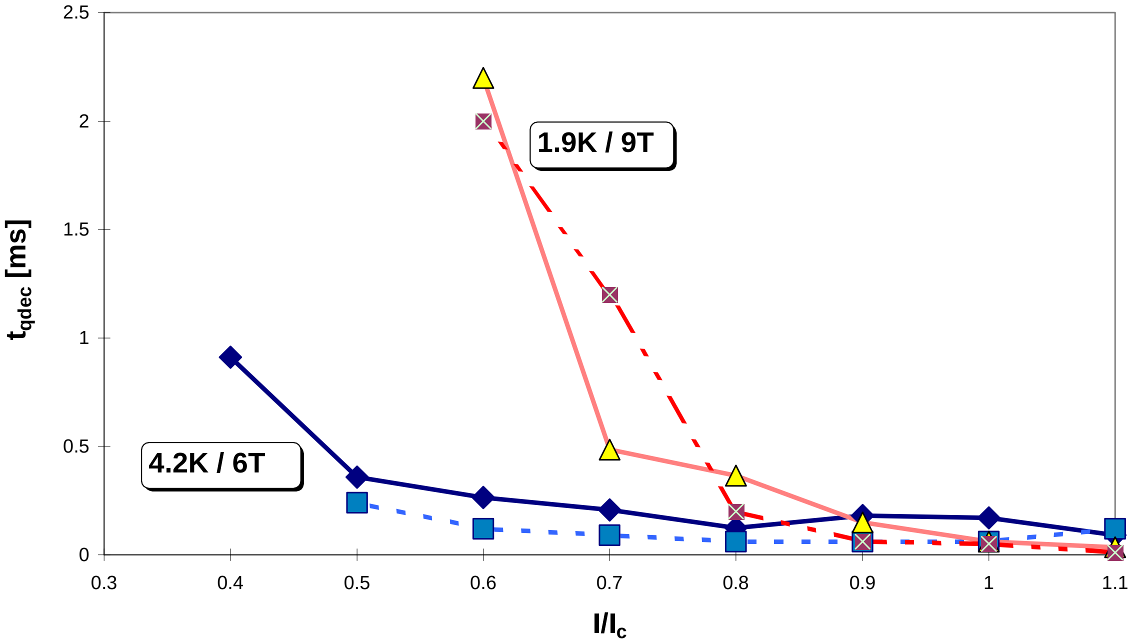

Figure 5.2-4: Quench decision time in 1mm-adiabatic conditions. Sleeve-effect measurement (line) and simulation (dotted), reference strand 1.9K/9T and 4.2K/6T. Contrary to the usual discrepancy of measurement and simulation the case of the quench decision time seems to show a good agreement. Unfortunately it is difficult to measure quench decision times with high accuracy. Therefore the experimental values presented here represent a lower limit, so that the usual discrepancy between measurement and simulation (e.g. Figure 5.2-7) due to partial inadequacy of the cooling model is restored.

uncooled length the case is definitely adiabatic. As soon as the MPZ emerges from under the sleeve, the quench decision length, quench decision time and MQE rise strongly to reach the cooled homologue. A MQE simulation including the "sleeve-effect" reproduces exactly this pattern (Figure 5.2-3), although the quantitative agreement with measurement is poor (factor 10 difference in MQE, bump onset for open bath conditions $0.8I_c$ in simulation and $1.1I_c$ in measurement). Interestingly calculated and measured quench-decision times agree very well for the no sleeve and 1mm sleeve case (Figure 5.2-4).

Metastable normal zones appeared in the sleeve-effect measurements. According to [Meuris 81] these zones appear at discontinuities in the cooling (e.g. edge of sleeve). Metastable normal zones never appeared in adiabatic conditions. It is useful to display some quench voltage curves: Figure 5.2-5 shows the non quench voltage (2cm voltage tap centered around the initially heated part) in a reference strand MQE measurement. The adiabatic quench decision times and lengths can be deduced from these data together with the voltages in the quench case. Figure 5.2-6 demonstrates the type of metastable normal zones encountered in the sleeve-effect measurements. For i>0.9 quench decision times are short and the MQE is essentially of the adiabatic kind. At $0.8I_c$ the quench decision length becomes comparable to the sleeve length. The sudden change in the heat transfer function at the edge of the sleeve results in a delay of the quench during 10 ms, followed presumably by on-set of burn-out at the end of the sleeve and completion of the quench. At 0.75I_c the MPZ becomes noticeably longer than the sleeve and cooling is switched on.

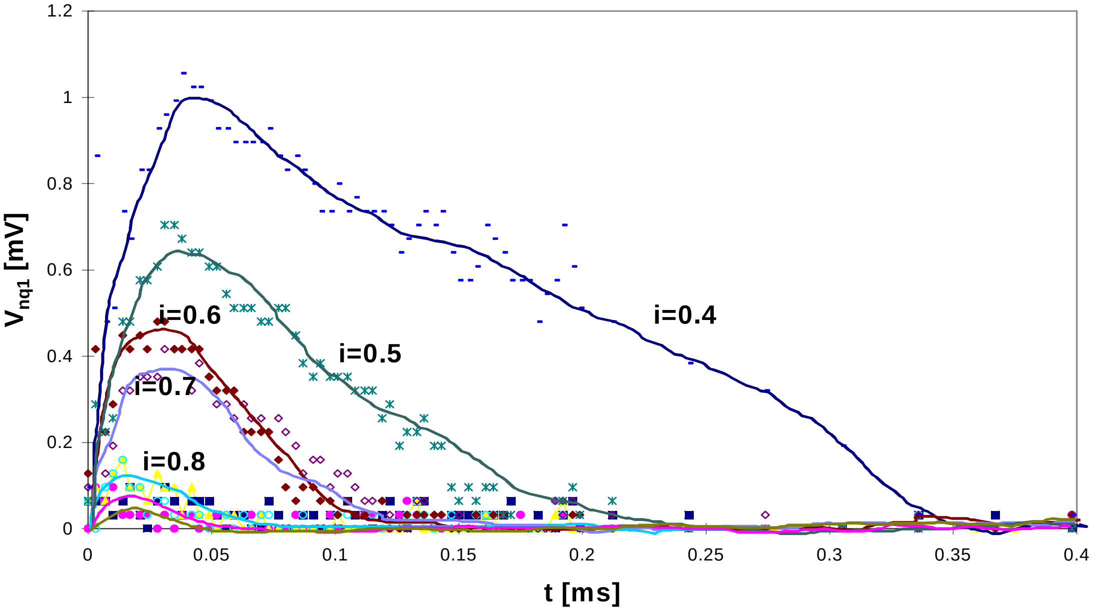

Figure 5.2-5: Non quench voltage at different currents (i=I/I_c), reference strand measurement, 1.9K/9T, adiabatic conditions. The quench decision lengths in the adiabatic case in Figure 5.2-2 are deduced from these curves. The 2 smallest curves bearing no legend correspond to i=0.9, i=1.

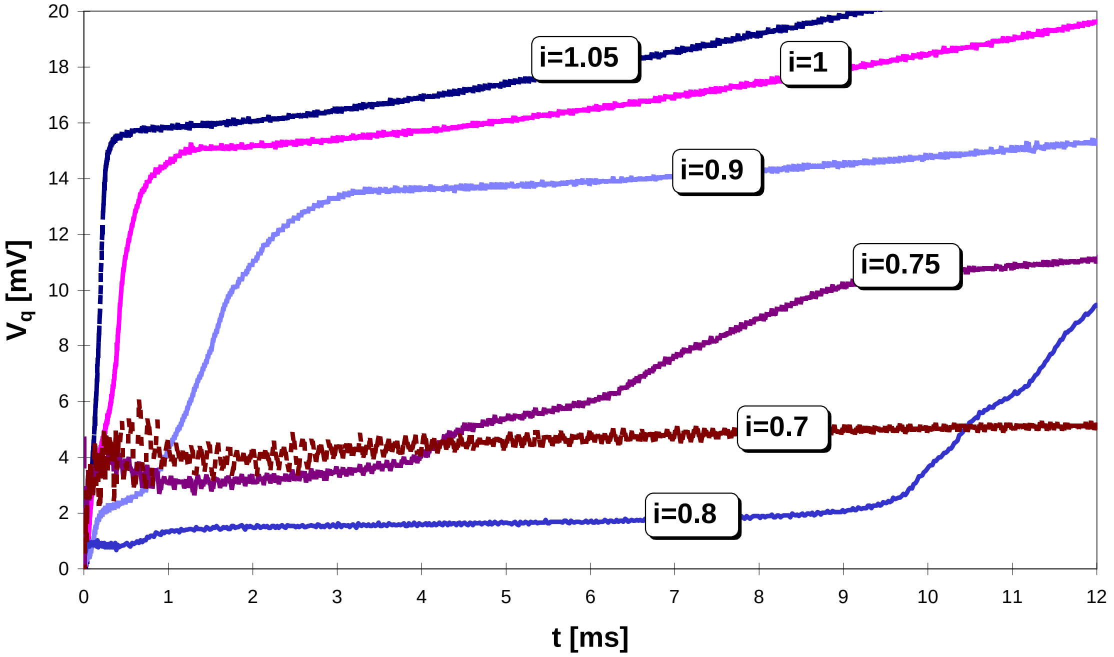

Figure 5.2-6: Quench voltages versus reduced current i (i=I/I_c), reference strand measurements, 1.9K/9T, 1mm sleeve case. The cases i≥0.9 are adiabatic. A 10ms-step occurs in the transition at 0.8I_c. The voltage corresponds a normal zone of ~ 1.5mm. At 0.75Ic the pulse energy rises

considerably (see Figure 5.2-1), the MPZ becomes longer than the sleeve and open bath conditions set in. At 0.7I_c a stable normal zone of ~7mm forms at 2.39mJ. It neither grows nor shrinks.

The discontinuity at the edge of the sleeve causes just a short moment of indecision in the voltage trace. At 0.7 I_c the MPZ becomes comparable to the size of the clamp (~7mm). The cooled perimeter fraction at the points where the clamp touches the strand is reduced below average. Therefore these points are discontinuities in the cooling function. A stable normal zone forms at 2.39mJ, and quench becomes impossible. Taking into account that the quench propagation velocity converges to zero at that current (see Figure 5.2-7), this case can be classified as “Maddock-stable”. A simple calculation (assuming the peak temperature to stay within 15K) yields an admittedly high steady state heat transfer rate of ~175kW/m^2 to be in balance with the heat generation at 0.7I_c.

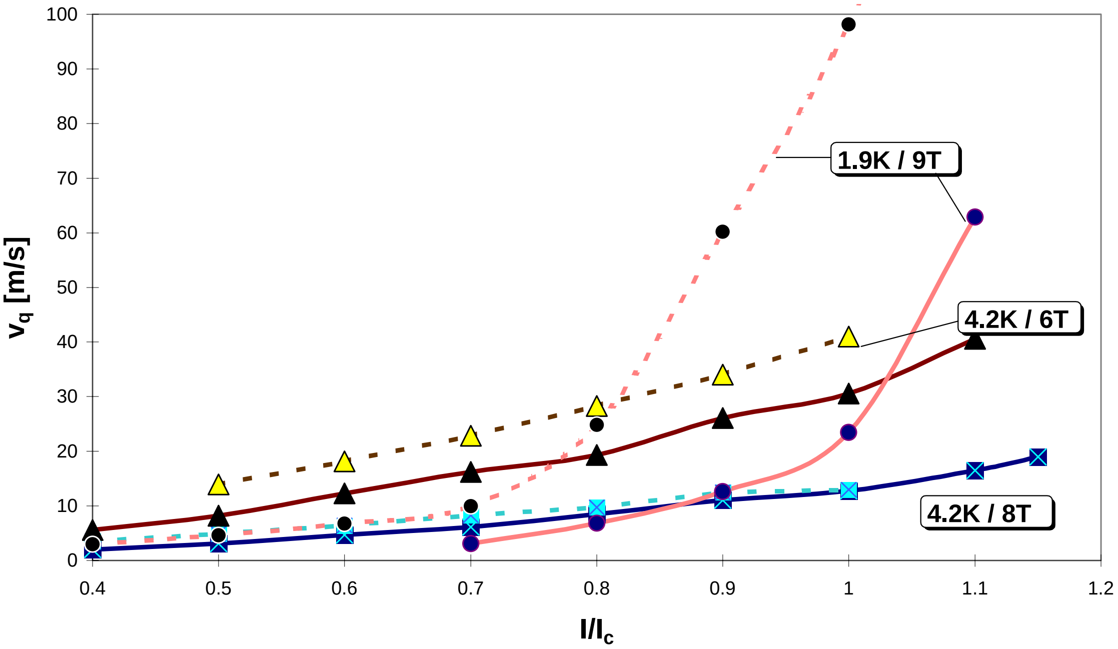

Figure 5.2-7: Quench propagation velocity, reference strand measurements and simulations (dotted) at 4.2K and 1.9K. The agreement of measurement and simulation is better in the pool-boiling cases than at 1.9K, mainly as a consequence of an inadequate cooling model. However, simulation and measurement indicate that the velocity converges to zero at i~0.7 in 1.9K/9T conditions.

5.2.2 Variation of the Cooled Perimeter

The cooled perimeter fraction f determines the strength of heat transfer because it appears in the heat balance equation describing the problem as a multiplier of the cooling function. Simulations of MQE with varying f (see next figure) produce a pattern similar to that encountered in the sleeve-effect case: MQE curves for the same helium volume parameter v (here v=1) but different f appear shifted along the current axis, with those having high cooled perimeter fraction having high superfluid enhancement onset currents. The specific shape of the curves, namely adiabatic tail, low current bump does almost not vary. The height of the “bump” is mainly determined by the helium volume parameters (more in chapter 5.2.3). The fact that the superfluid enhancement threshold current changes with the cooled perimeter fraction f (or heat transfer coefficient) shows that there is a threshold of cooling versus Joule heating which separates two regimes: one in which cooling acts and the other in which the cooling, though potentially present, cannot act.

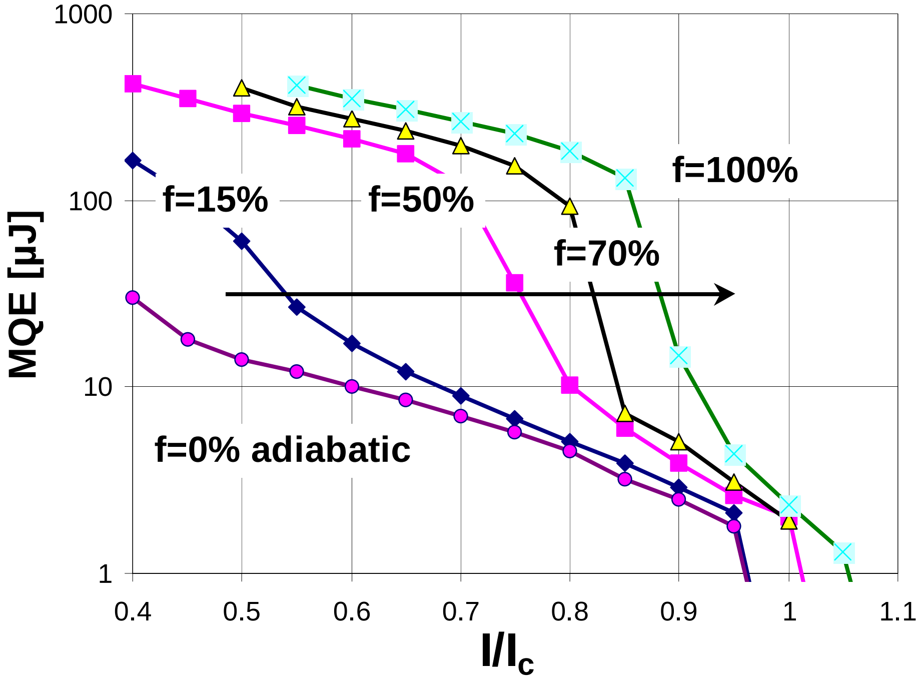

Figure 5.2-8: 1.9K/9T reference strand simulation of the effect of the cooled perimeter fraction f at fixed helium volume (200% of conductor volume). Heat transfer coefficients: a_K=180W/K^4/m^2 and a_{fb}=250W/K/m^2 for Kapitza heat transfer and film-boiling. An increased cooled perimeter fraction shifts the bump to higher currents (indicated by arrow).

The analysis of the simulated data reveals that the bump occurs when a recovery of the wire is possible even after the temperature has by far exceeded the critical temperature of the superconductor and partial burn-out along the initially heated length occurred. In this case heat transfer plays a noticeable role. Furthermore a prolonged quench decision time and an extended quench decision length amplify the positive effect of cooling. Above the bump, at high current, the MQE is hardly more than the enthalpy reserve of the wire between T_b and a temperature between T_{cs} and T_c. With the peak temperatures remaining below T_c the cooling rates are negligible. The superfluid enhancement of the MQE reflects not only the enthalpy reserve of the composite but also the heat absorption capacity of the volume of superfluid helium participating in the cooling process.

Some samples of the reference strand were partially covered around the perimeter in steps of 0, 10,30,50,70, 80 and 90% using a photosensitive varnish (commonly used in the production of printed circuit boards), exposing stripes of the extent listed above to UV-light using masks and dissolving the non-exposed part in a chemical bath. The experimental results (Figure 5.2-9) reproduced the pattern expected from the model calculations. The fact that the tip heater clamp allows the sample to be exposed maximally to a fraction of 90% explains why there is no f=1 measurement.

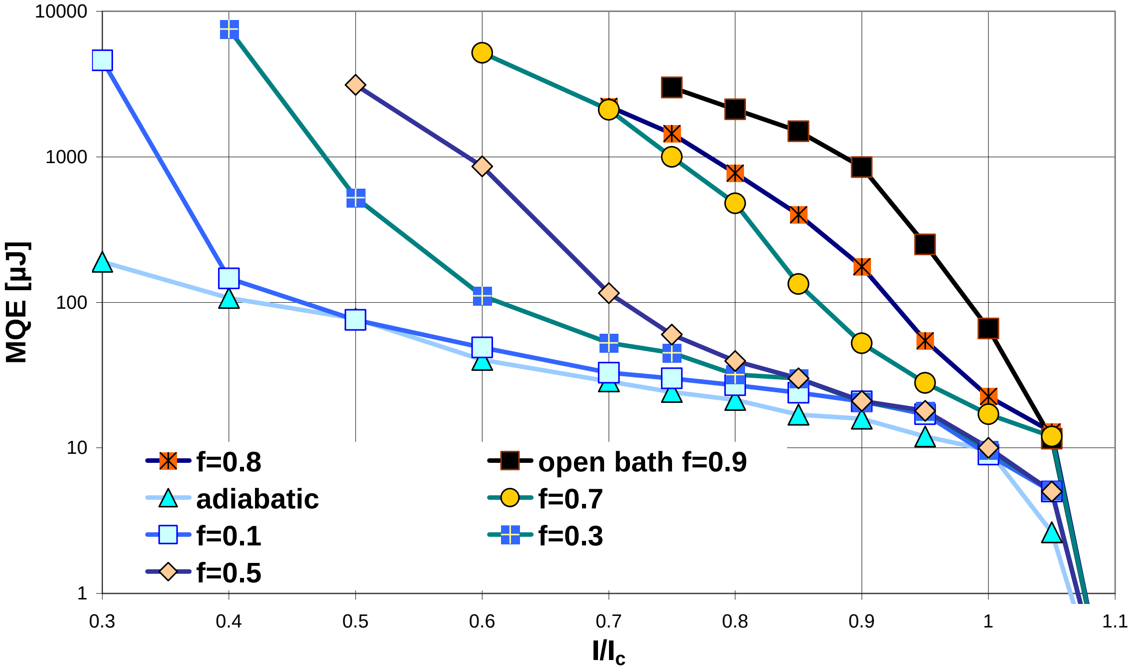

Figure 5.2-9: Reference strand MQE measurements at 1.9K/9T, open bath. Effect of the cooled perimeter fraction f on MQE. Compare to simulations in Fig. 5.2.8. Note that the experimental set-up is limited to E_{max}~5mJ. Therefore the convergence of the MQE curves at low i could not be verified. Nevertheless the trend of the curves indicates that they likely join above 10mJ.

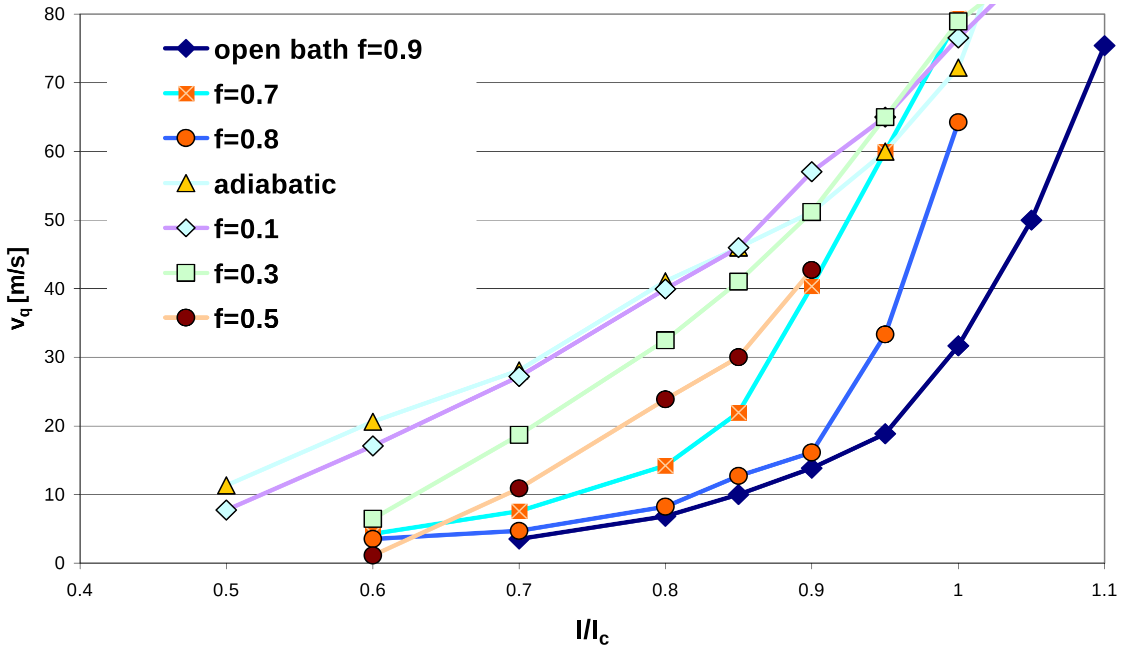

Figure 5.2-10: Quench propagation velocity, f-effect measurement, reference strand, 1.9K/9T. The

higher f, the higher the reduced current i at which v_q drops to the small values characterizing the "cooled regime".

There is a striking resemblance of sleeve- and f-effect. Comparing for example the i=0.5 point in the 1mm-sleeve measurement in Figure 5.2-1 and the f=0.5 case in Figure 5.2-9 (both have a MQE of ~3.1mJ and a quench decision length of ~9mm) reveals that in both cases the cooled fraction of surface along the quench decision length is ~0.55. This implies that for MQE only the average cooled surface along the MPZ counts and not the way the cooled spots are distributed. This can only be explained by a very good heat conduction within the matrix. This phenomenon is perhaps characteristic only of the type of strands discussed here. Strands of bigger size or different Cu/Sc ratio will certainly act differently. We believe that this observation, together with the good qualitative agreement of the MQE simulations and measurements in adiabatic conditions, is a retrospective justification of the one-dimensionality of the model explained in chapter 3. There remains a disadvantage of the sleeve-type set-up, the metastable normal zones.

The quench propagation velocity measurements (Figure 5.2-10) for varying cooled perimeter fraction reflects the same pattern as the MQE measurements.

5.2.3 Variation of the Bath Temperature

To test the predictions of the stability model concerning the effect of the reduced helium volume v (see chapter 3.11.4.1), an experimental set-up allowing the variation of the thickness of the helium layer surrounding the sample in steps of µm would be necessary. This is not easy to implement. Another way of testing the model predictions had to be found. As mentioned in chapter 3 the helium volume parameter in big open baths (~cm) becomes rather a critical time or energy related to a volume determined rather by the transient penetration depth of heat into the bath than by the real size of the bath. The following experiment verified the helium model in what refers to the "active" helium volume (the helium volume determined by the penetration depth of heat in a highly transient heat transfer process). The effect of a change in bath temperature at a given magnetic field on the MQE of a LHC-type strand is illustrated in Figure 5.2-11: A MQE curve at 10T/2K conditions clearly shows the effect of cooling to superfluid compared to a measurement at 10T/2.2K which occurred in helium I cooling conditions. Additionally a 2K/9T measurement is shown, revealing that at equal current and operating temperature the benefit of reducing the resistivity of the matrix (by-10%) and working further from I_c (e.g. 50% I_c instead of 90%) does not improve MQE as much as the change in cooling conditions from superfluid to normal fluid cooling (e.g. at 450A, factor 10 change for going from 2.2K to 2K, only factor 3 change for going from 10T to 9T).

By varying the temperature of the helium bath between 1.9K and 2.1K one does neither change drastically I_c (-8% from 1.85K to 2.1K) nor the specific heat (variation between 1.9K and 2.1K ~+15%) of the strand. Consequently, and this has been confirmed by measurement (Figure 5.2-12), the MQE should not vary strongly in the adiabatic case. Therefore only one curve is shown in Figure 5.2-12 to represent the adiabatic measurement (using thermo-sleeves to insulate the sample from the bath). On the other hand the open bath MQE reflects the variation in temperature because the diffusivity of helium II is a rapidly changing function of T between 1.9K and T_λ. The apparent heat conductivity of helium II is going from its maximum at 1.9K to zero at T_λ. The specific heat varies as well strongly in this temperature range and reaches its maximum at T_λ. The diffusivity therefore becomes a function which rapidly changes with temperature and it influences the heat transfer via the penetration depth of heat and henceforth the helium

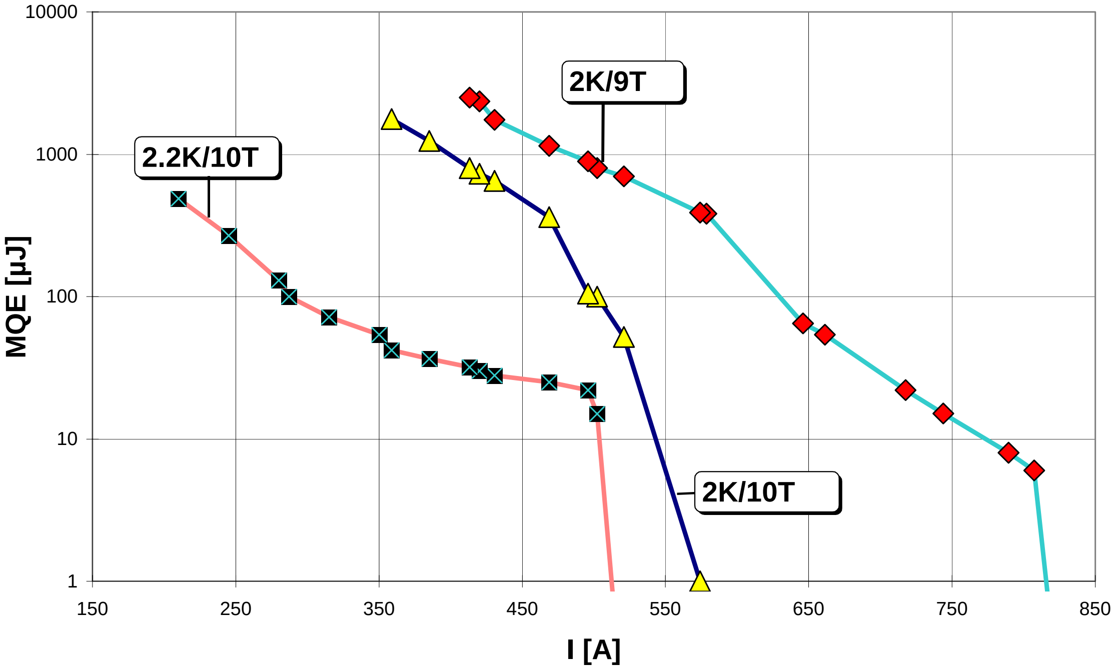

Figure 5.2-11: Reference wire MQE measurements below (2K) and above (2.2K) T_λ (10T) showing the effect of cooling to superfluid helium. And to illustrate the effect of a change in heat generation in equal cooling conditions (here B→9T) another measurement at 2K/9T.

volume participating in the heat transfer process (“active helium volume”). Therefore the experiment in Figure 5.2-12 is almost equivalent to varying the helium volume (“channel-limit”) in contact with the sample at a fixed temperature. Model calculations (see chapter 3.11.4.1) predict that the helium volume parameters affect mainly the amplitude of the “superfluid enhancement” in a MQE curve in a way similar to the stapled curves in Figure 5.2-12. Unfortunately the results in this figure cannot be related to the variation of diffusivity alone. Between the 1.9K and the 2.1K case the quench decision time drops roughly by 80% (e.g. in the i=0.9 case: from 0.4ms at 1.9K to 80µs at 2.1K). This effect adds to the difference in MQE for cases of varying bath temperature. Nevertheless, the MQE drops to a much lower value between 1.9K and 2.1K (down to 6% of the 1.9K value in the i=0.9 case), and this discrepancy can only be explained by the diffusivity effect. As expected the corresponding quench propagation velocity curves (Figure 5.2-13) show that with decreasing heat conductivity of the helium quench propagates faster. It is interesting to find the bell-shape of the apparent heat conductivity function of helium II as well in the quench propagation velocity measurements: the closer the bath temperature to 1.9K the smaller the slope of the bell-shaped curve and the closer together the stapled quench propagation velocity (and MQE) curves. A measurement at 1.85K (not added in Figure 5.2-12) was in the same range as the 1.9K and 1.95K measurements, which are indistinguishable with respect to the measurement uncertainty. Another prediction of the model, namely the saturation of the helium volume effect at approximately two times the conductor volume could not be tested. This supposes a "channel-limit" type of experiment where the real volume of helium in contact with the sample has to be controlled.

Just to provide an order of magnitude: in helium I a typical penetration depth of heat for a LHC strand in operating conditions would be of the order of some micrometer; in superfluid helium it is in the mm range!

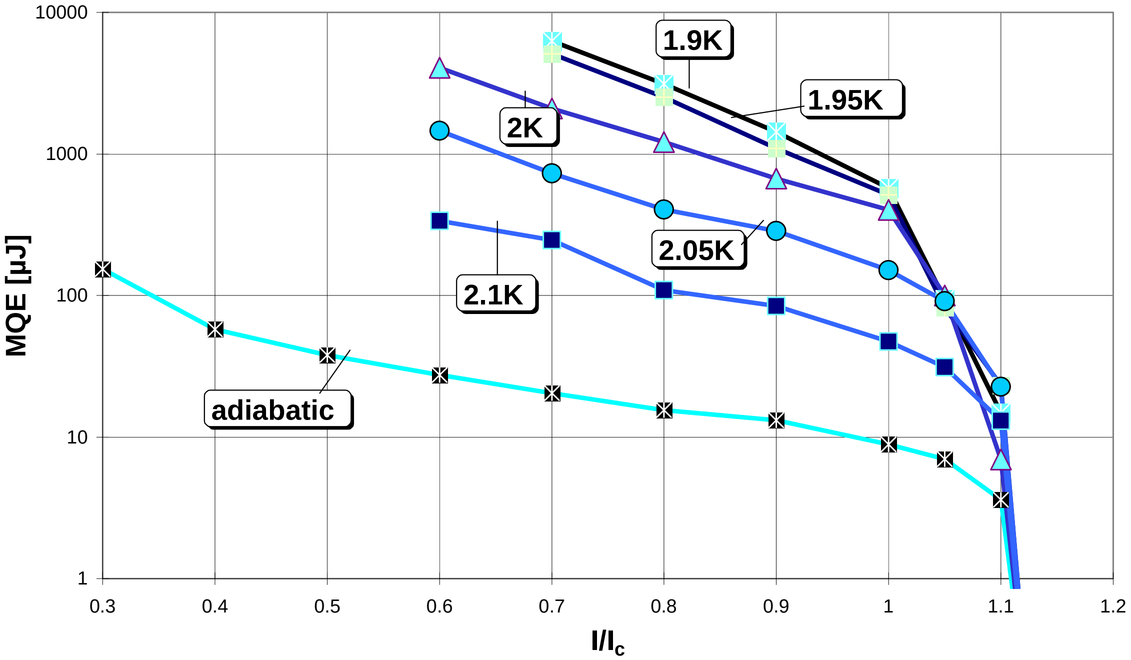

Figure 5.2-12: Reference strand MQE measurement: MQE at 9T in open bath conditions with varying bath temperature T_b between 1.9K and 2.1K. The variation of the bath temperature strongly affects the thermal diffusivity of the helium II in the bath. The lower the diffusivity the smaller the helium volume actively contributing with its heat absorption capacity (enthalpy) to the heat transfer from the strand. Therefore, the smaller the diffusivity, the smaller the amplitude of the superfluid enhancement.

As mentioned in chapter 4.4.1 the MQE measurement set-up used at BNL operates in saturated superfluid helium at ~1.9K. Measurements reported in [Wang 95] show that the difference between subcooled and saturated superfluid in what refers to the cooling potential in a transient heat transfer experiment can be easily related to the static and dynamic helium volume parameters. Saturated superfluid at the same temperature of the subcooled homologue has a smaller enthalpy reserve. Therefore the channel-limit (enthlapy reserve per unit of channel length) as well as the dynamic limits (Gorter-Mellink and Second Sound) are smaller in saturated superfluid than in subcooled superfluid at the same temperature. With regard to the above discussed experiment the effect of saturated superfluid on MQE should be an effect concerning essentially the amplitude of superfluid enhancement. The above said together with the experience gathered in chapter 5.2.2 facilitates the interpretation of the BNL measurement results as compared to Cern measurements in Fig. 4.4.2. The fact that the BNL measurement is in general slightly above the adiabatic Cern measurement indicates that there is a helium cooling effect. The fact that there is no change of slope of logMQE(i) over the whole current range indicates that there is no distinct superfluid enhancement. The superfluid enhancement onset current could as well be above Ic, but that would require exceptionally huge heat transfer coefficients. Resuming the BNL situation we believe that it is not a totally adiabatic case, but neither is it a case where the total cooling capacity of the adjacent superfluid helium is fully exploited. It is a case of modest departure from the adiabatic case due to a relatively high (~40%) cooled perimeter fraction with a small helium volume effect.

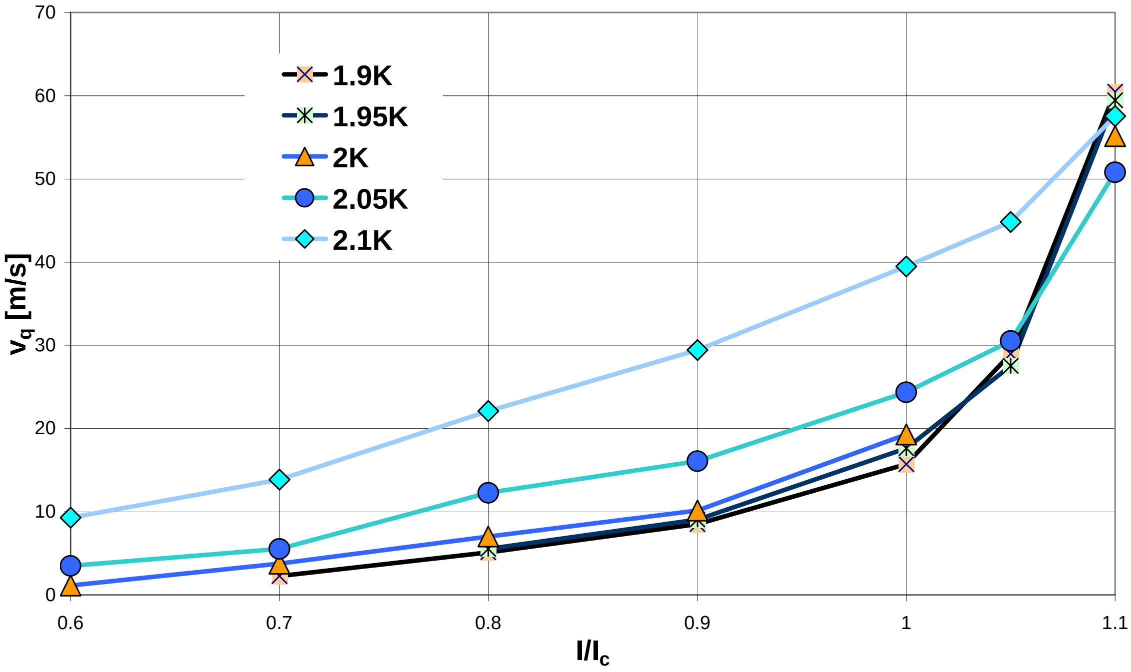

Figure 5.2-13: Reference strand quench propagation velocity measurement at 9T, varying the bath temperature between 1.9K and 2.1K (see Figure 5.2-12). In accordance with the MQE in Figure 5.2-12 the quench propagation velocity is highest at 2.1K and lowest at 1.9K, reflecting the change in helium II diffusivity and its dramatic effect on MQE.

5.2.4 CuNi Barrier

Two samples, taken from a specially prepared billet with a CuNi sheet incorporated in the outer copper shell along half its length were almost identical (see table below), except that one had a 10μm thick CuNi barrier. Unfortunately a rather big difference in Cu/Sc ratio contributed to the difference in MQE. However, the Cu/Sc ratio is known to improve MQE (in cooled conditions) for the composite with the higher Cu/Sc ratio (the sample with the CuNi barrier, see table below). Figure 5.2-14 indicates that the sample without barrier has a much better MQE performance than the sample with the barrier. Therefore the effect of the CuNi barrier on MQE is huge because it not only balances the disadvantage of the lower Cu/Sc ratio but causes the huge difference in MQE shown in

Figure 5.2-14. In adiabatic conditions the Cu/Sc ratio effect is expected to be small. In fact, in adiabatic conditions, there was no difference in MQE between the samples. Only one adiabatic curve, representing both samples, is shown in Figure 5.2-14. Interestingly the effect is similar in pattern to a variation in cooled perimeter fraction, namely shifting the superfluid enhancement to lower currents in the sample with the thermal barrier. The similarity in pattern found in the f-effect and the CuNi barrier measurements hints towards a common explanation: The thermal barriers, either incorporated or superficial reduce heat transfer in such a way that the adiabatic high current end regime is extended to smaller currents. Obviously the CuNi barrier traps the heat inside the strand, whereas it is less efficient in preventing the external initial heat pulse to come in. This can be explained by the factor 1000 difference in heating power between the initial heat pulse and the subsequent current sharing. The initial heat pulse is forced through the thermal barrier by temperature gradients much stronger than those appearing during the current sharing regime with T moderately above T_c. The fact that the CuNi barrier does not noticeably interact with the initial heat pulse can as well be deduced from the agreement of the adiabatic MQE as well as that of the adiabatic parts of the open bath curves of both samples (Figure 5.2-14).

Stability item	**Strands ID**	**Fil∅ [μm]**	**Stack**	**RRR**	**$\rho_{Cu}\cdot 10^{10}$ [Ωm]**	**Cu/Sc ratio**	**∅ [mm]**	**Coat**	**Ic [A] (1.9K/9T)**	**n (1.9K/9T)**
CuNi barrier	01B8772A1CuNi 01B8772B3	7 7	Single Single	209 215	5.5 4.9	**2.02*** **1.69***	1.065 1.065	no no	653.3 730.7	51 57

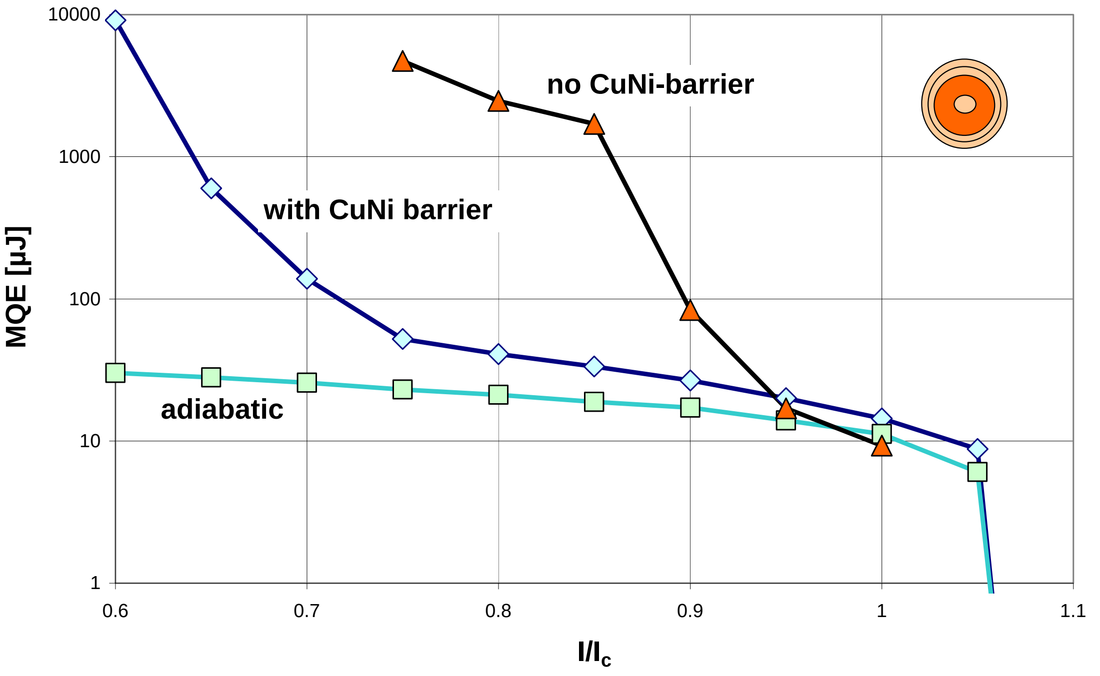

Figure 5.2-14: MQE at 1.9K/9T of 2 samples (01B8772..) with and without CuNi-barrier. Both strands have the same MQE in adiabatic conditions, but in open bath conditions their MQE differ considerably. A comparison with Figure 5.2-9 reveals a strong resemblance of the effect of an internal or external barrier to heat transfer: both shift the superfluid enhancement to smaller currents.

5.2.5 Four Different Coatings

The MQE of a special sample with different 1µm thick coatings (CuSn, SnAg, SnNi, bare) was measured in adiabatic and open bath conditions. The MQE curves in Figure 5.2-15 show that a variation in coating does not cause leaps in MQE as strong as those found when varying the cooled perimeter fraction. This shattered hopes that a suitable coating could significantly improve MQE. Nevertheless there are some differences between the samples. Again in agreement with model-calculations and with all former measurements involving a variation in the heat transfer properties, a variation of the Kapitza heat transfer coefficient traduces into a shift of the superfluid enhancement MQE bump along the current axis. The MQE data as well as the quench propagation velocity measurements (Figure 5.2-16) indicate that the SnAg coating is slightly better in terms of stability than the others. Eventually the SnNi coating could be classified as having the lowest MQE in the series.

Stability item	Strands ID	Fil∅ [µm]	Stack	RRR	$\rho_{Cu}\cdot 10^{10}$ [Ωm]	Cu/Sc ratio	∅ [mm]	Coat	Ic [A] (1.9K/9T)	n (1.9K/9T)
Comparison between different type of coating	01D95091A19N	7	Single	111	5.9	1.62	1.064	SnNi	785	?
	01D95091A19M	7	Single	96	6	1.62	1.064	CuSn	783	54
	01D95091A19S	7	Single	133	5.8	1.62	1.064	SnAg	786	54
	01D95091A19C	7	Single	132	5.8	1.62	1.064	no	789	55

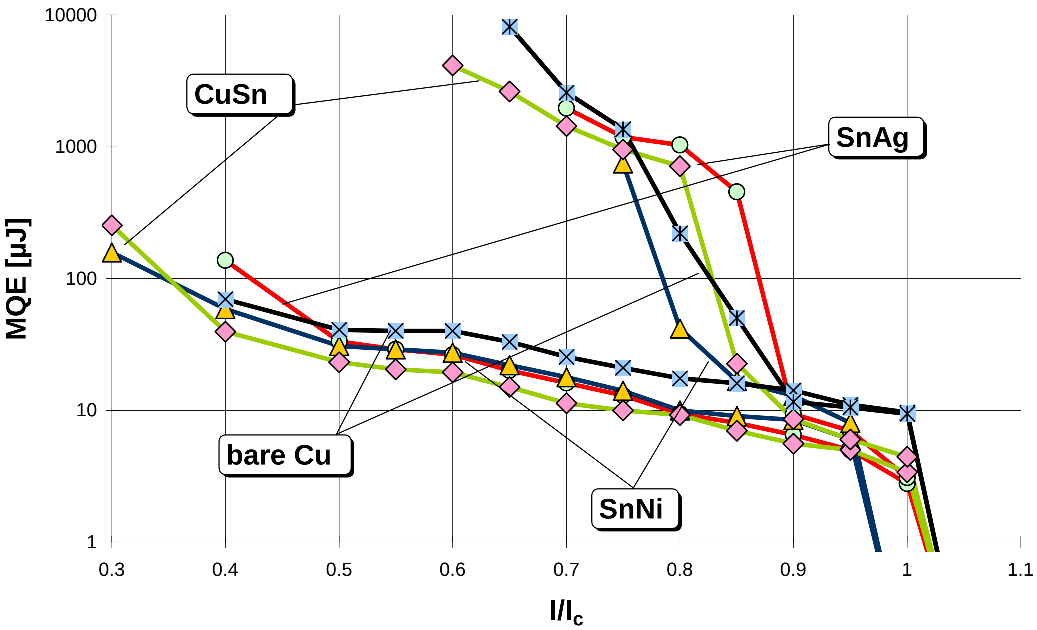

Figure 5.2-15: MQE of sample 01D95091A19 with different coatings (CuSn, SnAg, SnNi, bare) at 1.9K/9T in adiabatic (lower curves) and open bath conditions (upper curves). The effect of different coatings on MQE is not as big as that observed in experiments with varying cooled perimeter fraction (Figure 5.2-9) or CuNi-barrier (Figure 5.2-14) but nevertheless not negligible.

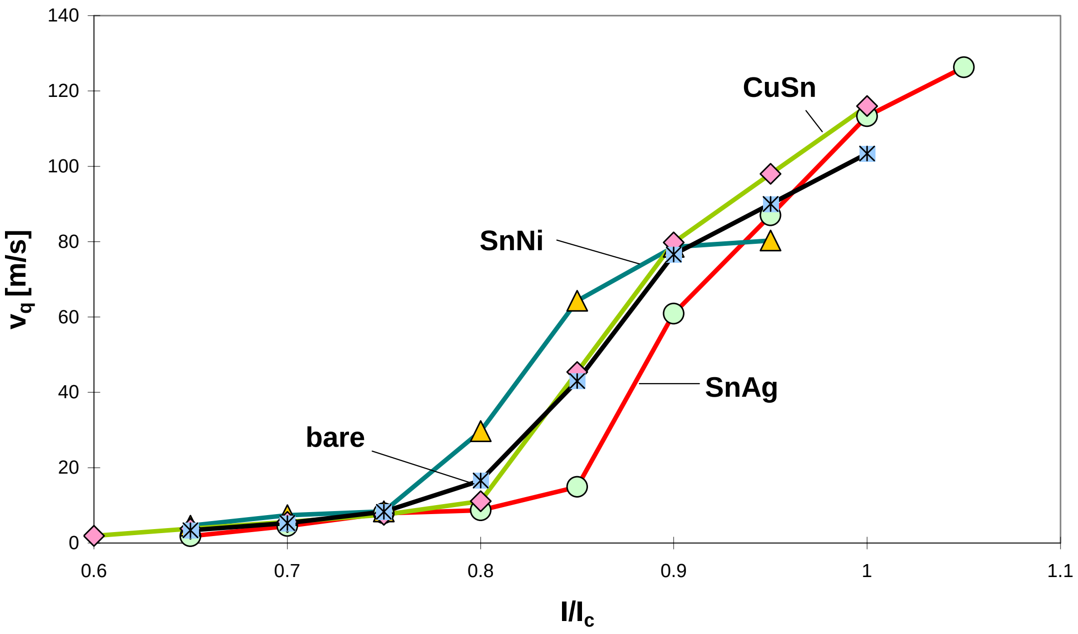

Figure 5.2-16: Quench propagation velocity of sample 01D95091A19 with different coatings (CuSn, SnAg, SnNi, bare) at 1.9K/9T open bath conditions (upper curves). The quench propagation velocity data confirm the characteristics of different coatings gathered from their MQE (Figure 5.2-15), namely that the SnAg coating is above average and the SnNi coating below average in what refers to stability.

These results have been confirmed at DRAL in inductive long heater experiments specially suited to evaluate the effect of coating on MQE [Baynham 98]. As described in detail in chapter 4.4.2 the team at DRAL used a 4cm long inductive heater. The long heater set-up offers the possibility to study the effect of the cooling parameters more directly than in the MQE type of measurement where heat conduction along the matrix is a dominant effect which adds to the complexity of the MQE process. A measurement series with the long heater at DRAL comparing a bare strand with two samples of a SnAg coated strand revealed huge differences (factor 5) between not only the bare and the SnAg sample, but also between the 2 samples of the same, SnAg coated strand. In fact small variations in Kapitza conductance can explain the differences in Quench Energy Margin QEM (J/m^3) found in the long heater experiments (Figure 5.2-18). The Kapitza parameters in Figure 5.2-19 are derived from the fits (using the long heater model briefly discussed in chapter 2.4.3 using the functions described in chapter 3.1-3.6) of the experimental curves in Figure 5.2-17. This means as well that the variations of the heat transfer coefficient (e.g. Kapitza conductance) along one sample can be of the same order as the variation between different coatings. Taking the cooling parameters which fit the QEM measurements in Figure 5.2-18. in a MQE type simulation (Figure 5.2-20) reveals not only the same spread as the MQE measurements in Figure 5.2-15 but also the same pattern of difference caused by the variation in the heat transfer coefficient (shift of superfluid enhancement along the current axis).

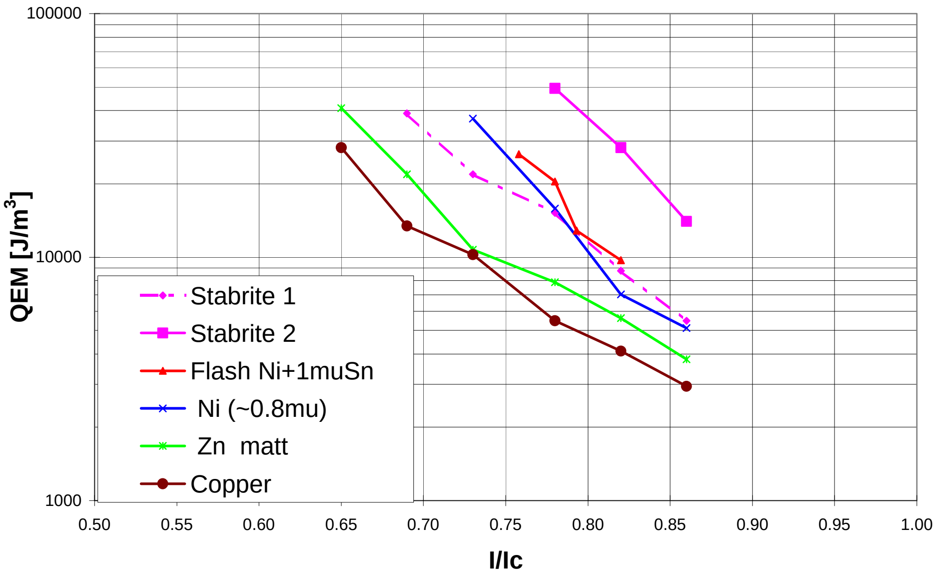

Figure 5.2-17: QEM measurement series at DRAL [Baynham 98], long heater, 1.9K/8T, QEM(i) of sample without coating and with SnAg (Staybrite), flash Ni plus Sn, Ni and Zn coating. Due to the sensitivity of the long heater set-up to small variations in the cooling parameters the differences between the QEM referring to the different coatings are huge. The SnAg coated samples show the best performance, whereas the Zn and the bare sample have the worst performance.

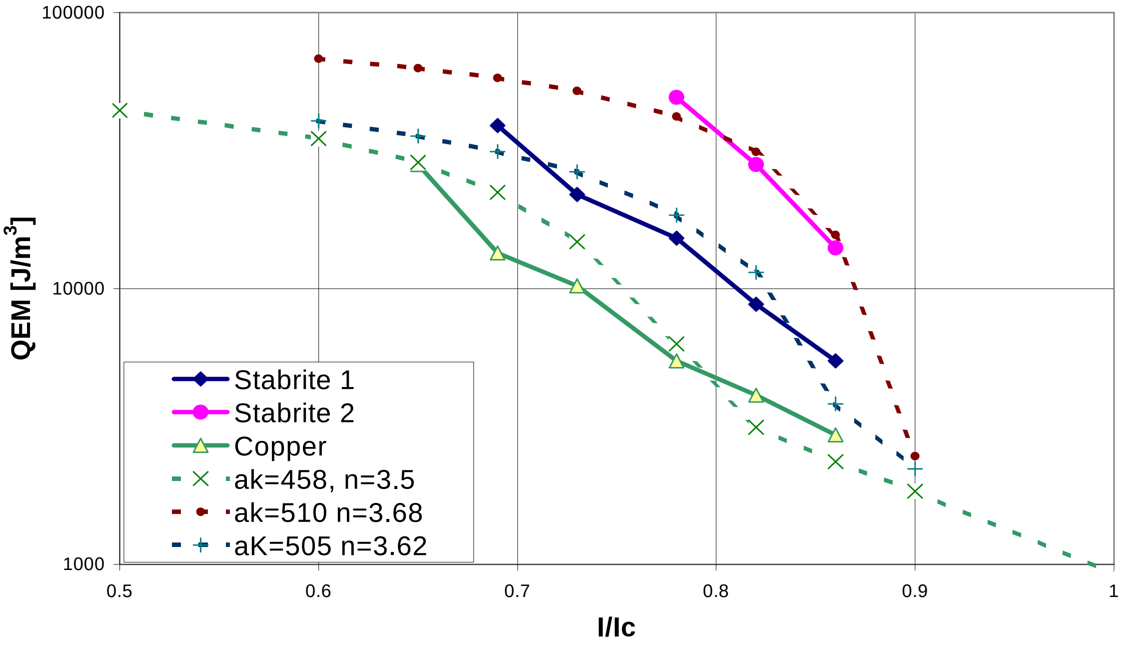

Figure 5.2-18: Simulations (dashed) and measurements (full line) of the QEM of samples with different coatings using the long heater model (see chapter 2.4.3, chapter 3.1-3.6). The Kapitza type heat transfer correlations used in the simulation are added in the legend. The lower two curves (bare and SnAg1 sample) have been simulated with a channel-limit corresponding to 85µm of helium, for the SnAg2 sample a higher channel limit corresponding to 110µm had to be used. Taking into account Fig. 4.4.4, namely that the measured curves have to be corrected to lower values at the low and high current ends, the simulations fit the measurements rather well.

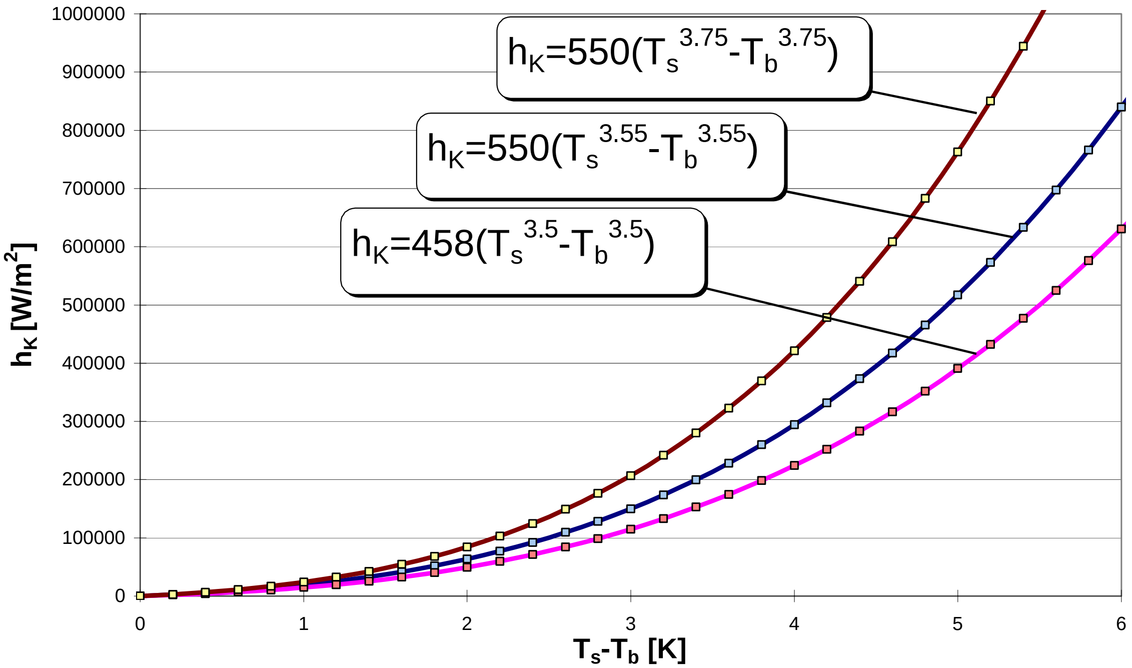

Figure 5.2-19: Kapitza-like heat transfer correlations used to fit the long heater measurements at DRAL (see Figure 5.2-18). The lowest curve represents the copper sample. The upper two curves represent the two SnAg coated samples.

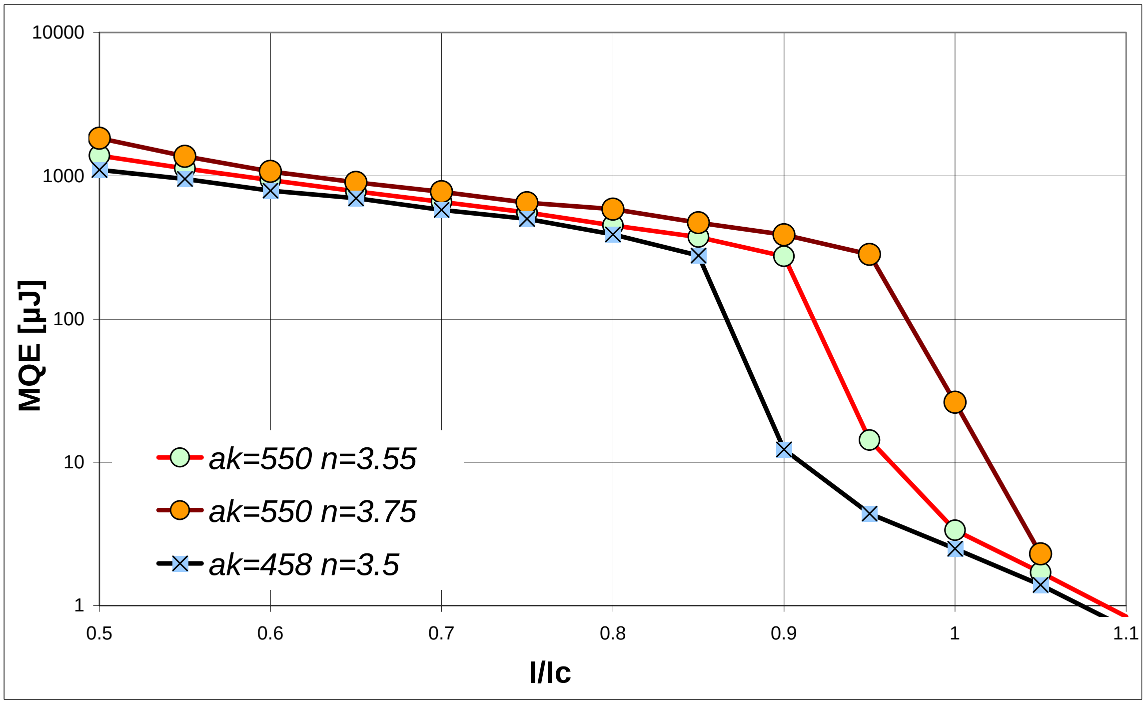

Figure 5.2-20: MQE simulations, 1.9K/9T, reference strand; Kapitza heat transfer coefficients ($h_K=a_K(T^n-T_b^n)$) taken from best fits of DRAL long heater measurements (Figure 5.2-19).

5.3 Effect of RRR on MQE

Simulations in adiabatic conditions (Figure 5.3-1) indicate that the RRR effect on MQE saturates at RRR~100. A higher RRR does not significantly change the matrix resistivity which is from then on dominated by the magneto-resistivity term. A strand with a RRR of less than 100 is expected to show a bad MQE performance: A simulation with RRR=40 in adiabatic conditions shows a decrease of MQE by 50% compared to a RRR=100 case.
A measurement series in open bath / 1.9K / 9T conditions agreed with the predictions from the model (Figure 5.3-2). Strands with a RRR as specified for the LHC strands (100-200) have identical MQE if they do not differ with respect to other parameters. In Figure 5.3-2 only one representative of the standard MQE is shown. A sample with an accidentally low RRR of 41 (no final annealing) showed a strongly reduced MQE (Figure 5.3-2). Although in this particular case the balance of cooling and heating is influenced via the heat generation term, the outcome is again that the MQE bump is shifted to lower currents.

Stability item	Strands ID	Fil∅ [μm]	Stack	RRR	$\rho_{Cu}\cdot 10^{10}$ [Ωm]	Cu/Sc ratio	∅ [mm]	Coat	Ic [A] (1.9K/9T)	n (1.9K/9T)
Comparison between different RRR	01B00011A05Y 01B19200W422B	7 4.75	Single Single	163 41	5.3 **8.5**	1.65 1.53*	1.067 1.076	no no	720 791?	40 ?

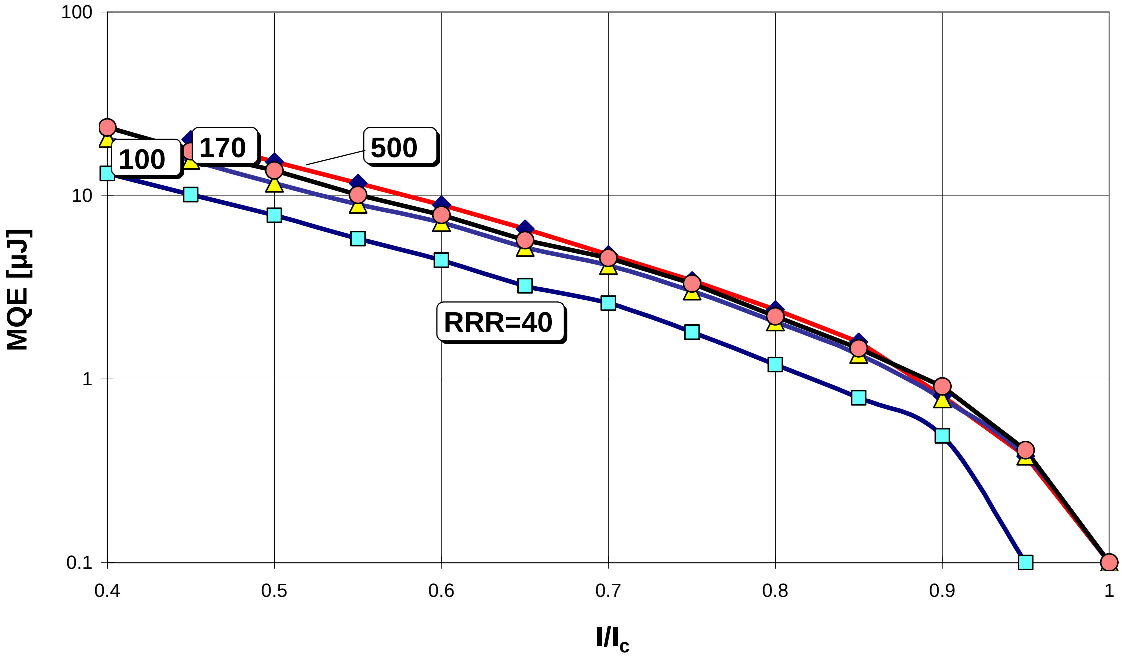

Figure 5.3-1: Reference strand MQE simulation, 1.9K/9T, adiabatic conditions, effect of RRR on MQE. A variation of RRR as specified for LHC-type strands between 100-200 (100-triangles, 170 - circles) produces only small variations in MQE (<15%). Raising MQE above 200 does not significantly improve MQE because the total electrical matrix resistivity becomes independent of RRR with RRR→∞. On the other hand a RRR of 40 reduces MQE by 50%!

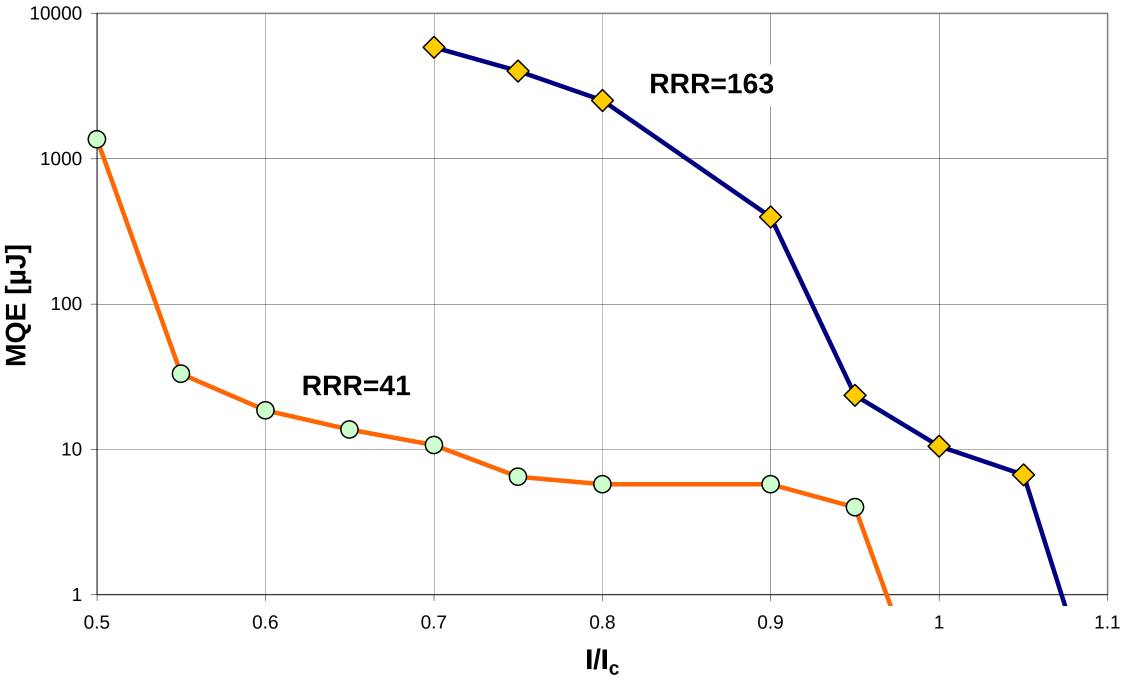

Figure 5.3-2: MQE measurement at 1.9K/9T, open bath conditions, 01B19200W422B (RRR=41, ρ_{Cu}=8.5·10^{-10}Ωm) and 01B00011A5Y (RRR=163, ρ_{Cu}=5.3·10^{-10}Ωm). The small difference in critical current (I_c=791A for 01B19200W422B compared to I_c=720A for the other sample) does not significantly alter the picture. The difference observed here is among the most pronounced throughout the whole measurement series. Interestingly the same pattern as for the variation of the cooling parameters is found again here, namely the shift of the "bump" to lower currents in the sample with the stronger matrix heating.

5.4 Effect of Cu/Sc Ratio on MQE

The MQE of two samples taken from different locations from the same billet with identical design but different Cu/Sc ratio is given in Figure 5.4-1. Simulations (see Fig. 3.11-23) indicate that in adiabatic conditions the strand with the lower Cu/Sc ratio has a higher MQE whereas in open bath conditions the situation reverses. Using a 1mm thermo-sleeve (see "sleeve-effect") the MQE curve was equally parted into an adiabatic part (at high currents) and a open bath part (at low currents).

Stability item	Strands ID	Stack	RRR	ρ_{Cu}·10^{10} [Ωm]	Cu/Sc ratio	∅ [mm]	Coat	Ic [A] (1.9K/9T)	n (1.9K/9T)
Comparison between different Cu/Sc ratio	1B8772B10X13 1B8772B10X155	Single Single	188 219	5.02 4.99	1.3 1.55	1.065 1.065	no no	834 751	58 54

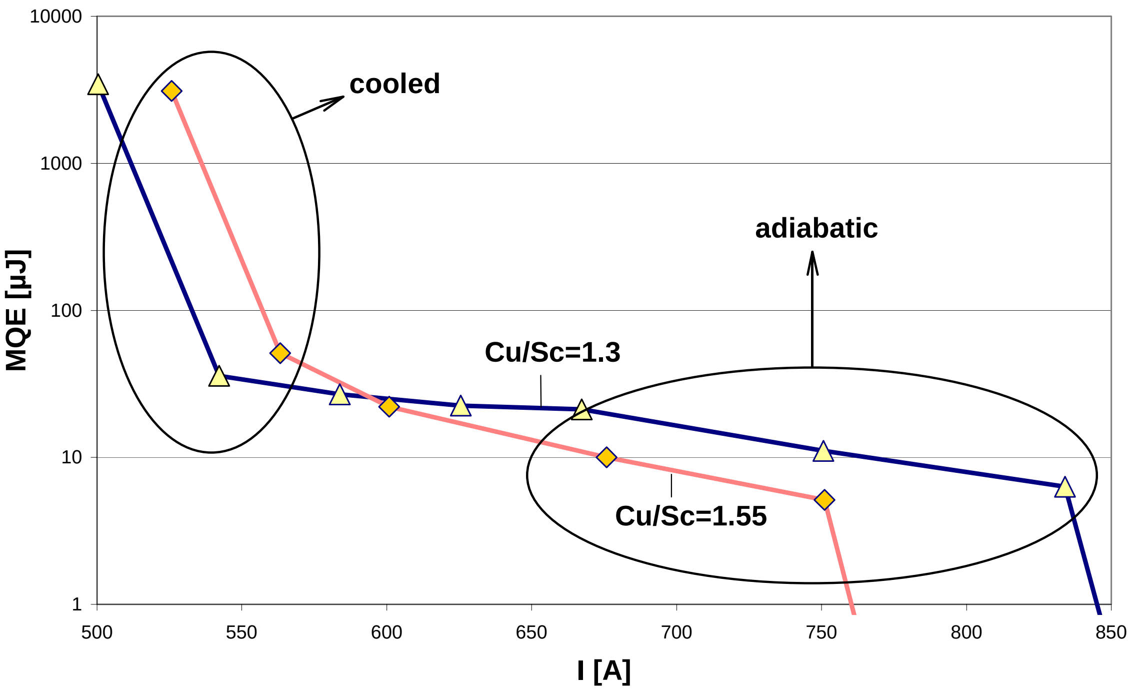

Figure 5.4-1: MQE measurement in open bath conditions with a 1mm sleeve (adiabatic and cooled regions along the MQE curve are indicated in the plot), 1.9K/9T, samples: 01B8772B10X with Cu/Sc-ratio 1.3 (triangles) and 1.55 (squares), taken from the middle and the end of a billet.

Hopefully the crossing of the MQE curves in Figure 5.4-1 expresses exactly the reversing of the stability between adiabatic and open bath cooling rather than the uncertainty of measurement. The confidence in the measurement is reinforced by the fact that MQE measurements on the same set of samples in poor cooling conditions presented in [Wilson 97] show the same pattern, with the Cu/Sc=1.55 being smaller at high currents and a crossing 45%I_c (Figure 5.4-2). Furthermore this comparative measurement shows how improved cooling conditions (going from the restricted cooling conditions in the BNL set-up to 1mm sleeve conditions in the Cern open bath set-up) amplify the differences in MQE caused by differences in Cu/Sc ratio.

In general it was found that the Cu/Sc variations tolerated in the LHC strand specification (1.6-1.7) is the main cause of MQE differences between LHC strands.

A compilation of the MQE measurement series at BNL ([Ghosh 98]) shows a correlation with small variations in Cu/Sc ratio (1.5-1.7). However, the spread in MQE between the different strands is small.

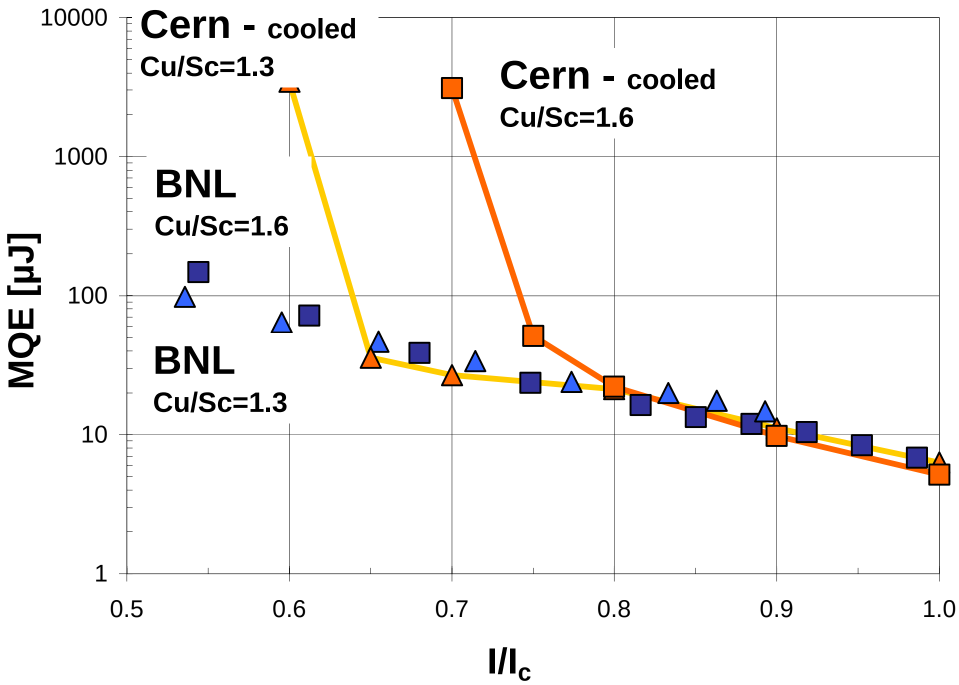

Figure 5.4-2: Comparison of measurements at Cern (1mm adia, open bath) and BNL (restricted cooling conditions), Cu/Sc ratio series, 1.9K/9T. As predicted by theory the composite with the higher Cu/Sc ratio has a higher MQE. The difference in MQE between the 2 samples (Cu/Sc ratio 1.3 and 1.6) is amplified with improved cooling conditions. This effect is as well predicted by the simulation in Fig. 3.11-23.

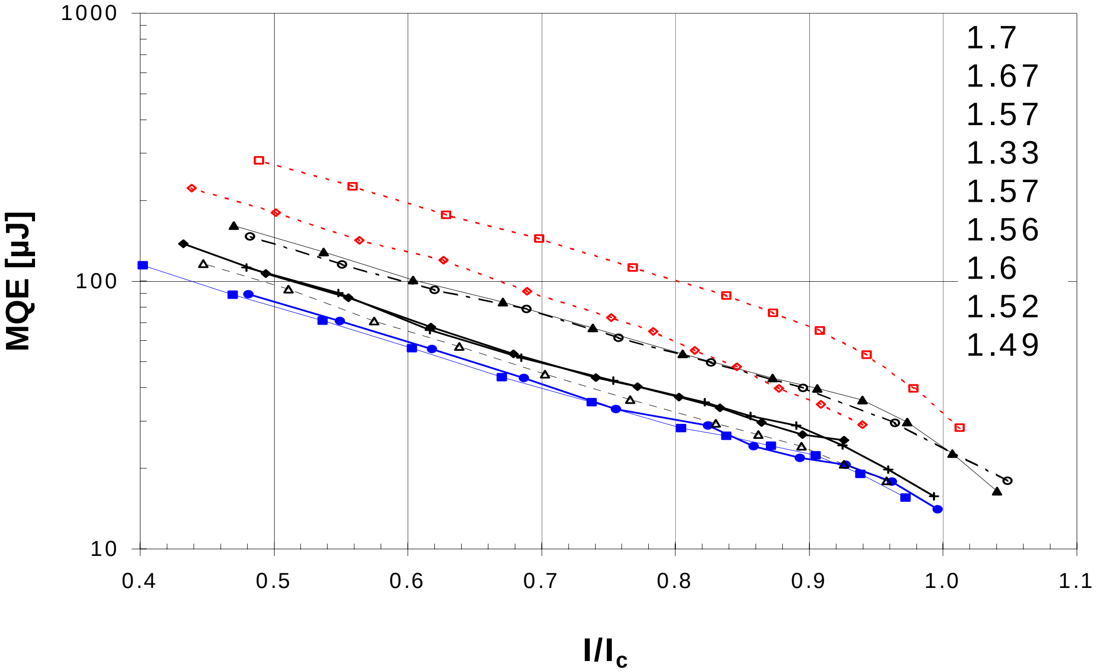

Figure 5.4-3: BNL measurement series published in [Ghosh 98], 4.2K/6T, restricted cooling conditions. The spread in MQE between the different LHC prototype strands is relatively small.

The spread in the MQE between the different samples can be partly explained by a small spread in Cu/Sc ratio, indicated in the plot in the order of ascending MQE from bottom to top. There is no such correlation with other parameters (RRR, coating, billet design, NbTi supplier).

5.5 Effect of Billet Design on MQE

An evaluation of the effect of the so called billet design parameters on stability has been vividly discussed recently. The billet design parameter comprises everything related to the distribution of the superconductor in the matrix. It addresses the question of double-stack/single-stack, of more or less copper in the inner core or the outer shell and the interfilament spacing. To investigate the effect of billet design on MQE (distribution of copper in the cross-section, double stack vs. single stack) a series of samples (see following table) with identical Cu/Sc ratio, dimension, coating, I_c and matrix resistivity but different billet designs were tested. The MQE in adiabatic and open bath conditions are identical within the limits of measurement uncertainty, indicating that the differences in MQE are relatively small.

Stability item	Strands ID	Fil∅ [µm]	Stack	RRR	$\rho_{Cu}\cdot 10^{10}$ [Ωm]	Cu/Sc ratio	∅ [mm]	Coat	Ic [A] (1.9K/9T)	n (1.9K/9T)
Comparison between different fabrication process	01B00017A06Y	7	Single	172	5.3	1.622	1.07?	no	720	50
	01B00011A05Y	7	Single	163	5.3	1.65	1.067	no	720	40
	01B00012A02X	7	Single	145	5.1	1.67	1.066	no	716	40
	01E00007A02XU	6.65	Double	158	5.2	1.6	1.064	no	755	38

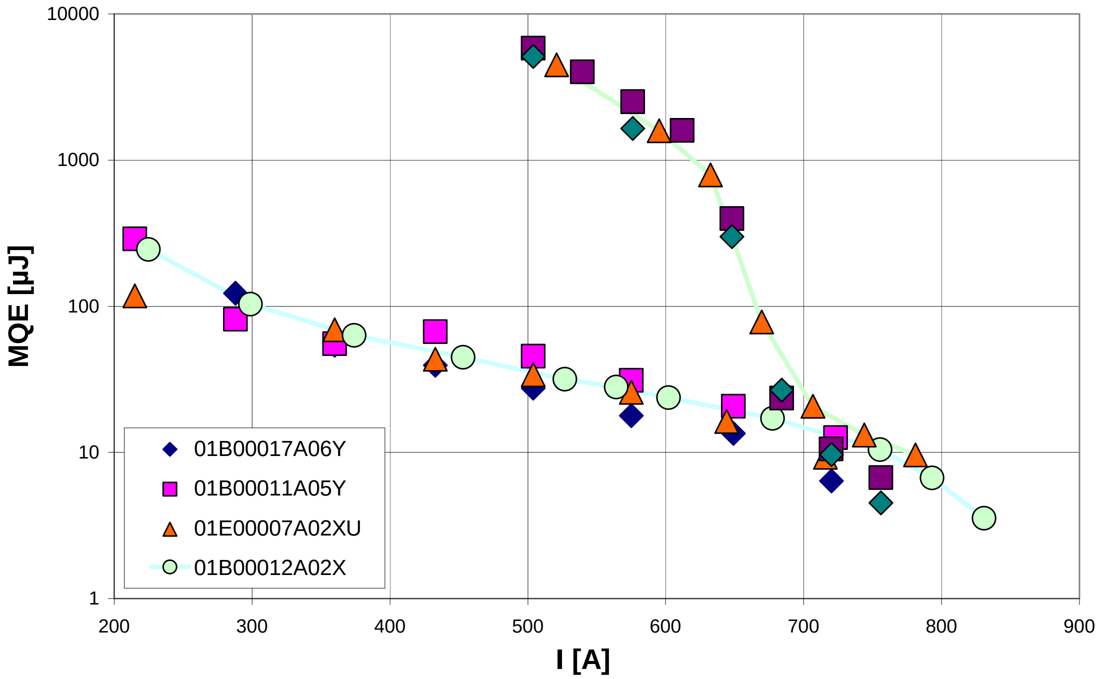

Figure 5.5-1: MQE measurement in adiabatic (lower curves) and open bath (upper curves) conditions at 1.9K/9T. Samples identical with respect to d~1.065mm, Cu/Sc~1.6 and filament diameter ~7µm, I_c~730A, n~45, RRR~160, ρ_{Cu}~5.3·10^{-10}Ωm, but with different billet designs.

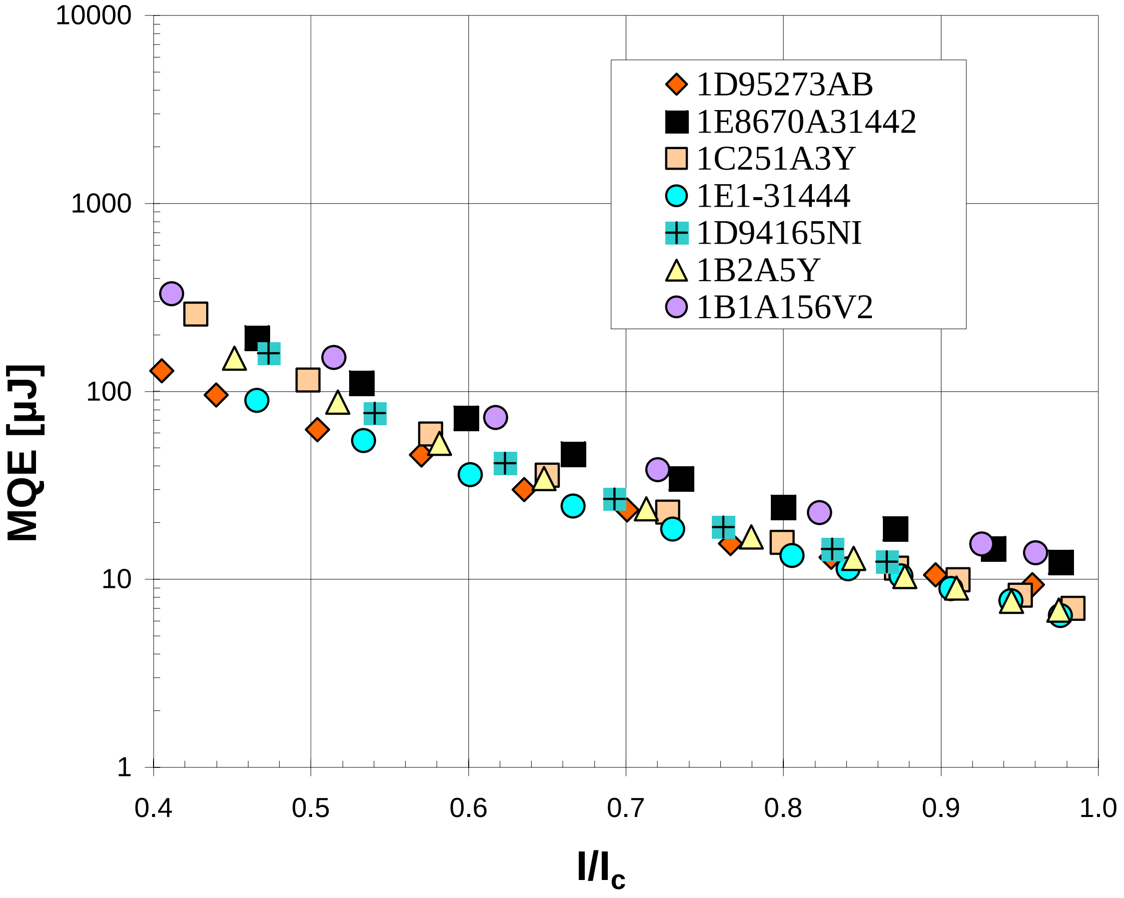

Figure 5.5-2: BNL measurement series ([Ghosh 98]) at 1.9K/9T, restricted cooling conditions. The measured samples have equal characteristics except the billet design and the NbTi supplier. The spread between the different measurements is hardly bigger than the worst case measurement uncertainty.

The MQE measurement in adiabatic conditions in Figure 5.5-1 confirms a previous measurement series performed at BNL where samples differing with respect to billet design and NbTi source had shown almost identical MQE (Figure 5.5-2). Comparative MQE measurements performed at Cern and BNL (Figure 5.5-3) revealed that the cooling conditions at BNL have to be considered as almost adiabatic. The BNL tests operated in saturated superfluid helium which has reduced cooling characteristics compared to subcooled superfluid. Furthermore particularities of the BNL heater design result in restricted cooling conditions as they might prevail in a cable environment in a real magnet.

Since the measurement uncertainty of all MQE set-ups discussed here (chapter 4) is large(>±20%) due to a lack of calibration, these measurements do not completely exclude that billet design may induce differences in what could be called the fine structure of MQE. However, in the case of a LHC strand operating in quasi-adiabatic conditions with a MQE margin of 50µJ an increase of MQE by 10% due to an improved billet design will not result in a spectacular improvement of the performance of the magnet.

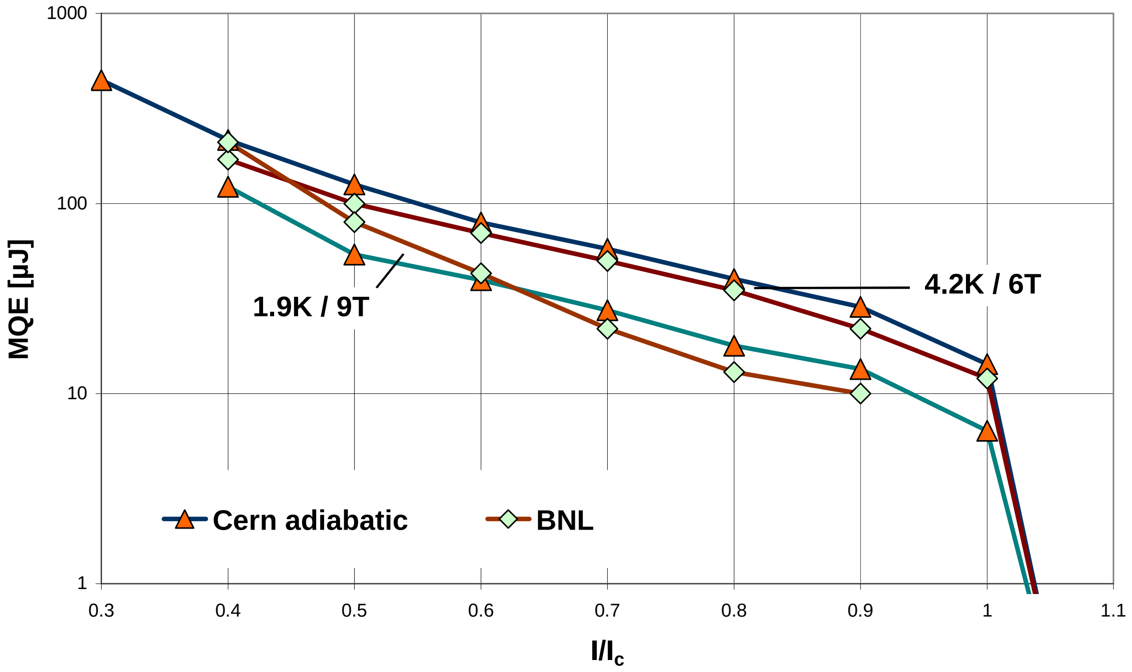

Figure 5.5-3: A comparison of Cern (01B00017A06Y) and BNL ("typical") MQE measurement at 4.2K/6T and 1.9K/9T revealed that the BNL set-up was operating in a poorly cooled environment. This may be explained by the heater used at BNL (which restricts the quantity of helium in contact with the sample) and by the fact that BNL operates at 1.9K in saturated vapor conditions (which reduces the heat absorption capacity of the superfluid helium).

5.6 Conclusions 1

The differences in MQE between various samples cannot be resolved in 4.2K/6T conditions as a consequence of the modest cooling properties of helium I. Nevertheless a comparison of some characteristic samples shows the spread of MQE which can be expected in 4.2K/6T conditions (Figure 5.6-1).

Stability item	**Strands ID**	**Fil∅ [μm]**	**Stack**	**RRR**	**$\rho_{Cu}\cdot10^{10}$ [Ωm]**	**Cu/Sc ratio**	**∅ [mm]**	**Coat**	**Ic [A] (1.9K/9T)**	**n (1.9K/9T)**
very stable and unstable	01B00017A06Y 01B19200W422B	7 4.75	Single Single	172 41	5.3 **8.5**	1.622 1.53*	1.07 1.076	no no	720 791?	50 ?
average	01D95091A19S	7	Single	133	5.8	1.62	1.064	SnAg	786	54

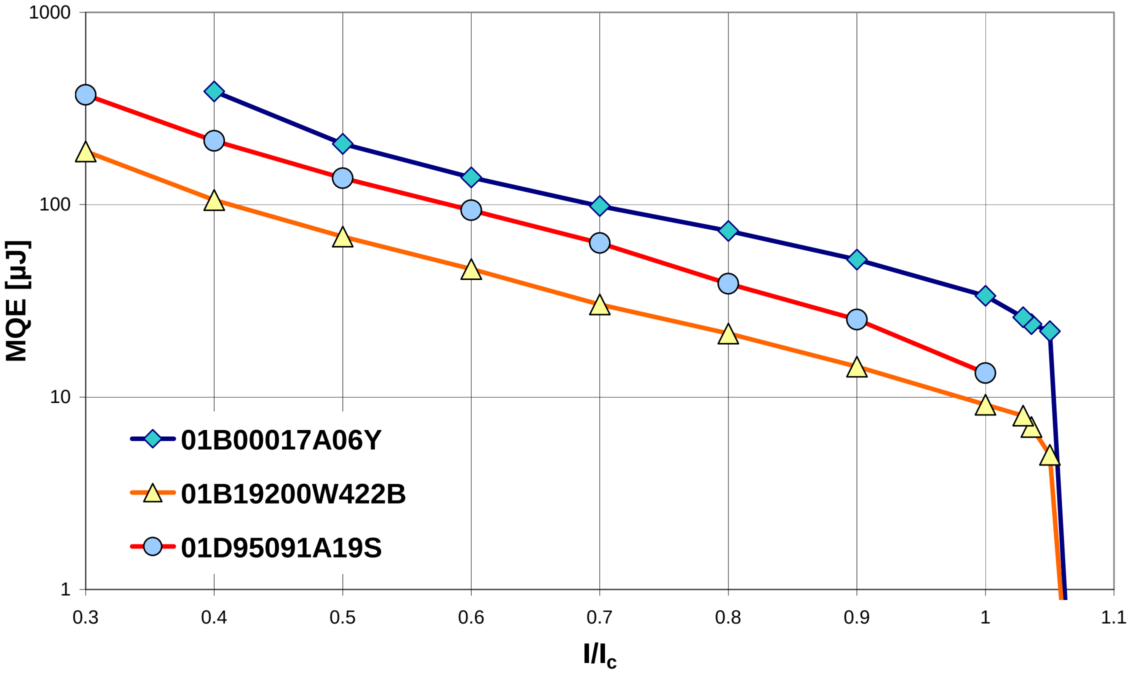

Figure 5.6-1: Spread of MQE measurements at 4.2K/6T (open bath conditions) over the entire series of samples, with bottom curve belonging to an exceptionally unstable strand with the lowest MQE in the complete pool (RRR=41) and with all the other samples being squeezed between the upper and the middle curve. The spread between different samples is relatively small, mainly because cooling to pool-boiling helium I is almost insignificant. The cooling normally acts as an amplifier of the differences in MQE. Therefore all the differences between samples in what refers to cooling are invisible and the remaining differences due to small variations in the matrix resistivity or Cu/Sc ratio are not amplified as with a strong cooling performance.

A global comparison of the MQE of all different samples measured at 1.9K/9T, presented in Figure 5.6-2, shows that apart from exceptional cases (exceptionally small RRR, artificially decreased cooling performance using inner resistive layers) most samples have a MQE between the lower and middle curve in Figure 5.6-2. Only a few samples, like the reference strand have higher MQE curves. So far no explanation was found for the extraordinary performance of the reference strand, except that it may simply be the consequence of an advantageous configuration in the known parameter space (SnAg coating, relatively low matrix resistivity,…). Some of the lowest curves in the spectrum have been found to suffer premature quenching in I_c-tests or a (perhaps) stability related decrease of (I_q-I_c) with decreasing temperature (see [Ghosh 97]). However, there is no clear sign of a correlation between less MQE and premature quenching. On the other hand there is no contraindication neither. In any way the investigation of premature quenching would represent a project as big in scale as the presently described. Perhaps the most interesting aspects of the here presented work is the establishment of the order of magnitude of change in MQE related to the variation of a certain parameter and the classification of the parameters into different classes, the "normal-coordinates" of single strand MQE:

- a separation into a rough scheme and a fine structure of MQE

- a separation of the relevant parameters into two groups: the helium volume related parameters affecting the height of the "superfluid enhancement bump" and the parameters related to heat transfer and heat generation which cause the superfluid enhancement bump to be moved along the current axis.

The fine structure of MQE (effect of small parameter variations, billet design parameters, ..etc..) could not be resolved with the present experimental technique. More precise (and calibrated) techniques using laser or ultrasound could be envisaged. The electrical heater technique could be improved for example by sputtering semi-conducting layers as heating elements directly on the sample. However it is unclear if a few percent variation in MQE will ever be an important item in the next few years.

Stability item	**Strands ID**	**Fil∅ [μm]**	**Stack**	**RRR**	**$\rho_{Cu}\cdot10^{10}$ [Ωm]**	**Cu/Sc ratio**	**∅ [mm]**	**Coat**	**Ic [A] (1.9K/9T)**	**n (1.9K/9T)**
Standard	01B00011A05Y	7	Single	163	5.3	1.65	1.067	no	720	40
unstable?	01B3A1X	7	Single	?	5.26	1.6	1.064	no	759	48
very stable	CERN REF 01E	7	Double	127	5.5	1.6	1.065	SnAg	739	38

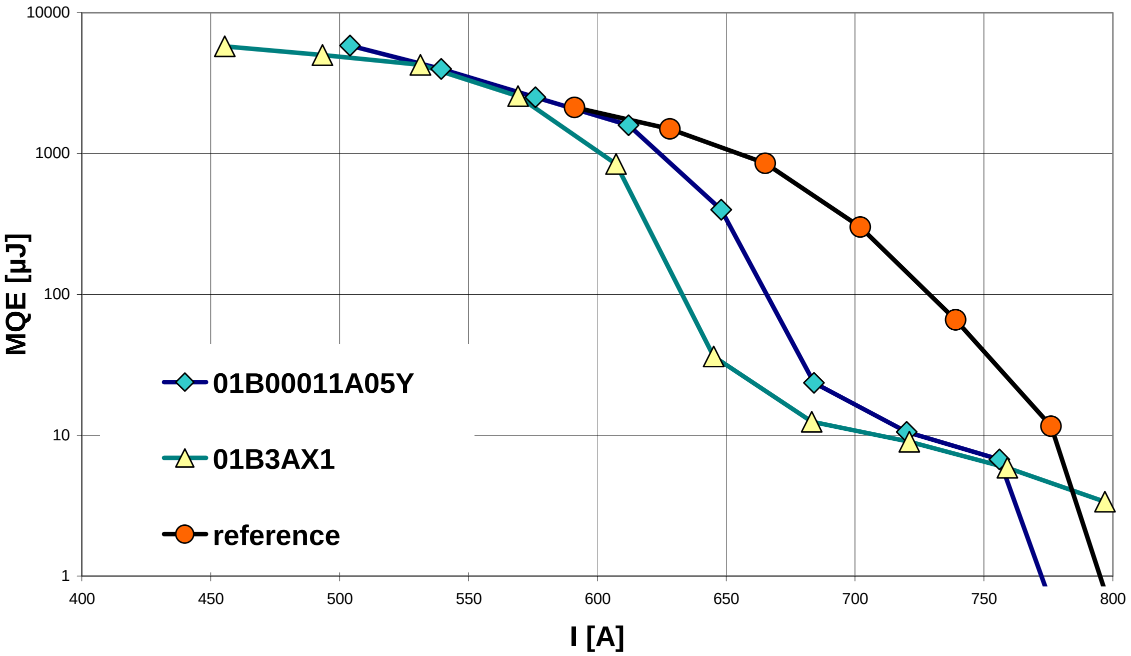

Figure 5.6-2: MQE measurement, 1.9K/9T, open bath conditions. Showing the exceptional behavior of the reference wire: Most of the samples following the LHC strand specification have MQE curves lying between the lower two curves in the plot. Only some, among them the reference wire, have a clearly higher MQE in the high current region. Why? The sample with the lowest MQE in open bath conditions 01B3AX1 showed pronounced premature quenching in Ic tests.

Concerning the effect of the different parameters on MQE it is indeed interesting that they fall into two classes, those which affect the "height" of the helium bump and those which affect position of the "bump" along the current axis. The former class of parameters is related to the burn-out phenomenon. It is less known and less accessible via experiments. Perhaps visualization techniques and separate heat transfer measurements could further improve the understanding. The latter class being much bigger contains all the parameters which affect heat generation or surface heat transfer. The fact that a multitude of different parameters of the second kind affect MQE in exactly the same way, shifting the “standard MQE-curve” along the current axis, undoubtedly hints towards a common mechanism. This common mechanism is related to the specific course of cooling h(ΔT) and heating g(ΔT) with ΔT. Roughly one can find three regimes, the adiabatic regime (in LHC type strands usually at $I \sim I_c$) in which the cooling correlation becomes partly smaller than the heating, the cooled regime at which cooling and heating mix and the cryostable regime (at I<0.6Ic in LHC-type strands in open bath cooling conditions) where the cooling is clearly bigger than heating (Figure 5.6-3). A precise analysis, even of the simulated case, is tremendously complicated because it would demand to check this relation at each space/time point along the strand/the process. At given peak temperature and critical steady state heat transfer flux the cryostable regime can be anticipated. The knowledge of the current at which the transition between the other two regimes occurs, requires numerical calculations and /or measurements.

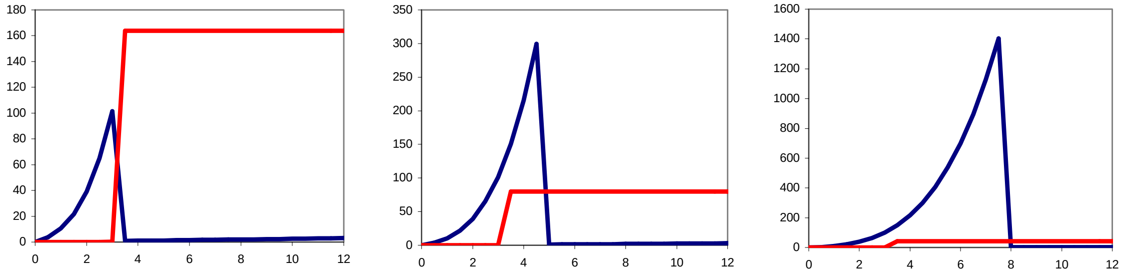

Figure 5.6-3: Illustration of the three characteristic cooling (spike) versus heating (step) patterns found at different stages of an MQE process. From left to right: Heat generation and cooling in kW/m^2 as function of ΔT [K], reference strand, 1.9K/9T; left: adiabatic ($I=I_c$), middle: cooled ($I=0.7I_c$), right: “cryostable” ($I=0.5I_c$). C. Meuris suggested there could even be a fourth regime (the rise of the superfluid enhancement) between the second and the third, when cooling and heating cross twice.

However there are parameters which do not fit into one of the two classes: c_p, k,.. . Certainly these parameters affect an MQE curve over the whole current range in the same way (in relative terms) and would therefore represent a third class of parameters. The samples used in the present work presumably did not vary significantly with respect to that third class (except for the Cu/Sc ratio series). The fact that within the range of measurement uncertainty all samples fell onto the same MQE curve in adiabatic conditions proves this statement.

5.7 Conclusions 2

- The technical specifications for LHC strands (see chapter 1.2) prescribes parameters (Cu/Sc ratio, RRR, coating) in a range compatible with the recommendations deduced from MQE measurements (chapter 5.2-5.5).
- In LHC type strands the billet design (=distribution of copper in the cross-section) plays no significant role in MQE.
- The largest contribution to stability comes from cooling to superfluid helium. Unfortunately single strands in Rutherford cables in accelerator magnets can hardly take advantage of the superfluid enhancement of MQE because of too small cooling parameters (helium volume, cooled perimeter fraction).

We hope that this work has clarified the impact of stability on strand design and that it is of some help for those working on the stability of cables for the LHC magnets.
Some future research can be concentrated eventually on the following questions:

- Measuring the effect of varying inter-filament spacing on MQE to elucidate the effect of the deterioration of the copper quality in the inter-filamentary region (suggested by Pierre Pugnat Cern/LHC/MTA).
- Measuring with the long heater set-up at DRAL the effect of the epoxy potting on QE and comparing it to vacuum or helium I.
- Measuring the effect of varnish coatings of varying thickness on MQE (suggested by Dieter Hagedorn Cern/LHC/ICP).

Unfortunately there was no time to finish a finite element heater model of the heater system as an attempt to calibrate the measurements. Only vague estimations of the thermal time constants of the heater system and of the loss-fraction during a measurement could be made.

6. REFERENCES

Adam J.D. Oberli L., “*Mesures Dimensionnelles des Câbles LHC pour les Aimants Dipolaires*”, Internal note LHC/MMS 96-12, Oct. 1996

Adam J.D. Richter D., Oberli L., Leroy D., Wilson M.N., Wolf R., *“Rutherford Cables with Anisotropic Transverse Resistance”*, IEEE Transactions on Appl. Superconductivity, Vol.7, N.2, June 1997

Aihara T. Okada S., *“Visualization of Thermal Disturbance and Quench Propagation in an Immersion-Cooled Superconducting Coil in Liquid Helium”*, Cryogenics, Vol.34, ICEC Supplement, p.721, 1994

Akopov S.G. Svalov G.G., *“Stability of Composite Superconductors with High Resistive Barriers”*, Cryogenics, Vol.25, p.251, May 1985

Altov V.V. Kremlev M.G., Sytchev V.V., Zenkevitch V.B., “*Calculation of Propagation Velocity of Normal and Superconducting Regions in Composite Conductors*”, Cryogenics, p.420, July 1973

Amemiya N. Tsukamoto O., “*Influence of Disturbance Characteristics and Copper to Superconductor Ratio on Stability*”, Advances in Cryogenic Engineering, Vol.37, Part A, p. 323, 1992

Amemiya N. Inaho K., Ishigami H., Tsukamoto O., Hlasnik I., *“Current Distribution in Multifilamentary Superconductors and their Quench Current Degradation”*, IEEE Transactions on Magnetics Vol. 30, No. 4, July 1994

Amemiya N. Tsukamoto O., “*Stability Analysis of Multi-Strand Superconducting Cables*”, IEEE Transactions on Applied Superconductivity, Vol. 5, No.2, p.218, Junq 1995

Anashkin P. Keilin V.E., Lyikov V.V., “*The Influence of Sc/Cu Ratio and Filament Distribution on the Stability of Superconductors with Respect to Local Heat Pulses*”, Cryogenics, p.169, March 1981

Arenz R.W. Clark C.F., Lawless W.N., “*Thermal Conductivity and Electrical Resistivity of Copper in intense Magnetic Fields at low Temperatures*” Physical Review B, 26/6, pp. 2727, Sept. 1982

Bauer P. Donnier J., Oberli L., *“Tip Heater for Minimum Quench Energy Measurements on Superconducting Strands”*, will be published in the Proceedings of the ASC in Palm Springs 1998a

Bauer P. Wolf R., Oberli L., Wilson M.N., *“Minimum Quench Energies of LHC Strands”*, will be published in the Proceedings of the ASC in Palm Springs 1998b

Baudouy B. Meuris C., Szeless B., Burnod L., Leroy D. *“Thermal Modelling of the LHC Dipoles Functioning in Superfluid Helium”*, LHC NOTE 281, Aug. 1994

Baudouy B. “*La Thermique d’un Aimant Supraconducteur d’Accélérateur Refroidis par Hélium Superfluide*”, PHD Thesis, CEA Saclay, 1996

Baynham D.E. Edwards V.W., Dean M.W., *“Transient Stability Enhancement in High Current Density Cables”*, in Stability of Superconductors, p.175, International Institute of Refrigeration Comission A ½, Saclay, France, 1981

Baynham D.E. “*Transient Stability in High Field Dipoles*”, IEEE Transactions on Magnetics, Vol. MAG-19, No.3, p.676, May 1983

Baynham D.E. Cragg D.A., Coombs R.C., Bauer P., Wolf R., *“Transient Stability of LHC Strands”*, will be published in the Proceedings of the ASC in Palm Springs 1998

Bejan A. Tien C.L., Cryogenics, Vol.18, p.433, 1978

Bon Mardion G. Claudet G., Seyfert P., *“Practical Data on Steady State Heat Transport in Superfluid Helium at Atmospheric Pressure”*, Cryogenics, p.45, Jan. 1979

Bottura L. Mitchell N., Minervini J.V., *“Design Criteria for Stability in Cable-in-Conduit Conductors*”, Cryogenics, Vol.31, p.510, July 1991

Bottura L.	Schneider M., *“Time Dependent Effect Analyses on the One Meter long LHC Dipole Model Magnets: MBSMS9V1,MBSMS10V1, MBSMS11V1 and MBSMT1V1”*, Internal note LHC/MTA-IN-97-13, Nov. 1997
Brentari E.G.	Smith R.V., *“Nucleate and Film Pool Boiling Design Correlations for O_2, N_2, H_2 and He”, Advances in Cryogenic Engineering”*, Vol.10, p.325, 1965
Buznikov N.A.	Pukhov A.A., *“Analytical Method to Calculate the Quench Energy of a Superconductor Carrying a Transport Current”*, Cryogenics, Vol.36, No.7, p.547, 1996
Casas J.	Rinderer L., “*Calculation of Normal Zone Propagation Velocities and Transient Thermal Effects Dependence on the Superconducting Wire Parameters*”, IEEE Transactions on Magnetics, Vol.25, No.2, p. 1492, March 1989
Caspi S.	“*Heat Transfer to Subcooled He I*”, Advances in Cryogenic Engineering, Vol. 29, p.281, 1984
CERN	*“The Large Hadron Collider-Yellow Book”*, Conceptual Design, CERN/AC/95-05, 1995
CERN	LHC/MMS, “*Technical Specification of the Dipole Inner Layer Superconducting Cable for LHC*”, IT-2472/LHC/LHC, July 1997
Cornelissen M.C.M.	Hoogendoorn C.J., *“Thermal Stability of Superconducting Magnets: Static Criteria”*, Cryogenics, Vol. 24, p.669, Dec.1984
Cryopac	Arp V., McCarty R.D., Hands B.A., Version 3.21, NIST Technical Note 1334
Challis L.J.	*“Some Experiments on the Kapitza Resistance Between Metals and Liquid Helium II”*, Proc. Phys. Soc., Vol. 80, p.759, 1962
Challis L.J.	*“A Resume of the Workshop Session on Heat Transfer”*, in Stability of Superconductors, p.13, International Institute of Refrigeration Comission A ½, Saclay, France, 1981
Chandratilleke G.R.	Nishio S., Ohkubo H., *“Pool Boiling Heat Transfer to Saturated Liquid Helium from Coated Surface”*, Cryogenics, Vol.29, p.588, June 1989
Chechetkin V.R.	Lutovinov V.S., Turygin A.Yu., *“Variational Principle for Critical Heat of Quench in Partially Stabilized Superconducting Magnets”*, Advances in Cryogenic Engineering, Vol.35, p.727, 1990
Chechetkin V.R.	Sigov A.S., “*Stability of Superconducting Magnet Systems Subject to Thermal Disturbances*”, Advances in Cryogenic Engineering, Vol.35, p. 683, 1990
Chen Z.	Van Sciver S.W., *“Channel Heat Transfer in He II - Steady State Orientation Dependence”*, Cryogenics, Vol.27, p.635, Nov.1987
Chuang C.	Caspi S., Kim Y.I., Frederking T.H.K., *“Recovery of Superconductivity of Formvar-Coated Composite Nb-Ti/Cu from Postquench Conditions”*, Advances in Cryogenic Engineering, Vol. 26, p.667, 1980
Chuang C.	Kamioka Y., Frederking T.H.K., *“Transient Triple-Phase Transitions in Superfluid Liquid He II”*, Advances of Cryogenic Engineering, Vol. 27, p. 493, 1982
Claudet G.	Lacaze A., Roubeau P., Verdier J., *“The design and operation of a refrigerator system using superfluid helium*”, Adv. In Cryog. Eng. Vol.5, p.265, 1974
Claudet G.	Meuris C., Parain J., Turck B., “*Superfluid Helium for Stabilizing Superconductors Against Local Disturbances*”, IEEE Transactions on Magnetics, Vol. MAG-15, No.1, p.340, Jan.1979
Claudet G.	Seyfert P., *“Bath Cooling with Subcooled Superfluid Helium”,* Advances in Cryogenic Engineering, Vol. 27, p.441, 1982
Claudet G.	Aymar R., *“Tore Supra and He II Cooling of Large High Field Magnets”*, Advances in Cryogenic Engineering, Vol. 35, p.55, 1990
Collings E.W.	Sumption M.D., Kim S.W., Wake M., Shintomi T., Nijhuis A., Ten Kate H.H., Scanlan R.M., “*Suppression and Control of Coupling Currents in Stabrite-Coated Rutherford Cable With Cores of Various Materials and Thicknesses*”, IEEE Transactions on Applied Superconductivity, Vol. 7, No.2, p. 962, June 1997
Denner H.D.	“*Kapitza Resistance of Lead, Copper, Aluminium and Nickel Between 0.3 and*

1.4K”, Proceedings of the ICEC 6, 1977

Depond J.M. Leroy D., Oberli L., “*Superconducting Cable Topology”*, Internal Note 97-09 CERN/LHC/MMS, 1998

Devred A. “*General Formulas for the Adiabatic Propagation Velocity of the Normal Zone*”, SSC Report 184, Sept. 1988

Devred A. “*Quench Origins*”, Lecture delivered at the 1989/1990 US Particle Accelerator School, Brookhaven National Laboratory, Upton, New York, Jul./Aug.1989

Dresner L. “*Transient Heat Transfer in Superfluid Helium*”, Advances in Cryogenic Engineering Materials, Vol. 27, pp.411, 1982

Dresner L. “*Transient Heat Transfer in Superfluid Helium-Part II*”, Advances in Cryogenic Engineering Materials, Vol. 29, pp.323, 1984

Dresner L. *“Quench Energies of Potted Magnets”*, IEEE Transactions on Magnetics, Vol. MAG-21, No.2, p.392, March 1985

Dresner L. *“A Rapid, Semiempirical Method of Calculating the Stability Margin of Superconductors Cooled with Subcooled He-II”*, IEEE Transactions on Magnetics, Vol. MAG-23, No.2, p.918, March 1987

Dresner L. *“Stability Margins of Superconductors Cooled with Subcooled He II”*, Cryogenics, Vol. 29, pp.668, June 1989

Dresner L. Winston J., Lubell M., “*Report on the analysis of the large propagation velocities observed in the full length SSC-Dipoles*”, SSCl 322, Sept. 1990

Dresner L. *“Stability of Superconductors”*, Plenum Press, NY, 1995

Duchateau J.L. Turck B., *“Dynamic Stability and Quenching Currents of Superconducting Multifilamentary Composites under Usual Cooling Conditions”*, Journal of Applied Physics, Vol. 46, No. 11, p. 4989-4995, Nov. 1975

Duchateau J.L. Schild T., Ciazynski D., “*Coupling Losses in Cables for Fusion Application: Influence of the Strand*”, IEEE Transactions on Applied Superconductivity, Vol.7, No.2, p.967, June 1997

Eckels P.W. “*Superconductor Stability and Helium Heat Transfer: the Minimum Propagation Zone Relationship in Design*”, Cryogenics, Vol.29, p.625, June 1989

Elrod S.A. Miller J.R., Dresner L., “*The specific heat of NbTi from 0-7T between 4.2 and 20K*”, Advances in Cryogenic Engineering Materials, Vol. 28, 1981

Elrod S.A. Lue J.W., Miller J.R., Dresner L., “*Metastable Superconductive Composites: Dependence of Stability on Copper-to-Superconductor Ratio*”, IEEE Transactions on Magnetics, Vol. MAG-17, No.1, p.1083, Jan. 1981

Fabbricatore P. Boldi L., Musenich R., Parodi R., Gemme G., “*Stability of Al-Stabilised Conductors for High Energy Physics Application*”, IEEE Transactions on Applied Superconductivity, Vol.7, No.2, p.633, June 1997

Fabjan C. *“LHC: Physics, Machine, Experiments”*, CERN internal note PPE/95-25, Feb. 1995

Filippov Yu.P. Minashkin V.F., Sergeyev I.A., *“Transient Heat Transfer into Liquid Helium under Controlled Heat Generation”*, Advances in Cryogenic Engineering, Vol. 35, p.387, 1990

Filippov Yu.P. Sergeyev I.A., *“Time-Dependent Recovery from Film Boiling”*, Advances in Cryogenic Engineering, Vol. 37, Part A, p.47, 1992

Frederking T.H.K. Chapman R.C., Wang S., *“Heat Transport and Fluid Motion During Cooldown of Single Bodies to Low Temperatures”*, Advances in Cryogenic Engineering, Vol.10, p.353, 1965

Fujiwara T. Ohnishi T., Noto K., Sugita K., Yamamoto J., *“Analysis on Influence of Temporal and Spatial Profiles of Disturbance on Stability of Pool-Cooled Superconductors”*, IEEE Transactions on Applied Superconductivity, Vol.4, No.2, p.56, June 1994

Gavrilin A.V. Konyukhov A., Malginov V.A., “*Computer Simulation and Experimental Study of Quench in Superconducting Epoxy-Impregnated Multi-Layer Coil*”, IEEE Transactions on Magnetics, Vol. 32, No.4, p.2990, July 1996

Gentile D. Hassenzahl W., Polak M., *“Temperature Measurements using a Monofilamentary Superconducting NbTi Wire in the Current Sharing State”*, Cryogenics, p.37, Jan. 1980

Gentile D. *“Contribution a l’Etude des Mecanismes de Transferts Thermiques a l’Helium - Application a la Stabilisation des Supraconducteurs par l’Helium Superfluide”*, Phd thesis, University Paris VI, April 1980 b

Gentile D. Hassenzahl W.V., “*Heat Transfer Measurement with a Small Superconducting Coil Submitted to Transient and Quasistatic Heating at Temperatures between 1.8 and 4,2K*”, Advances in Cryogenic Engineering Materials, Vol25, pp385, 1980c

Gentile D. Francois M.X., *“Heat Transfer Properties in a Vertical Channel Filled with Saturated and Pressurized Helium II”*, Cryogenics, Vol. 21, pp. 234, 1981

Gentile D. Francois M.X., Defresne G., *“Observation of Nucleate Boiling in Helium II and its Effect on Heat Transfer”*, in Stability of Superconductors, p.85, International Institute of Refrigeration Comission A ½, Saclay, France, 1981 b

Ghosh A.K. Garber M., Robins K.E., Sampson W.B., “*Training in Test Samples of Superconducting Cables for Accelerator Magnets*”, IEEE Transactions on Magnetics MAG-25, p.1831, 1989

Ghosh A.K. Sampson W.B., “*Critical Current Measurements of NbTi Wires in the Temperature Range 4.2-1.8K*”, IEEE Transactions on Applied Superconductivity, Vol. 7(2), p. 1459, June 1997

Ghosh A.K. Sampson W.B., Wilson M.N., “*Minimum Quench Energies of Rutherford Cables and Single Wires*”, IEEE Transactions on Applied Superconductivity, Vol. 7, No.2, June 1997

Ghosh A.K. Sampson W.B., Bauer P., Oberli L., *“Minimum Quench Energy Measurements on Single Strands for LHC Main Magnets”*, will be published in the Proceedings of the ASC Palm Springs 1998

Giarratano P.J. Frederick N.V., *“Transient Pool Boiling of Liquid Helium Using a Temperature Controlled Heater Surface”*, Advances in Cryogenic Engineering, Vol.25, p.455, 1979

Goodling J.S. Irey R.K., *“Non-Boiling and Film Boiling Heat Transfer to a Saturated Bath of Liquid Helium”*, “Advances in Cryogenic Engineering, Vol. 14, p.159, 1969

Gradt T. Kasao D., Ruppert U., Lueders K., *“Heat Transfer to Pressurized Superfluid Helium”*, Proc. of ICEC12, Butterworth, Guildford, UK, p.261, 1988

Gradt T. Ruppert U., Lueders K., Wang R., “*Transient Heat Transfer to Superfluid Liquid Helium*”, Advances in Cryogenic Engineering Materials, Vol34, pp.117, 1990

Guo T. Zhu T., *“Experimental Research on the Enhancement of Boiling Heat Transfer of Liquid Helium in Narrow Channels”*, Cryogenics, Vol.37, No.2, p.67, 1997

Hagedorn D. Coull L., *“Radiation Resistant Quench Protection Diodes for the LHC Magnet Quench Protection System”*, Advances in Cryogenic Engineering Materials, Vol. 40B, pp. 1437-1444, 1994

Hakuraku Y. *“Boiling Heat Transfer to Liquid Helium from Multilayered Porous Structure Fins”*, Cryogenics, Vol.27, p.590, Oct.1987

Hassenzahl W.V. “*Study of the Effects of Copper to Superconductor Ratio on Stability*”, Cryogenics, Vol.29, p.637, June 1989

Hilal M.A. Dawson J.W., Gonczy J.D., Turner L.R., Wang S.T., *“Vapor Formation and Heat Transfer in Liquid Helium Cooling Channels under Transient and Steady State Conditions”*, IEEE Transactions on Magnetics, Vol. Mag-15, No.1, p.59, Jan.1979

Holdredge R.M. McFadden P.W., *“Heat Transfer from Horizontal Cylinders to a Saturated Helium I Bath”*, Advances in Cryogenic Engineering, Vol.16, p.352, 1971

Holmes D.S. Menard A.R., “A Computer Model For Transient Heat Transfer To Liquid Helium”,

Huang X. Van Sciver S.W., *“The Influence of Cu/NbTi Ratio on the Stability of High*

Current Density Superconductor", Advances in Cryogenic Engineering, Vol. 37, Part A, p.299, 1992

Hudson P.A. Yin F.C., Jones H., "*Evaluation of the temperature and magnetic field dependence of critical current densities of multifilamentary superconducting composites*", IEEE Transactions on Magnetics, Vol. Mag-17,No.5, pp. 1651, Sept. 1981

Ibrahim E.A. Boom R.W., McIntosh G.E., *"Heat Transfer to Subcooled Liquid Helium"*, Advances in Cryogenic Engineering, Vol.23, p.333, 1978

Iida T. Murakami M., Shimazaki T., Nagai H., Furukawa T., *"Visualization of Highly Transient Thermo-Fluid Dynamic Phenomena in He II"*, Advances in Cryogenic Engineering, Vol. 41, p.249, 1996

Irey R.K. McFadden P.W., Madsen R.A., *"Heat Transfer to a Saturated Bath of Liquid Helium II"*, Proceedings of the 10th ICE Conference, p.361, 1984

Ito T. Kubota H., *"Dynamic Stability of Superconductors Cooled by Pool Boiling"*, Cryogenics, Vol.31, p.533, July 1991

Iwamoto A. Mito T., K. Takahata, N. Yanagi, J. Yamamoto, *"Heat Transfer of a Large Copper Plate to Liquid Helium Applicable to Large Scale Superconductors"*, Cryogenics, Vol.34, ICEC Supplement, p.321, 1994

Iwamoto A. Mito T., K. Takahata, N. Yanagi, J. Yamamoto, *"Dependence of Heat Transfer from a Wide Copper Plate to Liquid Helium on Heat Transfer Surface Orientation and Treatment"*, Cryogenics, Vol.36, No.3, p.139, 1996

Iwamoto A. Maekawa R., Mito T., Yamamoto J., *"Steady State Heat Transfer Characteristics in HeI with Different Surface Area"*, Advances in Cryogenic Engineering, Vol.44, 1998

Iwasa Y. Leupold M.J., Williams J.E.C., *"Stabilization of Large Superconducting Magnets: Experimental Models"*, IEEE Transactions on Magnetics, Vol. MAG-13, No.1, January 1977

Iwasa Y. Apgar B., *"Transient Heat Transfer to Liquid Helium from Bare and Coated Cu Surfaces in a Vertical Orientation"*, Cryogenics, Vol.18, p.267, 1978

Iwasa Y. Sinclair M., *"Transient Resitive Zones in NbTi Composites"*, IEEE Transactions on Magnetics, Vol.MAG-15, No.1, p.347, Jan.1979

Iwasa Y. "*Mechanical Disturbances in Superconducting Magnets - A Review*", IEEE Transactions on Magnetics, Vol. 28, No.1, p.113, Jan. 1992

Iwasa Y. *"Case Studies in Superconducting Magnets"*, Plenum Press, NY, 1994

James G.B. Lewis K.G., Maddock B.J., *"Critical Heat Fluxes for Liquid Helium Boiling in Small Channels"*, Cryogenics, p.480, Dec.1970

Jayakumar R. *"Critical Energy of Superconducting Composites"*, Cryogenics, Vol.27, p.421, Aug.1987

Jeanneret J.B. Leroy D., Oberli L., Trenkler T., *"Quench Levels and Transient Beam Losses in LHC Magnets"*, LHC Project Report 44, July 1996

Kapitza P.L. "*The Study of Heat Transfer on Helium II*", J.Phys. (USSR) 4, 181, 1941

Kapitza P.L. *"The Study of Heat Transfer in Helium II"*, Journal of Physics USSR, Vol.4, p.181, 1947

Kashani A. Van Sciver S.W., "*High Heat Flux Kapitza Conductance of Technical Copper with Several Different Surface Preparations*", Cryogenics, Vol. 25, p.238, May 1985

Katerberg J.A. Anderson A.C., *"Comparison of Steady-State and Second-Sound Measurements of the Kapitza Resistance"*, Journal of Low Temperature Physics, Vol. 42, No.1/2, p.165, 1981

Katsuki Y. Murakami M., Iida T., Shimazaki T., *"Visualization Study of Film Boiling Onset and Transition to Noisy Film Boiling in Helium II"*, Cryogenics, Vol.35, No.10, p.631, 1995

Khalatnikov I.M. *"An Introduction to the Theory of Superfluidity*", Benjamin Publ. Inc., NY 1965

Kim S.W. Shintomi T., Kimura N., Makida Y., Hirabayashi H., Mito T., Iwamoto A., Yamamoto J., Kimura A., "*Experimental Studies on Stabilities of Rutherford*

Cables for Superconducting Accelerator Magnets", IEEE Transactions on Magnetics, Vol.32, p.2784, 1996

Kim S.W. Adam J.D., "*Fabrication of Porous Metal Cable*", Internal Note, CERN/LHC/MMS 98-02, Jan. 1998a

Kim S.W. Leroy D., Wilson M.N., Ghosh A.K., Sampson W.B.,"*Stability Measurements on Rutherford Cables with Various Treatments*", Proceedings of ASC 98b

Kim S.W. Wolf R., "*Qualitative Model for MQE of a Superconducting Cable*", Proceedings ASC 98c

Kimura A. et al., "*Stabilities of Rutherford Cables with CuNi Matrix and CuMn barrier"*, IEEE Transactions on Applied Superconductivity, Vol. 5, p.385, 1995

Kitamura T. Shiramizu K., Fujimoto N., Rao Y.F., Fukuda K., *"A Numerical Model on Transient, Two-Dimensional Flow and Heat Transfer in He II"*, Cryogenics, Vol.37, No.1, p.1, 1997

Klimenko E.Yu. Martovetsky N.N., *"Stability of the Superconducting Wires. Modern State of the Theory"*, IEEE Transactions on Magnetics, Vol. 28, No.1, p. 842-845, Jan. 1992

Kobayashi H. Yasukochi K., Tokuyama K., *"Heat Transfer to Liquid Helium in a Narrow Channel below 4.2K*", Proc. 6th International Cryogenic Engineering Conference IPC Science & Technology Press, Guildford, England, p.307, 1976

Kobayashi H. Yasukochi K., *"Recovery Heat Flux from Silent and Noisy Film Boiling States in Saturated Liquid Helium II"*, Cryogenics, p.93, Feb. 1979

Kobayashi H. Yasukochi K. "*Stability Test of Superconducting Magnets when Cooled in Different Phases of Liquid Helium*", Advances in Cryogenic Engineering, Vol.27, p.451, 1982

Kobayashi H. Uchida M., Kajiiura Y., Konagaya T., Akedo Y., *"Heat Transfer in Branched Channels Filled with He II"*, Cryogenics, Vol.36, No.3, p.145, 1996

Komarek P. *"Summary of the Workshop on the Stability of Superconductors"*, in Stability of Superconductors, p.5, International Institute of Refrigeration Comission A ½, Saclay, France, 1981

Kremlev M.G. Cryogenics, Vol.7, p.267, 1967

Kupferman R. Mints R.G., Ben-Jacob E., "*Normal Zone Soliton in Large Composite Superconductors*", Advances in Cryogenic Engineering, Vol. 38, p. 509, 1992

Kutateladze S.S., Statistical Science & Technical Publications of Literature on Machinery, Atomic Energy Commission Translation 3770, Technical Information Services Oak Ridge, TN (1949), 1952

Landau L.D. Lifshitz E.M. "*Fluid Mechanics*", Course of Theoretical physics, Volume 6, Pergamon Press, Oxford, 1959

Larbalestier D.C. "*Nb-Ti alloy superconductors-present status and potential for improvement*", Advances in Cryogenic Engineering Materials, Vol. 26, ICMC 1979

Larbalestier D.C. "*Niobium-Titanium superconducting materials*", review presented at the NATO Advanced Study Institute, Sintra, Portugal, Aug. 1980

Leroy D. Perin R., Perini D., *"Design Issues of Superconducting Magnets"*, Proceedings of a lecture series, Academic Training Program CERN, Feb. 1997

Lezak D. Brodie L.C., Semura J.S., Roberts S.M., *"Temperature Dependence of the Time Delay to the Onset of Film Boiling in Liquid Helium"*, Advances in Cryogenic Engineering, Vol. 31, p.439, 1986

London F. "*Superfluids, Vol. II, Macroscopic Theory of Superfluid Helium*", John Wiley & Sons: New York, 1954

Lottin J.C. Miller J.R., Lue J.W., Dresner L., *"Measurements of Traveling Transition Zone Along a Superconductor"*, IEEE Transactions on Magnetics, Vol. MAG-15, No.1, p. 363, Jan. 1979

Lottin J.C. Miller J.R., *"Stability of Internally Cooled Superconductors in the Temperature Range 1.8K to 4.2K"*, IEEE Transactions on Magnetics, Vol. MAG-19, No.3, p.439, May 1983

Lubell M.S. *"Empirical Scaling Formulas for Critical Current and Critical Field for Commercial NbTi"*, IEEE Transactions on Magnetics 19, pp.754-757, 1983

Lyon D.N. *“Boiling Heat Transfer and Peak Nucleate Boiling Fluxes in Saturated Liquid Helium Between the λ and Critical Temperatures”*, Advances in Cryogenic Engineering, Vol.10, p.371, 1965

Maddock B.J. James G.B., Norris W.T., *“Superconductive Composites: Heat Transfer and Steady-State Stabilization”*, Cryogenics 9, p. 261-273, 1969

Malinowski L. *“Analytical Method for Calculation of Critical Energy of Technical Superconductors Taking into Account Transient Heat Transfer”*, Cryogenics, Vol.30, p.27, Jan.1990

Malinowski L. *“Novel Model for Evolution of Normal Zones in Composite Superconductors”* Cryogenics, Vol. 33, No. 7, p.724-728, 1993

Meaden G.T. “*Electrical resistance of metals*”, Plenum Press, NY, 1965

Meuris C. Mailfert A., *“Influence of the Spacers on the Stability of Channel Cooled Superconducting Coils”*, IEEE Transactions on Magnetics, Vol. MAG-17, No.1, p.1079, Jan. 1981

Meuris C. *“Experimental Study of the Stability of a Superconductor Cooled by a Limited Volume of Superfluid Helium”*, IEEE Transactions on Magnetics, Vol.MAG-19, No.3, p.272, May 1983

Meuris C. *“Heat Transport in Insulation of Cables Cooled by Superfluid Helium”*, Cryogenics, Vol.31, p.624, July 1991

Mints R.G. Rakhmanov A.L., *“Current-Voltage Characteristics and Superconducting State Stability in Composites”*, J.Phys. D: Appl. Phys., Vol.15, p.2297, 1982

NAG Fortran library, Numerical Algorithm Group, Wilkinson House, Jordan Rd Oxford OX2 8DR, UK

Nemirovskii S.K. Tsoi A.N., “*Transient Thermal and Hydrodynamic Processes in Superfluid Helium*”, Cryogenics, Vol. 29, pp 985, Oct. 1989

Nemirovskii S.K. Kondaurova L., Baltsevich A., *“Transient Heat Transport in Helium II in Cylindrical Space”*, Cryogenics, Vol.34, ICEC 15 Supplement, p.313, 1994

Ng K.Y “*Minimum Energy to Start a Quench and Optimum Copper-to-NbTi Ratio*”, IEEE Transactions on Magnetics MAG-25, p.506, 1989

Nick W. Krauth H., Ries G., *“Cryogenic Stability of Composite Conductors Taking into Account Transient Heat Transfer”*, IEEE Transactions on Magnetics, Vol.MAG-15, No.1, p.359, Jan 1979

Nick W. Schmidt C., “*Thermal Magnetoresistance of Copper Matrix in Compound Superconductors, a New Measuring Method*”, IEEE Transactions on Magnetics, Vol. Mag.-17, No.1, p.217, Jan. 1981

Nick W. “*Theoretical Results of Stability in Pool Boiling Helium-I*”, in Stability of Superconductors, p.139, International Institute of Refrigeration Comission A ½, Saclay, France, 1981

Ninomiya A. Inada T., Akiba K., Kanda Y., Uriu Y., Ishigohka T., “*Quench of Superconducting Magnet Induced by Mechanical Disturbance Using Impact Hammer*”, IEEE Transactions on Magnetics, Vol. 32, No .4, p. 3081, July 1996

Ogata H. Kuwahara H., Noguchi H., Nakagawa T., *“Boiling Heat Transfer to Liquid Helium from Surface with Pin-Fins”*, Cryogenics, Vol. 31, p.392, May 1991

Ogata H. Nakayama W., *“Heat Transfer to Boiling Helium from Machined and Chemically Treated Copper Surfaces”*, Vol.27, p.309, 1982

Ogitsu T. Tsuchiya K., Devred A., “*Investigation of Wire Motion in Superconducting Magnets*”, IEEE Transactions on Magnetics, Vol. 27, No.2, p.2132, March 1991

Ogitsu T. “*Magexec*”, Superconductor data bank, supermag2.kekjp/~programs/magexec/SCViewer.html

Pasztor G. Schmidt C., Journal of Applied Physics, Vol.49, p.886, 1978

Pavlov Yu.M. Babitch V.I., *“Transient Burn-Out in Liquid Helium with Rapid Rise of Heat Flux”*, Cryogenics, Vol.27, p.641, Nov. 1987

Perin R. “*The Superconducting Magnet System for the LHC”*, IEEE-TMAG, 1991

Perin R. *“State of the LHC Main Magnets”*, LHC Project Report 108, July 1997

Perini D.	Buckley J., Hirsbrunner J.J., Karpinnen M., Kurtika T., Leroy D., Poncet A., Robatto F., Savary F., Spigo G., Vanenkov I., *“Mechanical Behavior During Excitation of the First CERN 10T Dipole Model Magnet for LHC”*, LHC note 282, 1994
Pfotenhauer J.M.	Van Sciver S.W., *“Stability Measurements of a Superconductor Cooled by a Two-Dimensional Channel”*, Advances in Cryogenic Engineering, Vol. 31, p.391-398, 1986
Pugnat P.	Siemko A., “*Interpretation of the Quench Behavior of MBL1AJ2*”, Int. Note CERN/LHC/MTA-IN-97-019, Dec. 1997
Pukhov A.A.	“*Development of “Explosion”-Type Instability in Superconductors with Transport Current*”, Superconductor Science and Technology, Vol. 19, p.547, 1997
Rao Y.F.	Fukuda K., Horie H., *“A Two-Fluid-Model Analysis on Transient, Internal-Convection Heat Transfer of He II in a Vertical Gorter-Mellink Duct Heated at the Bottom Surface”*, Cryogenics, Vol.36, No.6, p.457, 1996
Richter D.	Adam J.D., Depond J.M., Leroy D., Oberli L., *“DC Measurement of Electrical Contacts between Strands in Superconducting Cables for the LHC Main Magnets”*, IEEE Transactions on appl. Superconductivity, Vol.7, N.2, June 1997
Rodriguez-Mateos F.	Coull L., Hagedorn D., Remondino V., *“LHC Magnet Quench Protection System”*, IEEE Transactions on Magnetics, Vol.30, 1994
Romanovskii V.R.	“*Theoretical Study of Quench in Superconducting Magnetic Systems*”, Advances in Cryogenic Engineering, Vol. 35, p.709, 1990
Saclay	Proceedings of the workshop*: “Stability of Superconductors in helium I and helium II”*, Saclay (France), issued by the Intern. Inst. of Refrigeration, 1981
Sakurai A.	Shiotsu M., Hata K., *“Boiling Phenomenon Due to Quasi-Steadily and Rapidly Increasing Heat Inputs in* LN_2 *and LHeI”*, Cryogenics, Vol.36, No.3, p.189, 1996
Simon N.G.	Reed R.P., “Cryogenic properties of Copper and Copper Alloy”, preliminary draft, National Bureau of Standards, Boulder, Colorado, March 1997
Schmidt C.	*“Thermal Boundary Resistance (Kapitza Resistance) at Interfaces between Copper and Type II Superconductor”*, Journal of Applied Physics, Vol.46, No.3, p.1372, March 1975
Schmidt C.	Pasztor G., “*Superconductors under Dynamic Mechanical Stress*”, IEEE Transactions on Magnetics, Vol. MAG-13, No.1, p.116, 1977
Schmidt C.	*“Transient Heat Transfer to Liquid Helium and Temperature Measurement with a Response Time in the Microsecond Region”*, Applied Phys. Letters, Vol.32, p.827, 1978
Schmidt C.	“*Review of Steady-State and Transient Heat Transfer in Pool Boiling Helium I*”, in Stability of Superconductors, p.17, International Institute of Refrigeration Comission A ½, Saclay, France, 1981
Schmidt C.	“*Transient Heat Transfer into a Closed Volume of Liquid or Supercritical Helium*”, Cryogenics Vol. 28, p.585, Sept. 1988
Schmidt C.	“*Transient Heat Transfer to a Closed Volume of He I and its Influence on Superconductor Stability*”, Cryogenics Vol. 31, pp.618, July 1991
Schwall R.E.	Reles F.J., Heinrich J.P., *“Measurements of Heat Transfer and Helium Replenishment in Long Narrow Channels”*, Advances in Cryogenic Engineering, Vol.25, p.406, 1980
Scott C.A.	*“Minimum Heat Pulse to Quench a Superconducting Magnet*”, in Stability of Superconductors, p.189, International Institute of Refrigeration Comission A ½, Saclay, France, 1981
Senba T.	Yamaguchi S., Yanagi N., Mito T., Yamamoto J., Motojima O., Emoto M., “*Thermal Behavior of a Composite Superconductor in Stability Margin Experiments*”, IEEE Transactions on Magnetics, Vol.32, No.4, p.3085, July 1996

Seo K. Morita M., Nakamura S., Yamada T., Jizo Y., *"Minimum Quench Energy Measurement for Superconducting Wires"*, IEEE Transactions on Magnetics, Vol. MAG-32, No.4, p.3089, July 1996a

Seo K. Morita M., Yamamoto S., *"Stability of Synthetic Enameled Superconducting Wires"*, Proceedings of ICEC/ICMC 16, May 1996b

Seo K. Morita M., Yoshimura H., Nishijima S., Okada T., *"Thermal Properties of Impregnating Materials for Stable Superconducting Magnets"*, IEEE Transactions on Applied Superconductivity, Vol.7, No.2, p.155, June 1997

Seol S.Y. Chyu M.C., *"Prediction of Superconductor Behavior When Subjected to a Local Thermal Disturbance"*, Cryogenics, Vol.34, No.6, p.521, 1994a

Seol S.Y. Chyu M.C., *"Stability Analysis for a Composite Superconductor Subjected to a Linear Thermal Disturbance"*, Superconductor Science-Technology, Vol.7, No.11, p.841, Nov. 1994b

Seyfert P. Claudet G., McCall M.J., Aymar R., *"Transient Heat Transfer in Boiling Helium-I and Subcooled Helium II"*, Advances in Cryogenic Engineering, Vol. 25, p. 378, 1980

Seyfert P. *"Results on Heat Transfer to He II for Use in Superconducting Magnet Technology"*, Proc. of the 9th Int. Cryog. Eng. Conf., p.263, 1980 b

Seyfert P. Claudet G., McCall M.J., Aymar R., *"Transient Heat Transfer in Boiling Helium-I and Subcooled Helium-II"*, Advances in Cryogenic Engineering, Vol. 25, p.378, 1980 c

Seyfert P. Lafferanderie J., Claudet G., "*Time Dependent Heat Transport in Subcooled Superfluid Helium*", Cryogenics 22, pp401, 1982

Shimazaki T. Murakami M., Iida T., *"Second Sound Wave Heat Transfer, Thermal Boundary Layer Formation and Boiling: Highly Transient Heat Transport Phenomena in He II"*, Cryogenics, Vol.35, No.10, pp.645, 1995

Shiotsu M. Hata K., Sakurai A., *"Comparison of Transient Heat Transfer Characteristics for Large Stepwise Heat Input in He I and He II"*, Cryogenics, Vol. 32, No.5, p.455, 1992

Shiotsu M. Hata K., Sakurai A., *"Transient Heat Transfer from a Horizontal Wire in Subcooled He II at Atmospheric Pressure for a Wide Range of Wire Diameter"*, Advances in Cryogenic Engineering, Vol. 41, p.241, 1996

Siemko A. Billan J., Gerin G., Leroy D., Walckiers L., Wolf R., "*Quench Location in the Superconducting Model Magnets for the LHC By Means of Pick-Up Coils*", IEEE Transactions on Applied Superconductivity, Vol.5, No.2, p.1028, June 1995

Siemko A. *"MBSMS13.V1 Short Dipole Model - Summary of Training Quench Performance"*, Internal Note MTA-IN-97-017, Dec. 1997

Simon N.G. Reed R.P., "Cryogenic properties of Copper and Copper Alloy", preliminary draft, National Bureau of Standards, Boulder, Colorado, March 1997

Stekly Z.J.J. Zar J.L., *"Stable Superconducting Coils"*, IEEE Transactions on Nuclear Science 12, p. 367-372, 1965

Steward W.G. *"Transient Helium Heat Transfer / Phase 1 - Static Coolant"*, International Journal of Heat and Mass Transfer, Vol.21, p.863, 1978

Superczynski M.J. "*Heat Pulses Required to Quench a Potted Superconducting Magnet*", IEEE Transactions on Magnetics, Vol. MAG-15, No.1, p.325, Jan. 1979

Swartz P.S. Bean C.P., Journal of Applied Physics 39 (11), p.4991, 1968

Takao T. Honjo S., Tsukamoto O., "*Frictional Motion of Conductor in Superconducting Magnet and Quantification of Disturbance Energy*", Advances in Cryogenic Engineering, Vol. 35, p.737, 1990

Takao T. Michael P.C., Tsukamoto O., "*Influence of Copper-to-Superconductor Ratio on the Stability of High Current Density Superconductor*", IEEE Transactions on Magnetics, MAG-30, No.4, p.2439, July 1994

Takao T. Tsukamoto O., Furuse M., Tsuchiya K., "*Statistical Estimation of Quench Characteristics of Quadrupole Magnets*", IEEE Transactions on Applied

	Superconductivity, Vol.7, No.2, p.183, June 1997
Tamada N.	Fuchino S., Agastuma K., Ishii I., Kaiho K., Okano M., "*Observation of Transient Cooling Phenomenon in Liquid Helium by an Optical Measurement*", Cryogenics, Vol.34, ICEC Supplement, p.345, 1994
Tamai T.	"*Singularity of Contact Resistance at very Low Temperature*", IEEE Transactions on Components, Hybrids, and Manufacturing Technology, Vol. CHMT-9, No.1, p.40-45, March 1986
Taneda M.	Miki T., Ohtani T., "*The Kapitza Conductance of PVF-Coated Copper and Some Materials Used for Superconducting Magnets*", Cryogenics, Vol.32, No.5, p.479, 1992
Tsuda M.	Shimada T., Takada Y., Ishiyama A., "*Thermal and Electromagnetic Behavior in NbTi/CuNi Superconducting Wires Under Fast Changing Transport Current*", IEEE Transactions on Magnetics, Vol.30, No.4, p.2487, 1994
Tsuda M.	Toyoda N., Matsui M., Ishiyama A., "*Stability of Non-Insulated A.C. Multi-Strand Superconducting Cables*", IEEE Transactions on Magnetics, Vol. 32, No. 4, p. 2854, July 1996
Tsukamoto O.	Miyagi F., "*Analysis of Propagation of Normal Zones in Immersion Cooled Composite Superconductors*", IEEE Transactions on Magnetics, Vol. MAG-15, No.1, p.367, 1979
Tsukamoto O.	Nakada M., "*Stability of High Current Density Composite Superconductor Subject to Pulsive and Local Disturbance*", IEEE Trans. on Magnetics, Vol. MAG-21, No.2, p. 370, March 1985
Tsukamoto O.	Nakada M., "*Stability of High-Current-Density Composite Superconductor Subject to Pulsive and Local Disturbance*", IEEE Transactions on Magnetics, Vol. MAG-21, No.2, p.370, March 1985
Tsukamoto O.	Kobayashi H., Akita S., "*Stability of Epoxy-Impregnated AC Superconducting Winding*", IEEE Transactions on Magnetics, Vol.24, No.2, p.1170, March 1988
Tsuruga H.	Kobayashi H., "*Effect of Channel Geometry on Heat Transfer in He II Chamber*", Cryogenics, Vol. 31, p.927, Nov.1991
Tyler W.W.	Wilson A.C., Knolls atomic laboratory report 803, pp. 41, 1952
Usak P.	"*Indirect Measurement of NbTi Wire Temperature Field Response to Local Heat Input*", Cryogenics, Vol. 34, p.531, ICEC Supplement, 1994
Van Sciver S.W.	"*Transient Heat Transport in He II*", Cryogenics 19, pp.385, July 1979
Van Sciver S.W.	Lee R.L., "*Heat Transfer to Helium II in Cylindrical Geometry*", Advances in Cryogenic Engineering, Vol. 25, p.363, 1980
Van Sciver S.W.	"*Some Experiments with Helium II Above the Critical Heat Flux*", in Stability of Superconductors, p.75, International Institute of Refrigeration Comission A ½, Saclay, France, 1981
Van Sciver S.W.	"*Developments in He II Heat Transfer and Applications to Superconducting Magnets*", Advances in Cryogenic Engineering, Vol. 27, p. 375, 1982
Van Sciver S.W.	"*Helium Cryogenics*", Plenum Press, NY, 1986
Van Sciver S.W.	"*Stability of Superconductors Cooled Internally by He II Heat Transfer*", Cryogenics, Vol. 31, p.516, July 1991
Van Sciver S.W.	Kingsbury D., "*Transient Thermal Processes in He II: Vorticity and Boiling*", 1995
Verkin B.I.	Kirichenko Yu.A., Kozlov S.M., Rusanov K.V., "*Heat Transfer During Pool Boiling of Subcooled Helium*", Proceedings of the 8th International Conference on Cryogenic Engineering", p.256, 1980
Verweij A.P.	Wolf R., "*Field errors due to Interstrand Coupling Currents in the LHC Dipole and Quadrupole*", CERN Internal Note AT-MA 94-97, 1994
Verweij A.P.	"*Electrodynamics of Superconducting Cables in Accelerator Magnets*" , Doctoral thesis, TU Twente, 1995
Verweij A.P.	"*Current Redistribution in the Cables of LHC Magnets*", LHC Project Note 90, May 1997

Vinen W.F. *"Mutual Friction in a Heat Current in Liquid Helium II"*, Proc. Roy. Soc., 242, N1231, p.493, 1957

Vinen W.F. "*Physical Properties of Superfluid Helium - a General Review*", in Stability of Superconductors, pp.43, International Institute of Refrigeration Comission A ½, Saclay, France, 1981

Wang R. Gradt T., Ruppert U., Lie X., Denner H.D., Klipping G., *"Film Boiling Onset Time in Subcooled Superfluid Helium: the Influence of Bath Temperature and Pressure"*, Cryogenics, Vol. 30, pp.360, September Supplement 1990

Wang R. "*Criterion for Quantum Turbulence Onset after Rectangular Heat Pulse in Superfluid Helium*", Cryogenics, Vol. 35, pp.883, Dec.1995

Warren R.P. Caspi S., *"Measurements of Heat Transfer to He II at Atmospheric Pressure in a Confined Geometry"*, Advances in Cryogenic Engineering, Vol.27, p.459, 1982

White G.K. Woods S.B., Can. Journal of Physics 35, pp. 892, 1957

Wilks J. Betts D.S., *"An Introduction to Liquid Helium"*, 2nd edition, Clarendon Press, Oxford 1987

Willig R.L. "*Recovery Velocities For Composite Superconductors*", Advances in Cryogenic Engineering, Vol. 23, p.179, 1978

Wilson M.N. Iwasa Y., *"Stability of Superconductors Against Localized Disturbances of Limited Magnitude"*, Cryogenics, p.17, Jan.1978

Wilson M.N. *"Superconducting magnets"*, Oxford University Press, NY, 1983

Wilson M.N. *"Stabilization, Protection and Current Density: Some General Observations and Speculations"*, Cryogenics, Vol 31, p. 499-503, July 1991

Wilson M.N. Ghosh A.K., Sampson W.B., *"Cable conductors for High Field Accelerator Magnets"*, Internal Note LHC/MMS 96-03, March 1996

Wilson M.N. Sampson W.B., Ghosh A.K., "*Experimentally measured Minimum Quench Energies of LHC Cables"*, LHC Project report 86, CERN, Jan. 1997a

Wilson M.N. "*Computation of Minimum Quench Energies in LHC Cables*", LHC Project Report 82, CERN, Jan 1997b

Wilson M.N. Ghosh A.K., Sampson W.B., "*Minimum Quench Energies of Rutherford Cables and Single Wires*", IEEE Transactions on Applied Superconductivity, Vol. 7, No.2, June 1997c

Wilson M.N. Wolf R., "*Calculation of Minimum Quench Energies in Rutherford cables*", IEEE Transactions on Applied Superconductivity, Vol. 7, No.2, June 1997d

Wipf S.L. Martinelli A.P., "*Stability and MPZ*", Proc. 1972 Applied Superconductivity Conference, Anapolis, IEE, NY, p. 331, 1972

Wipf S.L. *"Stability and Degradation of Superconducting Current Carrying Devices"*, Los Alamos Scientific Laboratory Report LA-7275, 1978

Wipf S.L. *"Stability of the Superconductive Mode in High Current-Density Devices"*, IEEE Transactions on Magnetics, Vol. Mag-15, No.1, p.379, Jan.79

Wolf R. *"Persistant Currents in LHC Magnets"*, IEEE Transactions on Magnetics 28, p.374-377, 1992

Wolf R. "*Optimum Copper to Superconductor Ratio in Cables for Superconducting Magnets at 1.9K*", IEEE Transactions on Magnetics, Vol.30, No.4, p.1786, July 1994

Yoda K. Morita M., *"Minimum Quench Energy Measurement of NbTi Wires Using a Small Ceramic Heater"*, IEEE Transactions on Magnetics, Vol.27, No.2, p.2159, March 1991